

Guiding and decelerating cold, heavy, polar molecules

Thomas Edward Wall

Thesis submitted in partial fulfilment of the requirements for the degree of
Doctor of Philosophy of the University of London and the
Diploma of Membership of Imperial College

Department of Physics

Imperial College

University of London

July 2010

Declaration of originality

I declare that the research presented in this thesis is my own work. Any research or data presented herein that was performed by someone else has been correctly referenced.

Abstract

Cold molecules are extremely useful for tests of fundamental physics. Unlike many atomic species, molecules cannot generally be laser cooled, and another interaction is required to exert control over them. The Stark interaction with an applied electric field changes the energy of a molecule and can be used to affect its motion. This thesis describes experiments in which applied electric fields have been used to guide and decelerate beams of CaF radicals.

Two Stark decelerators have been built and tested. One, a 21-stage decelerator, has been used to slow ground-state molecules from 433 ms^{-1} to 403.5 ms^{-1} . The other, a 100-stage decelerator, has been used to decelerate molecules in the fourth rotationally excited state from 343 ms^{-1} to 247 ms^{-1} , a removal of 48% of their initial kinetic energy. It was found that the switching electric fields inside a decelerator can drive non-adiabatic transitions out of the desired state of the molecule, and that this can severely reduce the flux of molecules out of a decelerator. Applying a bias field was found to inhibit these transitions, and to vastly increase the number of molecules making it out of the decelerator.

A 1 m-long alternating gradient guide has been built and used to transport ground-state CaF molecules from a supersonic source, and to focus them into a detection region. A novel guiding mode was discovered, in which the guide is operated with a static applied voltage.

A detailed spectroscopic investigation of CaF measured the $^2\Pi_{1/2}$ state lifetime and hyperfine interval to be $19.2 \pm 0.7 \text{ ns}$ and $4.8 \pm 1.1 \text{ MHz}$ respectively, and the Franck-Condon factor of the $A-X$ (0-0) transition to be $0.987^{+0.013}_{-0.019}$.

Acknowledgments

This thesis describes three and a half years' work, all of which would not have been possible without the help and support of many people. Of these many, several deserve particular mention.

I have been extremely lucky to have had BES and MRT as my supervisors. Not only have they taught and trained me, they have done so with seemingly limitless patience and good humour. It has been a particular privilege to work for EAH – he is an inspirational boss.

KAPW, PMH, CWPP and JWH have been exceptional teachers, and I have been extremely fortunate to have met them.

None of the experiments would have been possible without the amazing technical capabilities of the CCM Mechanical Workshop. Without JMD and DW there would have been no decelerators. Or a great many other things.

I would like to thank all the members of the CCM. In particular, SKT for many enlightening discussions, and for being an excellent friend and flat-mate. I should also like to thank the two post-docs I have had during my PhD, JFK and SA.

I would like to thank GMT for her incredible support and companionship. There are so many things for which to thank Pj, but in particular he has put up with me while I was writing this. His continued interest in what I do is a source of great motivation for me, more than he knows.

Finally, my family has always been the most extraordinary source of inspiration, and I dedicate this thesis to them.

Contents

1	Testing fundamental physics with cold molecules	14
1.1	Why molecules?	14
1.1.1	The electric dipole moment of the electron	14
1.1.2	Measuring time-variation of fundamental constants	18
1.1.3	Observing parity violation	19
1.2	Why <i>cold</i> molecules?	20
1.2.1	Indirect methods	20
1.2.2	Direct methods	21
1.3	Motivation for this thesis	23
2	Introduction to molecular physics	26
2.1	Basic diatomic molecular structure	26
2.1.1	Born-Oppenheimer Approximation	26
2.1.2	Eigenstates of the nuclear wave equation	28
2.1.3	Electronic States	28
2.1.4	Vibrational States	29
2.1.5	Rotational energy levels	30
2.1.6	The separation of molecular energies	30
2.2	Coupling angular momenta	30
2.2.1	Hund's case (a)	31
2.2.2	Hund's case (b)	31
2.3	Molecular transitions	32
2.3.1	Electric dipole matrix element	32
2.3.2	The hyperfine interaction	33
2.3.3	Selection rules for electronic transitions	33
2.4	The Stark effect	34
2.5	Stark Deceleration	37
2.6	Focussing a molecular beam	41

3	Making and detecting CaF	42
3.1	Overview	42
3.2	Producing a molecular beam	42
3.2.1	Supersonic Expansion	43
3.3	Detection	47
3.3.1	Detection overview	47
3.3.2	The probe laser	50
3.3.3	Electronic transitions in CaF	50
4	Measuring molecular parameters	57
4.1	Motivation	57
4.2	Saturation mechanisms	58
4.3	Summary of what is to come	59
4.4	Measuring spectra	60
4.4.1	Transitions	60
4.4.2	Experimental set-up	61
4.4.3	Linearization	63
4.4.4	Frequency scanning with an AOM	66
4.4.5	Accounting for drifts in source flux	67
4.4.6	Magnetic Field	70
4.5	Experimental results	70
4.6	Model	76
4.6.1	Rate Equations	76
4.6.2	Molecular population dynamics	79
4.6.3	Running the model	81
4.7	Comparing the model with experimental data	82
4.8	Evaluating the molecular parameters	82
4.8.1	Systematic errors	84
5	Decelerating weak-field seeking CaF molecules	87
5.1	Motivation	87
5.2	Brief review of Stark deceleration of weak-field seeking molecules	87
5.3	Experimental details	88
5.3.1	The decelerator	88
5.3.2	Electric fields and high voltage electronics	91
5.4	The Stark shift and the hyperfine structure	99
5.5	Transverse focussing of weak-field seeking molecules	102
5.6	Longitudinal focussing in a Stark decelerator	106
5.6.1	Phase stability in a Stark decelerator	106

5.6.2	Longitudinal dynamics in the 100-stage decelerator	111
5.7	Preliminary deceleration results	114
5.8	Non-adiabatic transitions	117
5.8.1	The Hamiltonian in a rotated coordinate system	118
5.8.2	The effect of the changing field magnitude	119
5.8.3	The effect of the electric field rotation	120
5.9	Preventing non-adiabatic transitions	126
5.10	Final deceleration data	128
5.11	Conclusions	132
6	Guiding ground-state CaF molecules	134
6.1	Motivation	134
6.2	Guiding strong-field seekers	135
6.3	A review of previous AG guiding experiments	136
6.4	An ‘ideal’ guide	137
6.4.1	Equations of motion	137
6.4.2	Courant-Snyder parameters	139
6.4.3	Molecular trajectories	141
6.5	A realistic guide	145
6.5.1	Non-linear equations of motion	145
6.5.2	Effective potential	147
6.6	Experimental details	151
6.7	Modelling the AG guide	155
6.8	AG results	157
6.9	DC results	164
6.10	Conclusions	169
7	Decelerating ground-state CaF molecules	172
7.1	Motivation and general physical principles	172
7.2	A brief review of previous research	173
7.3	Experimental set-up	174
7.4	The axial electric field	175
7.5	Dynamics inside the AG decelerator	178
7.5.1	Longitudinal dynamics	178
7.5.2	Transverse dynamics	180
7.6	Experimental procedure	183
7.7	Results	184
7.7.1	Deceleration with $z_{on} = 0$ mm and $z_{off} = 6$ mm	184
7.7.2	Deceleration with $z_{on} = 6$ mm and $z_{off} = 10$ mm	195

7.8	Conclusions	202
8	Conclusions and Outlook	204
8.1	Measuring molecular parameters	204
8.2	Guiding ground-state CaF	205
8.3	Decelerating CaF	206
8.4	Outlook	212
A	Branching ratios	214
B	The Optical Bloch Equations and Rate Equations	215
C	Stark interaction in a rotating frame	217

List of Figures

2.1	The Stark shift of a rigid rotor as a function of applied electric field.	36
2.2	The electric field at which the Stark-shifted state $ \mathcal{N}, M_N = 0\rangle$ experiences its maximum Stark shift for $0 \leq \mathcal{N} \leq 9$	37
2.3	A schematic diagram showing the general structure of a Stark decelerator. .	38
2.4	A mechanical model of a Stark decelerator.	40
3.1	Schematic diagram of the creation and detection of pulsed beams of CaF. .	43
3.2	A photograph of the vacuum chamber	48
3.3	An example time-of-flight profile for CaF in an Ar-carried beam.	49
3.4	Rotational levels of the $X^2\Sigma^+(v=0)$ and $A^2\Pi_{1/2}(v'=0)$ states.	53
3.5	Experimental spectrum of CaF measured by laser induced fluorescence. . .	54
3.6	The $Q_{11}(\frac{9}{2})$ and $R_{21}(\frac{7}{2})$ lines originating from the $N=4$ state of CaF. . . .	55
4.1	The energy levels of CaF relevant to the measurement of molecular parameters.	60
4.2	An example laser beam profile.	62
4.3	An example of scan linearization.	64
4.4	The RF power transmitted to the AOM and the laser power in the first order beam, both as a function of VCO frequency.	66
4.5	Two linearized spectra.	71
4.6	Peak height versus peak laser intensity for the $F=1$ and $F=0$ peaks. . . .	73
4.7	The linearized widths of the $F=0$ and $F=1$ peaks as a function of probe beam intensity.	75
4.8	$F=1$ peak width measured at various weak laser intensities, both by scanning the laser lock-cavity, and by scanning an AOM.	76
4.9	Fractional state populations of a molecule traversing the probe beam. . . .	80
4.10	Peak height versus peak laser intensity for the $F=1$ peak and the $F=0$ peak, with simulations.	82
4.11	The width of the $F=0$ and $F=1$ peaks as a function of probe beam intensity, with simulations.	83

5.1	A cross-section of two field stages of the 100-stage decelerator.	88
5.2	A schematic diagram of the 100-stage decelerator	89
5.3	Three photographs of the 100-stage decelerator.	90
5.4	Three deceleration stages of the 100-stage decelerator, and the axial electric field profiles created by charging these electrodes in two high voltage states.	92
5.5	The circuitry used to switch the voltage applied to each of the four rods of the 100-stage decelerator from the ‘high’ state, V_{HI} , to the ‘low state’, V_{LO}	93
5.6	The measured voltage of the two oppositely polarized rods corresponding to one set of 50 deceleration stages in the 100-stage decelerator.	95
5.7	The measured voltage of the same two rods as in figure 5.6, but no longer switching to ground.	98
5.8	The Stark shift of the $\mathcal{N} = 4$ states of a CaF.	100
5.9	The mapping of the 36 M_F states of the four field-free states ($F = 5, 4, 3, 4$) to the five Stark-shifted rigid rotor sub-level groups ($ M_N = 0, 1, 2, 3, 4$).	101
5.10	Two scans over the $Q_{11}(\frac{9}{2})$ and $R_{21}(\frac{7}{2})$ lines of CaF, taken with the decelerator off (blue points) and with ± 13 kV applied (red data).	102
5.11	Measured signal ratios of the $Q_{11}(\frac{9}{2})$ and $R_{12}(\frac{7}{2})$ lines as a function of applied voltage to the 100-stage decelerator, used in DC guiding mode.	103
5.12	The mean trapping frequencies of the magnetic sub-levels of the $\mathcal{N} = 4$ rigid rotor state as a function of voltage applied to the 100-stage decelerator.	104
5.13	The total trapping frequency of all the guided rigid rotor states associated with the measured $Q_{11}(\frac{9}{2})$ and $R_{12}(\frac{7}{2})$ lines.	105
5.14	Longitudinal effective potential energy in a weak-field decelerator	110
5.15	The Stark shift experienced by CaF radicals with ± 15 kV applied to the decelerator in states 1 and 2. Also shown is the difference of these two profiles.	111
5.16	Phase space trajectories inside the 100-stage decelerator calculated with the decelerator charged to ± 15 kV, and with $\phi_{sync} = 0, \frac{\pi}{6}$ and $\frac{\pi}{3}$	113
5.17	The longitudinal acceptance of the weak-field decelerator with ± 15 kV applied to the electrodes.	114
5.18	Experimental and simulated time-of-flight profiles taken with the 100-stage decelerator operating with $V_{LO} = 0$, $V_{HI} = 14$ kV, $\phi_{sync} = 0$	115
5.19	Experimental and simulated time-of-flight profiles taken with the 100-stage decelerator operating with $V_{LO} = 0$, $V_{HI} = 14$ kV, $\phi_{sync} = 75^\circ$	117
5.20	The angular rotation rate of the electric field inside the decelerator, shown for a range of longitudinal phase positions.	122
5.21	The probability of a molecule occupying each of the different magnetic sub-levels $ \mathcal{N} = 4, M_N \neq 0\rangle$ after a field-switch.	124

5.22	The probability of a molecule occupying any of the different magnetic sub-levels $ \mathcal{N} = 4, M_N \neq 0\rangle$ after a field-switch.	125
5.23	Experimental and simulated time-of-flight profiles measured with $V_{HI} = 14$ kV, $\phi_{sync} = 0$ and $v_{sync} = 370 \text{ ms}^{-1}$. V_{LO} is varied between 0 and 1.45 kV.	127
5.24	Experimental and simulated time-of-flight profiles with $V_{HI} = 14$ kV, $v_{sync} = 350 \text{ ms}^{-1}$ and $\phi_{sync} = 75^\circ$. V_{LO} was varied between 0 and 1.95 kV.	129
5.25	Experimental and simulated deceleration data of CaF radicals in the $ 4, 0\rangle$ state, with $V_{HI} = 18$ kV and $V_{LO} = 1$ kV.	130
5.26	The time-of-flight profile measured with ± 18 kV applied to the 100-stage decelerator, operated with a phase angle of 75°	131
5.27	The longitudinal acceptance of the decelerator as a function of synchronous phase, compared with the area of the decelerated peak.	132
6.1	The form of a trajectory in an AG guide.	142
6.2	The 1D acceptance of a harmonic AG guide, as a function of κL and κS	143
6.3	The 1D acceptance of a gapless guide, and three example molecular trajectories.	144
6.4	The effect of the cubic term on the effective potential inside a realistic AG guide.	148
6.5	The effect of the coupling term on the effective potential in a guide.	150
6.6	Two photographs of the AG guide.	152
6.7	Set-up of the AG guiding experiment.	153
6.8	The two transverse electric field states inside the the AG guide.	154
6.9	The acceptance and an example trajectory for the constructed AG guide calculated by four different models.	155
6.10	Data and simulations showing signal ratio versus lens duration.	158
6.11	The $F = 1$ peak amplitude and area signal ratios measured with the guide operated at 8.0 kV.	161
6.12	The HV switching pattern sent to the AG guide for operation at three lens durations.	163
6.13	The signal ratio with the AG guide used in ‘DC’ mode, in which it acts as a single 1 m-long lens.	165
6.14	The transverse electric field produced by the guide charged to ± 10 kV, and the Stark shift experienced by ground-state CaF.	166
6.15	Simulated trajectories along the guide operated in DC guiding mode for a range of applied voltages.	168
7.1	A typical deceleration stage in an AG decelerator.	173
7.2	A diagram of the AG decelerator	175

7.3	A photograph of three deceleration stages in the AG decelerator.	176
7.4	The electric field profiles and Stark shifts inside the AG decelerator.	177
7.5	The Stark shift and longitudinal dynamics of CaF radicals in the AG decelerator.	179
7.6	Electric field magnitude on the $z = 0$ plane with ± 20 kV applied to the AG decelerator.	180
7.7	The transverse forces exerted on a CaF radical in the $ 4, 0\rangle$ state inside a charged stage of the AG decelerator.	181
7.8	The Stark potential and effective longitudinal potentials inside a charged deceleration stage, with $z_{on} = 0$ mm and $z_{off} = 6, 8, 10$ mm.	183
7.9	Deceleration data taken with the AG decelerator operating at ± 20 kV, and with $z_{on} = 0$ mm and $z_{off} = 6$ mm.	185
7.10	The delay plotted as a function of the number of decelerator stages used. The decelerator was charged to ± 20 kV, and $z_{on} = 0$ mm and $z_{off} = 6$ mm.	187
7.11	Simulated speed profiles calculated with the AG decelerator operating at ± 20 kV, with $z_{on} = 0$ and $z_{off} = 6$ mm.	188
7.12	The signal ratio of the decelerated peak, and the entire time-of-flight profile as a function of the number of stages used.	190
7.13	The sum of the transverse force constants, $k_x + k_y$, inside a field stage of the AG decelerator, charged to ± 20 kV.	192
7.14	The source distribution of molecules that successfully make it through the AG decelerator.	192
7.15	The position inside the first stage of the AG decelerator occupied by five velocity groups when the stage is charged.	194
7.16	Experimental and simulated time-of-flight profiles taken recorded with the AG decelerator operating at ± 20 kV, and with $z_{on}/z_{off} = 6/10$ mm.	196
7.17	Experimental and simulated delay data recorded with the AG decelerator operating at ± 20 kV, and with $z_{on}/z_{off} = 6/10$ mm.	197
7.18	The effective potential well calculated for $z_{on}/z_{off} = 6/10$ mm inside the AG decelerator, operating at ± 20 kV.	199
7.19	The signal ratio of both the decelerated peak and the entire recorded time-of-flight profile versus the number of stages used.	201
7.20	The experimental signal ratios taken with the AG decelerator operating with $z_{on}/z_{off} = 0/6$ mm and $z_{on}/z_{off} = 6/10$ mm.	201
8.1	Simulations of deceleration with a 200-stage Stark decelerator.	208
8.2	The 1D acceptance of an AG guide, highlighting the effect of changing the beam speed.	210

List of Tables

5.1	Magnetic sub-level components of the field-free states	101
-----	--	-----

Chapter 1

Testing fundamental physics with cold molecules

Much fundamental physics is not properly understood. From theories of particle physics beyond the standard model to the development of life as we know it, there is uncertainty. Laboratory-based experiments with cold molecules offer the prospect of extremely high-precision tests of fundamental symmetries, which can resolve these uncertainties.

This chapter gives an introduction to why molecules are useful in experimental tests of fundamental physics. The emphasis is on the measurement of the electric dipole moment of the electron, as this measurement was the motivation for the research reported in this thesis. However, several other experiments using molecules are described to give an overview of the field.

The chapter then describes why cold molecules in particular are useful, and gives a brief description of the various methods used to produce cold molecules. Finally there is a discussion of the motivations and objectives of the experiments with CaF radicals described in this thesis.

1.1 Why molecules?

1.1.1 The electric dipole moment of the electron

CPT symmetry

Symmetry lies at the heart of physics. The development of much 20th century physics has been concerned with a description of the symmetries of fundamental interactions. An early assertion was that of P-symmetry, in which a system is symmetric under a parity transformation, $\vec{r} \rightarrow -\vec{r}$. The laws of physics were expected to be invariant under a parity transformation. If a given interaction between particles is observed in nature, then the parity-transform of that interaction should be observed with equal probability. In 1957

the first experimental evidence was presented of a process for which this is not true [1]. This experiment measured β -decay in ^{60}Co . ^{60}Co decays to ^{60}Ni , emitting an electron. Consider the electron to be emitted at some angle, θ , to the direction of the axial vector defined by the nuclear spin. In the parity-transform of this interaction the nuclear spin vector is pointing in the same direction as in the original nucleus, although the direction of the emitted electron is reversed. The angle between the emitted electron's trajectory and the nuclear spin vector is thus $\pi - \theta$ in the mirror image. If P-symmetry is obeyed then both decay angles should be detected with the same probability. The 1957 experiment, however, found that one direction was preferred over the other, indicating that P-symmetry is violated.

Investigation of this violation led to the assertion that the decay asymmetry is opposite for an anti-particle than for its associated particle. The combination of the symmetry associated with exchanging a particle for its anti-particle (known as 'charge conjugation' or C-symmetry) and P-symmetry can be described by the compound CP-symmetry. It was thus asserted that the measured decay asymmetry in ^{60}Co is consistent with CP invariance. However, experimental evidence has since been found for CP violations, most notably in kaon decay [2].

There is a theory in which the total parity, charge conjugation and time symmetry (the symmetry of a system under the transformation $t \rightarrow -t$) of a system is invariant. This CPT theory allows for CP violation during a process, as long as T-symmetry is also broken during this process. The standard model of particle physics includes a mechanism for T-violation. This mechanism predicts a non-zero electric dipole moment (EDM) of the electron. Theories of particle physics that go beyond the standard model also predict EDMs, but with values much larger than that in the standard model [3]. A measurement of the electron EDM would thus be a confirmation of T-violation, and could be used to discount and refine theories of particle physics.

Measuring electron dipole moments with molecules

The method of measuring the EDM of a particle is to place the particle in an applied electric field, and measure the interaction energy. This is exactly the method used to measure the neutron EDM [4]. Of course, this method cannot be used to measure the EDM of any charged particle because the particle would be accelerated away from the experiment by the applied field. The technique used to measure the EDM of charged particles is to use an atom or molecule. There is a theorem, known as Schiff's theorem [5], which states that for a bound system of point charges, in which only electromagnetic forces act and in which relativistic effects are neglected, the internal electric field of the system exactly cancels any applied electric field at the position of each charge, so that the net electric field experienced by each charge is zero. There can thus be no interaction between an applied electric field

and the EDM of an electron inside an atom or molecule. This renders such a system useless for measuring the size of an EDM. However, Schiff went on to discuss the limitations of this theorem: the particles are not all point-like, and the electron moves quickly enough for relativistic effects to become non-negligible. The non-point-like nature of a particle can lead to incomplete shielding of an EDM from an applied field as the distribution of the EDM is different from the charge distribution in that particle. This is particularly evident when measuring the EDM of a large nucleus. However, this argument makes no difference to the measurement of an electron's EDM as it *is* a point particle. The measurement of an electron EDM thus relies on relativistic effects, in particular the Lorentz contraction of the EDM in the laboratory frame [6]. Consider measuring the electron EDM in an atom, with proton number, Z . The relativistic correction applies most strongly to the fast-moving s -electrons close to the nucleus. Given that the EDM, d_e , points along or against the direction of the electron spin, $\vec{\sigma}$, the total EDM of a closed shell is zero. Consequently, to measure the EDM of a single electron requires using an atom with a single unpaired s -electron. The electric field experienced by this electron is dominated by the nucleus' Coulomb field: $Z\hat{r}/r^2$. It can be shown [3] that the first order interaction energy between such an electron and this field is

$$\langle H^1 \rangle = \left\langle \phi_{s_{1/2}} \left| 2d_e \vec{\sigma} \cdot \frac{Z\hat{r}}{r^2} \right| \phi_{s_{1/2}} \right\rangle = 0. \quad (1.1)$$

This energy is zero because the operator \hat{r} has odd parity. Applying an electric field to this system will mix the electronic states, and this mixing can lead to a non-zero value of $\langle H^1 \rangle$. The dominant mixing is with the $p_{1/2}$ state. It can be shown [3] that there is a non-zero matrix element in $\langle H^1 \rangle$:

$$\left\langle \phi_{s_{1/2}} \left| 2d_e \vec{\sigma} \cdot \frac{Z\vec{r}}{r^2} \right| \phi_{p_{1/2}} \right\rangle \sim 4Z(Z\alpha)^2 d_e, \quad (1.2)$$

where α is the fine-structure constant. This non-zero matrix element allows for a non-zero EDM interaction energy, and can amplify the interaction, particularly for heavy atoms (large Z). This amplification depends on the strength of the applied field, and is described by the 'enhancement factor', $\alpha(E)$ (not to be confused in notation with the fine-structure constant). Heavy atoms, such as Tl [7], have thus been used in measurements of the electron EDM. This enhancement can be even greater in polar molecules, where the inter-nuclear electric field strongly mixes the electronic states. An applied electric field mixes the rotational states, polarizing the molecule. The electron EDM interacts with the polarization that results from the inter-nuclear and applied electric fields.

The electron's EDM, d_e , can be either parallel or antiparallel to the direction of its spin magnetic dipole moment, $\vec{\sigma}$. The interaction Hamiltonian between this dipole moment and an applied electric field, \vec{E} , is $-d_e \alpha(E) \vec{\sigma} \cdot \vec{E}$, where $\alpha(E)$ is the enhancement factor. For all reasonable fields created in the laboratory, $\alpha(E)$ is constant for an atom, but can vary

for a molecule. For a Tl atom the enhancement factor is -585 [8]. In an applied electric field of 13 kV/cm, the heavy dipolar radical YbF is found to have an enhancement factor of around 10^6 [9]. This very large enhancement allows the interaction of the EDM of the valence electron in a YbF molecule with an electric field to be measured experimentally.

At Imperial College London there is currently an ongoing experiment to measure the electron EDM using a supersonic beam of YbF radicals. The experiment measures the energy difference between the $F = 1$, $M_F = \pm 1$ magnetic sub-levels of ground-state YbF molecules. The molecules are created by supersonic expansion of a seeded carrier gas and laser ablation of a solid Yb target (more details of this method are given in sections 1.2.2 and 3.2). The molecular states of interest in this experiment are the $|F = 0, M_F = 0\rangle$, $|F = 1, M_F = 0\rangle$ and $|F = 1, M_F = \pm 1\rangle$ levels of the absolute ground state. The energy interval between these levels is small enough, and the source hot enough, that the levels are equally populated. The first stage of the experiment is to prepare the molecules in the $|0, 0\rangle$ state. This is done by a laser, which drives electronic transitions from the $|1, 0\rangle$ and $|1, \pm 1\rangle$ states. Having been excited the molecules then decay back to the ground electronic state. This pumping scheme causes the population to build up in the $|0, 0\rangle$ state, and empties the $|1, 0\rangle$ and $|1, \pm 1\rangle$ states. In the second stage of the experiment an RF transition at 170 MHz drives the $|0, 0\rangle$ molecules into a superposition of the $F = 1$, $M_F = \pm 1$ states, $\frac{1}{\sqrt{2}}(|1, 1\rangle + |1, -1\rangle)$. The molecules then traverse a region of applied electric field, \vec{E} , and magnetic field, \vec{B} . During the time, τ , that the molecules are in the field region they acquire the phase

$$\Delta\phi = \frac{\tau}{\hbar} \left(\mu_B B - \alpha(E) d_e E \right), \quad (1.3)$$

leaving them in the state $\frac{1}{\sqrt{2}}(e^{i\Delta\phi}|1, 1\rangle + e^{-i\Delta\phi}|1, -1\rangle)$. After the field region a second 170 MHz RF pulse drives the transition back to the $|0, 0\rangle$ state, with an efficiency that depends on the acquired phase. The amplitude of the $|0, 0\rangle$ state after the second RF pulse is $\frac{1}{2}(e^{i\Delta\phi} + e^{-i\Delta\phi})$. The molecules are then probed by laser induced fluorescence, with a laser beam tuned to an electronic transition from the $|0, 0\rangle$ state. The intensity of the measured fluorescence depends on the final population of the $|0, 0\rangle$ state,

$$I \propto \frac{1}{4} \left(e^{i\Delta\phi} + e^{-i\Delta\phi} \right)^2 = \cos^2 \Delta\phi. \quad (1.4)$$

The intensity is thus a periodic function, consisting of fringes as $\Delta\phi$ is varied. For a constant applied magnetic field, changing the electric field (for example, by switching its direction) will lead to a variation in measured intensity which depends on d_e . The purpose of the magnetic field is to set $\Delta\phi$ to $\pi/4$ where the experiment is most sensitive to variations in phase.

Further details of this experiment can be found in [10], [11] and [12]. In addition to the YbF experiment there are several other experiments, planned or in progress, to measure the electron EDM with molecules, most notably PbO [13], PbF [14, 15], and ThO [16].

1.1.2 Measuring time-variation of fundamental constants

Theoretical work on string theory and the expansion of the universe has suggested that physical constants can vary over time [17]. Experimental methods for observing such variation have focussed on the ratio of the electron and proton masses, $\mu = m_p/m_e$, and the fine structure constant, α . Because the variation is expected to be very small over extremely long timescales, an obvious technique to measure any change is to analyse spectral data from astrophysical objects at a variety of red-shifts. This allows the comparison of data from a wide range of cosmological time-scales, typically of order 10 GYr. Some of these analyses indicate an observed variation in α , measuring $\Delta\alpha/\alpha \sim 10^{-5}$ [18, 19]. Despite the huge time-span available to these astrophysical measurements they have not yet produced consistent evidence of time-variation [20]. An alternative is to make a much more precise measurement on a system, but over a much smaller time-scale. For example, laboratory-based experiments can compare the transitions in a test system with those in a caesium fountain over a number of years. Molecules, with their rich structure, provide excellent test systems for measuring time-variation of constants, and several experiments have been suggested. One such experiment would use ultracold trapped HD^+ or H_2^+ ions [21] to measure μ (and also the proton-to-deuteron mass ratio). It is stated in [21] that the narrow linewidth of vibrational transitions in these ions can allow measurements of time-variation of order 10^{-15} yr^{-1} . An experiment to measure vibrational transitions in SF_6 has measured the upper limit on the time-variation of $\Delta\mu/\mu$ to be $(-3.8 \pm 5.6) \times 10^{-14} \text{ yr}^{-1}$ [22]. More recently a new experiment has been proposed which would measure two-photon transitions in molecular beams with sufficient precision to allow for a measurement of the upper limit of the time-variation of μ of 10^{-15} yr^{-1} [23]. The sensitivity of molecular transitions to variations in α or μ can be considered within the structure of the Born-Oppenheimer model (see chapter 2) in which the electronic, vibrational and rotational energies are separated. To first order the dependence of each energy on μ is given in [23], and it is shown that pure electronic transitions are not sensitive to changes in μ , whereas transitions between low-lying vibrational states and between low-lying rotational states of molecules are sensitive. The proposed experiment involves measuring the frequency between two near-degenerate states. As an example the authors consider a particular state ($a^3\Pi(v=0)$) of CO. A comprehensive review of the sensitivity of 2-photon rotational transitions in the different isotopomers of CO shows a large isotope shift in these transitions, which indicates sensitivity to variation in μ , and in particular a transition between two states separated by 1.648 GHz in $^{12}\text{C}^{16}\text{O}$ shows particularly great sensitivity [23].

1.1.3 Observing parity violation

Since the 1957 ^{60}Co experiment that measured parity violation [1] there have been efforts to measure this violation and its effects in molecular chirality [24]. A chiral molecule is one that cannot be superimposed on its mirror image. The two mirror images are designated as being ‘left-’ or ‘right-handed’, with pairs of opposite-handedness known as enantiomers. Chirality occurs in many molecules in nature, most notably in amino acids and sugars. Parity violation should lead to (very small) differences in the spectral characteristics of enantiomers [24]. The experimental search for parity violation in enantiomers thus requires high-resolution spectroscopy experiments to measure these energy differences. In an early attempt, for example, the hyperfine components of vibration-rotation transitions in the two enantiomers of CHFClBr were compared and measured to be identical to within 13 Hz [25]. Theoretical analysis of CHFClBr has, however, shown that parity-violating effects are considerably smaller, on the order of several mHz [26]. However, further calculations in [26] show that CHBrFI enantiomers are expected to experience greater energy shifts by a factor of 10. More recent theoretical work has suggested an alternative method of measuring parity-violating effects in chiral molecules by using optical activity [27]. A chiral molecule rotates the polarization of light incident upon it. It is proposed in [27] to measure the time-averaged optical activity of a sample of molecules all of the same chirality. The rotation angle of light at a given position inside the sample will be affected by parity-violation.

The measurement of parity violation in chiral molecules is of great importance not only to the physical sciences, but also the biological sciences, through the phenomenon of biomolecular homochirality. This is the strong preference observed in nature for certain handedness in biomolecules, with most amino acids being ‘left-handed’, and most monosaccharides being ‘right-handed’ [24]. Many hypotheses have been suggested for homochirality. Quack [24] categorizes these into those requiring chance and those requiring necessity. For example one suggestion is that, near the beginning of an evolutionary process a local chiral system, such as a circularly-polarized light-field, could influence amino acid formation in favour of one handedness. This explanation falls into the ‘chance’ category. On the other hand, it has been suggested that parity violation could affect a low-temperature phase transition in such a way as to favour one particular handedness — an explanation which falls into the ‘necessity’ category¹. Parity-violation will cause an energy difference between enantiomers. It is possible that this difference might favour the production of one of the enantiomers in nature, and thus lead to the observed homochirality. Measurement of parity-violating effects in biomolecules is thus an important endeavour in answering questions about the evolution of life.

¹For a more detailed description of these explanations and their references, see Quack’s excellent review article [24].

1.2 Why *cold* molecules?

The experiments discussed above all require molecules in a particular state. In order to generate large densities of molecules in a particular state the molecules must be cold. This means that the electronic, vibrational and rotational distributions of an ensemble of molecules should be narrow, and preferably centred on the desired state. This requires creating the molecules in such a way that they are already in the desired state, or can be transferred to the desired state. As well as cooling the internal degrees of freedom, it can also be useful for the molecule's translational motion to be cold. This is, for example, important in the YbF electron EDM experiment, because it means that pulses of molecules do not spread much in their flight through the experiment. As discussed in [28] it is important to note that for an ensemble of molecules to be translationally cold does not require them to be slow-moving, or for the ensemble to have zero mean speed. Rather, the distribution of speeds must be narrow. In the experiments discussed in this thesis, molecular beams are made with translational temperatures around 3 K, but travelling at mean speeds between 360 ms^{-1} and 600 ms^{-1} . Obtaining molecules with low velocity is also useful for many experiments because this increases the amount of time each molecule spends in the experiment.

The methods used to create cold molecules are often categorized into two types [29]: direct and indirect. The indirect method involves cooling atoms to ultracold temperatures, and then combining them to create an ultracold ensemble of molecules. The direct method involves making the molecules first, and then cooling them.

1.2.1 Indirect methods

Photoassociation

The first experiments to create molecules indirectly used photoassociation [31]. In this method a laser is used to drive a transition between two atoms from an unbound to a bound state. If the atoms are initially cold, then the resulting molecule will be too. Thus this technique has been applied to ultracold atoms that have been laser-cooled. Photoassociation tends to create molecule in excited electronic and vibrational states. This is not desirable because, in collisions between vibrationally excited molecules the vibrational energy can be transferred to translational energy, which heats the ensemble up from ultracold temperatures ($< 1 \text{ mK}$) to cold temperatures (around 1 K) [30]. It is possible for the molecules to decay spontaneously to the vibrational ground state, or one can use a second laser to stimulate this decay. The efficiency of this method depends on the overlap of the vibrational states, known as the Franck-Condon factor. It turns out that the Frank-Condon factor is more favourable in heteronuclear molecules. Thus heteronuclear photoassociation is well-suited to creating ground state molecules, such as

the creation of LiCs molecules in the absolute ground state by Deiglmayr *et al.* in 2008 [32].

The disadvantage of photoassociation is that it is limited to the creation of molecules comprising only those atoms that can be laser-cooled, typically alkalis. This limits the application of photoassociation in testing fundamental physics.

Feshbach resonance

Another method of creating molecules from ultracold atoms is via a Feshbach resonance. In this technique an applied magnetic field is used to vary the scattering length of two atoms. If the energy of two colliding atoms is the same as that of a bound state, then it is possible for the atoms to enter this bound state, forming a molecule. It is unlikely that the energy associated with the atoms will exactly match the bound state energy. If the bound and unbound states have different spin configurations, they will have different magnetic moments. Thus, the two states will experience different Zeeman shifts in an applied magnetic field. By applying the correct magnetic field it is possible to induce an overall Zeeman shift that reduces the energy difference to zero. When this happens the bound state can be formed. This method has been used to create molecules from a variety of ultracold atoms, such as Rb₂ [33], Li₂ [34] and Na₂ [35]. Feshbach resonance can be used to create molecules directly from an atomic Bose-Einstein condensate (BEC). This has been demonstrated, for example, by Danzl *et al.*, in an experiment in which deeply-bound Cs₂ molecules were formed from a Cs BEC [36]. However, as with photoassociation, Feshbach resonance is limited to molecules formed from atoms that can be laser-cooled.

1.2.2 Direct methods

Supersonic expansion

The supersonic expansion method starts with a gas at high pressure (typically several bars) contained in a line at room temperature. At the end of this line is a valve which separates the high pressure region from a low pressure region (typically high vacuum, around 10^{-7} mbar). Opening this valve allows the gas to flow into the vacuum. The gas expands as it flows into the vacuum, which causes it to cool. This cooling arises because, before the valve is opened the gas has no net flow (the average speed of the molecules is zero), but has random thermal motion, the distribution of which defines the temperature. As the gas enters the low-pressure region it gains a net flow, and the energy of this flow comes from the thermal motion. Collisions between molecules expanding into the low-pressure region cool the translational, rotational and vibrational degrees of freedom as energy is transferred to forward kinetic energy. The expansion takes a gas with a wide speed distribution, centred on $v = 0$, and creates a narrow distribution, centred on $v > 0$.

Were the collisions to continue for long enough the translational, vibrational and rotational temperatures would eventually reach zero. However, as the gas expands its pressure and temperature drop rapidly. As the pressure drops the mean free path increases until there are no more collisions. At this point cooling stops, leaving the molecules with a non-zero temperature.

The final speed of the beam is determined by the initial temperature of the gas and its molecular mass. Heavier gases will travel more slowly. The use of a mixed-gas expansion can vary the final speed attained by a supersonic beam. A mixed gas may also have the advantage of preventing condensation [28]. Collisions between the gas molecules can cause condensation nuclei, whereas mixing the desired molecules with a large volume of some other gas inhibits this as the other gas (the ‘carrier’ gas) prevents these collisions.

A skimmer, located downstream of the valve, allows only those molecules with limited transverse temperatures to pass, and thus can be used to create a supersonic, cold beam of molecules.

Supersonic beams can be created both directly and indirectly. In the direct method the desired molecules are prepared before the expansion, such as in [37], where a beam of 5% CO and 95% Xe was made by supersonic expansion. In the indirect method, a gas of precursor molecules is supersonically expanded, and then, during the expansion, takes part in a reaction to create some product molecule. This product then forms a part of the supersonic beam. This method was used to create a beam of YbF radicals in 2002 [38]. A mixture of 5% SF₆ and 95% carrier gas (typically Ar or Xe) was expanded into a vacuum chamber. Inside the chamber, located next to the valve nozzle was a target of solid Yb. Very shortly after the valve opened, and while the gas was still expanding into the chamber, a pulse from a Q-switched Nd:YAG laser was fired onto the Yb, ablating the surface and causing a plume of hot Yb atoms. This hot plume intersected the supersonically expanding beam and the Yb atoms reacted with the SF₆ to form YbF radicals. These radicals were then entrained in the beam, travelling at a speed determined by the carrier gas.

Buffer gas cooling

A method for producing high densities of low temperature molecules is buffer gas cooling [39]. This technique involves loading molecules into a magnetic trap, which is itself located inside a cryostat. Molecules which experience an increase in energy in a magnetic field (a positive Zeeman shift) will be trapped by a local minimum of magnetic field. A cold buffer gas present in the cryostat can then be used to cool the molecules in the trap. Colder buffer gases offer more cooling, although this is limited by the associated reduction in vapour pressure. ³He maintains a large vapour pressure until very low temperatures, and can be used to cool trapped molecules down to around 240 mK [39]. The first buffer-gas cooled molecule was CaH [40], which was magnetically trapped in a cryogenic cell filled

with ^3He , and cooled to about 400 mK.

Buffer gas cells can be used to produce beams of cold molecules. In this case the molecules are not magnetically trapped, but simply formed in a cell located in a cryostat. They can be loaded into the cell through a capillary (such as in [41]), from an external beam [42], or can be created by laser ablation inside the cell (such as in [43]). The buffer-gas cooled molecules can then leave the cell through an aperture in one of the walls, and can be guided out magnetically or electrically. The first molecular beam out of a buffer gas cell was a beam of PbO , reported in 2005 [43]. The molecules were cooled in a cell cooled by He to a typical temperature of 5 K. Measurements of the beam’s velocity profiles found the transverse, longitudinal and rotational temperatures to be around 5 K, indicating full thermalization inside the buffer gas cell. By varying the He density in the cell the forward velocity of the beam could be varied between 40 ms^{-1} and 80 ms^{-1} .

Molecular beams cooled by buffer gas cells offer the possibility of cold, high density, slow-moving beams, and are thus a very exciting prospect for experiments that use molecular beams.

1.3 Motivation for this thesis

The purpose of the experiments reported in this thesis was to investigate the methods of generating a slow, intense beam of heavy, polar molecules for the measurement of the electron electric dipole moment (EDM), d_e , described in section 1.1.1. The experiment currently uses a beam of Ar-carried YbF from a supersonic source travelling at a speed of 600 ms^{-1} . It can be shown [44] that the statistical error in the measurement of the electron EDM in this experiment is given by

$$\delta d_e = \frac{\hbar}{e} \frac{1}{\alpha(E)E} \frac{1}{\tau\sqrt{N}} \quad (1.5)$$

(in units of e cm), where E is the magnitude of the applied field, $\alpha(E)$ is the enhancement factor, τ is the amount of time each molecule spends inside the experiment, and N is the total number of molecules used in the experiment. The experiment is almost completely automated and can run for long periods (several days) without needing to stop. The current sensitivity is $7 \times 10^{-28} \text{ e cm}/\sqrt{\text{day}}$ [44]. This sensitivity can be improved by increasing the number of participating molecules, N , and the time they spend in the experiment, τ . The supersonic source used is currently the best method of creating a high-flux beam of cold YbF molecules. There is an experiment at Imperial College to create a buffer gas source of YbF molecules [45]. This promises to produce larger fluxes of molecules in a slower moving beam, however, the supersonic source is currently the better method.

Regardless of the source used it is important to find a method of coupling as many molecules into the experiment as possible. For this reason, one of the goals of this PhD

project was to investigate a method for transporting ground-state molecules from a source to an experiment. This involved building a 1 m-long guide, capable of transporting molecules from a high density source, such as a supersonic source or a buffer gas cell, and delivering them to an experiment in such a way that maintains their phase-space density. The properties of this molecular guide were extensively characterized, and the results are described in chapter 6.

As well as increasing N , the other method for reducing δd_e is to increase the time the molecules spend in the experiment. This requires finding a slower source of molecules, or decelerating the current, fast-moving beam. The buffer-gas source promises a slower beam of molecules, but this has not yet been demonstrated. The supersonic beam currently used in the EDM experiment is Ar-carried, and travels at 600 ms^{-1} . Heavier carrier gases will reduce this speed. However, it has been found that these slower beams have smaller fluxes, which reduces N in such a way that the Ar-carried beam is optimal. The best option for increasing τ is to decelerate the molecules. This has been the main objective of this thesis. Two types of molecular decelerator have been investigated. These devices use a sequence of time-varying electric fields to remove kinetic energy from the molecules. The results are presented in chapters 5 and 7.

In order to distinguish a true measured value of the EDM from a false measurement resulting from systematic effects, it is necessary to carry out many control experiments. One important control method is to repeat the experiment with a different molecule that has a much smaller enhancement factor. If this experiment still measures the same value for the EDM then there is an error, and the measurement is not a value of the EDM. The enhancement factor is found to be proportional to Z^3 . In YbF the valence electron that is probed by the EDM experiment is strongly bound to the Yb nucleus, and it is the value of Z for this nucleus that largely determines the enhancement factor. The molecule of choice for the control experiment is CaF. This radical has a structure very similar to YbF, but with a mass of 59 amu (compared with 192 amu for YbF), it is very much lighter. The Ca nucleus has a proton number of 20, compared with 70 for Yb, giving it an enhancement factor 43 times smaller than that of YbF. This is too small for the current experiment to measure the electron EDM in CaF, and so it serves as a good system for measuring systematic effects.

CaF was the molecule chosen to be decelerated in this PhD project. For a given beam speed (determined by the carrier gas) CaF will be easier to decelerate than the much heavier YbF radical. Thus CaF allows for an easier method of testing and calibrating deceleration devices. CaF is very similar to YbF and is made in exactly the same way. Thus, once an efficient method of decelerating CaF has been found, the experimental set-up can easily be modified to decelerate YbF. As well as this, a slow beam of CaF is itself useful in the determination of the electron EDM.

This thesis describes experiments to guide and decelerate cold beams of CaF. In addition to these experiments, a further experiment to determine various molecular parameters has been performed (chapter 4). As well as investigating the structure of CaF, this spectroscopic experiment also shows that CaF is a good candidate for laser cooling, a powerful cooling technique applied so far only to atoms.

Chapter 2

Introduction to molecular physics

2.1 Basic diatomic molecular structure

There are many fine introductions to molecular structure, in particular Herzberg [46], Bransden and Joachain [47] and Wang [48].

2.1.1 Born-Oppenheimer Approximation

A diatomic molecule consists of two nuclei, A and B (mass M_A and M_B respectively) separated by some distance \vec{R} , and N electrons. The time-independent Schrödinger equation for this system is

$$\left[\hat{\mathcal{T}}_N + \hat{\mathcal{T}}_e + V \right] \Psi(\vec{R}, \vec{r}_i) = E \Psi(\vec{R}, \vec{r}_i), \quad (2.1)$$

where $\hat{\mathcal{T}}_N$ is the kinetic energy operator for the nuclei, $\hat{\mathcal{T}}_e$ is the kinetic energy operator for the electrons and V is the *total* potential energy of the system, comprising all Coulomb interactions. E is the total molecular energy. The variable written as \vec{r}_i represents the list of all the electronic positions, $\vec{r}_i = \vec{r}_1, \vec{r}_2, \dots, \vec{r}_N$. Expressed in terms of the reduced mass, $m_r = M_A M_B / (M_A + M_B)$:

$$\hat{\mathcal{T}}_N = \frac{-\hbar^2}{2m_r} \nabla_R^2, \quad \hat{\mathcal{T}}_e = \sum_{i=1}^N \frac{-\hbar^2}{2m_e} \nabla_{r_i}^2. \quad (2.2)$$

Consider now the nuclei to have some fixed positions. The Schrödinger equation simplifies to

$$\left[\hat{\mathcal{T}}_e + V \right] \Phi_q(\vec{R}; \vec{r}_i) = E_q(\vec{R}) \Phi_q(\vec{R}; \vec{r}_i). \quad (2.3)$$

Note the argument of the wavefunction: \vec{R} is a parameter, not a variable. For a given \vec{R} there is a set of electronic eigenfunctions $\Phi_q(\vec{R}; \vec{r}_i)$, with corresponding total energies $E_q(\vec{R})$.

For a given \vec{R} the wavefunctions Φ_q form a complete set, and so the total wavefunction can be expanded in terms of Φ_q :

$$\Psi(\vec{R}, \vec{r}_i) = \sum_q G_q(\vec{R}) \Phi_q(\vec{R}; \vec{r}_i). \quad (2.4)$$

An equation for $G_q(\vec{R})$ can be found in the usual way by premultiplying the total wavefunction by one of the electronic wavefunctions, $\Phi_m(\vec{R}; \vec{r}_i)$ and then integrating over all electronic positions:

$$\sum_q \int \Phi_m^*(\vec{R}; \vec{r}_i) \left[\hat{T}_N + \hat{T}_e + V - E \right] G_q(\vec{R}) \Phi_q(\vec{R}; \vec{r}_i) d\vec{r}_i = 0. \quad (2.5)$$

There are four terms in equation 2.5. Consider now only the second to fourth terms (that is, the energy terms $(\hat{T}_e + V - E)$). The operator \hat{T}_e is a function of \vec{r}_i only, and V and E are numbers. Thus the orthonormality condition and equation 2.3 give

$$\sum_q \int \Phi_m^*(\vec{R}; \vec{r}_i) \left(\hat{T}_e + V - E \right) G_q(\vec{R}) \Phi_q(\vec{R}; \vec{r}_i) d\vec{r}_i = \left(E_m(\vec{R}) - E \right) G_m(\vec{R}), \quad (2.6)$$

where $E_m(\vec{R})$ is the energy associated with the electronic motion and all Coulomb interactions. Substituting equation 2.6 into equation 2.5 gives

$$\begin{aligned} \sum_q \int \Phi_m^*(\vec{R}; \vec{r}_i) \hat{T}_N G_q(\vec{R}) \Phi_q(\vec{R}; \vec{r}_i) d\vec{r}_i &= -(E_m(\vec{R}) - E) G_m(\vec{R}) \\ \Rightarrow -\frac{\hbar^2}{2m_r} \sum_q \int \Phi_m^*(\vec{R}; \vec{r}_i) \vec{\nabla}_R^2 G_q(\vec{R}) \Phi_q(\vec{R}; \vec{r}_i) d\vec{r}_i &= -(E_m(\vec{R}) - E) G_m(\vec{R}) \end{aligned} \quad (2.7)$$

This equation for the function $G_m(\vec{R})$ is a differential equation coupled to all other $G_q(\vec{R})$. An analytical solution is not possible. To continue with this analysis the usual step is to make the Born-Oppenheimer approximation in which the derivatives of $\Phi_q(\vec{R}; \vec{r}_i)$ with respect to R are ignored. At this stage in the analysis nothing is known about the form of the wavefunctions $\Phi_q(\vec{R}; \vec{r}_i)$ as the Schrödinger equation has yet to be solved. The assumption that the functions $\Phi_q(\vec{R}; \vec{r}_i)$ are insensitive to changes in \vec{R} is a mathematical guess. Only after solution of the Schrödinger equation can this approximation be known to be good. The Born-Oppenheimer approximation results in the following simplification

$$\vec{\nabla}_R^2 \left(G_q(\vec{R}) \Phi_q(\vec{R}; \vec{r}_i) \right) = G_q(\vec{R}) \left(\vec{\nabla}_R^2 \Phi_q(\vec{R}; \vec{r}_i) \right) + \left(\vec{\nabla}_R^2 G_q(\vec{R}) \right) \Phi_q(\vec{R}; \vec{r}_i) \quad (2.8)$$

$$\begin{aligned} &+ 2 \left(\vec{\nabla}_R G_q(\vec{R}) \right) \cdot \left(\vec{\nabla}_R \Phi_q(\vec{R}; \vec{r}_i) \right) \\ &\approx \left(\vec{\nabla}_R^2 G_q(\vec{R}) \right) \Phi_q(\vec{R}; \vec{r}_i), \end{aligned} \quad (2.9)$$

where the first and third terms on the right-hand side of equation 2.8 have been ignored.

The time-independent Schrödinger equation is now

$$\left[\frac{-\hbar^2}{2m_r} \nabla_R^2 + E_m(\vec{R}) - E \right] G_m(\vec{R}) = 0. \quad (2.10)$$

This is known as the *nuclear wave equation*. It looks like the time-independent Schrödinger equation for a particle of mass m_r moving in a potential $E_m(\vec{R})$, the \vec{R} -dependent electronic energy. The eigenfunctions, $G_m(\vec{R})$ describe the relative motion of the nuclei.

2.1.2 Eigenstates of the nuclear wave equation

Equation 2.10 describes the motion of the nuclei in the potential created by the electronic motion and all the molecular Coulomb interactions. The molecule investigated in this thesis is the diatomic radical, CaF. For a diatomic molecule, the vector \vec{R} describes the separation of the nuclei and the orientation of the inter-nuclear axis. In the absence of an applied field the electronic energy of a diatomic molecule will not depend on the orientation of the molecule - only on the separation of the nuclei. Thus the electronic energy is a function only of the internuclear separation. The potential term is now a function of radial coordinates only: $E_m(R)$. The nuclear wavefunction, however, is a function of both radial and angular variables, and can be separated. The Laplacian operator can be written

$$\nabla_R^2 = \frac{1}{R^2} \frac{\partial}{\partial R} \left(R^2 \frac{\partial}{\partial R} \right) - \frac{\hat{N}^2}{R^2}, \quad (2.11)$$

where \hat{N} is the total molecular orbital angular momentum operator (comprising the nuclear rotation and electronic orbital angular momentum operators).

$G_m(\vec{R})$ can be separated into a radial and an angular part. Substitution of this into the nuclear wave equation (equation 2.10) finds the separated function to be [47]:

$$G_m(\vec{R}) = \frac{1}{R} g_{m,N}(R) Y_{N,M_N}(\theta, \phi). \quad (2.12)$$

Substituting the expression for the Laplacian operator (equation 2.11) into the nuclear wave equation and then separating, the radial component of the nuclear wave equation is found to be

$$\left[\frac{-\hbar^2}{2m_r} \left(\frac{d^2}{dR^2} - \frac{N(N+1)}{R^2} \right) + E_m(R) - E \right] g_{m,N}(R) = 0. \quad (2.13)$$

E is the total molecular energy, $E_m(R)$ is the electronic energy. The second term is the separation term and is found from the solution to the angular equation. This term relates to the rotational energy of the molecule. The first term relates to changes in the internuclear axis length, and will be shown to relate to the vibrational energy of the molecule.

2.1.3 Electronic States

A diatomic molecule has a strong electric field along the internuclear axis (unit vector \vec{k}). The component of the total electronic angular momentum, \vec{L} along \vec{k} is a constant of motion, and so its quantum number, M_L is a good quantum number and can be used to denote electronic states. Reversing the direction of motion of all the electrons does not

(to first order) affect the molecule's energy, and so states of $\pm M_L$ are degenerate. States are therefore labelled by the number $\Lambda = |M_L|$.

The term symbols used to denote these states are written in analogy to the atomic states:

$$\begin{aligned} \text{State: } \Lambda &= 0, 1, 2, \dots \\ \text{Label: } &= \Sigma, \Pi, \Delta, \dots \end{aligned}$$

The orbital motion of the electrons generates an internal magnetic field along the inter-nuclear axis, $\vec{B} = B\vec{k}$. Any molecular spin, \vec{S} will interact with this field. The resulting interaction Hamiltonian is proportional to $\vec{L} \cdot \vec{S}$. The component of \vec{S} along \vec{k} is (confusingly) labelled Σ . For a given \vec{S} there are $2S + 1$ values of Σ .

The total component of electronic angular motion along \vec{k} is $\Omega = \Lambda + \Sigma$. The angular momentum state of a given electronic state is denoted by $^{2S+1}\Lambda_\Omega$.

The electronic states are denoted by capital Roman letters. The ground state is X , and successive excited states are generally labelled alphabetically, A, B, C, \dots

2.1.4 Vibrational States

To solve the radial Schrödinger equation (equation 2.13) consider the form of the effective potential, $E_m(R)$. The general form can be deduced from its physical construction: the kinetic energy of the electrons plus all Coulomb interactions. For small R this energy will be dominated by the Coulomb repulsion of the nuclei: $E_m(R)$ drops rapidly with R . In the limit of large R the nuclei are far apart and the energy approaches that of two distant neutral atoms, E_m^{atom} . If, in the intermediate region between these two limits the energy $E_m(R)$ drops below E_m^{atom} then a potential well is formed. The molecule's equilibrium internuclear separation is then R_0 , the position of this minimum.

The potential around the minimum can be Taylor expanded and, to first order, considered as a harmonic potential. This turns out to be a good approximation for low-lying states of most molecules. The effective potential is thus

$$\begin{aligned} E_m(R - R_0) &= E_m(R_0) + \frac{1}{2} \frac{d^2 E_m(R)}{dR^2} \bigg|_{R=R_0} (R - R_0)^2 \\ &= E_m(R_0) + \frac{1}{2} k_{nuc} (R - R_0)^2. \end{aligned} \quad (2.14)$$

The second term of the right-hand side of equation 2.14 is the potential energy of a harmonic oscillator.

Equation 2.13 can now be written:

$$\left[\frac{-\hbar^2}{2m_r} \frac{d^2}{dR^2} + \frac{1}{2} k_{nuc} (R - R_0)^2 + \frac{\hbar^2}{2m_r} \frac{N(N+1)}{R^2} + E_m(R_0) - E \right] g_{m,N}(R) = 0. \quad (2.15)$$

Considering just the first two terms in equation 2.15 renders the Schrödinger equation for a harmonic oscillator, whose eigenstates are $E_v = \hbar\sqrt{k_{nuc}/m_r}(v + \frac{1}{2})$, where $v = 0, 1, 2, \dots$ is the vibrational quantum number. The radial wave equation thus becomes

$$\left[\frac{\hbar^2}{2m_r} \frac{N(N+1)}{R^2} + E_v + E_m(R_0) - E \right] g_{m,N}(R) = 0, \quad (2.16)$$

where E_v is the nuclear vibrational energy, and $E_m(R_0)$ is the electronic energy at the equilibrium inter-nuclear length.

2.1.5 Rotational energy levels

The second term in equation 2.13 contains information about the rotation of the molecule. The above analysis of the vibrational motion identified an equilibrium bond length, R_0 , and approximated the motion about this position. As a further approximation, the rotational motion can be analysed by considering the molecule to be a rigid rotor of length R_0 . The angular term thus becomes

$$E_r = \frac{\hbar^2}{2m_r R_0^2} N(N+1) = BN(N+1), \quad (2.17)$$

which is indeed the energy of a rigid rotor in the N th excited state. B is known as the rotational constant.

2.1.6 The separation of molecular energies

The total molecular energy has now been separated into $E = E_m(R_0) + E_v + E_r$, the electronic energy, the vibrational energy and the rotational energy respectively. For a given electronic state, m , the total molecular wavefunction is:

$$\begin{aligned} \Psi_m(\vec{R}, \vec{r}_i) &= \frac{1}{R} g_{m,N}(R) \times Y_{N,M_N}(\theta, \phi) \times \Phi_m(\vec{R}; \vec{r}_i) \\ &= \frac{1}{R} \psi_v(R) \times \psi_{N,M_N}(\theta, \phi) \times \Phi_m(\vec{R}; \vec{r}_i), \end{aligned} \quad (2.18)$$

where ψ_v is the vibrational wavefunction with vibrational quantum number v , ψ_{N,M_N} is the rotational wavefunction and Φ_m is the electronic wavefunction.

2.2 Coupling angular momenta

The angular momenta associated with the nuclei and electrons are \vec{L} , the total electronic orbital angular momentum, $\vec{\mathcal{R}}$, the total nuclear orbital angular momentum, \vec{S} , the total electronic spin and \vec{J} , the total angular momentum.¹ All of these momenta can couple with each other. By convention the sum of the electronic orbital angular momentum and

¹Nuclear spin is still, at this stage, being neglected.

nuclear rotation angular momentum operators is defined as $\vec{N} = \vec{L} + \vec{R}$, and the sum of this operator with the spin operator is $\vec{J} = \vec{N} + \vec{S}$. Of the many coupling schemes Hund identified the five most important cases, labelled Hund's cases (a) through to (e). Of these (a) and (b) are the most common and are the two cases relevant to this thesis.

2.2.1 Hund's case (a)

In this case the spin-orbit interaction energy is much greater than the rotational energy. The electronic motion and spin are strongly coupled to each other and to the internuclear axis. The basis states that describe a Hund's case (a) molecule are $|\Lambda\rangle|S, \Sigma\rangle|J, \Omega, M_J\rangle$, where the good quantum numbers are defined by:

$$L_{z'}|\Lambda\rangle = \Lambda|\Lambda\rangle, \quad (2.19)$$

$$\vec{S}^2|S, \Sigma\rangle = S(S+1)|S, \Sigma\rangle, \quad (2.20)$$

$$S_{z'}|S, \Sigma\rangle = \Sigma|S, \Sigma\rangle, \quad (2.21)$$

$$\vec{J}^2|J, \Omega, M_J\rangle = J(J+1)|J, \Omega, M_J\rangle, \quad (2.22)$$

$$J_{z'}|J, \Omega, M_J\rangle = \Omega|J, \Omega, M_J\rangle, \quad (2.23)$$

$$J_z|J, \Omega, M_J\rangle = M_J|J, \Omega, M_J\rangle. \quad (2.24)$$

Primes denote coordinates in the molecular frame (that is, the z' -component of an operator acts along the internuclear axis). From the definition of J above the total angular momentum operator is $\vec{J} = \vec{L} + \vec{S} + \vec{R}$. \vec{R} acts perpendicularly to the internuclear axis and so the component of \vec{J} along the internuclear axis is $J_{z'} = L_{z'} + S_{z'}$, from which it can be seen that the quantum number $\Omega = \Lambda + \Sigma$.

2.2.2 Hund's case (b)

In Hund's case (b) the rotational energy is much larger than the spin-orbit interaction energy. The electron spin is only weakly coupled to the internuclear axis. The basis that describes a molecule in Hund's case (b) is $|\Lambda\rangle|(N, S)J, M_J\rangle$. The quantum numbers are defined by the following eigenvalue equations:

$$L_{z'}|\Lambda\rangle = \Lambda|\Lambda\rangle \quad (2.25)$$

$$\vec{N}^2|(N, S)J, M_J\rangle = N(N+1)|(N, S)J, M_J\rangle, \quad (2.26)$$

$$\vec{S}^2|(N, S)J, M_J\rangle = S(S+1)|(N, S)J, M_J\rangle, \quad (2.27)$$

$$\vec{J}^2|(N, S)J, M_J\rangle = J(J+1)|(N, S)J, M_J\rangle, \quad (2.28)$$

$$J_z|(N, S)J, M_J\rangle = M_J|(N, S)J, M_J\rangle. \quad (2.29)$$

2.3 Molecular transitions

2.3.1 Electric dipole matrix element

Electric dipole transitions can be treated analytically by applying the dipole operator \vec{D} to the total molecular wavefunction. The transition probability amplitude from an initial state with quantum numbers $\{m, v, J, M_J\}$ to one with $\{m', v', J', M'_J\}$ is given by the matrix element

$$\begin{aligned} \langle \Psi' | \vec{D} | \Psi \rangle &= e \int \int \frac{1}{R^2} \psi_{v'}^*(R) \psi_{N', M'_N}^*(\theta, \phi) \Phi_{m'}^*(\vec{R}; \vec{r}_i) \left(Z_A \vec{R}_A + Z_B \vec{R}_B - \sum_i^N \vec{r}_i \right) \\ &\quad \times \psi_v(R) \psi_{N, M_N}(\theta, \phi) \Phi_m(\vec{R}; \vec{r}_i) d\vec{R} d\vec{r}_i. \end{aligned} \quad (2.30)$$

The integral $\int d\vec{R}$ is over all nuclear coordinates, and $\int d\vec{r}_i$ is over all electron coordinates. Consider the first two terms in the above integral. Performing first the integral over all electronic positions, $d\vec{r}_i$, gives:

$$\begin{aligned} &e \int \frac{1}{R^2} \psi_{v'}^*(R) \psi_{N', M'_N}^*(\theta, \phi) \Phi_{m'}^*(\vec{R}; \vec{r}_i) \left(Z_A \vec{R}_A + Z_B \vec{R}_B \right) \\ &\quad \times \psi_v(R) \psi_{N, M_N}(\theta, \phi) \Phi_m(\vec{R}; \vec{r}_i) d\vec{r}_i \\ &= \left[\int \Phi_{m'}^*(\vec{R}; \vec{r}_i) \Phi_m(\vec{R}; \vec{r}_i) d\vec{r}_i \right] \times \vec{r}_i\text{-independent terms} \\ &= \delta_{m', m} \times \vec{r}_i\text{-independent terms.} \end{aligned}$$

For an electronic transition this term is thus zero. Consider now the remaining term in equation 2.30. To solve this equation, the coordinate system is rotated such that the rotated z -axis, z' , points along the inter-nuclear axis. The dipole operator in the lab frame is related to that in the molecular frame by the elements of the 3×3 rotation matrix:

$$\sum_i^N \vec{r}_i = \sum_{k=1}^3 \sum_i^N D_{0k}(\theta, \phi) \vec{r}_i'. \quad (2.31)$$

It should be noted that the electronic wavefunctions, Φ_m , are eigenfunctions defined with stationary nuclei, whereas the position vectors, \vec{r}_i , are defined in the lab frame. The electronic wavefunctions should therefore be described in the rotated frame, in which the coordinates, \vec{r}_i' are referenced to the inter-nuclear axis.

The Born-Oppenheimer approximation was based on the assumption that the electronic wavefunction, $\Phi_m(\vec{R}; \vec{r}_i)$, is relatively insensitive to changes in \vec{R} . Applying that assumption to the remaining term in equation 2.30 it is possible to extract the electronic wavefunction from the integral over nuclear coordinates and define a separate electronic integral: $\vec{D}_{el} = -e \int \Phi_{m'}^* \left(\sum_i \vec{r}_i' \right) \Phi_m d\vec{r}_i'$. The angular and radial parts of the matrix

element can now be separated:

$$\begin{aligned} \langle \Psi' | \vec{D} | \Psi \rangle &= \sum_{k=1}^3 \left[\int \psi_{N,M_N}(\theta, \phi) D_{0k}(\theta, \phi) \psi_{N',M'_N}^*(\theta, \phi) \sin \theta d\theta d\phi \right. \\ &\quad \left. \times \vec{D}_{el} \int \psi_{v'}^*(R) \psi_v(R) dR \right]. \end{aligned} \quad (2.32)$$

Of course \vec{D}_{el} is a function of \vec{R} , because the electrons' coordinates are in part determined by the positions of the nuclei. However, given a weak dependence of the electronic wavefunction on \vec{R} it is possible to write an expansion for $\langle \Psi' | \vec{D} | \Psi \rangle$ in R . In this case equation 2.32 is the first term in this expansion. It is important to consider the eigenfunctions contained in equation 2.32. In the case of the rotational and electronic wavefunctions, each respective wavefunction forms part of a complete set. In the case of the electronic wavefunctions this was defined in the nuclear wave equation (equation 2.4). The rotational wavefunctions are spherical harmonics, which form a complete set. Consequently the integrals for these (properly normalised) wavefunctions will yield selection rules, which determine whether a transition can or cannot take place. The vibrational wavefunctions for different electronic states, however, do not form a complete set. This integral therefore measures the overlap of the two vibrational wavefunctions. This overlap is known as the 'Franck-Condon factor'. It determines the strength of any transitions allowed by the selection rules.

2.3.2 The hyperfine interaction

Nuclear spin has so far been neglected. Let the two nuclei have respective nuclear spin vectors \vec{I}_1 and \vec{I}_2 . These couple to give the total nuclear spin vector, $\vec{I} = \vec{I}_1 + \vec{I}_2$, which can have the following quantum numbers, $I = (I_1 + I_2), (I_1 + I_2 - 1), \dots, |I_1 - I_2|$. The energy of interaction of the nuclear spin with the other angular momenta of the molecule is usually much weaker than the rotational and spin-orbit energies. Consequently, its place in the coupling scheme is last: it couples with \vec{J} to give the total angular momentum vector, $\vec{F} = \vec{J} + \vec{I}$, with quantum numbers $F = (J + I), (J + I - 1), \dots, |J - I|$.

2.3.3 Selection rules for electronic transitions

The selection rules for electric dipole transitions will be dictated by the coupling case into which the molecule in question falls. It is worth noting that Hund's cases are limiting cases - often very good approximations. This renders most selection rules approximate. The strictness of the rules varies. The following rules will not be derived; the derivations can be found in many sources, such as [50].

There are two over-riding selection rules which apply regardless of the angular momentum coupling scheme. Firstly, the total angular momentum quantum number must

vary as follows over a transition: $\Delta F = 0, \pm 1$, with the stipulation that if the initial state is $F = 0$, then the final state must have $F \neq 0$. This selection rule results from the conservation of angular momentum.

The second general selection rule states that the parity of the state must change during an electric dipole transition. It is worth noting that for a Σ state, if the total spatial angular momentum (everything except spin) is even/odd, the parity is $+/-$. For all other states ($\Lambda \neq 0$) the state is doubly-degenerate. This manifold is made up of the symmetric and anti-symmetric superpositions of states with $M_L = \pm 1$, with one state having positive parity, and the other negative.

2.4 The Stark effect

When a heteronuclear molecule is exposed to an applied electric field $\vec{E}(x, y, z)$ the field polarises the molecule, creating a molecular dipole, $\vec{d} = \sum_i q_i \vec{r}_i$, where the sum is over all the electrons and nuclei, and \vec{r}_i are the coordinates of these charged particles. The Hamiltonian of the interaction between the applied field and the dipole is $\hat{H}_s = \vec{d} \cdot \vec{E}(x, y, z)$. The resulting energy shift is the Stark shift, $W_s(x, y, z)$, which can be used to affect the molecule's motion.

To investigate the Stark shift further consider a diatomic molecule with Hamiltonian, \hat{H}_0 , and field-free states $|m, v, J, M_J\rangle$, where m and v are the electronic and vibrational quantum numbers respectively, J is the total angular momentum quantum number, and M_J is the quantum number of the z -component of the total angular momentum. In the presence of an applied electric field the total Hamiltonian is $\hat{H}_{tot} = \hat{H}_0 + \hat{H}_s$. The eigenkets of \hat{H}_{tot} can be written as a linear sum of the field-free eigenkets. The Stark shift is found by diagonalizing the matrix of elements $\langle m', v', J', M_J' | \vec{d} \cdot \vec{E} | m, v, J, M_J \rangle$, where for now the spatial argument of \vec{E} is omitted for brevity. Let \vec{E} point along the z -direction. The molecular dipole, \vec{d} , points along the direction of the internuclear axis, \hat{k} , which makes an angle θ with \hat{z} . The matrix elements can thus be rewritten as $E \langle m', v', J', M_J' | d_z | m, v, J, M_J \rangle$. Consider now the operator d_z in a rotated coordinate space (X', Y', Z') , where Z' is parallel to the internuclear-axis. This is the molecular frame. In this frame $d_z = c_1 d_{X'} + c_2 d_{Y'} + c_3 d_{Z'}$, where c_1, c_2 and c_3 are elements of the rotation matrix, which have only an angular dependence. The electronic and vibrational states have much greater energy intervals than the rotational states and so it is possible to neglect the mixing of different electronic and vibrational states by the Stark interaction. Therefore, only those matrix elements in which $(m', v') = (m, v)$ contribute significantly to the Stark shift. The dipole terms have only radial dependence. c_1, c_2 and c_3 have only

angular dependence. Thus the matrix elements can be separated:

$$\begin{aligned}
 \langle m, v, J', M'_J | c_1 d_{X'} + c_2 d_{Y'} + c_3 d_{Z'} | m, v, J, M_J \rangle &= \langle m, v | d_{X'} | m, v \rangle \langle J', M'_J | c_1 | J, M_J \rangle \\
 &+ \langle m, v | d_{Y'} | m, v \rangle \langle J', M'_J | c_2 | J, M_J \rangle \\
 &+ \langle m, v | d_{Z'} | m, v \rangle \langle J', M'_J | c_3 | J, M_J \rangle.
 \end{aligned} \tag{2.33}$$

In the frame of a diatomic molecule there can be no component of the dipole perpendicular to the internuclear axis, and so $\langle m, v | d_{X'} | m, v \rangle = \langle m, v | d_{Y'} | m, v \rangle = 0$. This leaves

$$\langle m, v, J', M'_J | c_3 d_{Z'} | m, v, J, M_J \rangle = \langle m, v | d_{Z'} | m, v \rangle \langle J', M'_J | c_3 | J, M_J \rangle \tag{2.34}$$

The first factor in equation 2.34, $\langle m, v | d_{Z'} | m, v \rangle$, is the body-fixed molecular dipole moment, which shall be referred to as μ henceforth. Consider now the second factor. For a diatomic molecule the rotation matrix element, c_3 , is simply $\cos \theta$. It will be useful later on (below, and in chapter 5) to write this as a component of the rank 1 spherical harmonic operator, $\hat{C}_q^{(1)} = \sqrt{\frac{4\pi}{3}} \hat{Y}_q^{(1)}$. In this case $\cos \theta = \hat{C}_0^{(1)}$.

In all calculations of the Stark shift considered in this thesis only diatomic molecules will be considered, and they will be treated as rigid rotors. This is a good approximation for Σ states of diatomic molecules in which there is no spin-orbit interaction, and so the rotational energies dominate. A field-free rigid rotor is described by the states $|N, M\rangle$, which are eigenstates of the total rotational angular momentum operator, \vec{N}^2 , and its z -component, N_z . The matrix elements of the Hamiltonian for the interaction of a rigid rotor with an applied electric field are $\mu \langle N', M' | \hat{C}_0^{(1)} | N, M \rangle$.

Spherical tensors can be defined by two general commutation relations [49], one of which states that the commutation between a spherical tensor operator and a z -component angular momentum operator is $[N_z, \hat{C}_q^{(k)}] = \hbar q \hat{C}_q^{(k)}$. It follows from the commutation relation that:

$$\begin{aligned}
 \langle N', M'_N | [N_z, \hat{C}_q^{(k)}] - \hbar q \hat{C}_q^{(k)} | N, M_N \rangle &= \hbar (M'_N - M_N - q) \langle N', M'_N | \hat{C}_q^{(k)} | N, M_N \rangle \\
 &= 0.
 \end{aligned} \tag{2.35}$$

Consequently $\langle N', M'_N | \hat{C}_q^{(k)} | N, M_N \rangle = 0$ unless $M'_N = q + M_N$. In the case of the Stark interaction with an electric field along the z -direction, $q = 0$, and so the interaction mixes states of different N , but the same M .

In zero field the states are labelled by the quantum numbers $\{N, M\}$. When the electric field is applied N is no longer a good quantum number. However, in this case the states are labelled by $\{\mathcal{N}, M\}$, where \mathcal{N} is equal to the rotational quantum number of the zero-field state that the Stark-shifted state becomes when the field is reduced to zero adiabatically. Figure 2.1 shows the energy levels of a rigid rotor as a function of

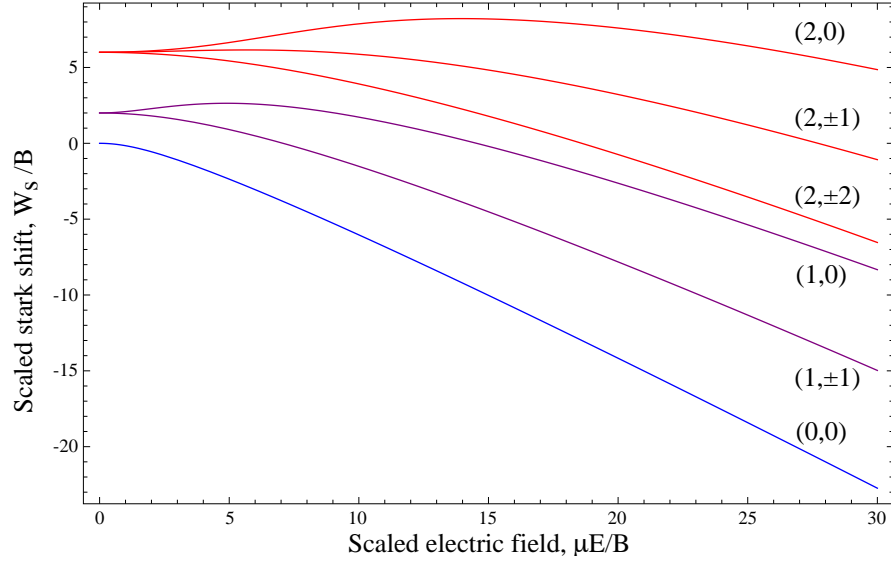


Figure 2.1: The Stark shift of a rigid rotor as a function of applied electric field. The Stark shift is given in units of the rotational constant, B . The field is given in terms of the dimensionless parameter $\lambda = \mu E/B$. The perturbed states are labelled by $\{\mathcal{N}, M\}$ where $\mathcal{N} = N$ when the field is reduced adiabatically to zero.

applied electric field. The ground state has relatively simple behaviour in an electric field: the energy is always reduced by the Stark interaction. In the limit of very low field the energy decreases quadratically with E , whereas in the limit of strong field the Stark shift is linear in E . Such a rigid rotor will tend to regions of strong-field, and as such is known as a strong-field (SF) seeker. The excited states exhibit more complicated behaviour. In a given \mathcal{N} manifold the sub-levels with the same value of $|M_N|$ experience the same Stark shift. This shift can have the same form as the ground state. Alternatively the Stark shift can increase with E , making the rotor a weak-field (WF) seeker. In the limit of very weak electric field the Stark shift is again quadratic in E . A rigid rotor will be a weak-field seeker only to a finite field, beyond which, as E is increased the gradient of the Stark shift flips and the rotor becomes a strong-field seeker. In a sufficiently strong field these ‘flipped’ Stark shifts will become linear in E . The field at which this WF–SF turn-over occurs increases for increasing \mathcal{N} .

In a given \mathcal{N} manifold, with $\mathcal{N} > 0$, the state with $M_N = 0$ always experiences the greatest positive Stark shift. Figure 2.2 shows the electric field, E_{max} , at which the state $|\mathcal{N}, M_N = 0\rangle$ experiences a maximum of electric field (after which the state becomes strong-field seeking) for $0 \leq \mathcal{N} \leq 9$. Also shown is a quadratic fit of the form $\mu E_{max}/B = f\mathcal{N}^2$. With $f = 2.46$ the fit matches the points quite well². This quadratic relationship will prove useful when discussing perturbations to the Stark-shifted rigid rotor

²In this thesis, B is an energy, rather than an angular frequency

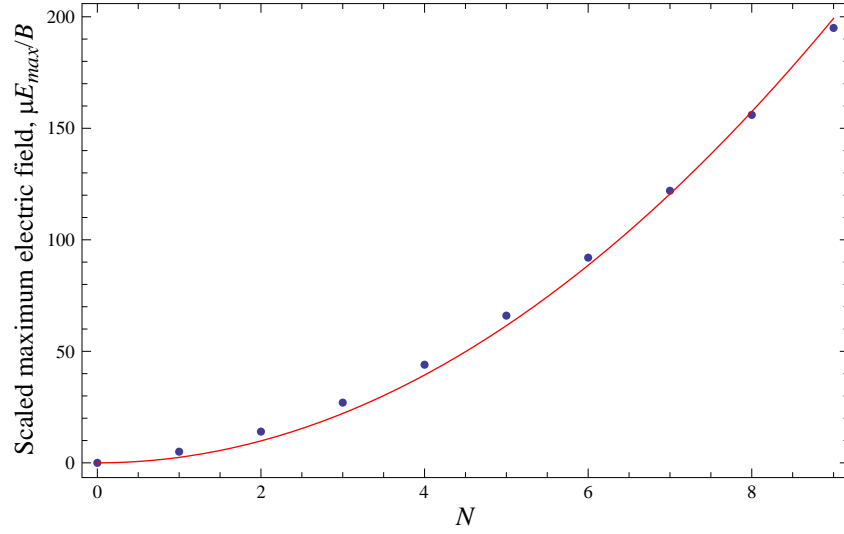


Figure 2.2: The electric field, E_{max} , at which the Stark-shifted state $|\mathcal{N}, M_N = 0\rangle$ experiences its maximum Stark shift for $0 \leq \mathcal{N} \leq 9$ (blue points). Also shown is a quadratic fit (red line) of the function $\mu E_{max}/B = f\mathcal{N}^2$, where $f = 2.46$.

states.

The Stark shift can be described in terms of a field-dependent ‘effective dipole moment’: $\mu_{eff}(E) = -\frac{dW_s}{dE}$. In the limit of very strong field μ_{eff} tends towards the value of the body-fixed dipole moment, μ .

2.5 Stark Deceleration

The energy change resulting from the Stark interaction between a polarized molecule and an applied electric field, $\vec{E}(x, y, z)$ can be used to affect the molecule’s motion. As a molecule traverses an inhomogeneous field there is a force exerted on it equal to the spatial derivative of the Stark energy, $\vec{F}(x, y, z) = -\nabla W_s(x, y, z)$.

Consider the set-up shown in figure 2.3. A weak-field seeking molecule is travelling along the z -direction with kinetic energy E_k and total internal energy (energy associated with electronic and nuclear motion and interactions), W . At some point along z are two oppositely polarised electrodes, positioned symmetrically about the z -axis. Approaching the electrodes along z the field increases until it reaches a maximum between the electrodes. Continuing along z after this point the E-field decreases.

As the weak-field seeker approaches the E-field maximum the Stark shift increases its total internal energy. By the conservation of energy it pays for this increase by losing kinetic energy — it decelerates. Once the molecule has reached the peak of this Stark potential hill it is at its slowest. Continuing along z the molecule ‘rolls down’ the potential hill, regaining its original kinetic energy. There has been no net loss of kinetic energy.

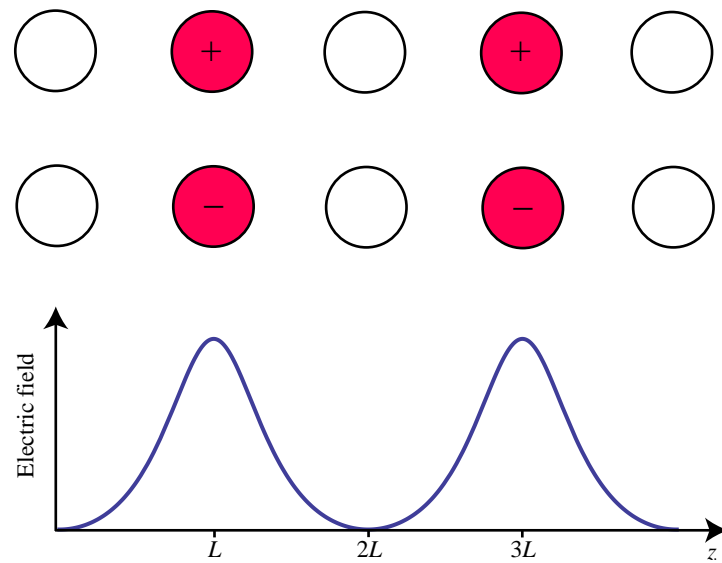


Figure 2.3: A schematic diagram showing the general structure of a Stark decelerator. The decelerator comprises an array of electric field stages along and about the beam-line (z -axis), here shown as a sequence of electrode pairs. At a given moment in time half the field stages will be grounded (white electrodes in the figure) and the other half charged at high voltage (red electrodes), with the field stages alternating between these two states along the length of the decelerator. A charged pair is polarized such that one electrode is at positive high voltage, and the other negative high voltage. The figure shows the decelerator in one configuration. Below the electrodes the form of the electric field magnitude along the beam-line is shown.

Consider now what would happen if the field were switched off with the molecule at the top of the potential hill. The field drops rapidly to zero, and so does the Stark shift. So what happens to the potential energy? Is it transferred back to the molecule's kinetic energy? Is there a difference between allowing the molecule to roll down the potential hill and 'forcing' the molecule to lose potential energy by turning off the field? To answer these questions consider the following mechanical analogy. Consider a bowling alley (figure 2.4). It is covered in a thin, flexible, elastic membrane. At some point along the alley is a piston set in the floor. The piston is controlled by a hydraulic line. With the piston at its lowest it is flush with the floor: the bowling alley is completely flat. Flicking a switch in the hydraulic system causes the piston to rise out of the floor rapidly, stretching the membrane, and creating a hill in the membrane.

Consider bowling a ball along the alley with the piston in the 'up' position. It moves forward with total energy equal to its kinetic energy, E_k . Encountering the raised membrane it travels up the hill, gaining gravitational potential energy and losing the same amount of kinetic energy. Once at the top of the hill the molecule is travelling very slowly. If it rolls down the hill it regains its kinetic energy. However, consider what happens if, with the ball on top of the hill, the hydraulics switch is flipped and the piston is allowed to fall: the hill collapses. Let the piston fall on a time-scale much shorter than that of the motion of the ball over the potential hill. The ball is sitting on top of the piston, exerting a downwards force on it. As the piston falls the ball falls with it, pushing down on the piston: it is coupled to the piston/hydraulics system. The ball transfers its potential energy to the hydraulics. It does not regain its original kinetic energy.

This is exactly the method used by a Stark decelerator. A weak-field seeker enters the field between two electrodes and climbs a potential hill. With the molecule at the top of the hill the field is switched off: the electrodes discharge to ground. The molecule is coupled to this system and transfers its potential energy to the electrical circuitry, and so continues along z with reduced kinetic energy.

A more quantitative argument for the deceleration mechanism can be found by considering the force exerted on the molecule by the deceleration stage. As the molecule climbs the potential hill it experiences a retarding force, $F_{decel} = -\partial W_s / \partial z$, the rate of change of energy with respect to space. When the molecule is at the top of the hill and the field is switched off, the Stark shift changes in time, not space and there is no force associated with this change. The molecule is decelerated only when it moves in a spatially-varying electric field.

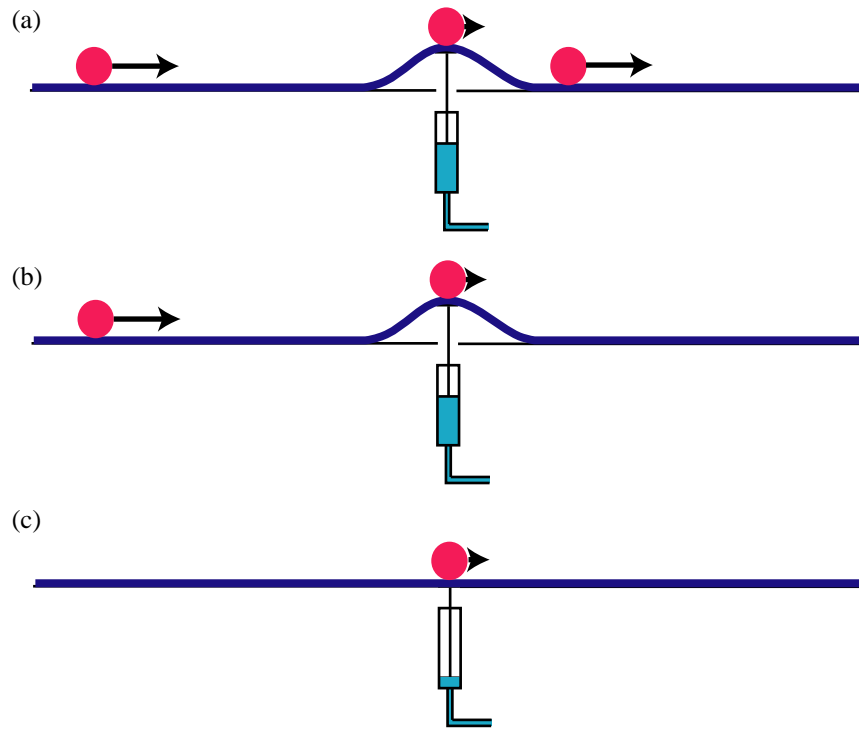


Figure 2.4: A mechanical model of a Stark decelerator. The model comprises a bowling alley, the surface of which is covered in an elastic membrane (shown in blue). At some distance down the alley is a hydraulically controlled piston, which has two states: ‘up’ and ‘down’. In (a) the piston is in the ‘up’ state, in which it sticks up through the alley floor, stretching the membrane and thus creating a gravitational potential hill. A ball bowled down the alley loses kinetic energy as it climbs this hill and then gains it as it rolls down again. In (b) the bowling ball is at the top of this hill with reduced kinetic energy, at an instant before it has started to roll down. In (c) the piston has just returned to its ‘down’ state. The piston fell down on a faster time-scale than the motion of the ball over the hill. The ball has transferred its gravitational potential energy to the piston/hydraulics system and continues along the bowling alley with reduced kinetic energy.

2.6 Focussing a molecular beam

In order to decelerate a divergent molecular beam it will be necessary to confine its transverse motion about the beam-line. It is possible to use the same electric fields that decelerate to guide the molecules. Much work was done on the theory of guiding molecular beams by Auberbach, Bromberg and Wharton [51].

In order to guide a diverging molecular beam along a beam-line it must be possible to apply a focussing force towards this axis. Consider using an electric field to apply this force, by means of the Stark interaction. To achieve static confinement two criteria must be met: firstly there must be no transverse force along the beam-line; secondly everywhere in transverse space around the beam-line the force must be restorative. Choosing a coordinate system in which the off-diagonal elements of the dyadic force gradient, $\nabla \vec{F}(\vec{r})$ are zero ($\frac{dF_i}{dj} = \delta_{ij}$, $i = x, y, z$), it can be seen that a necessary but not sufficient condition for static confinement is that $\nabla \cdot \vec{F}(\vec{r}) < 0$. However, it will be shown (chapter 6) that, although static guiding is not possible when $\nabla \cdot \vec{F}(\vec{r}) \geq 0$, it is possible to vary the field along the beam-line in such a way as to achieve dynamic guiding.

Chapter 3

Making and detecting CaF

3.1 Overview

The experiments discussed in this thesis concern pulsed beams of CaF radicals. The molecular beam is created in a chamber under high vacuum. The beam passes through a skimmer into a second high vacuum chamber which can contain a high voltage device to decelerate or guide the beam. Downstream of the device the molecules are detected by laser induced fluorescence (LIF) with a probe beam at 606.3 nm and a photomultiplier tube (PMT) used either in photon-counting or current mode. The photosignal is then acquired by a data acquisition (DAQ) card and analysed in Mathematica.

In this chapter the experimental apparatus concerned with the production and detection of beams of CaF will be described. Experimental details of the high voltage devices acting on the beam will be described later in the relevant chapters.

3.2 Producing a molecular beam

The molecule used throughout this project was the radical CaF. These molecules are created by laser ablation and supersonic expansion (see figure 3.1) in a source chamber (which is maintained below 10^{-7} mbar when the valve is closed). In the centre of the end flange of the source chamber is a solenoid valve. Outside the vacuum chamber, on the high pressure side of the valve is a 4 bar mixture of 98% inert carrier gas (typically Ar, Kr or Xe) and 2% SF₆. Inside the vacuum chamber, close to the valve opening, is a steel wheel of radius 50 mm. The rim of this wheel is covered in a roughly 2 mm-thick layer of calcium, glued into place with Torr-seal. The wheel is positioned such that the calcium surface is located around 2 mm away from the valve opening. To create a pulsed beam of CaF the valve is opened for between 100 μ s and 200 μ s. The high pressure gas mixture expands supersonically into the source chamber. After a short delay (typically 390 μ s – this will be discussed in section 3.2.1) light from a Q-switched Nd:YAG laser

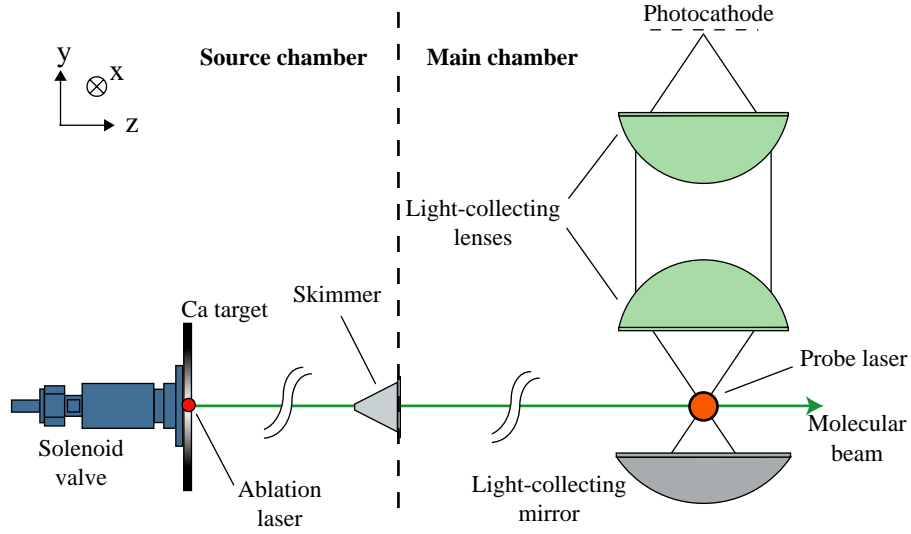


Figure 3.1: Schematic diagram of the creation and detection of pulsed beams of CaF. The beam is created by supersonic expansion of a carrier gas and SF₆, and ablation of a Ca target. The beam travels along the z -direction.

ablates the surface of the calcium next to the valve, resulting in a hot plume of Ca atoms around the ablation spot. The Nd:YAG laser has a wavelength of 1064 nm, a 10 ns pulse duration, 50 mJ maximum pulse energy and a 10 Hz repetition rate. The plume intersects the expanding gas mixture, and the hot Ca atoms react with the SF₆ to form, amongst other things, CaF radicals. The source is typically operated at a repetition rate of 10 Hz.

3.2.1 Supersonic Expansion

Basic theory

The 4 bar carrier gas expands supersonically into the vacuum chamber. A full description of supersonic expansion is very complicated and will not be given in detail here. For more details see [52].

The basic dynamics of supersonic expansion can be considered with the following model which closely resembles the experimental set-up. The system comprises two chambers, the valve and the vacuum chamber, initially separated by a wall. On one side of the wall there is a high pressure ideal gas with no net flow (said to be in the *stagnation state*). The pressure and temperature are $\{p_0, T_0\}$. On the other side the temperature are $\{p_1, T_1\}$. This second chamber is at much lower pressure: $p_1 \ll p_0$.

The first law of thermodynamics states that the change in total internal energy of a system is equal to the heat added to the system minus the work done by the system ($\Delta U = \Delta Q - \Delta W$). Enthalpy, H , is defined as follows: the change in enthalpy is the heat

transfer during a quasistatic process:

$$\Delta H = \Delta U + \Delta(pV). \quad (3.1)$$

Although enthalpy is better thought of in terms of a change in heat, a total enthalpy can be defined: $H = U + pV$.

If a small opening is made in the wall joining the two subsystems the ideal gas will flow through into the low pressure subsystem, with macroscopic flow speed v . In a supersonic expansion no heat is added to the system ($\Delta Q = 0$), whereas work is done ($\Delta W = p_1 V_1 - p_0 V_0$) and the total energy changes ($\Delta U = U_1 + \frac{1}{2}m_t v^2 - U_0$), where U_0 is the total internal energy of the gas in the left-hand subsystem and U_1 the total internal energy in the right-hand subsystem. m_t is the total mass of the gas flowing into the low-pressure chamber.

Assembling these changes in the first law gives:

$$\begin{aligned} U_1 + \frac{1}{2}m_t v^2 - U_0 &= p_0 V_0 - p_1 V_1 \quad \Rightarrow \quad \frac{1}{2}m_t v^2 = (U_0 + p_0 V_0) - (U_1 + p_1 V_1) \\ &= H_0 - H_1 \\ \Rightarrow \quad \frac{1}{2}v^2 &= h_0 - h_1, \end{aligned} \quad (3.2)$$

where $h = H/m_t$ is the specific enthalpy.

The heat capacity of an ideal gas at constant pressure is defined as $C_p = \left(\frac{\partial Q}{\partial T}\right)_p$. Now, combining equation 3.1 with the first law of thermodynamics gives $dH = dU + p dV + V dp = dQ + V dp$. A change in enthalpy *at constant pressure* is thus equal to the change in heat: $(dH)_p = (dQ)_p$. Thus

$$C_p = \left(\frac{\partial Q}{\partial T}\right)_p = \left(\frac{\partial H}{\partial T}\right)_p. \quad (3.3)$$

The heat capacity of an ideal gas at constant volume is defined to be $C_V = \left(\frac{\partial Q}{\partial T}\right)_V$. The first law shows that when volume is kept constant $(dQ)_V = (dU)_V$. The heat capacity at constant volume can thus be written:

$$C_V = \left(\frac{\partial Q}{\partial T}\right)_V = \left(\frac{\partial U}{\partial T}\right)_V. \quad (3.4)$$

If these thermodynamic quantities (C_V , C_p , U etc.) are defined for some mass m of gas, then dividing the quantities by m leaves what are known as the “specific” thermodynamic quantities. These are written in lower case letters. Equation 3.3 shows that the specific enthalpy, h , and specific heat capacity at constant pressure, c_p , are related differentially by

$$dh = c_p dT. \quad (3.5)$$

This allows equation 3.2 to be rewritten

$$v = \sqrt{2 \left(\int_0^{T_0} c_p dT - \int_0^{T_1} c_p dT \right)} = \sqrt{2 \int_{T_1}^{T_0} c_p dT} = \sqrt{2c_p (T_0 - T_1)}, \quad (3.6)$$

where c_p has been assumed constant. The temperature inside the source region, T_1 , relates to the translational motion along the beam-line axis. The temperature associated with transverse motion is different from this longitudinal temperature.

Consider the heat capacity of an ideal gas consisting of N molecules. The ideal gas law is $pV = Nk_B T$, from which it follows that $\left(\frac{\partial V}{\partial T}\right)_p = Nk_B/p$. It is also known for an ideal gas that the total energy is a function of temperature only, and so $\left(\frac{\partial U}{\partial T}\right)_V = \left(\frac{\partial U}{\partial T}\right)_p$. Combining these ideal gas characteristics gives:

$$\begin{aligned} C_p &= \left(\frac{\partial U}{\partial T}\right)_p + Nk_B \\ &= \left(\frac{\partial U}{\partial T}\right)_V + Nk_B \\ &= C_V + Nk_B = \frac{C_p}{\gamma} + Nk_B \\ \Rightarrow C_p &= \frac{Nk_B \gamma}{\gamma - 1}, \end{aligned} \quad (3.7)$$

where $\gamma = C_p/C_V$. If the molecules in this ideal gas have mass m_{mol} , then dividing both sides of equation 3.7 by Nm_{mol} gives the specific heat capacity: $c_p = \frac{k_B \gamma}{m_{mol}(\gamma - 1)}$. Substituting this into equation 3.6 gives

$$v = \sqrt{\frac{2k_B \gamma (T_0 - T_1)}{m_{mol}(\gamma - 1)}} \quad (3.8)$$

as the final longitudinal jet speed of a gas of translational temperature T_1 expanding from a valve at temperature T_0 into an evacuated chamber.

The speed of sound in an ideal gas with longitudinal translational temperature T_1 is $v_s = \sqrt{\gamma k_B T_1 / m_{mol}}$ [52]. The ratio of the gas jet speed to the speed of sound is defined as the ‘Mach number’, $M = v/v_s$. This definition of M is given in terms of thermodynamic quantities. However, it is also possible to derive an expression for M by solving the hydrodynamic state equations for supersonic expansion, which correspond to the conservation of mass, momentum and energy. This definition of Mach number is a function of position inside the source chamber, $M(x, y, z)$. It is independent of thermodynamic quantities, and so can be used as an independent parameter in the equation for the beam’s temperature. By substituting in the Mach number, equation 3.8 can be rearranged to give the beam longitudinal temperature as a function of position:

$$T_1(x, y, z) = T_0 \left(\frac{M(x, y, z)^2}{2} (\gamma - 1) + 1 \right)^{-1}. \quad (3.9)$$

Knowing that the beam speed increases as the molecules travel through the source chamber, $M(x, y, z)$ must also increase proportionally. Equation 3.9 thus shows that the beam temperature drops along the longitudinal coordinate, z . However, the final beam temperature might not correspond to the final beam speed. This is because as the beam expands its density decreases, until the mean free path of the molecules is sufficiently great that there are no collisions between molecules in the beam or with the chamber walls. When this point is reached the beam's longitudinal translational temperature is then effectively constant. This temperature can be obtained from the time-of-flight profile. The speed distribution of a supersonic beam with central longitudinal speed v_0 can be modelled in terms of a Gaussian distribution [38]. In this distribution the molecular flux in the longitudinal speed range between v and $v + dv$ is

$$f(v)dv = Av^3 \exp \left[\frac{-m_{mol}(v - v_0)^2}{2k_B T} \right] dv, \quad (3.10)$$

where A is a normalizing parameter and T is the longitudinal translational temperature. Assuming an infinitely short pulse at the source, the resulting time-of-flight profile measured a distance L downstream of the source can be modelled by [38]:

$$h(t) = \frac{AL^4}{t_0^5} \exp \left[\frac{-m_{mol}L^2}{2k_B T t_0^4} (t - t_0)^2 \right], \quad (3.11)$$

where $t_0 = L/v_0$ and it has been assumed that the times in the distribution are very close to t_0 : $(t - t_0)/t_0 \sim 1$.

Experimental details

The CaF radicals produced in the ablation source are entrained in the supersonic expansion. 70 mm downstream of the valve the source chamber ends in a wall, in the centre of which is a skimmer with a 2mm diameter orifice. Those molecules that are able to pass through the skimmer enter the second chamber (referred to henceforth as the 'main chamber').

Because the beam is predominantly composed of the carrier gas the beam speed is determined by equation 3.8, where m_{mol} is the atomic mass of the carrier gas species. The three carrier gases used (Ar, Kr and Xe) are all monatomic, and so $\gamma = \frac{5}{3}$. The temperature of the expanded gas can be assumed to be considerably smaller than the temperature of the valve, which is at room temperature ($T_0 = 293 \text{ K} \gg T_1$). The axial speed of the resulting beams in the three cases are then calculated to be 304 ms^{-1} for Xe, 380 ms^{-1} for Kr and 550 ms^{-1} for Ar.

The time-averaged effect of the supersonic expansion is that the source chamber's pressure raises from 10^{-7} mbar to around 10^{-4} mbar when the experiment is running at 10 Hz. This pressure can be varied by controlling how far back the valve poppet is pulled.

This can be controlled directly by varying the solenoid voltage and opening duration. It was found empirically that the signal is maximized when the valve voltage and opening duration are set such that the source chamber pressure is between 2×10^{-4} mbar and 4×10^{-4} mbar when running at 10 Hz.

The investigation of experimental parameters to produce the desired molecular beam fluxes, speeds and temperatures was performed by Darnley [53]. An important parameter which determines properties of the molecular beam is the Nd:YAG pulse energy. The pulse energy can be varied by two experimental parameters: by varying the delay between the laser’s flashlamp trigger and its Q-switch trigger (the ‘flash-to-Q’ delay), and by a variable infra-red filter on the output of the laser. Darnley [53] found that with the flash-to-Q delay set to $150 \mu\text{s}$ the maximal filter transmission gave a pulse energy of 35 mJ. The pulse energy that maximizes the molecular flux varies with the quality of the Ca target. The usual method of varying the pulse energy is to leave the flash-to-Q delay constant and change the transmission of the variable filter. Typical pulse energies used are 25 mJ.

The other main parameter that affects the molecular beam’s properties is the delay between the valve opening and the Q-switch trigger, known as the ‘valve-to-Q’ delay. Firing the Nd:YAG when the carrier gas density is at its greatest next to the Ca target maximizes the CaF beam flux. For example, for a beam with Ar carrier gas Darnley [53] found that a valve-to-Q delay of $340 \mu\text{s}$ maximized the CaF beam flux. This delay corresponds to the time response of the solenoid valve; it is the delay between trigger and the valve being most open. However, it was also found that the valve-to-Q delay affects the beam’s longitudinal speed and temperature. A valve-to-Q delay of $390 \mu\text{s}$ was found to minimize the temperature. Given that molecular signal was rarely a problem in these experiments the valve-to-Q delay was chosen so as to minimize speed and temperature of the beam.

Figure 3.2 is a photograph of the vacuum chamber used in the experiments described in this thesis.

3.3 Detection

3.3.1 Detection overview

The molecules are detected in the main chamber by laser-induced fluorescence (LIF). The main detection apparatus can be located either 810 mm or 1215 mm downstream of the source. At one of these points a 606.3 nm cw laser beam enters the chamber orthogonally to the molecular beam through a Brewster-angled window (figure 3.2). The laser intersects the molecular beam and drives the $A^2\Pi_{1/2}(v' = 0) - X^2\Sigma^+(v'' = 0)$ electronic transition. By varying the laser frequency the molecules in selected rotational states can be detected. The photons emitted by the decaying molecules are then detected by a PMT, operated

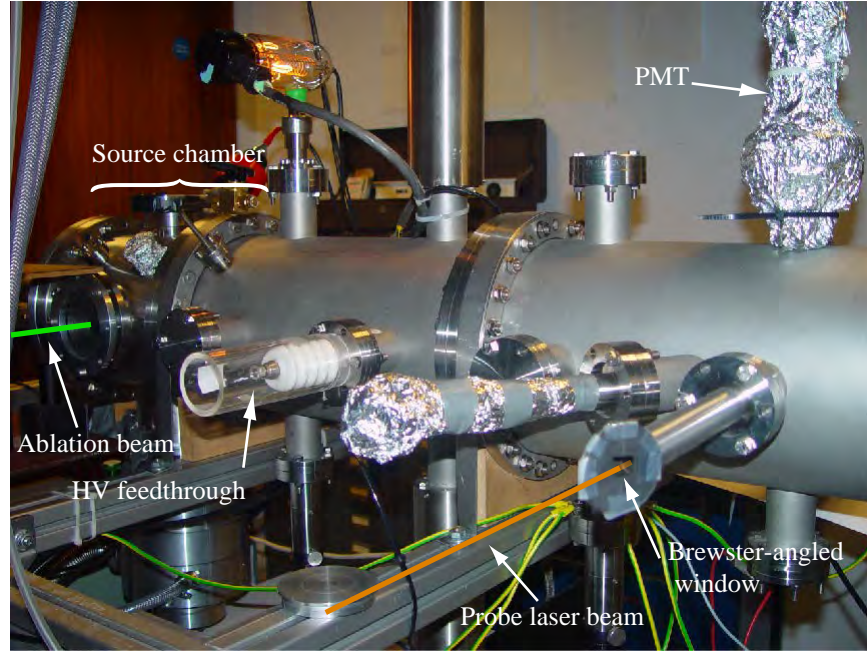


Figure 3.2: A photograph of the vacuum chamber.

either in photon-counting or current mode. In current mode the PMT signal is sent to a pre-amplifier with a given gain. The pre-amplifier converts the PMT current, integrated over a time constant of about $1\ \mu\text{s}$, to a voltage which is then sent to the DAQ card. The pre-amplifier output voltage, V_{pre} , was calibrated by scattering probe beam light onto the PMT photocathode. For a given light intensity the pulsed photon counting PMT output rate, R_{pc} , was measured with a counter and then V_{pre} was measured. For PMT signal strengths of the magnitude obtained in measuring laser-induced fluorescence a linear relationship was found between R_{pc} and V_{pre} :

$$R_{pc} = 1.33V_{pre} + 2.02, \quad (3.12)$$

where R_{pc} is measured in kHz and V_{pre} in mV. The photon-detection system can be operated with resolution as fine as $1\ \mu\text{s}$. However, in this limit the resolution of a time-of-flight profile is limited by the transit time of a molecule through the laser probe beam: the uncertainty in a molecule's position in the laser probe beam when it is detected creates uncertainty in its time of detection. Consider a beam of CaF radicals travelling around $600\ \text{ms}^{-1}$. With a probe beam width of 2 mm, and assuming that the molecule has an equal probability of being detected anywhere in its transit of the probe beam (this will be discussed in more detail in chapter 4), then the uncertainty in the the time-of-flight profile is $2\ \text{mm}/600\ \text{ms}^{-1} \approx 3\ \mu\text{s}$. This uncertainty rises for slower beams.

Figure 3.3 shows a recorded time-of-flight profile for CaF seeded in an Ar carrier, with a source-to-detector distance of 1215 mm. The Q-switch of the ablation laser defines the zero of time. The data were fitted to the function given in equation 3.11. This fit

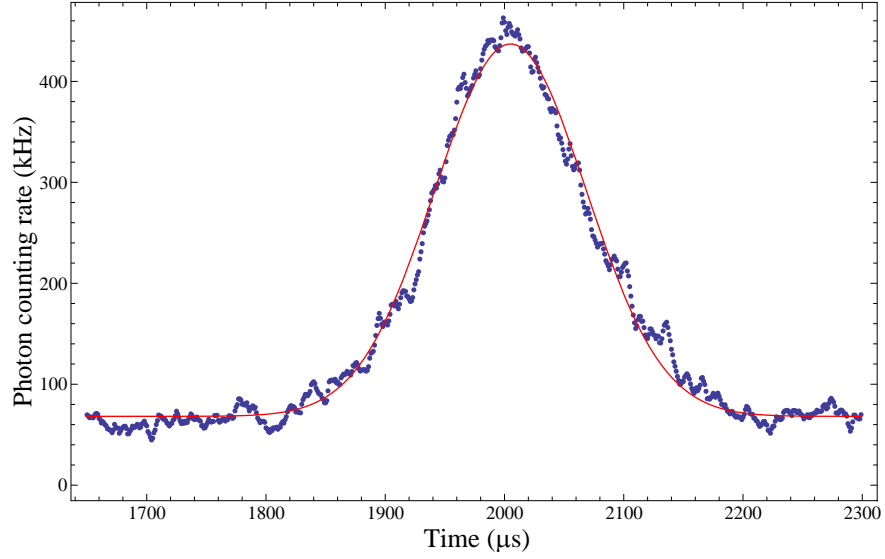


Figure 3.3: An example time-of-flight (TOF) profile for CaF in an Ar-carried beam (blue points) detected 1215 mm downstream from the source. The data are fitted to the Gaussian function given in equation 3.11. The resulting fit (red line) gives a longitudinal translational temperature of 2.6 K and a central speed of 2005 μs . The signal is an average of approximately 500 shots with the laser on resonance with the $Q_{11}(\frac{1}{2})$ transition from the $F = 1$ ground state hyperfine level.

yields a longitudinal translational temperature of 2.6 K and a peak time of 2005 μs . This peak time corresponds to a central speed of 606 ms^{-1} . This is greater than predicted by equation 3.8. Analysis of TOFs for beams with Xe and Kr carrier gases also find central speeds approximately 10% greater than predicted. Various reasons have been suggested for this. Tarbutt *et al.* [38] suggest that heating by the solenoid in the valve causes T_1 to be greater than room temperature. However, it is found that gas temperatures of around 350 K would be necessary to bring the theoretical prediction into line with the measured speeds. Another factor (although a minor one) is that the expanding gas is not just noble gas, it is also 2% SF_6 . With many degrees of freedom one molecule of SF_6 can transfer much more energy to longitudinal jet kinetic energy than a monatomic noble gas molecule. Inclusion of this in the theoretical analysis will increase the predicted speed, but only negligibly as SF_6 makes up such a small proportion of the expanding gas. Other suggestions for a greater-than-predicted speed are cluster formation of noble gas during expansion (a process which releases heat) and the possibility that during the expansion the CaF does not come fully into thermal equilibrium with the carrier gas and so will not travel at a speed entirely dictated by the latter.

3.3.2 The probe laser

The probe laser is a ring cavity Coherent 699 dye laser, using rhodamine 6G. It is pumped by an Argon Ion laser (Coherent Innova 310). For a typical pumping power of 6 W and a fresh batch of dye the dye laser outputs around 250 mW at 606.3 nm. Single longitudinal mode operation is achieved by the use of a birefringent filter and a thin etalon in the laser cavity. The longitudinal mode frequency is stabilized against mechanical jitter by a piezo-driven thick etalon. A beam-splitter picks off a small fraction of the laser output and directs it to a confocal reference cavity. The laser frequency can be locked to the transmission signal of the reference cavity by the use of a high-frequency piezo-mounted mirror and a scanning Brewster plate, both inside the laser cavity. Tilting a galvo-plate inside the cavity (which scans the optical path length of the cavity) scans the laser output frequency. A -5 V to +5 V signal controlled by a PC is used to scan the laser frequency. The Coherent 699 claims a maximum scan width of 30 GHz, but in practice it has been found that mode-hopping limits the scan width to under 10 GHz.

The laser frequency-stabilised beam then traverses beam-shaping optics and a 750 MHz confocal reference cavity. This second cavity is used as a secondary method of locking the laser frequency as the cavity mentioned above suffers from thermal variations over the course of several minutes, causing the laser frequency to drift by several MHz. At various points in the experiments an acousto-optic modulator (AOM) was also used both for the purposes of frequency fine-tuning and intensity control. This will be discussed in more detail in the relevant chapter.

3.3.3 Electronic transitions in CaF

In all experiments in this thesis the molecules probed were in the ground electronic ($X^2\Sigma^+$) and vibrational ($v = 0$) state, and were excited to the first excited electronic state ($A^2\Pi_{1/2}$, $v' = 0$). By varying the probe laser frequency it was possible to measure an extensive spectrum of transitions between different rotational states in these two manifolds.

The ground electronic state is a $^2\Sigma^+$ state, described well by Hund's case (b). The component of the orbital angular momentum along the inter-nuclear axis is zero, $\Lambda = 0$. The total spin, \vec{S} (magnitude $S = \frac{1}{2}$) couples with the rotational angular momentum, \vec{N} to give $\vec{J} = \vec{N} + \vec{S}$. The basic analysis of rotational energy levels in chapter 2 shows that for a given vibrational state the rotational energy levels are given by $BN(N + 1)$, where B is the rotational constant. This analysis ignores the non-rigidity of the diatomic molecule as well as some smaller interactions that occur within the molecule. Consider the first point: the rotation of a non-rigid rotor causes the internuclear axis to stretch, an effect known as the 'centrifugal distortion'. This stretching increases the moment of inertia which affects the rotation frequency. The second point concerns additional interactions so

far ignored. Of these the most important is the spin-rotation interaction, $\gamma \vec{N} \cdot \vec{S}$. This is the interaction between the magnetic dipoles associated with the electron spin and the molecule's rotation. It is reasonable to assume that the magnitude of the interaction energy will increase with N and will also be affected by the centrifugal distortion. The sign of the energy shift is dictated by the orientation of \vec{S} relative to \vec{N} . When $J = N + \frac{1}{2}$, the state is labelled \mathcal{F}_1 . When $J = N - \frac{1}{2}$, the state is labelled \mathcal{F}_2 .

The approach to dealing with these interactions is to write the energy of a given electronic and vibrational state as a polynomial in $N(N+1)$. Much work on the spectrum of CaF was performed by Kaledin *et al.* [54]. The expressions used by Kaledin for the electronic ground state energies (in vibrational state v) are

$$\begin{aligned} \mathcal{F}_{1_v}(N) = & T_v + B_v(N(N+1)) - D_v(N(N+1))^2 + H_v(N(N+1))^3 \\ & + \frac{1}{2}(\gamma_v + \gamma_{D_v}(N(N+1))^2)N \end{aligned} \quad (3.13)$$

$$\begin{aligned} \mathcal{F}_{2_v}(N) = & T_v + B_v(N(N+1)) - D_v(N(N+1))^2 + H_v(N(N+1))^3 \\ & - \frac{1}{2}(\gamma_v + \gamma_{D_v}(N(N+1))^2)(N+1). \end{aligned} \quad (3.14)$$

The first term, T_v , is the vibrational energy ($T_{v=0} = 0$). The next three terms in equations 3.13 and 3.14 represent the rotation with centrifugal distortion. The final two terms in each equation represent the spin-rotation interaction, which includes a centrifugal distortion of its own. The sign of the spin-rotation shift is positive/negative in the $\mathcal{F}_1/\mathcal{F}_2$ states. Interactions involving nuclear spin are not yet included.

The state excited by the probe laser is the $^2\Pi_{1/2}(v' = 0, f)$ state¹. It is described well by Hund's case (a). Both \vec{L} and \vec{S} are strongly coupled to the internuclear axis. The component of \vec{J} along the internuclear axis is either $\Omega = \frac{1}{2}$ or $\Omega = \frac{3}{2}$, where the energies of these two states are split by the spin-orbit interaction. These two states are described approximately by the pure Hund's case (a) states, $|^2\Pi_{\frac{1}{2}}\rangle$ and $|^2\Pi_{\frac{3}{2}}\rangle$: the spin-orbit interaction Hamiltonian is diagonal in this basis, however, the molecular rotation energy is not. The two states are thus described by linear superpositions of $|^2\Pi_{\frac{1}{2}}\rangle$ and $|^2\Pi_{\frac{3}{2}}\rangle$:

$$\mathcal{F}_1 = c'_1|^2\Pi_{\frac{1}{2}}\rangle + c'_2|^2\Pi_{\frac{3}{2}}\rangle \quad (3.15)$$

$$\mathcal{F}_2 = c''_1|^2\Pi_{\frac{1}{2}}\rangle + c''_2|^2\Pi_{\frac{3}{2}}\rangle, \quad (3.16)$$

where the term amplitudes are determined by the relative strength of the spin-orbit interaction and rotation energies.

¹The state is made up of a superposition of states with $\Lambda = 1$ and $\Lambda = -1$. The letter f in the term notation denotes that this is the superposition with negative parity.

In addition the centrifugal distortion and spin-orbit interaction couple different electronic states. Kaledin *et al.* found that to describe the system well required the inclusion of only one more excited state, the second excited state, $B^2\Sigma_{\frac{1}{2}}^+$. The new basis set for describing the excited state is thus $\{|^2\Pi_{\frac{1}{2}}\rangle, |^2\Pi_{\frac{3}{2}}\rangle, |^2\Sigma_{\frac{1}{2}}\rangle\}$. Kaledin *et al.* modelled each matrix element in the Hamiltonian in terms of expansions and then used experimental data to deduce the value of all the expansion coefficients. Finding the eigenstates of this matrix with these coefficients gives the energy levels of the system. One of the effects of the interactions between different electronic states is to lift the degeneracy of symmetric and antisymmetric superpositions of $\Lambda = \pm 1$ (' Λ -doubling'). In these experiments transitions are driven only to the antisymmetric state, f , because it has negative parity, and the ground $N = 0$ state has positive parity. Despite the mixing of states, the excited state shall be referred to as the $A^2\Pi_{\frac{1}{2}}(v' = 0, f)$ state, because the coefficient of the $|A^2\Pi_{\frac{1}{2}}\rangle$ state is close to 1. The vibrational quantum number and parity term will be omitted when they are not needed.

Using the constants quoted in [54] the energy level structure of CaF has been constructed. Figure 3.4 shows the first four rotational levels of the $X^2\Sigma^+(v = 0)$ state and the first four rotational states of the $A^2\Pi_{\frac{1}{2}}(v' = 0)$ state (all of the latter are \mathcal{F}_1 states). The hyperfine interaction has not been included in the calculations and hyperfine splittings are not shown in figure 3.4. The figure also shows a number of allowed transitions. The relevant electric dipole selection rules are $\Delta J = \pm 1, 0$ and that parity must change. Defining $\Delta J = J_{\text{excited}} - J_{\text{ground}}$ the transitions are labelled as follows: if $\Delta J = 1$ it is an R transition; if $\Delta J = 0$ it is a Q transition; and if $\Delta J = -1$ it is a P transition. A transition from a state \mathcal{F}_i to state \mathcal{F}_j is labelled with the subscript ij , where the indices can be 1 or 2. Finally, the value of J of the initial state is shown in parenthesis. For example, the transition from $X^2\Sigma^+(v = 0, J = \frac{1}{2}, \mathcal{F}_2)$ to $A^2\Pi_{\frac{1}{2}}(v' = 0, J' = \frac{3}{2})$ is labelled $P_{21}(\frac{1}{2})$.

Figure 3.5 shows spectral lines in CaF recorded by LIF. The data were taken in three sections: a continuous spectrum from 494486 GHz to 494453 GHz, a second from 494449 GHz to 494481 GHz and a third from 494479 GHz to 494492 GHz. Each of these sections is the mean of a number of smaller, overlapping scans, typically between 3 GHz and 10 GHz wide. The central frequency of each scan is known from a wavemeter reading (accurate to 500 MHz). Transmission fringes from the 750 MHz confocal cavity provide a relative frequency scale and allow individual scans to be joined together accurately. The overlapped scans were binned into 20 MHz sections, and the mean signal found for each bin. This is what is plotted in figure 3.5.

It is worth noting that many overlapping scans were recorded and so each spectral line shown in figure 3.5 is the mean of several scans. Flux variations due primarily to Ca target degradation will cause the constituent lines in each average to have different amplitudes. Thus the final mean amplitude is determined not only by the theoretical line strength,

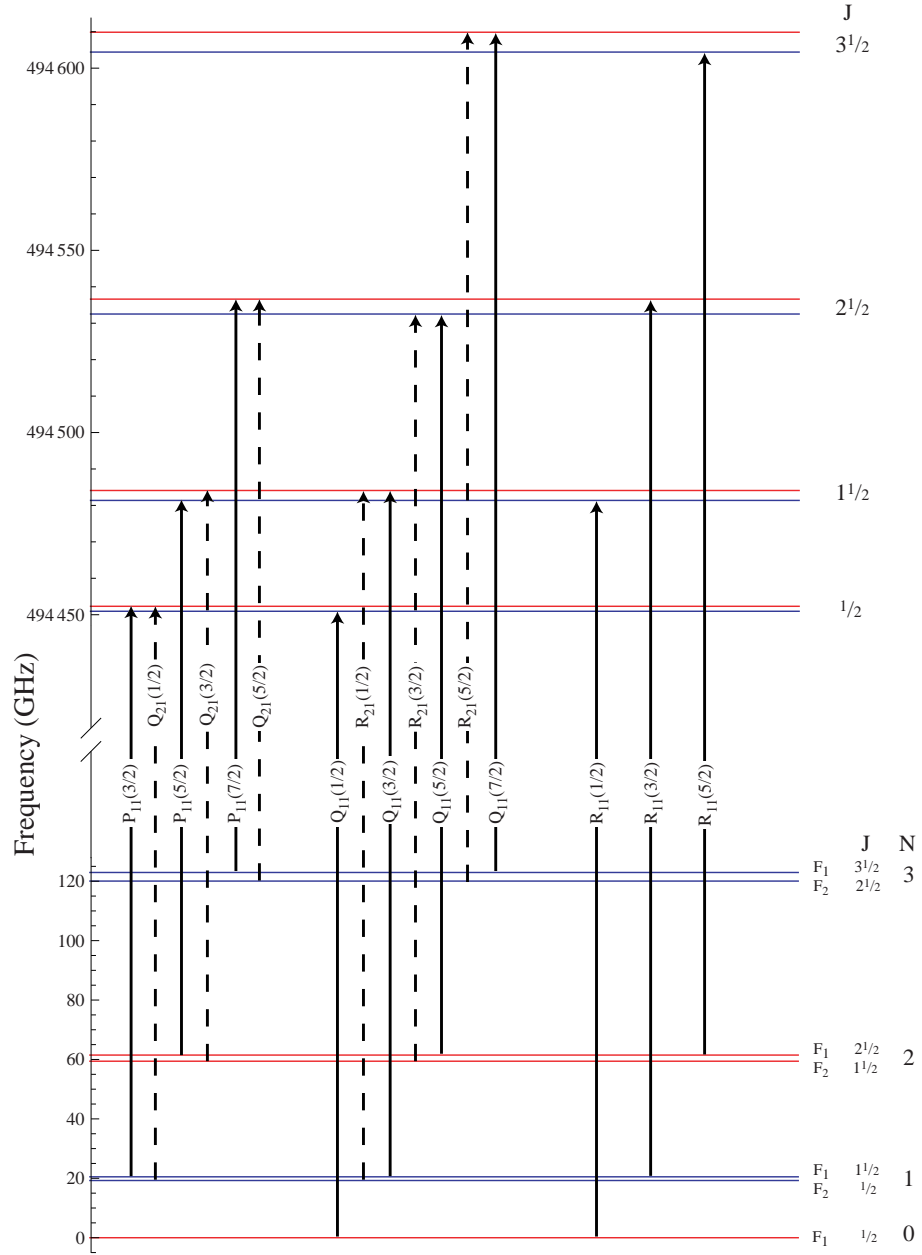


Figure 3.4: The first four rotational levels of the $X^2\Sigma^+(v=0)$ and $A^2\Pi_{1/2}(v'=0)$ states. The spin-rotation splitting in the X state has been magnified by a factor of 10 for clarity. The Λ -doubling in the A state has not been magnified. Also shown are a number of allowed $\mathcal{F}_1 \rightarrow \mathcal{F}_1$ transitions (solid lines) and $\mathcal{F}_2 \rightarrow \mathcal{F}_1$ transitions (dashed lines). States with positive parity are shown in red, and those with negative parity are shown in blue.

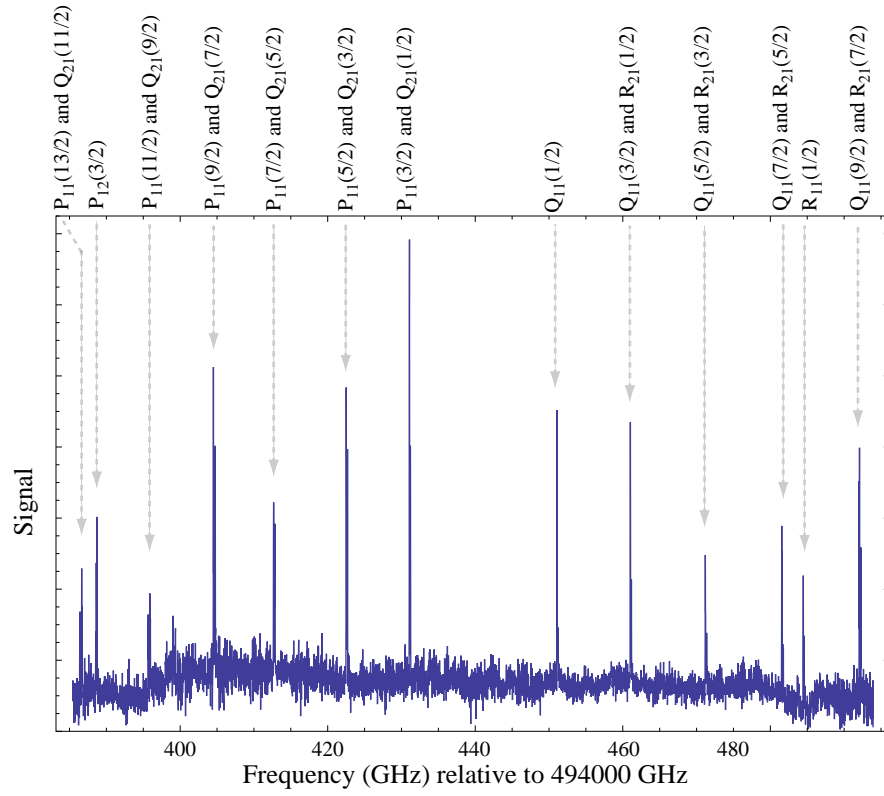


Figure 3.5: Experimental spectrum of CaF measured by laser induced fluorescence. The lines are identified by dashed grey lines and match the frequencies predicted from the Hamiltonian and constants given by Kaledin *et al.* [54].

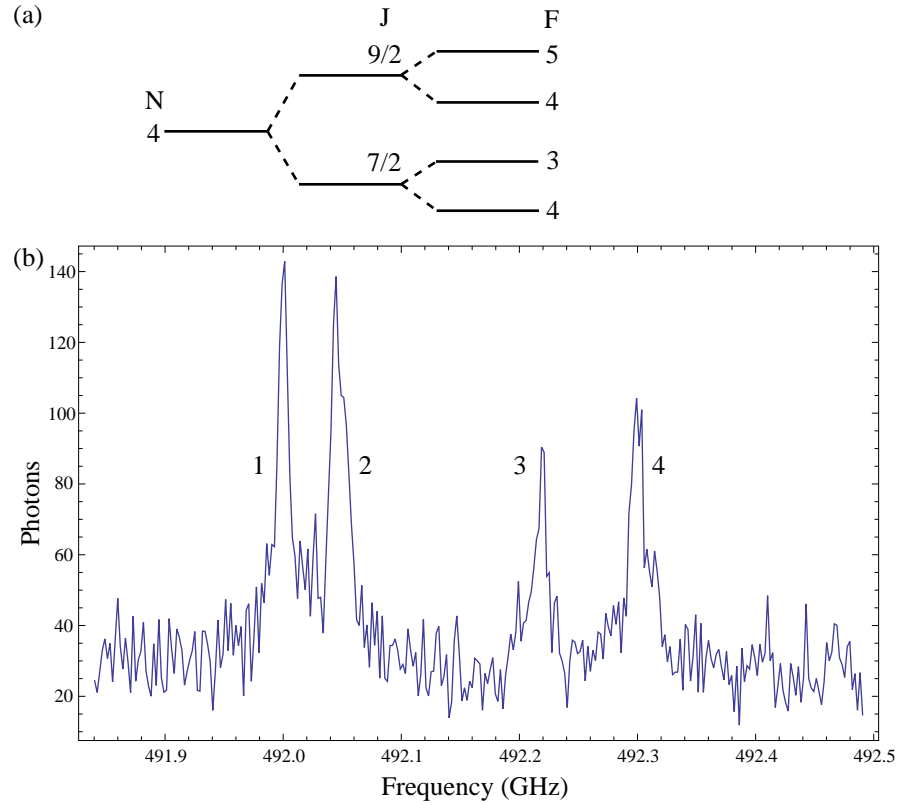


Figure 3.6: (a) A schematic diagram showing the effect of the spin-rotation and hyperfine interactions on the $N = 4$ state. (b) The $Q_{11}(\frac{9}{2})$ and $R_{21}(\frac{7}{2})$ lines originating from the $N = 4$ state of CaF. The lines have been numbered from 1 to 4 in order of increasing frequency. The splitting between lines 1 and 2 and lines 3 and 4 comes from the spin-rotation interaction, whereas the splitting within each of those pairs comes from the hyperfine interaction. The lines correspond to transitions from states with $F = 5$ (line 1), $F = 4$ (line 2), $F = 3$ (line 3) and $F = 4$ (line 4).

but by variations in the molecular flux. It should also be noted that these three sections were taken at different times during this project, and under different conditions. The first and third spectra were taken with the PMT operating in photon counting mode, while the second was taken in current mode. In addition the probe beam shapes and intensities were different in the three spectra ($210\mu\text{W}$, $165\mu\text{W}$ and $315\mu\text{W}$ respectively). Consequently it is difficult to compare the signal strengths in these three spectra. For clarity the set have been scaled such that their background signal levels match. For these reasons the relative line strengths are not comparable. The purpose of this spectrum is to identify the lines and confirm the molecular constants found by Kaledin. Very good agreement was found between the lines in figure 3.5 and those predicted from the constants in [54].

Figure 3.6 (a) shows the effect of the spin-rotation and hyperfine interactions on the $N = 4$ state. As a result of the spin-rotation interaction, \vec{N} and \vec{S} couple to give \vec{J} .

The hyperfine interaction then couples in the nuclear spin, leading to states described by the total angular momentum quantum number, $F = I + J$. Figure 3.6 (b) shows a scan over the $Q_{11}(\frac{9}{2})$ and $R_{21}(\frac{7}{2})$ lines. The excited state hyperfine splitting is much smaller than any of the observed structure in the ground state, and is not resolved². The four spectral lines in figure 3.6 result from the spin-rotation and hyperfine interactions that split the $N = 4$ rotational state. The Hamiltonian for these interactions is $\hat{H}_{int} = \gamma \vec{S} \cdot \vec{N} + b \vec{I} \cdot \vec{S} + c(\vec{I} \cdot \vec{k})(\vec{S} \cdot \vec{k}) + C \vec{I} \cdot \vec{N}$ [55], where \vec{S} is the total electronic spin operator, \vec{I} is the total nuclear spin operator and \vec{k} is the unit vector along the internuclear axis. The constant, γ , b , c and C have been determined for CaF by Childs and Goodman [56]. The spectral lines are numbered from 1 to 4 in order of frequency. Diagonalizing the above Hamiltonian with a large basis of field-free rigid rotor eigenstates identifies the lines as follows: lines 1 and 2 correspond to transitions from the \mathcal{F}_1 state with $J = \frac{9}{2}$; lines 3 and 4 correspond to transitions from the other spin-rotation state, the \mathcal{F}_2 state with $J = \frac{7}{2}$. Lines 1 and 4 correspond to states where the nuclear spin z -component is added positively ($F = J + \frac{1}{2}$), giving states with $F = 5$ and $F = 4$ respectively; and lines 2 and 3 correspond to states where the nuclear spin z -component subtracts ($F = J - \frac{1}{2}$), giving states with $F = 4$ and $F = 3$ respectively.

²The excited state hyperfine splitting is measured in chapter 4 to be 4.8 ± 1.1 MHz

Chapter 4

Measuring molecular parameters

4.1 Motivation

This chapter describes the measurement of molecular parameters of CaF by the saturation of laser-induced fluorescence (LIF). By measuring the amplitude and width of two spectral lines as a function of probe beam power the Franck-Condon factor of the $A-X$ (0-0) transition was measured to be $Z = 0.987^{+0.013}_{-0.019}$, and the hyperfine interval and lifetime of the $^2\Pi_{\frac{1}{2}}$ state were measured to be $\Delta_e = 4.8 \pm 1.1$ MHz and $\tau = 19.2 \pm 0.7$ ns respectively.

These measurements are important for several reasons. Firstly, the value of the Franck-Condon factor is very important in determining whether laser cooling is possible for CaF. Laser cooling of molecules is generally regarded as impractical, because of the many possible dark states into which a molecule can be pumped, especially in other vibrational states. However, there are molecules for which the transition probabilities to other vibrational states are small enough to make laser cooling feasible [57]. Laser cooling of molecules is extremely desirable, with several applications for molecular beams. Firstly, transverse cooling can be used in the source chamber to increase beam flux. Secondly, longitudinal cooling can be used to bunch the molecules into a narrow velocity group, vastly increasing the number of molecules that can be loaded into the travelling potential well of a Stark decelerator (see chapter 5). Laser cooling could also potentially be used to decelerate a beam directly, and then cool molecules in a MOT to ultracold temperatures. The efficiency of laser cooling is determined by the number of photons scattered before the molecule enters a dark state. A Franck-Condon factor close to unity reduces the probability of the molecule entering a dark state in another vibrational state, and increases the number of scattered photons. For example DeMille [58] has investigated the potential for laser cooling SrF. It was found that, with an $A-X$ (0-0) Franck-Condon factor of 0.98, a laser cooling scheme with a repump laser out of the X ($v' = 1$) state can scatter around 150 photons per molecule. Calculations with Franck-Condon factors for transitions to higher vibrational states shows that adding just one more vibrational repump laser increases this to around

10^5 photons per molecule. The measurement of the $A-X$ (0–0) Franck-Condon factor in this chapter indicates that CaF is a good candidate for laser cooling.

Secondly the measurements serve as an experimental test of theoretical calculations of molecular parameters. In particular a recent theoretical study of CaF by Pelegrini [59] found the $A-X$ (0–0) Franck-Condon factor to be 0.964 and the $^2\Pi_{\frac{1}{2}}$ state lifetime to be 19.48 ns, both in very good agreement with the measurements presented in this chapter.

Thirdly, these measurements allow for the determination of the mean number of photons scattered by each CaF molecule in the detection region, which is needed for an accurate measurement of the molecular flux created in the beam machine.

The experimental procedure used to make these measurements is very simple, involving only a single cw probe beam. This is considerably simpler than the usual method of measuring these molecular parameters. Franck-Condon factors are typically measured by absorption or emission spectroscopy. For example, Anderson [61] measured Franck-Condon factors of PO by driving a $B-X$ (0–0) transition and then using a monochromator to detect fluorescence to the $v'' = 0, 1, 2$ states. The CaF Franck-Condon measurement presented in this chapter involves a much simpler experimental set-up, with detection of only the (0–0) fluorescence necessary. The usual method of measuring state lifetimes involves driving a transition to an excited state with a fast pulsed laser beam, and then measuring the resulting fluorescence with a fast, high-temporal-resolution detector. For example, Dagdigian [60] measured the lifetime of the $^2\Pi_{\frac{1}{2}}$ state in CaF to be 21.9 ± 4.0 ns by driving the $X^2\Sigma^+ - A^2\Pi_{\frac{1}{2}}$ transition with a 5 ns pulsed laser beam, and then measuring the decay fluorescence with a fast photomultiplier. The measurement presented in this chapter is more precise than that of Dagdigian.

4.2 Saturation mechanisms

Consider a two-level molecule irradiated by a laser beam. The molecule traverses the width of the laser beam in time T . The laser drives the transition from the ground state, $|1\rangle$, to the excited state, $|2\rangle$. The molecule then decays to the ground state, emitting a photon, and can then be excited again. If the excitation rate, R , greatly exceeds the decay rate, Γ , then the fluorescence saturates: supplying a greater flux of photons will not increase the fluorescence because the rate of the excitation–decay cycle is limited by the decay rate. This will be referred to as ‘saturation of the first kind’.

Now consider a three-level molecule in the same circumstances. The excited state can decay to the ground state with probability, p . However, it can also decay to the third state, $|3\rangle$, with probability $(1 - p)$. When a molecule enters state $|3\rangle$ it no longer interacts with the laser beam. The decay to state $|3\rangle$ is the last transition that the molecule will make in this system, and the photon associated with this transition is the last photon it

will emit.

Assuming a light detector than can detect photons from either decay route ($|2\rangle \rightarrow |1\rangle$ or $|2\rangle \rightarrow |3\rangle$) how many photons on average will a molecule emit during a long transit time in the laser beam? The expectation is given by

$$\begin{aligned}
 \text{Expectation} &= \sum_i (i \text{ photons}) \\
 &\quad \times (\text{prob. of returning to the ground state } i - 1 \text{ times}) \\
 &\quad \times (\text{prob. of going into state } |3\rangle \text{ on the last decay}) \\
 &= \sum_i i p^{i-1} (1 - p) \\
 &= (1 - p) [1 + 2p + 3p^2 + 4p^3 + \dots + np^{n-1} + \dots] \\
 &= \frac{1}{(1 - p)}. \tag{4.1}
 \end{aligned}$$

The fluorescence from this three-level system will saturate when $RT \gg \frac{1}{(1-p)}$. This will be referred to in full as ‘saturation of the second kind’; however, unless otherwise stated ‘saturation’ will henceforth refer to this kind.

Saturation of the second kind is the more common in molecular beam experiments with cw probe lasers, because there is always a readily accessible state $|3\rangle$. The degree of saturation in the wings of a transition is less than on resonance because R decreases away from resonance. This leads to spectral line broadening - an effect known as power broadening. Controlling other sources of broadening (Doppler broadening in the case of this experiment) and measuring power broadening as a function of laser intensity allows the natural linewidth to be inferred from the shape of the data in limit of low power. In addition, measuring how the saturation varies with intensity gives information on the probability, p , in a three-level system. CaF is such a system in which decay to $|3\rangle$ represents all possible decays from the excited state to other vibrational levels ($v \neq 0$) in the ground electronic state and other rotational states within the ground electronic state $v = 0$ manifold. The probability p associated with the $A - X(0 - 0) Q_{11}(\frac{1}{2})$ line can thus be used to determine the Franck-Condon factor of the $A - X(0 - 0)$ transition.

4.3 Summary of what is to come

The purpose of this experiment is to determine properties of the excited state, $|A^2\Pi_{\frac{1}{2}}\rangle$ by investigating the saturation of laser-induced fluorescence. In particular, to measure the Franck-Condon factor of the $A - X(0 - 0)$ transition and the excited state lifetime and hyperfine splitting by investigating the amplitude and width of a spectral line as a function of probe laser intensity. This measurement requires careful control over the laser beam properties, careful linearization of the laser frequency scans, and elimination of the

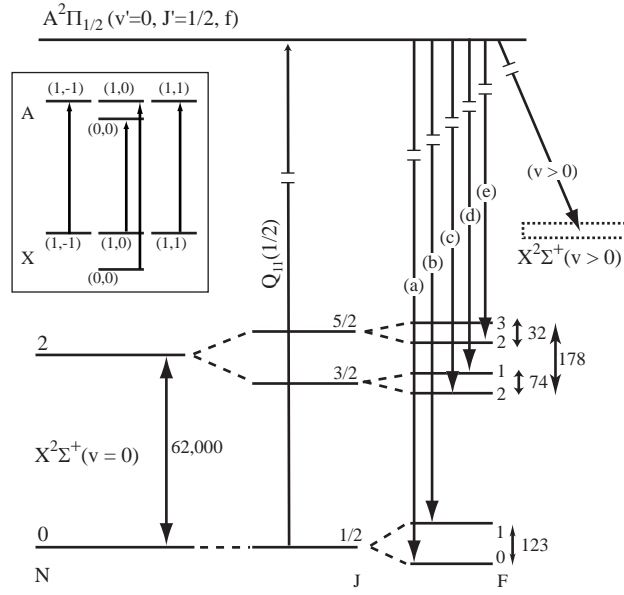


Figure 4.1: Schematic diagram of the energy levels of CaF relevant to the measurement of fluorescence saturation in this experiment. The probe laser excites $Q_{11}(\frac{1}{2})$ from the ground state ($v = 0$, $N = 0$). The allowed decay channels to the ground electronic levels with $v = 0$ are labelled from (a) to (e). Also shown is the decay channel to all other states, i.e. those with $v > 0$. The inset shows the four possible excitation channels available over the hyperfine levels of both the ground and excited states.

effects of a slowly drifting source flux. The following section describes the experimental technique, including how these control measures were implemented. Then the data are presented, followed by a description of how the experiment was modelled. Finally, the model is compared with the experimental data, and the above molecular parameters are determined.

4.4 Measuring spectra

4.4.1 Transitions

The probe laser beam was used to excite transitions from the ground state, $X^2\Sigma^+(v'' = 0, N = 0)$ to the first excited state, $A^2\Pi_{1/2}(v' = 0, J' = \frac{1}{2}, f)$. Interaction of the respective total angular momenta, \vec{J} , of these states with the total nuclear spin, $I = \frac{1}{2}$, leads to each state having a new total angular momentum, $\vec{F} = \vec{J} + \vec{I}$. A state with a given J can give two values of F , $F = J \pm \frac{1}{2}$.

Figure 4.1 shows the levels of interest in the study of fluorescence saturation. The two ground state levels, corresponding to $N = 0, F = \{0, 1\}$ are split by the hyperfine interaction, with an interval of 123 MHz. The hyperfine splitting of the excited state has

the same form as that of the ground state, but the splitting energy is very much smaller and is not shown in the main body of figure 4.1.

The probe laser beam drives the $Q_{11}(\frac{1}{2})$ transition as shown in figure 4.1, the inset of which shows a schematic of the hyperfine sub-levels and the allowed transitions from the four ground-state sub-levels when driven by a plane-polarized laser whose electric field is along z (as in this experiment).

Once in the excited state the molecule has many decay channels available. Transitions to the ground electronic states in the vibrational ground state ($v = 0$) can occur with branching ratio Z , whereas decay to any other vibrational levels in the $X^2\Sigma$ state has branching ratio $1 - Z$. Within the first ground vibrational states transitions can occur that obey the usual selections rules: parity must change and $\Delta F = \pm 1, 0$, where $F = 0$ cannot go to $F' = 0$. Figure 4.1 shows the five decay channels in the $X^2\Sigma$ state that obey these rules. The transitions are labelled from (a) through to (e). Note that no transitions can occur to the $N = 1$ manifold because these states have negative parity. It might seem that transition (e) should not be allowed as $\Delta J = 2$. However, J is no longer the total angular momentum and so the J selection rule no longer holds rigorously. The hyperfine interaction Hamiltonian is not diagonal in J and so the level written as having $\{J = \frac{5}{2}, F = 2\}$ should be described by a state vector that is a linear combination of the two $|N = 2, F = 2\rangle$ states. That is, the state described as $\{J = \frac{5}{2}, F = 2\}$ is in fact of mixed J character. The stronger the hyperfine interaction the greater this mixing and the ‘more allowed’ transition (e) is.

The branching ratios for all the transitions from the excited state to the $X^2\Sigma(v = 0)$ state are derived in [62]. For reference they are given in appendix A.

4.4.2 Experimental set-up

The experimental set-up is exactly as described in chapter 3: CaF radicals are produced in a supersonic source, pass through a 2 mm skimmer, and are detected by laser induced fluorescence 810 mm downstream from the source. The optics form an image of the molecular beam at the PMT photocathode with a magnification of 2. A rectangular mask is placed in front of the PMT photocathode. Measuring 20 mm along the molecular beam direction (z -direction) and 9 mm along the transverse direction in which the probe beam travels (x -direction) this mask limits the visible part of the molecular beam to a region 4.5 mm wide along x . A molecule that has a component of velocity along x experiences a Doppler shift in its interaction with the laser beam. The Doppler shift in terms of angular frequency is $\delta\omega = -2\pi vx/\lambda D$, where v is the forward beam velocity in the z -direction, x is the position along the x -axis in the probe beam ($x = 0$ is located on the molecular beam-line axis), λ is the laser wavelength and D is the distance from the valve to the detection region. The PMT mask limits the Doppler broadening in the LIF signal to 5

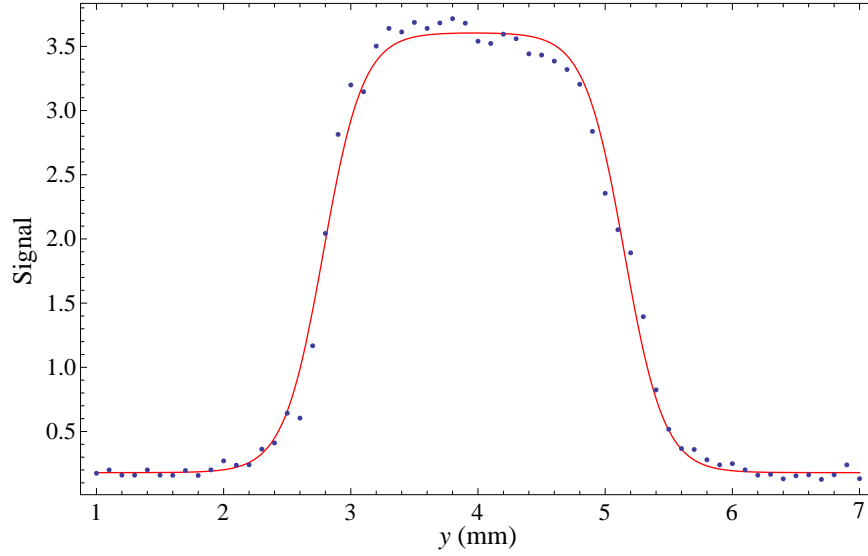


Figure 4.2: An example beam profile taken vertically along the centre of the probe beam. The profile was fitted to the function defined in equation 4.2.

MHz in this experiment.

For this experiment, careful measurements of the probe laser power, divergence and beam profile are important because it is necessary to know the absolute intensity in the detection volume. The probe beam is shaped such that it has a top-hat profile with a nearly circular cross-section. Figure 4.2 shows an example beam profile, measured with a linear array of 61 100 μm -wide CCD pixels. A mirror was used to reflect the probe beam through 90° just before it passed through the Brewster-angled window, into the vacuum chamber. The beam profile shown in figure 4.2 (and all other beam profiles used in this experiment) was measured at exactly the same distance away from the mirror that the beam would have travelled from the mirror's position to the centre of the detection volume, were the mirror not there. In this way the profile measures exactly the shape that the laser beam has in the detection volume. The beam profile is fitted to the function

$$I(y, z) = I_0 \frac{\tanh(\frac{r}{d} + \frac{L}{d}) - \tanh(\frac{r}{d} - \frac{L}{d})}{\tanh(\frac{L}{d})}, \quad (4.2)$$

where $r = \sqrt{z^2 + \epsilon^2 y^2}$. L describes the size of the beam, ϵ the roundness, and d the slope of the profile edges. Typically $L = 1.5\text{mm}$, $\epsilon = 1$ and $d = 0.4\text{mm}$.

The laser beam is polarized along z . The power is measured just before the beam enters the chamber. The transmission of the Brewster window was measured and so the probe beam power inside the chamber was calculable.

The laser is locked to a tunable reference cavity. Scanning a galvo-plate in this cavity allows the laser frequency to be scanned. The laser also passes through an AOM which can be used for fine-tuned frequency scanning over tens of MHz as well as frequency or

amplitude modulation, as will be discussed later.

The laser is scanned over the $A - X(0 - 0) Q_{11}(\frac{1}{2})$ transitions from the two hyperfine sub-levels of the ground state. These levels, with $F = \{1, 0\}$, are separated by 123 MHz. These spectral lines resulting from transitions from these two hyperfine states shall be known as the ' $F = 1$ ' and ' $F = 0$ ' peaks. The two spectral lines are scanned for a range of laser intensities. The laser scan is non-linear in frequency due to a non-linear response of the galvo-plate in the lock-cavity. A portion of the laser beam traverses an evacuated confocal cavity with free spectral range 250 MHz and finesse 2.1. Its transmission is measured simultaneously with the spectral data. The resulting fringe pattern can then be used to linearize the frequency scan. The linearization method is described below with reference to an example spectrum.

4.4.3 Linearization

Figure 4.3(a) shows a scan over the $F = 1$ and $F = 0$ transitions to the excited state. The PMT signal is shown against the voltage sent to the lock-cavity. In theory a scan from -5V to +5V covers a range of 1 GHz in laser frequency. The lower part of the figure shows the cavity transmission data (red points) taken simultaneously with the spectral scan. It can be seen that the fringes are not ideal Airy-fringes as the laser frequency does not scan linearly with applied voltage.

In order to linearize the scan it is necessary to know exactly what sort of fringes would be expected were the scan to be linear. The Airy function has form

$$y(x) = y_0 + \frac{B}{1 + F \sin^2 \left(\pi \frac{(x-x_0)}{\delta x} \right)}, \quad (4.3)$$

with parameters y_0 , B , which relate to the fringe amplitude and offset, F , which relates to the finesse, x_0 , which is an arbitrary frequency offset, and δx , which is the free-spectral range (FSR). The FSR is known from design and from previous calibration to be 250 MHz. F is known to be 1.93. To characterise the ideal fringe pattern as a function of the scan voltage sent to the laser the parameters y_0 , B and δx are needed. δx cannot be deduced directly from the scan because of the non-linearity. However, as the scan is normalised to laser power the fringe amplitudes are unaffected by power variations. The signal voltage of the fringe peaks (y_{max}) and troughs (y_{min}) can be found directly from the data. It can be readily shown from the turning points of an Airy function that y_{max} and y_{min} are related to y_0 and B by

$$y_0 = \frac{y_{min}(1 + F) - y_{max}}{F} \quad (4.4)$$

$$B = \frac{(1 + F)(y_{max} - y_{min})}{F} \quad (4.5)$$

With the measured values of y_{min} and y_{max} the form of the ideal fringe pattern is now known in frequency space. An Airy function with all parameters held fixed except x_0 and

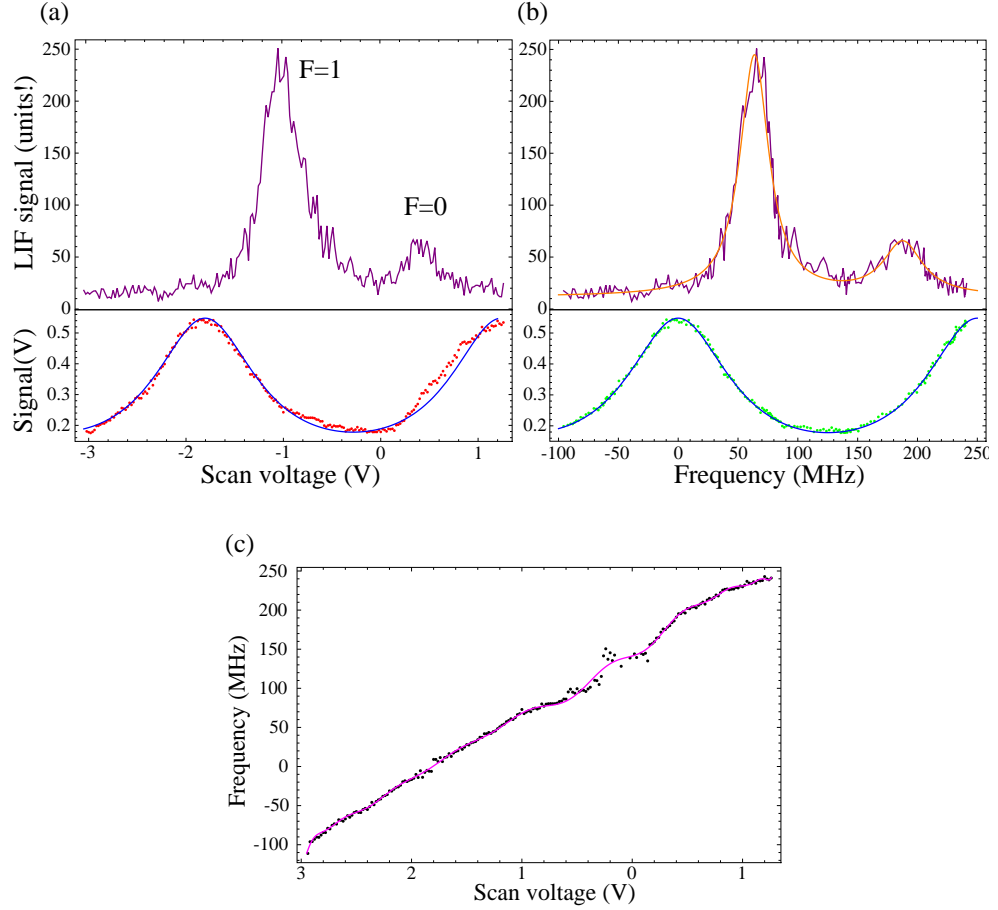


Figure 4.3: An example of scan linearization. (a) The initial, non-linearized scan (taken with a probe beam intensity of 97.6 Wm^{-2}) and the associated cavity data. The cavity data are shown with an Airy function whose maxima and minima match the data. This Airy function is for illustrative purposes only and is not used in the linearization. (b) The linearized scan and cavity data. The scan has been fitted to a double-Lorentzian function and the cavity data show the same Airy function as (a), but now in frequency units. This Airy function is not a fit of the linearized data, but shows the good agreement found between an Airy function and the linearization fringe data. (c) The inverted Airy function which gives the frequency as a function of scan voltage.

δx can be fitted to the cavity data to illustrate the expected shape of the linearised scan fringes. The lower part of figure 4.3(a) shows such a fit. The error in δx from this scan will affect the shape of this function, however this fit is for illustrative purposes only and does not form a part of the linearization analysis. It was found that, for the data taken in the molecular parameter measurement experiment, the scans were fairly linear in the centre, but were extremely non-linear near the start and end.

The Airy function can be inverted to give x as a multi-valued function of y . The transmission signal from a given data-point in the cavity data can thus be related to a frequency. The scan voltage from this datum can be compared with the frequency found by the inversion of the Airy function with y_{min} and y_{max} . Performing this operation for the entire data-set shows how the scan voltage relates to frequency over the scan. Figure 4.3(c) shows this data for the example scan. If the scan were completely linear then these data should fall on a straight line. It might be expected that the linearization is now complete. However, it is not. Figure 4.3(c) shows gaps. These correspond to scan data around the turning points of the fringes which fall outside the region bounded by y_{min} and y_{max} . For these signals the Airy function cannot be inverted and so these data are missing. These points arise out of noise in the transmission signal and any errors in choosing y_{min} and y_{max} . The points which do fall within y_{min} and y_{max} can in theory be matched to a frequency exactly. However, this is not done for two reasons. Firstly, there is signal noise in the cavity data; a point-by-point linearization ignores this and assigns every transmission signal to a frequency, resulting in an artificially clean linearized Airy pattern. Secondly a point-by-point linearization misses out all the points which lie outside y_{min} and y_{max} . Instead of a point-by-point analysis the calibration data in figure 4.3(c) have been fitted to a high order polynomial (20th order). This fit is then used as the calibration between scan voltage and frequency.

Figure 4.3(b) shows the results of the linearization of this example scan. The lower part shows the linearized cavity data. Also shown is the same fit as shown in the lower part of figure 4.3(a), except now scaled to frequency space. Although this fit was performed only for illustrative purposes, it is pleasing to note the good agreement between the form of the expected Airy function and the linearized cavity data. The upper part of 4.3(b) shows the linearized PMT signal data. The data are fitted to a double-Lorentzian function in which all peak parameters are floating, and there is one background offset. The data fit well and crucially fulfill the acid test for linearization: the linearized peak separation is found in this case to be 123.9 ± 1.6 MHz, in good agreement with the known value of 123 MHz.

Errors in this linearization arise from a number of sources, such as the selection of y_{min} and y_{max} and the high order polynomial fit. It was found that the selection of y_{min} and y_{max} dominated the error on the linearization. Consequently, for every scan a range

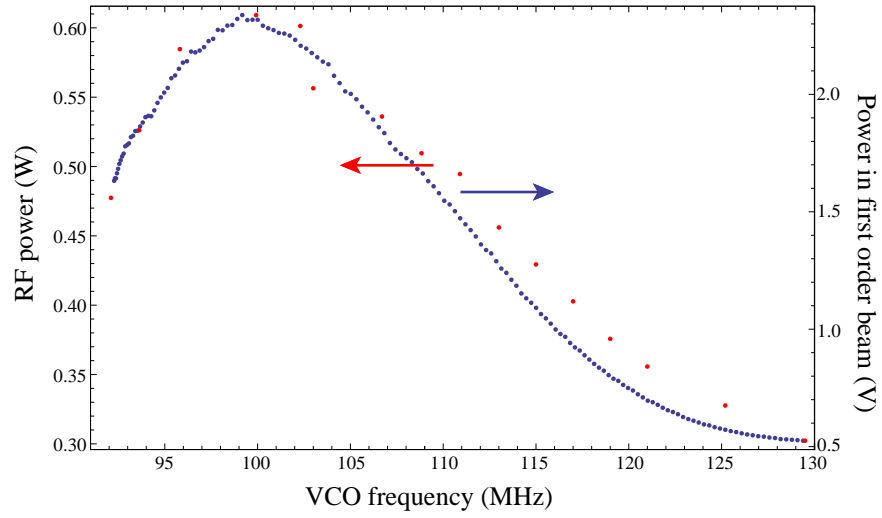


Figure 4.4: The RF power transmitted to the AOM (red points) and the laser power in the AOM first order beam (blue points), both as a function of VCO frequency. The laser power is measured in volts by a photodiode; the absolute power is not needed as the variable under investigation is the relative response of the AOM as frequency is varied.

of reasonable values for y_{min} and y_{max} were found and the linearization analysis was then run over all possible combinations of these two values. In the case of the scan shown this analysis resulted in a mean peak separation of 124.2 ± 1.7 MHz.

4.4.4 Frequency scanning with an AOM

The limit of low probe beam intensity is of great interest as it can be used to deduce the natural linewidth of the excited state. However, the small peak widths also lead to greater width errors because the peaks occupy only a narrow portion of the frequency scans. The peaks occupy only a handful of shots in the overall scan, and cavity transmission signal noise can cause large frequency noise over such a small frequency region. It was not possible to increase the resolution of the scans as the non-linearity becomes much worse the more the scan zooms in. In order to test the quality of the low-intensity linearized data the laser beam was locked to its reference cavity and its frequency scanned by an AOM. Before traversing the beam-shaping optics the laser beam was focussed through an AOM with peak response at 100 MHz¹. The first order beam was then retro-reflected back through the AOM. The double-passed beam was then directed to the beam-shaping optics. The frequency of the double-passed beam was varied with a voltage controlled oscillator (VCO). The VCO signal was sent to an RF amplifier with variable gain.

¹This is actually the peak response of the RF amplifier coupled to the AOM. This will be discussed in more detail below.

Before using this AOM in the experiment, its frequency response was carefully determined. This calibration was performed with the beam making a single-pass through the AOM, before being detected by a photodiode. Scanning the frequency of the VCO output, the efficiency of the conversion of light energy into the first order dropped rapidly to zero (see figure 4.4), with a full width at half maximum of roughly 20 MHz. To analyse the reason for this behaviour the output of the RF amplifier was measured with a -20 dB directional coupler (with the output still connected to the AOM), while the RF reflection was measured with a -10 dB directional coupler. The RF amplifier output and AOM reflection powers were measured as the VCO frequency was varied between 91 MHz and 130 MHz. The AOM's minimum RF reflection was found to be 1 mW and to lie at 112.5 ± 1 MHz. This is the optimal frequency for the AOM. However, the frequency response of the AOM was found not to vary significantly over this range: at the edges of this scan the AOM reflection power was approximately 10% of the incoming power. The RF amplifier's frequency response was the main contributor to the overall frequency characteristics of this system. Its peak power output was found to be at 99 ± 1 MHz, dropping away with a FWHM of approximately 20 MHz. The RF amplifier output falls to 72% of its peak value by 112.5 MHz, the AOM's peak response.

Figure 4.4 shows the total RF power into the AOM (RF amplifier output minus AOM reflection power) between 91 MHz and 130 MHz. Also shown is the measured power of the 1st order beam out of the AOM over this frequency range for constant laser input power. The laser power follows the RF input very closely.

In order to keep the probe beam intensity constant while scanning the frequency a portion of the AOM first order beam was directed to a photodiode whose signal was sent to a differential amplifier which compared it with the photodiode voltage at peak efficiency. The difference between these two voltages, the error signal, was sent (with some variable gain) to the gain control of the RF amplifier. This feedback mechanism allowed the amplifier to increase its gain away from the peak efficiency in order to keep the probe beam power constant over a scan. This feedback mechanism was limited by the gain of the RF amplifier, which limited the single-pass scan width to 25 MHz (between 95 MHz and 120 MHz). The data were taken with the AOM double-passed, allowing a scan width of up to 50 MHz. Thus this scanning technique, although extremely linear, was only applicable in the limit of very low intensities, where the power broadening is small. This also limited the scan width, meaning that only one hyperfine line could be scanned.

4.4.5 Accounting for drifts in source flux

As well as the peak widths, the peak amplitudes were measured as a function of probe beam intensity. In principle this should be trivial: scan over the two lines at a given intensity and record the data; change the intensity and repeat. However, the difficulty in

amplitude analysis was the molecular beam flux. The number of molecules in the beam is determined by a number of factors, as discussed in section 3.2.1. However, the dominant factor which determined the beam flux on the time-scale of a day's data-gathering was the quality of the Ca target. Ablation of the target soon degrades the area of the target being ablated. There are two mechanisms for this: a long term degradation which is almost certainly a chemical change due to build up of sulphates on the surface, and a short-term degradation which might result from heating of the target. The exact mechanism is not known. It was found experimentally that increasing the SF_6 concentration in the gas mixture caused the target to degrade very quickly (over a few shots) and this was almost certainly due to sulphate build-up on the Ca surface, which blocked the Nd:YAG beam. This decrease in molecular flux is easily fixed by moving the target - the 100 mm-diameter target wheel is able to rotate, thus exposing a fresh region of Ca surface to the ablation beam. However this technique is entirely qualitative: the beam starts off strong and then decays; moving the target increases the signal again, but it is impossible to compare the measured LIF signal before and after a target 'tweak'. A more quantitative analysis of monitoring the molecular beam strength is needed. It is also necessary to determine the time-scale of the target decay.

The general time-evolution of the molecular flux after the target is moved starts with a huge spike in flux, after which the flux rapidly decays to a lower value and plateaus there. This flux is then stable for several minutes, allowing a number of scans to be taken. After this time the flux decays until the LIF signal becomes too weak to be of use. It is thus of interest to take data while the flux is in the 'plateau' regime, and data were only recorded under these circumstances.

As well as measuring the signal decay over a number of scans it was important to measure any decay which occurred over the course of one scan, as this would affect both the amplitude and width measurements. In order to measure the decay the ratio of the $F = 1$ and $F = 0$ peaks was investigated over time for a given probe beam intensity. The $F = 0$ peak lies 123 MHz higher than the $F = 1$ peak and in the scans taken in this analysis the laser frequency reached the $F = 0$ line around 30 seconds after the $F = 1$ line. Many scans were taken over both lines with the target in the plateau regime. The ratio of the $F = 1$ to $F = 0$ peak amplitudes was then compared between the scans and found not to vary significantly, consistent with the target not decaying noticeably during a scan. These data, however, might also be explained by a constant target decay, consistent in all the scans. In order to measure any decay it is necessary to measure the amplitude ratio simultaneously. This was achieved by using the AOM to modulate the laser frequency. The AOM was driven such that its first order beam increased the laser frequency by 123 MHz. The AOM was operated in single-pass. A beam-splitter picked off some of the laser beam before it entered the AOM. This unmodulated beam was then overlapped with the

modulated beam. A fast mechanical shutter was used to switch the unmodulated beam on and off, and the frequency-shifted beam could be turned on and off by switching the AOM on and off. Thus it was possible to alternate the frequency of the probe beam by 123 MHz on successive shots. Variable filters were used to ensure that both the beams had the same intensity. In this way scanning the laser frequency with the lock cavity produced two interleaving spectra of the $F = 1$ and $F = 0$ lines, one taken at 123 MHz above the other. Consequently the ‘AOM on’ scan recorded the $F = 0$ peak at the same time as the ‘AOM off’ scan recorded the $F = 1$ peak. Thus the two peak amplitudes were measured near-simultaneously. Analysis of the near-simultaneous amplitude ratios showed good agreement with the ratios of peaks separated by ~ 30 seconds. It was concluded that target decay over the course of a scan was not significant.

Satisfied that target degradation does not affect the signal amplitudes over the course of a scan, the task of measuring the peak amplitudes as a function of probe beam intensity required the degradation to be accounted for when comparing different scans taken at different laser intensities. This was achieved by normalizing out the signal decay by modulating the laser intensity using the AOM as an amplitude modulator. The AOM was used in single pass and the zeroth order was picked off and sent to the beam-shaping optics. With the AOM off the full intensity (minus some reflections at the crystal surfaces) was transmitted. With the AOM on and driven with a certain voltage some of this intensity was taken out of the zeroth order and shared among the higher orders. By varying the driving voltage from the RF amplifier the intensity in the zeroth order beam could be varied. When scanning over the two spectral lines the laser intensity was modulated by turning the AOM on and off. The AOM driving voltage was set such that the probe beam power alternated between a high intensity (AOM off) and a lower intensity (AOM on). The low intensity could be varied by changing the AOM driving voltage (in practice this was achieved by varying the gain in the RF amplifier). In this way it was possible to vary the probe beam power while always having a near-simultaneous scan taken at a constant intensity for all scans. These high-intensity scans serve as a normalization tool as the only variable that can change between these reference scans is the molecular flux. Linearizing the scans and setting the $F = 1$ amplitude to unity for all the high intensity scans allowed the corresponding $F = 1$ and $F = 0$ amplitudes in each lower intensity scan to be normalized.

In practice the AOM was limited in how much energy it could transfer from the zeroth order and so it was not possible to modulate from a very high to a very low intensity. Consequently several reference intensities were used, with lower reference intensities used to measure the low intensity peak amplitudes. Each reference intensity was compared near-simultaneously with the next one up, and so all the data were in effect normalized to one high intensity scan.

4.4.6 Magnetic Field

The magnetic field in the detection region was measured by a fluxgate magnetometer (*Lake Shore 421 Gaussmeter*) to be $B_x = -45 \pm 5\text{mG}$, $B_y = -212 \pm 2\text{mG}$, $B_z = -143 \pm 1\text{mG}$. The resulting Zeeman splittings between the $M_F = \pm 1$ sub-levels are calculated to be < 1 MHz in both the ground and excited states. In the ground state this is much smaller than the hyperfine splitting (123 MHz), and so the Zeeman interaction causes negligible mixing of the F -states (the Zeeman interaction is not diagonal in F).

It is also important to consider the effect of the magnetic field on the excited state. The excited state hyperfine splitting, Δ_e , and lifetime had not been determined prior to this experiment. However, the hyperfine splitting was not resolved in any recorded fluorescence spectra indicating that it was unlikely to be greater than 10 MHz. The lifetime had previously been measured by Dagdighian [60] to be 21.9 ± 4 ns. It is possible that the magnetic field could mix the two hyperfine states. However, the precession frequency associated with the Zeeman interaction is much slower than the excited state lifetime, and so the effect of any such mixing can be ignored. If the value of Δ_e is near its expected upper limit (~ 10 MHz) then it is greater than the Zeeman splitting and so there is negligible mixing of the excited state $F = 0, 1$ levels.

For the above reasons the magnetic field in the detection region is ignored henceforth and is not included in the analysis or the model.

4.5 Experimental results

Figure 4.5 shows examples of two linearized scans. Each scan is in fact the mean of several scans, each of which was linearized before averaging. Also shown is an Airy function fit to the cavity data for one of the scans. It shows that the linearization has worked well. Each scan has two peaks: one at lower frequency is fluorescence from decay when the laser is resonant with the transitions from the $X(F = 1)$ states, and one at greater frequency corresponding to fluorescence when the laser is resonant with the $X(F = 0)$ states. The scan labelled (i) was taken at a laser intensity of 11.5 W/m^2 and has peak widths (FWHM) of 17 MHz ($F = 0$ peak) and 13 MHz ($F = 1$). The peak labelled (ii) was taken with a laser intensity of 97.6 W/m^2 and has widths of 39 MHz ($F = 0$) and 28 MHz ($F = 1$). By comparing the two scans the power broadening is obvious, resulting from saturation of the second kind occurring at greater intensity in the wings than at the central frequencies. It is also interesting to note the ratio of the $F = 1$ peak amplitude to the $F = 0$ amplitude. The three-fold degeneracy of the $F = 1$ states would suggest an amplitude ratio of 3, whereas in these data (and indeed in all the other high power data) the ratio is close to 4.5. This can be explained by the fact that when the laser is on resonance with the transitions from the $F = 1$ states there is a greater probability of a molecule returning

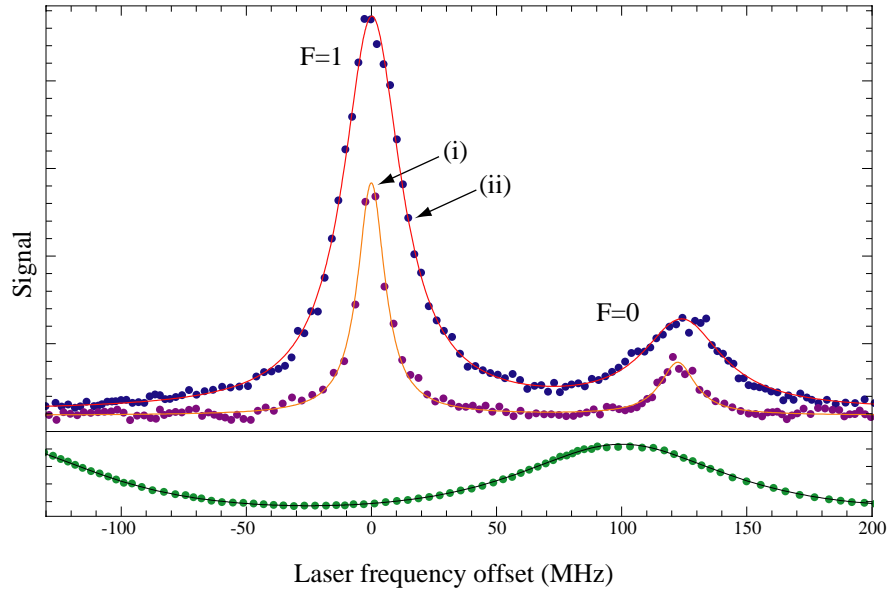


Figure 4.5: Two linearized spectra taken with the probe beam laser scanning over transitions from the $X(F = 1)$ and $X(F = 0)$ states. The peaks are labelled according to the ground state hyperfine level being driven by the laser. Below the spectra are the transmission data of the 250 MHz FSR cavity used in the linearization. In all cases, data are shown as points and fits as lines. The spectra are fitted to a double Lorentzian and the cavity data to an Airy function. The spectrum labelled (i) was taken with peak laser intensity, $I_0 = 11.5 \text{ Wm}^{-2}$, and the spectrum labelled (ii) at an intensity of $I_0 = 97.6 \text{ Wm}^{-2}$.

to its original state and scattering another photon than when the laser is tuned to the $F = 0$ transition. To investigate this more quantitatively requires a thorough modelling of all allowed transitions, including those to other vibrational states, and off-resonance transitions in the limit of intense laser fields. This modelling was performed for all the data, and is discussed in section 4.6. However, the amplitude ratio can be estimated by assuming the limiting case in which the laser power is sufficiently great that saturation of the second kind occurs during the transit time, but not high enough to drive any off-resonant transitions. Transitions to states with $v > 0$ are also ignored. In this case the number of photons scattered by a molecule is simply $1/(1 - p)$, where p is the probability of returning to the same state (equation 4.1). It can be seen from the branching ratios in matrix A.1 that for a molecule excited (i) to the $A(0, 0)$ state, $p = 6/9$; (ii) to the $A(1, -1)$ state, $p = 4/9$; (iii) to the $A(1, 1)$ state, $p = 4/9$. Using equation 4.1 it is found that each of these excited states contributes, on average, $9/3$, $9/5$ and $9/5$ photons respectively before the molecule will enter a dark state. The same analysis for the $A(1, 0)$ state gives $p = 2/9$ and an average of $9/7$ photons before saturation of the second kind occurs. Assuming an homogeneous distribution among the magnetic sub-levels, there will be N molecules in each of the sub-levels. Thus, with the laser resonant with the $F = 1$ transitions there would be on average $(\frac{9}{3} + \frac{9}{5} + \frac{9}{5})N = \frac{33}{5}N$ photons scattered. With the laser tuned to the $F = 0$ transition there would be $\frac{9}{7}N$ photons scattered on average. The ratio of the $F = 1$ signal to the $F = 0$ signal is thus $\frac{33}{5}/\frac{9}{7} = 5.1$. This is close to the measured value and is an overestimate as the analysis assumed a Franck-Condon factor of 1, which will likely prove an overestimate, and it ignored the effect of off-resonant transitions, which would allow a laser tuned to the $F = 0$ line to excite molecules in the three $F = 1$ states, resulting in greater fluorescence at this frequency. The same occurs for a laser tuned to the $F = 1$ transition, but it now has access to only one more state (the $F = 0$ state) and so its increase in fluorescence is comparatively smaller. Thus off-resonance excitations will benefit the $F = 0$ peak amplitude more than the $F = 1$ amplitude and cause the above calculated ratio to decrease.

Note that, for a given intensity, the $F = 0$ peak has a greater width than the $F = 1$ peak. This is a result of greater power broadening in the $F = 0$ peak: the $F = 1$ states can scatter more photons than the $F = 0$ state before reaching saturation of the second kind, and so saturation occurs at a smaller intensity for the $F = 0$ line.

Amplitude data

Figure 4.6 shows the experimentally measured amplitudes of the $F = 1$ and $F = 0$ peaks, all normalized to the amplitude of a high intensity $F = 1$ peak (both data-sets are normalized to the same peak).

It can be seen that for very small intensities, as I is increased both peaks experience a

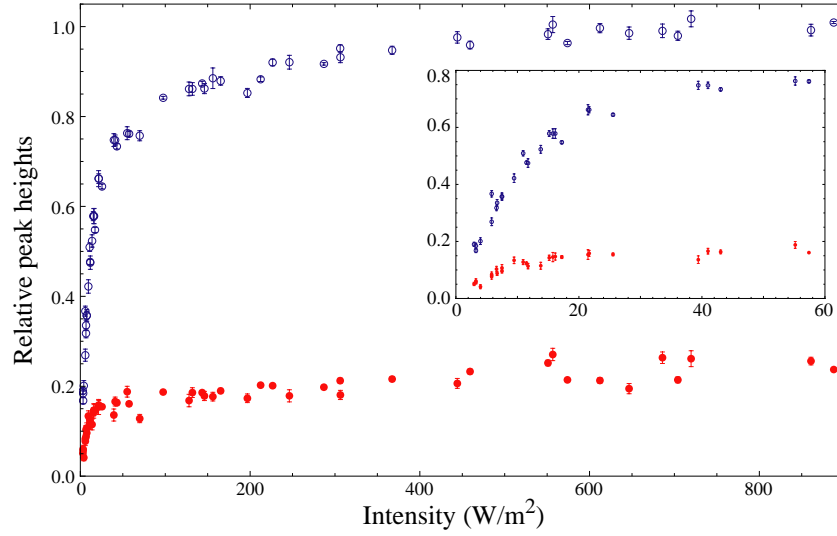


Figure 4.6: Relative peak height versus peak laser intensity for the $F = 1$ peak (blue points) and the $F = 0$ peak (red points). The inset shows the low intensity data for both peaks in more detail. The peak amplitudes for both data-sets have been normalized to a reference $F = 1$ amplitude at a high intensity.

rapid increase in amplitude. This is because in the limit of small I the excitation rate, R is very small and so $RT \ll 1$. Saturation is a long way off and so including more photons in the probe beam allows more photons to be scattered, increasing the PMT signal. As the intensity is increased further the resonant molecules in the beam are increasingly scattered to other, non-resonant states; consequently the slope of amplitude increase with intensity decreases. It can be seen from the inset of figure 4.6 that this saturation occurs at smaller intensity for the $F = 0$ peaks than the $F = 1$ peaks. This is because, as discussed above, a molecule in the $F = 0$ state, when interacting with the probe beam resonant with the transition from the $F = 0$ state, is less likely to return to its original $F = 0$ state and scatter again. The $F = 0$ state saturates more quickly than the $F = 1$ states.

Figure 4.6 also shows that even at the greatest intensities used in this experiment, the amplitudes were still not saturated: the peak amplitudes are still increasing at the upper intensity limits in the graphs. The reason for this is off-resonant excitation. When the probe beam has very great intensity it is able to excite molecules in the other hyperfine state. A given state doesn't have one exact energy, it has a spread of energies; for example at the central energy of the $F = 0$ state the $F = 1$ states' energy distributions have a small but non-zero amplitude. An intense enough laser beam tuned to the transition from the $F = 0$ state can also excite the $F = 1$ states at this energy and drive transitions from them. It can be seen from figure 4.6 (although not easily at first!) that the fractional increase in peak amplitude with intensity in the limit of great intensity is greater for the

$F = 0$ peak than the $F = 1$ peak. This is because there are more $F = 1$ states for the laser to drive ‘off-resonantly’ when tuned to the $F = 0$ transition than vice versa. Increasing the intensity further will eventually saturate the amplitudes when the laser (tuned to a given resonance) is intense enough to drive molecules out of both ground hyperfine states and achieve saturation of the second kind. However, it was found from simulations that the required intensity is around 20 times as great as was used in the experiment. It is interesting to calculate the number of photons scattered per molecule in this limit: assuming the Franck-Condon factor has value $Z = 1$ the total number of scattered photons per molecule is $1/(1 - \frac{2}{3}) = 3$.

Width data

Figure 4.7 (a) and (b) shows the results of the measurements of the widths of the $F = 1$ and $F = 0$ peaks measured by scanning the laser and linearizing. The data show an increase in width with increased intensity, exactly as would be expected from power broadening. The slope of the width data drops as the intensity increases. This is a result of saturation of the second kind. It can be seen that the broadening is greater for the $F = 0$ peak than the $F = 1$ peak, and that the $F = 0$ peak width saturation starts at a smaller intensity. This is exactly as discussed above: the $F = 0$ state is more likely to be emptied by the probe beam at lower intensity and so the $F = 0$ peak amplitude saturates earlier. The wings of the peak, however, are still rising with intensity when the centre has saturated, thus increasing the peak width.

Note that there are fewer data in the width analysis than the amplitude analysis. This is largely because the linearization process is a very strict analysis - if a peak suffers from a particularly bad non-linearity in the scan, or even a frequency glitch, linearization will not be possible. However, often in these cases it is possible to fit the peak and ascertain the amplitude, which will not be affected by the non-linearity (unless the non-linearity is so strong that the data cannot be fitted).

Figure 4.8 shows the linearized width data of the $F = 1$ peak in the limit of small intensity. Also shown are $F = 1$ widths measured directly by the AOM. The linearized widths show very good agreement with the direct width measurements, which gives confidence that the linearization procedure works well, even in the limit of thin peaks, which are the most difficult to linearize with reasonable errors. Note that the frequency response of the RF-driver limited the AOM to scanning over only the $F = 1$ peak and only at small intensities where the peak width was small.

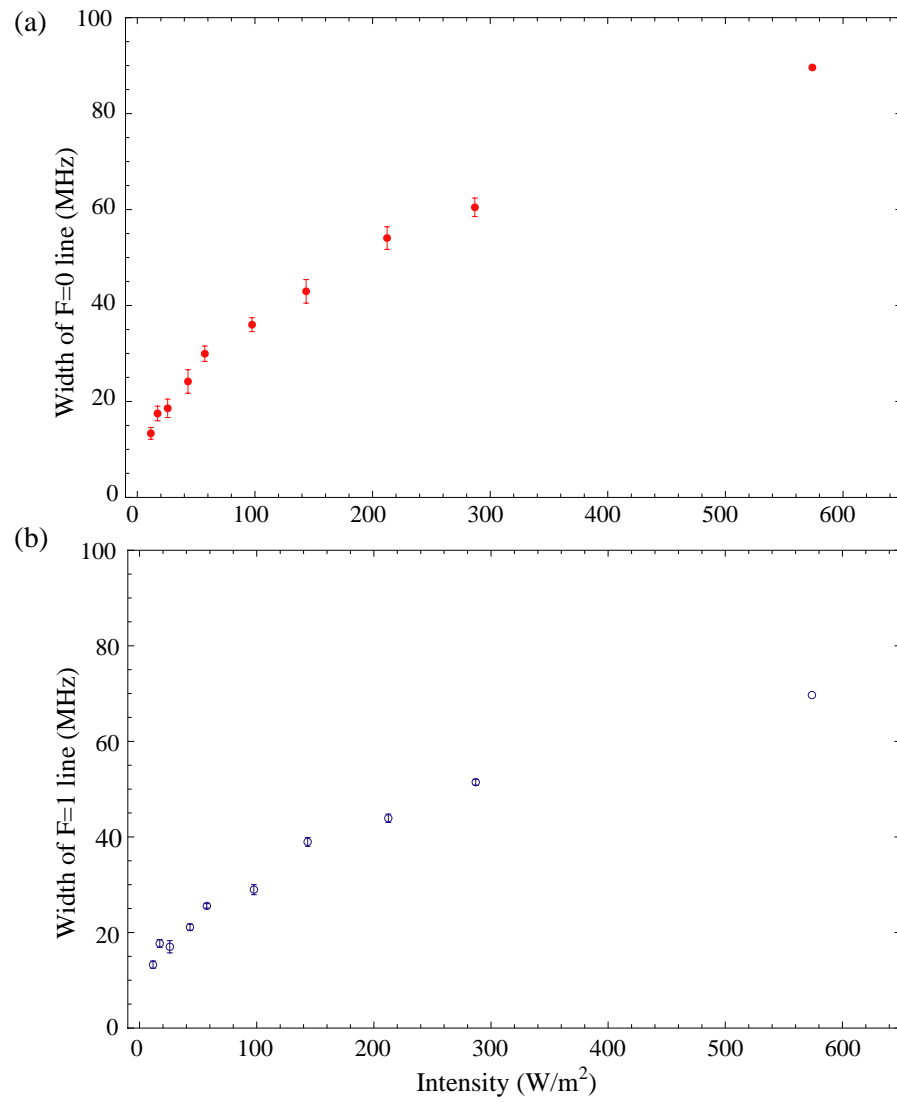


Figure 4.7: The linearized widths (FWHM) of the (a) $F = 0$ and (b) $F = 1$ peaks as a function of probe beam intensity.

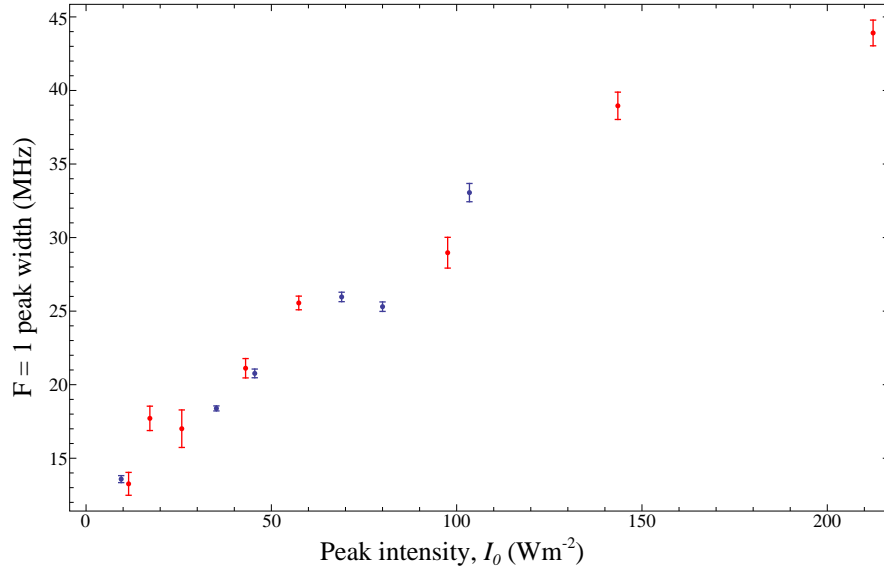


Figure 4.8: $F = 1$ peak width measured at various weak laser intensities. The figure shows the results of spectra taken by scanning the laser and linearizing (red points) and by scanning the laser frequency with an AOM (blue points). The linearized widths show very good agreement with the widths measured directly by the AOM.

4.6 Model

The probe beam was plane-polarized along the beam axis direction, z . It drives the transitions shown in the inset in figure 4.1. Each sub-level in the ground state can be driven to only one sub-level in the excited state. In the following analysis the sub-levels in the excited state are labelled by j and in the $J = \frac{1}{2}$ electronic ground state by i . The excited state can decay to five different states in the ($v = 0$) ground state and many others in the $v > 0$ states. It is known [59] that decay to the $v > 0$ states is very unlikely compared with decay to the $v = 0$ states. All the possible states that the excited state can decay to (including those with $v' > 0$) are labelled by k (this includes the subset of $J = \frac{1}{2}$ states, i .) The coherences reach steady state on the time-scale of the excited state lifetime, τ , which was known [60] prior to this experiment to be far smaller than the molecules' transit time through the probe beam. Consequently the experiment can be modelled in terms of rate equations.

4.6.1 Rate Equations

The laser excitation rate is found to be (see appendix B):

$$R(\delta) = \frac{\frac{\Gamma}{2}}{1 + 4\frac{\delta^2}{\Gamma^2}} \frac{2\Omega^2}{\Gamma^2} = \frac{\frac{\Gamma}{2}}{1 + 4\frac{\delta^2}{\Gamma^2}} \frac{I}{I_s}, \quad (4.6)$$

where Γ is the excited state spontaneous decay rate, $\delta = \omega_L - \omega_{ij}$ is the laser detuning (ω_L is the laser angular frequency) and $\Omega = E_o z_{ij}/\hbar$ is the Rabi frequency for intensity $I = \frac{1}{2}c\epsilon_0 E_o^2$. $z_{ij} = \langle i|\vec{d} \cdot \vec{z}|j\rangle$ is the matrix element coupling the states i and j by the electric dipole operator, \vec{d} (\hat{z} is the unit vector along z -direction – the direction of the laser light’s polarization). I_s is the ‘saturation intensity’; it is defined by $I/I_s = 2\Omega^2/\Gamma^2$ and is the characteristic intensity for saturation of the first kind (section 4.2).

The total spontaneous decay rate of an excited state, $|b\rangle$, in some general atomic or molecular system to all possible decay states, $|a\rangle$, is (see, for example [64]):

$$\Gamma = \frac{1}{3\pi\epsilon_0\hbar c^3} \sum_a \omega_{ba}^2 M_{ba}^2, \quad (4.7)$$

where $M_{ba}^2 = |\langle a|\vec{d}|b\rangle|^2$. Consider now the transitions from the excited states labelled j . According to the matrix of branching ratios (A.1) given in appendix A, each j state has several decay channels in which $\Delta m = 0$, and the radiation is plane polarized along the laser polarization direction, \hat{z} . As well as these channels it has a number of other transitions in which the resulting radiation is not polarized along \hat{z} . It can be seen from the branching ratios in matrix A.1 that the radiation from many decays from the j states will be isotropic. The rotational structure of higher vibrational states (in the ground electronic state) will be the same as in the $v = 0$ ground state. Decay from the j states to states with $v' > 0$ will thus also be isotropic. It is thus exact, in this case, to replace the general matrix element in equation 4.7, M_{ba} , with the matrix element for z -polarized radiation, z_{jk} , and multiply through by a scaling factor of 3 to account for the other two polarization directions. The equation for the decay rate of the j states thus becomes:

$$\Gamma = \frac{1}{\pi\epsilon_0\hbar c^3} \sum_k \omega_{jk}^2 z_{jk}^2. \quad (4.8)$$

In order to come up with an expression for I_s in terms of parameters relevant to this experiment an approximation will be made: all the possible decay transitions have frequencies that differ only by a part in 10^4 , and so it will be assumed that all these frequencies are equal: $\omega_{jk} = 2\pi c/\lambda$. Combining these approximations in equation 4.8 with the expression for intensity, $I = \frac{1}{2}c\epsilon_0 E_o^2$ gives

$$I_s = \frac{\pi\hbar c\Gamma}{\lambda^3} \frac{\sum_k z_{jk}^2}{z_{ij}^2}. \quad (4.9)$$

It is possible to define the branching ratio of transitions from j to the original i states: $r = \sum_i M_{ji}^2 / \sum_k M_{jk}^2$, where M_{ba} is a general matrix element linking states labelled a and b through the dipole operator, in which the radiation polarization vector has some general direction, \vec{R} . As the decay radiation is isotropic all Cartesian components of the total matrix element count equally. r can thus be written just as well in terms of only

the transitions with z -polarized radiation: $r = \sum_i z_{ji}^2 / \sum_k z_{jk}^2$. Equation 4.9 can thus be written

$$I_s = \frac{\pi h c \Gamma}{\lambda^3} \frac{1}{r} \frac{\sum_i z_{ji}^2}{z_{ij}^2}. \quad (4.10)$$

For a given j state there is only one allowed decay with z -polarized radiation (matrix A.1 and inset to figure 4.1). Thus $\sum_i z_{ji}^2 / z_{ij}^2 = 1$. It can readily be seen from that the branching ratio, r , is the Franck-Condon factor, Z , multiplied by the sum of ratios in matrix A.1 in which $\Delta m = 0$, which gives $r = 2Z/3$. Thus I_s can be expressed in terms of Γ and Z

$$I_s = \frac{\pi h c \Gamma}{\lambda^3} \frac{3}{2Z}. \quad (4.11)$$

Comparing equations 4.6 and 4.11 it can be seen that the excitation rate, $R(\delta)$ has now been expressed in terms of the parameters Γ and Z .

With these definitions it is now possible to write the rate equations that govern the dynamics of the i states (X state with $N = 0$) and the j states (A states with $J' = \frac{1}{2}$). These are the 8 states shown in the inset of figure 4.1. In writing the rate equations only these states need to be considered. The probe laser in this experiment was always sufficiently weak and far-detuned to avoid driving transitions between other levels.

The symmetry between the (1,1) and (1,-1) levels in both the X and A states allows just one rate equation to describe each pair. The populations in the ground (0,0) and (1,0) states are labelled N_{g0} and N_{g1} respectively; the sum of the populations in the ground (1, \pm 1) states is labelled N_{g2} . The ground state hyperfine splitting is labelled Δ_g . The excited states are labelled in exactly the same manner, except g is replaced with e . The laser detuning, δ , is referenced to the $X(F = 0, M_F = 0) \rightarrow A(F' = 1, M_F' = 0)$ transition. The rate equations are thus:

$$v \frac{dN_{g0}}{dz} = R(\delta)[N_{e1} - N_{g0}] + \frac{r}{3} \Gamma [N_{e1} + N_{e2}] \quad (4.12)$$

$$v \frac{dN_{g1}}{dz} = R(\delta + \Delta_g + \Delta_e)[N_{e0} - N_{g1}] + \frac{r}{3} \Gamma [N_{e0} + N_{e2}] \quad (4.13)$$

$$v \frac{dN_{g2}}{dz} = R(\delta + \Delta_g)[N_{e2} - N_{g2}] + \frac{r}{3} \Gamma [2(N_{e0} + N_{e1}) + N_{e2}] \quad (4.14)$$

$$v \frac{dN_{e0}}{dz} = R(\delta + \Delta_g + \Delta_e)[N_{g1} - N_{e0}] - \Gamma N_{e0} \quad (4.15)$$

$$v \frac{dN_{e1}}{dz} = R(\delta)[N_{g0} - N_{e1}] - \Gamma N_{e1} \quad (4.16)$$

$$v \frac{dN_{e2}}{dz} = R(\delta + \Delta_g)[N_{g2} - N_{e2}] - \Gamma N_{e2} \quad (4.17)$$

By means of an explanation of the rate equations consider as an example the equation for the rate of change of the population in the ground (1,0) state, N_{g1} (equation 4.13). The total rate of change of N_{g1} as a molecule traverses the probe beam has four contributing mechanisms. The first term on the right-hand side of equation 4.13 is the rate of increase in

N_{g1} through stimulated emission from the excited (0,0) states. The second term represents the loss of population through excitation to the excited (0,0) state. Note that these are the only transitions that the laser can drive because of its polarization. The third and fourth terms lead to increases in N_{g1} from the spontaneous decay of the excited (0,0) state and the combined spontaneous decays of the excited (1,1) and (1,-1) states. In all cases the decay rate is clearly proportional to the excited state decay rate, Γ . The rates are also scaled by the branching ratio, r (defined above), which accounts for the probability of decaying to the $v > 0$ states and the ($v = 0, N > 0$) states. Each of the excited states (j states) has three decay channels available to the original ground states (i states), each occurring with equal probability. Consequently the branching ratio to the ground (1,0) state is $r/3$.

The rate equations model the population of the ground and excited states as a function of a molecule's position in the probe beam. They are parameterized in terms of the three molecular properties of interest: the excited state decay rate, Γ , the Franck-Condon factor, Z , and the excited state hyperfine splitting, Δ_e .

4.6.2 Molecular population dynamics

Figure 4.9 shows the population probability of the (0,0), (1,0), and (1, ± 1) levels of the ground and excited states as calculated by solving the rate equations (equations 4.12 – 4.17) with the parameters $Z = 0.96$, $\Gamma/(2\pi) = 8$ MHz and $\Delta_e = 0$. In the simulations the laser beam was tuned to the transition from the X state $F = 0$ level to the A state $F' = 1$ level. In figure 4.9 (a) and (b) the intensity was weak, $I = 0.02I_s$, whereas in figure 4.9 (c) and (d) the beam was very strong, $I = 4I_s$. In the following section the ground states will be labelled $X(0,0)$, $X(1,0)$ etc., and likewise the excited states with A .

Consider first the effect of a weak probe beam ($I = 0.02I_s$) on a molecule traversing the detection region. Figure 4.9 (a) shows that as the molecule traverses the probe beam the $X(0,0)$ state population drops steadily and is pumped into the $A(1,0)$ state. Consequently figure 4.9 (b) shows the $A(1,0)$ population rises rapidly and peaks by the time the molecule is in the region of peak intensity. The $A(1,0)$ population then drops through decay (including stimulated emission). Some of this decay will be to the $X(1,\pm 1)$, and figure 4.9 (a) shows this in a steady increase in the $X(1,\pm 1)$ states' populations. Once in this state the molecule is out of resonance with the laser and so remains in these states for the rest of the transit time. The transition from the $A(1,0)$ to the $X(1,0)$ state is not allowed and so the $X(1,0)$ state population does not change.

Now consider the limit of a very strong laser beam ($I = 4I_s$). Figure 4.9 (c) shows that as soon as the molecule begins to enter the probe beam the $X(0,0)$ population drops rapidly to zero. The $A(1,0)$ state population rises sharply and peaks when the molecule is still on the edge of the laser beam. After this point it decays rapidly. Decay to the

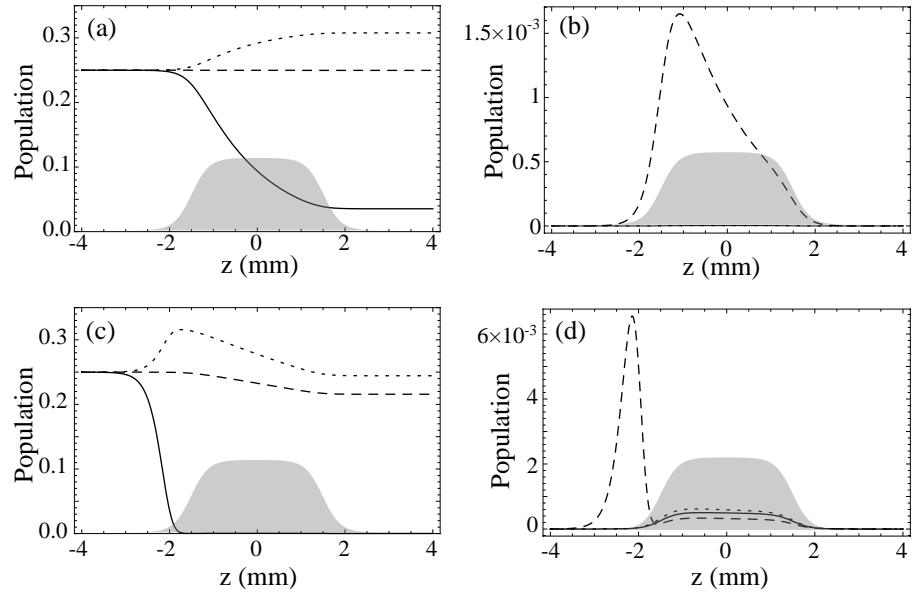


Figure 4.9: Fractional state populations of a molecule traversing the probe beam (shown shaded in grey) as calculated by solving the rate equations with $Z = 0.96$, $\Gamma/(2\pi) = 8$ MHz and $\Delta_e = 0$. Figures (a) and (c) show the ground state populations and (b) and (d) the excited state populations. In all figures the (0,0) population is shown by the solid lines, the (1,0) population by the dashed lines, and the (1,±1) populations by the dotted lines. The populations in figures (a) and (b) were calculated with peak laser intensity (see equation 4.2) $I_0 = 0.02I_s$ and (c) and (d) with $I_0 = 4I_s$.

$X(1,\pm 1)$ states shows an increase in the population of these states - a more rapid increase than in the above example. However, the laser is now intense enough that it can excite transitions from the $X(F = 1)$ levels, despite being tuned to the transitions from the $X(F = 0)$ levels. Through this mechanism the $X(F = 1)$ population can be driven to the $A(1,\pm 1)$ and $A(0,0)$ states, although at a much slower rate than the populations transfer from the $X(F = 0)$ state. This is reflected in figure 4.9 (d) as a slow increase in the $A(1,\pm 1)$ populations, whose total magnitude follows the probe beam intensity.

The number of scattered photons in each of the above examples is calculated by multiplying the total excited state population by the scattering rate, Γ and then integrating over the beam transit time. The total decay radiation is isotropic. Consequently the PMT signal is proportional to the total number of photons emitted. It is found in the above examples that with $I = 0.02I_s$ a molecule will scatter on average 0.28 photons during its transit time; and with $I = 4I_s$ it will scatter 0.82 photons. If the laser is tuned to the transitions from the $X(F = 1)$ states these numbers increase to 1.07 when $I = 0.02I_s$ and 1.89 when $I = 4I_s$.

4.6.3 Running the model

To model the experiment the rate equations (4.12–4.17) are solved for a large array of transverse molecular positions in the detection region, $\{x, y\}$, for a given laser frequency and intensity. This step is necessary to account for Doppler shifts and the spatial variation in the laser intensity integrated along the molecule's path. This calculation is then repeated over a range of frequencies to produce a spectrum. The spectrum is then fitted to the same double-Lorentzian function that is used with the experimental data. The amplitudes and widths of the two peaks are determined. The process is then repeated for a range of laser intensities. This entire process is performed over an array of values for Γ , Z and Δ_e . Every time a simulation is performed with a given set of values for these three parameters the simulated widths and amplitudes are plotted against intensity and compared with the experimental data. In order to quantify how well the simulation results match the experimental results, the value of χ^2 is calculated using the errors on the experimental data points as weights. The particular simulation which minimizes the value of χ^2 simultaneously for both the amplitude and width data gives the central values of the three parameters. Following standard statistical procedures, statistical errors on these values are found by determining the volume of parameter space that leads to a change in χ^2 of one.

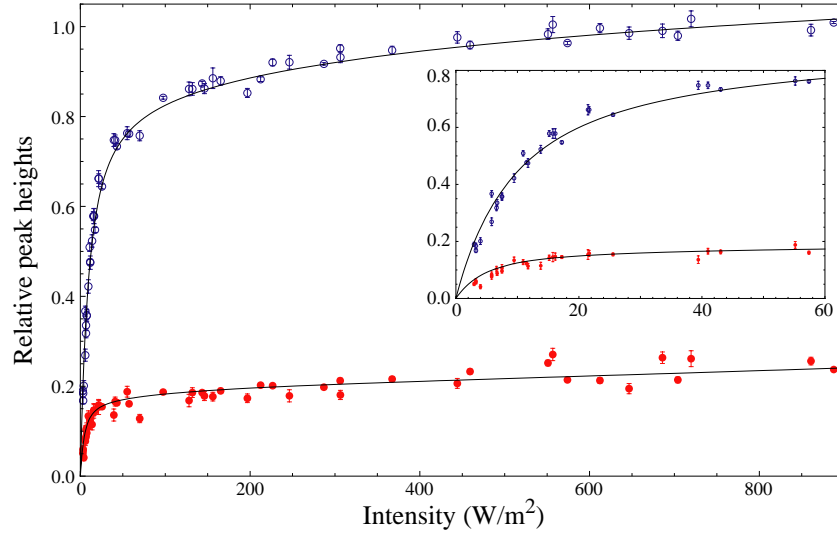


Figure 4.10: Relative peak heights versus peak laser intensity for the $F = 1$ peak (blue points) and the $F = 0$ peak (red points). The inset shows the low intensity data for both peaks. The peak amplitudes for both data-sets have been normalized to a reference $F = 1$ amplitude at a high intensity. Also shown are the results of simulations (black lines) solved with $\Gamma/(2\pi) = 8.29$ MHz, $Z = 0.987$ and $\Delta_e = 4.8$ MHz.

4.7 Comparing the model with experimental data

Figure 4.10 shows the measured amplitude data for the $F = 1$ and $F = 0$ peaks as a function of probe beam intensity. Also shown are the simulated amplitude curves found by the procedure described above and with the optimal parameters that minimize χ^2 : $\Gamma/(2\pi) = 8.29$ MHz, $Z = 0.987$, and $\Delta_e = 4.8$ MHz (errors will be discussed later). The model and data show striking agreement.

Figure 4.11 shows the width data of (a) the $F = 0$ peak, and (b) the $F = 1$ peak as a function of probe beam power. The results of the rate equations are also shown, calculated with the same optimal parameters as in figure 4.10. As with the amplitude data very good agreement is found between the experimental data and the results of the rate equation modelling. This indicates that the rate equations are a good model of the light-matter interaction in this experiment.

4.8 Evaluating the molecular parameters

All three parameters, Γ , Z and Δ_e are found by comparing the model results with experimental data. It is both satisfying and instructive to explain physically the effect of these parameters on the experimental data.

In the limit of saturation of the second kind the number of photons scattered is de-

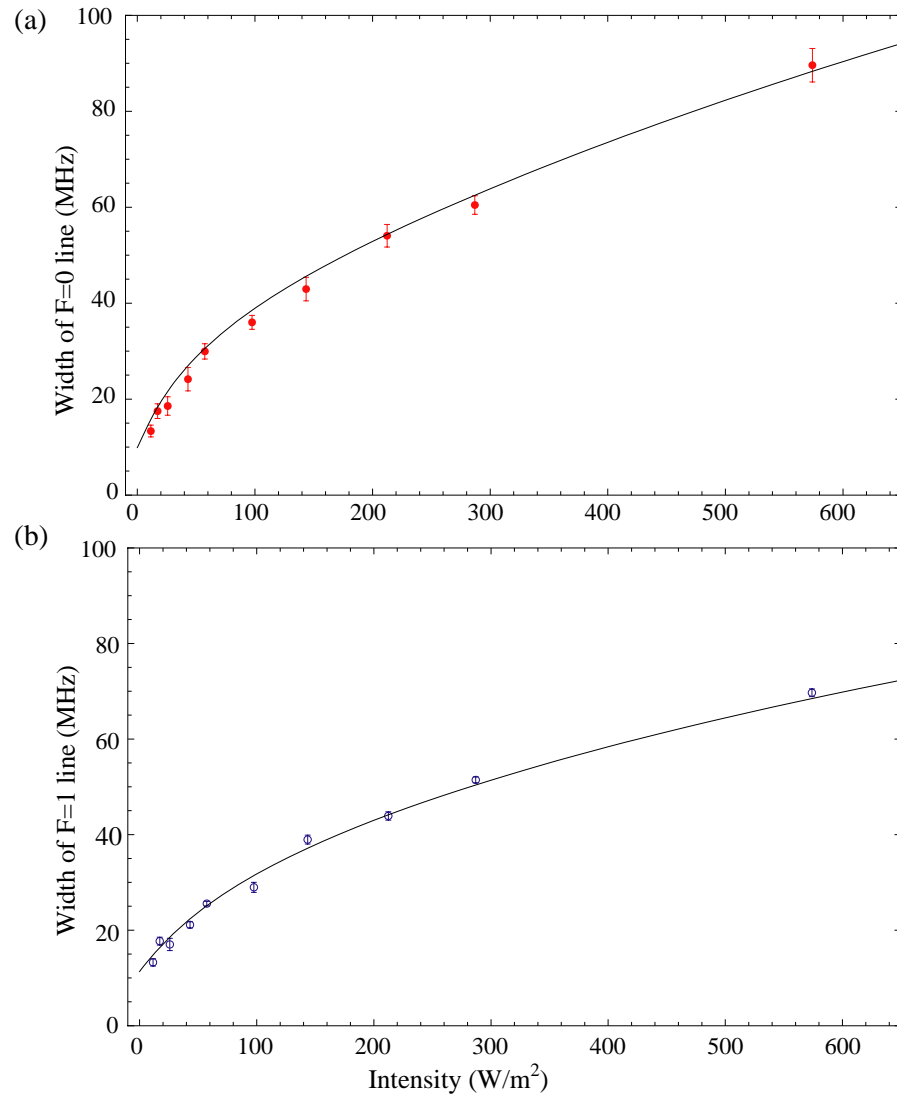


Figure 4.11: The width of (a) the $F = 0$ peak, and (b) the $F = 1$ peak as a function of probe beam intensity. The solid lines show the simulated widths, found by solving the rate equations with the same parameters as for the amplitude data (figure 4.10).

terminated by Z (equation 4.1), the Franck-Condon factor, which is the probability of the molecule remaining in the $v = 0$ manifold when it decays. Thus the form of the peak amplitude versus intensity data is largely determined by Z . The form of the amplitude data is also dependent on the mechanism of saturation of the first kind, but to a much lesser degree. This saturation is determined by I_s , which can be expressed in terms of Γ (see equation 4.6 and the succeeding paragraph). In this way the peak amplitudes are weakly dependent on Γ . The peak widths, however, are largely determined by Γ .

It can thus be seen how Γ and Z can be inferred physically from the experimental data. Δ_e is unresolved in the spectral scans and so its effects are more subtle. The most obvious effect that Δ_e has on the data is that it broadens the $F = 1$ peak and not the $F = 0$ peak, as the $X(F = 1)$ states are driven to both excited hyperfine states, whereas the $X(F = 0)$ is driven only to the $A(F' = 1)$ state (see inset of figure 4.1). A more subtle effect is on the amplitude data. The effect of the excited state hyperfine splitting is that the excitations from the three $X(F = 1)$ states do not occur at the same frequencies. The centre of the $F = 1$ peak does not correspond to all three transitions being on-resonance. Thus at this frequency the laser is driving transitions that are slightly off-resonance. This slightly decreases the excitation rate and so the photon scattering rate is slightly reduced by the hyperfine splitting. As a result it will take a slightly greater intensity to achieve $F = 1$ amplitude saturation. Δ_e thus has the capability to decrease the low intensity saturation gradient in the $F = 1$ peak data, but not in the $F = 0$ data. By these mechanisms the width and amplitude data are both slightly affected by Δ_e .

The best-fit parameters were found to be $Z = 0.987 \pm 0.012$, $\Gamma/(2\pi) = 8.28 \pm 0.08$ MHz and $\Delta_e = 4.8 \pm 0.4$ MHz.

As a first order assessment of the validity of the simultaneous fit the amplitude data and width data were also fitted separately. As discussed above, the Franck-Condon factor, Z , largely determines the amplitude data, and fitting the model to just this data-set gave $Z = 0.98$. The width data were largely determined by Γ , and fitting the model to just the $F = 0$ width data rendered $\Gamma/(2\pi) = 8.0$ MHz as the best-fit natural linewidth. Fitting just to the $F = 1$ width data rendered $\Gamma/(2\pi) = 8.5$ MHz. These ‘separate fitting’ numbers agree well with the parameters obtained from the simultaneous fit.

4.8.1 Systematic errors

The statistical errors result from the errors in the experimental amplitude and width data combined with the error in finding the best-fit model. In addition to these errors are several systematic errors in the experimental apparatus.

Firstly, the measurement of beam intensity has two sources of error. The power-meter calibration has a 5% error. Including this in the model is found to lead to a ± 0.2 MHz error in $\Gamma/(2\pi)$, but not to affect the other parameters significantly. In addition there was

a 10% error in the diameter of the probe laser beam. This was found to give an error of ± 0.14 MHz in $\Gamma/(2\pi)$, but again not to affect the other two parameters significantly.

Another source of systematic error is the degradation of the molecular beam flux during a scan. The AOM frequency-modulated data were used to measure the variation of the $F = 1$ to $F = 0$ peak amplitude ratio both over the course of a scan and (near-)simultaneously. Analysing this for many scans revealed a shift in amplitude from beam flux degradation consistent with zero, and having an upper limit of 1.5%. This contributes an error of $^{+0.013}_{-0.015}$ to Z , ± 1 MHz to Δ_e and a negligible error to Γ .

The model includes Doppler broadening by accounting for each simulated molecule's transverse position in the detection region. The mask in front of the PMT photocathode and the detection optics' magnification of $\times 2$ limit the detectable region to a beam width of 4.5 mm. An error in the magnification, mask width and mask alignment will change the Doppler broadening and lead to an error in the model. It is difficult to measure this quantitatively, but a very conservative estimate places the error in the Doppler width at $\pm 20\%$. However, within these errors the Doppler width is still always less than the natural linewidth. Reducing the photocathode mask width by 20% is found to reduce the value of $\Gamma/(2\pi)$ by only 0.2 MHz. Increasing the mask width is found to have two possible effects depending on the intensity regime. In the limit of small intensity, increasing the mask width increases the width of the spectral peaks, due simply to increased Doppler broadening when the more divergent portions of the molecular beam are included in the PMT signal. However, in the regime of high intensity the effect of increasing the mask width is more subtle and counter-intuitive. At high intensity the central part of the spectral peak is saturated, and the wings less saturated, as has already been discussed. This is power broadening. Increasing the mask width increases the beam divergence. This reduces the average number of photons scattered by each molecule. It takes more power to saturate a more divergent beam. Thus, the effect of an increase in the photocathode mask when at high intensities is in fact to reduce the peak widths. It was found in this regime that increasing the mask width by 20% decreases the best-fit value of $\Gamma/(2\pi)$ by 0.2 MHz.

A further potential source of error in the width comes from the linearization procedure. Statistical errors associated with the choice of cavity data parameters (y_{max} and y_{min}) and the fitting procedures have already been included in the error bars in the data, and the model accounts for these. The linearization technique was known to be good from the consistent agreement between theory and post-linearization data in the $F = 1/F = 0$ hyperfine splitting (123 MHz). Any further systematic source of error has been eliminated by comparing the linearized data with the data in which the AOM scanned the laser frequency.

Combining all these sources of errors renders the following final values for the molecular

parameters: $Z = 0.987^{+0.013}_{-0.019}$, $\Gamma/(2\pi) = 8.29 \pm 0.30$ MHz, and $\Delta_e = 4.8 \pm 1.1$ MHz. The inverse of the excited state decay rate gives the excited state lifetime to be 19.2 ± 0.7 ns. These results are consistent with the theoretically derived values from [59]: $Z = 0.964$, $\tau = 19.48$ ns and with the previous, less accurate, lifetime measurement [60], $\tau = 21.9 \pm 4$ ns.

Chapter 5

Decelerating weak-field seeking CaF molecules

5.1 Motivation

One of the principle aims of the research presented in this thesis is the deceleration of heavy molecules, in particular CaF radicals. Techniques for the Stark deceleration of molecules in weak-field seeking states are well-developed. Although the Stark shifts of weak-field seeking states are typically smaller than for the strong-field seeking ground state, weak-field seeking molecules are easier to guide. Consequently it is possible to obtain a high throughput of molecules through long Stark decelerators with many field stages.

This chapter describes the experimental set-up used to decelerate CaF radicals in the excited rotational state, $|\mathcal{N} = 4, M_N = 0\rangle$. The effects of non-adiabatic transitions caused by the switching electric fields inside the decelerator are discussed. Such transitions have a considerably detrimental effect on the molecular flux emitted by the decelerator, and a method for successfully inhibiting these transitions is reported.

5.2 Brief review of Stark deceleration of weak-field seeking molecules

The first deceleration of weak-field seeking molecules by the Stark effect was reported by Bethlem *et al.* in 1999 [37]. In this experiment a 35 cm-long Stark decelerator was constructed from an array of 63 deceleration stages. Each stage was composed of two oppositely polarized rod-shaped electrodes. Axial electric field strengths of up to 100 kV/cm were used to decelerate a pulsed beam of metastable CO. Molecules were slowed from an initial longitudinal speed of 225 ms^{-1} down to 98 ms^{-1} . In 2000 the same group reported the Stark deceleration of deuterated ammonia, ND₃, from 280 ms^{-1} to 13 ms^{-1} ,

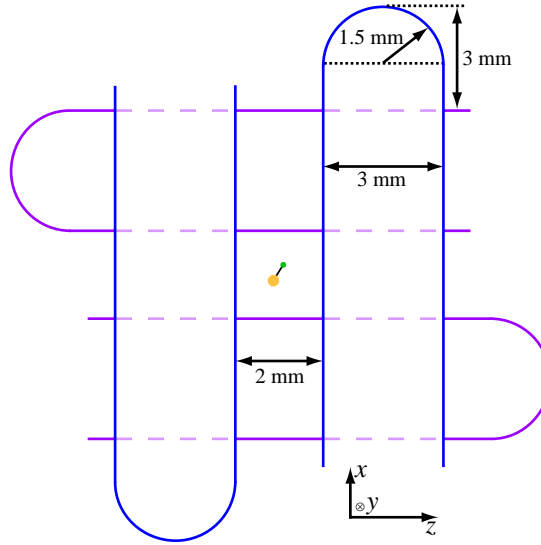


Figure 5.1: A cross-section of two deceleration stages, looking down the decelerator. The upstream deceleration stage (shown in blue) is vertical, and the downstream stage (purple) horizontal. Each stage consists of a pair of rod-like electrodes (circular cross-section, diameter 3 mm) with hemispherically-rounded ends (radius 1.5 mm). The successive deceleration stages create a square aperture of side 2 mm around and along the molecular beam-line.

which molecules were then trapped in an electrostatic trap [65]. Since then many other molecules in weak-field seeking states have been Stark-decelerated, such as OH [66, 67], NH [68], H₂CO [69], SO₂ [70], and LiH [71].

5.3 Experimental details

5.3.1 The decelerator

A 100-stage decelerator for weak-field seeking molecules was built. Each of the 100 deceleration stages consists of two parallel stainless steel rod-like electrodes, lying in a plane perpendicular to the molecular beam-line. The electrodes have circular cross-section, with diameter 3 mm, and have hemispherically-rounded ends of radius 1.5 mm (see figure 5.1). The separation between the closest surface of the two electrodes is 2 mm. The deceleration stages are arranged such that each stage is rotated about the beam-line through $\pi/2$ compared with the stages immediately before and after it. The molecules pass through the resulting square aperture of side 2 mm. The centre-to-centre distance between successive deceleration stages is 6 mm. There are 200 electrodes in total. Each electrode is held in place by one of four 16 mm-diameter, 594 mm-long stainless steel support rods (see figure 5.2). The support rods run the length of the decelerator and are held in place at each end

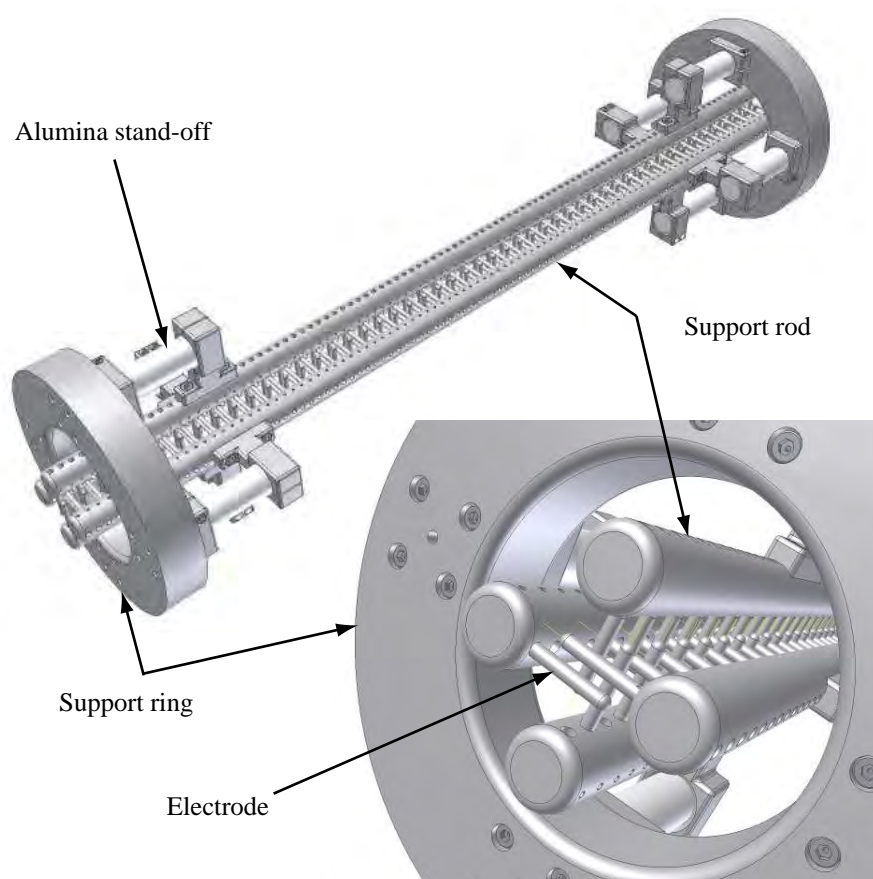


Figure 5.2: Two images of the 100-stage decelerator, showing how the electrodes, support rods and support rings are assembled.

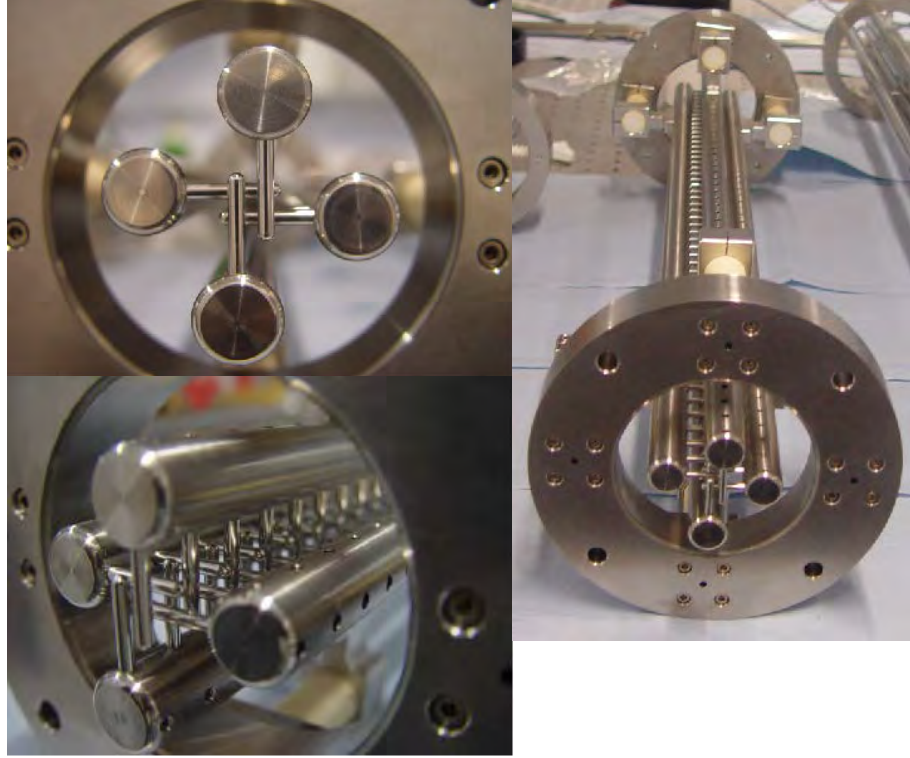


Figure 5.3: Three photographs of the 100-stage decelerator.

by a stainless steel support ring of inner diameter 80 mm and thickness 25 mm. The rods are attached to the support rings by an 80 mm-long, 18 mm-radius insulating alumina stand-off. Figure 5.3 shows three photographs of the decelerator after construction and cleaning, and prior to its installation in the vacuum chamber.

Inside the vacuum chamber the decelerator was held in a cradle. The cradle was held in place by two sets of spring-loaded vertical and horizontal pushers - one set nearer the skimmer, the other nearer the detection region. The pushers could be moved with a precision of about $10\ \mu\text{m}$ by feedthroughs. This allowed for the decelerator to be aligned with the beam-line. This alignment was checked with a theodolite looking down the beam-line: with the source chamber removed the theodolite could be used to image light with variable focus down the beam-line axis. Cross-hairs centred on the beam-line at the skimmer-end and the far-end of the main chamber allow the theodolite to be aligned with the beam-line. By varying the focus between the front end and far-end of the decelerator and varying the pushers the decelerator's alignment could be carefully monitored. The distance between the source and the centre of the first deceleration stage was 132 mm, and between the source and the centre of the detection region was 810 mm.

High voltage is applied to each of the decelerator's four support rods by four spring-loaded high voltage feedthroughs. Each feedthrough pushes into a hole drilled several millimetres into one of the support rods. The feedthrough is pressed onto the support rod

and kept under tension such that good electrical contact is maintained even when the decelerator is moved (which happens only during alignment). Pressing the feedthrough into a several-millimetre deep hole keeps the feedthrough in position and stops it from ‘springing out’ and losing contact. Applying high voltage to a feedthrough charges the support rod onto which it is pressing, and thus charges all the electrodes attached to that support rod.

The molecular beam was made and detected as described in chapter 3. The PMT was used in photon-counting mode. The beams used were Xe-carried, with typical mean speeds of around 365 ms^{-1} .

5.3.2 Electric fields and high voltage electronics

Figure 5.4 shows a schematic side view of three deceleration stages, numbered n , $n + 1$ and $n + 2$, where n is an odd number. The odd-numbered stages (shown in red) consist of electrodes pointing into the page; the even-numbered stages (shown in blue) consist of electrodes pointing along the page. The decelerator is switched between two high voltage states. In state 1 all the odd-numbered deceleration stages are held at ground and all the even-numbered stages are polarized to high voltage, V_{HI} . In state 2, the odd-numbered stages are at high voltage, V_{HI} , and the even-numbered stages are grounded. In the upper part of figure 5.4 the electrodes are shown in state 1. The lower part of figure 5.4 shows the electric field along the beam-line axis with the decelerator in state 1 (blue line) and in state 2 (red line), with $V_{HI} = \pm 15 \text{ kV}$. The fields were calculated by a finite element analysis. Consider the decelerator in state 1. The axial field is periodic in y , with maxima at the centre of even-numbered stages and minima at the centre of odd-numbered stages. A weak-field seeking molecule travelling along the beam-line will acquire an increased Stark potential as it enters an even-numbered stage. At a time when the molecule is a certain distance into an even-numbered stage the electrode polarities are switched into state 2. The axial electric field is now the one shown in red in the lower part of figure 5.4, and the molecule finds itself at the bottom of another Stark potential hill.

It is important to note that in figure 5.4 the coordinate axes are changed from all previous analysis in this thesis. The reason for this is that in section 5.8 there is a detailed analysis of the interaction between the molecules and the applied fields when the fields are switching from one state to the next. This analysis involves a rotating transverse electric field, and the analysis is easier in a rotating frame in which the rotating field points along z . For now it is important to note that in this chapter the coordinate axes are defined such that y points along the beam-line axis, rather than z which is the convention used everywhere else in this thesis.

Figure 5.5 is a schematic of the circuitry used to switch the four decelerator support rods, each of which holds 50 electrodes. The rods are labelled from 1 to 4. At a given

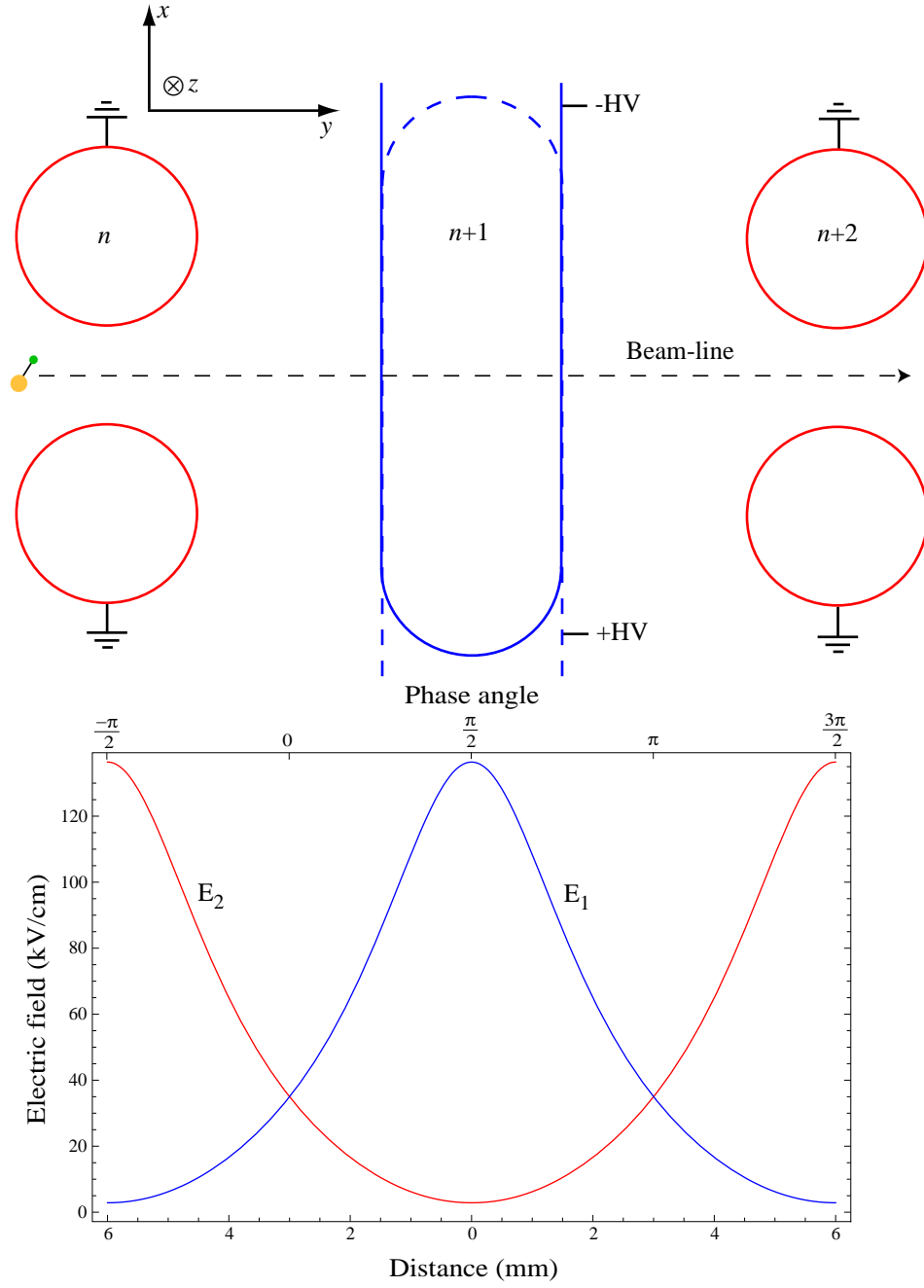


Figure 5.4: *Upper part*: A schematic diagram showing three deceleration stages of the 100-stage decelerator. The electrodes are numbered, with n an odd number. The decelerator is shown in state 1, in which the even-numbered stages are charged to $\pm V_{HI}$ and the odd-numbered stages are grounded. *Lower part*: The calculated field along the beam-line in state 1 (blue line) and state 2 (red line) when $V_{HI} = 15$ kV. The field is shown as a function of longitudinal position, as well as a function of a phase angle, which will be defined in section 5.6.1

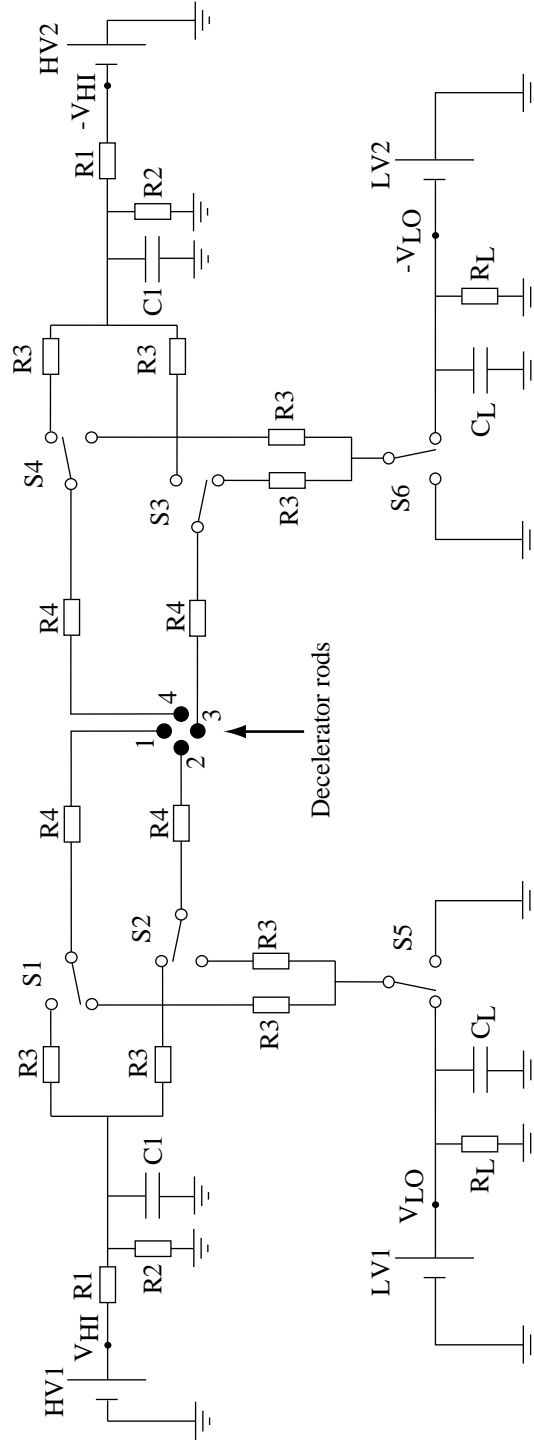


Figure 5.5: The circuitry used to switch the voltage applied to each of the four rods of the 100-stage decelerator from the ‘high’ state, V_{HI} , to the ‘low state’, V_{LO} . S1, S2, S3 and S4 are TTL-controlled high voltage switches; S5 and S6 are manual switches. HV1 and HV2 are high voltage supplies (maximum output 20 kV), and LV1 and LV2 are lower voltage supplies (maximum output 2 kV). $R1 = 2.2 \text{ k}\Omega$, $R2 = 100 \text{ M}\Omega$, $R3 = 1.4 \text{ k}\Omega$, $R4 = 800 \text{ }\Omega$, and $C1 = 0.5 \text{ }\mu\text{F}$. The values of C_L and R_L are discussed in the text.

time one set of 50 electrodes will be charged to positive high voltage, V_{HI} , and the 50 opposite electrodes will be charged to $-V_{HI}$. The 100 electrodes held by the remaining two support rods will be grounded, as described above, or can be held at some voltage, V_{LO} much lower than V_{HI} . The reason for holding them at V_{LO} will be described later. In a given switching state the two charged arrays of 50 electrodes act as the two sides of a capacitor. The total capacitance of the two arrays and the braided high voltage cables that supply them was measured to be $C_{decel} = 100$ pF. In a given switching state the two charged electrode arrays can thus be considered as the two sides of a 100 pF capacitor. The four TTL-controlled high voltage switches (*Behlke* HTS 201-03-GSM) S1, S2, S3 and S4 switch the rods (1, 2, 3 and 4 respectively) between high and low voltage.

The following discussion describes the charging and discharging of rods 1 and 3, whose (oppositely polarized) electrodes form 50 deceleration stages. It can be seen from figure 5.5 that when S1 is in the ‘up’ position rod 1 is connected to the output of a high voltage power supply, HV1, supplying voltage V_{HI} . HV1 is kept on permanently and is in parallel with a $0.5 \mu\text{F}$ capacitor, the purpose of which will be explained shortly. At the same time S3 connects rod 3 to high voltage supply, HV2, (and $0.5 \mu\text{F}$ capacitor) with output $-V_{HI}$. The potential difference across the gap between the rods is thus $2V_{HI}$. After some delay S1 and S3 flip simultaneously. Both rods can now discharge through one of two possible routes, chosen by manual switches, S5 and S6. Both positive rods (rods 1 and 2) discharge through the same route, controlled by switch S5, and both negative rods (rods 3 and 4) discharge through the same route, controlled by S6.

Consider for now the case in which S5 and S6 are both set to ground. Discharging to ground reduces a rod’s voltage from $\pm V_{HI}$ exponentially with time constant $2.2 \text{ k}\Omega \times 100 \text{ pF} = 220 \text{ ns}$. With S5 and S6 connected to ground, switching S1 and S3 simultaneously and in phase thus switches the potential difference across the gap between rods 1 and 3 between 0 V and $2V_{HI}$.

Switches S2 and S4 are switched in phase with each other, but π out of phase with S1 and S3, such that when rods 1 and 3 are connected to high voltage, rods 2 and 4 are grounded, and vice versa. The effect of all four switches is to switch the axial electric field between states 1 and 2 shown in figure 5.4. The switching is sufficiently fast that the two high voltage power supplies, HV1 and HV2 are not able to supply the required charging current. The current is in fact supplied by the $0.5 \mu\text{F}$ capacitors in parallel with the power supplies. These are charged to $+V_{HI}$ and $-V_{HI}$ respectively, and are able to supply the required current to charge the rods quickly. In one shot each rod is switched between ground and V_{HI} 50 times, known as a ‘burst’.

Figure 5.6 (a) shows the recorded voltages of two oppositely polarized rods corresponding to the same deceleration stages. The voltages were measured at the feedthroughs supplying the rods by a fast high voltage probe (*Tektronix* P6015A). In this case the rods

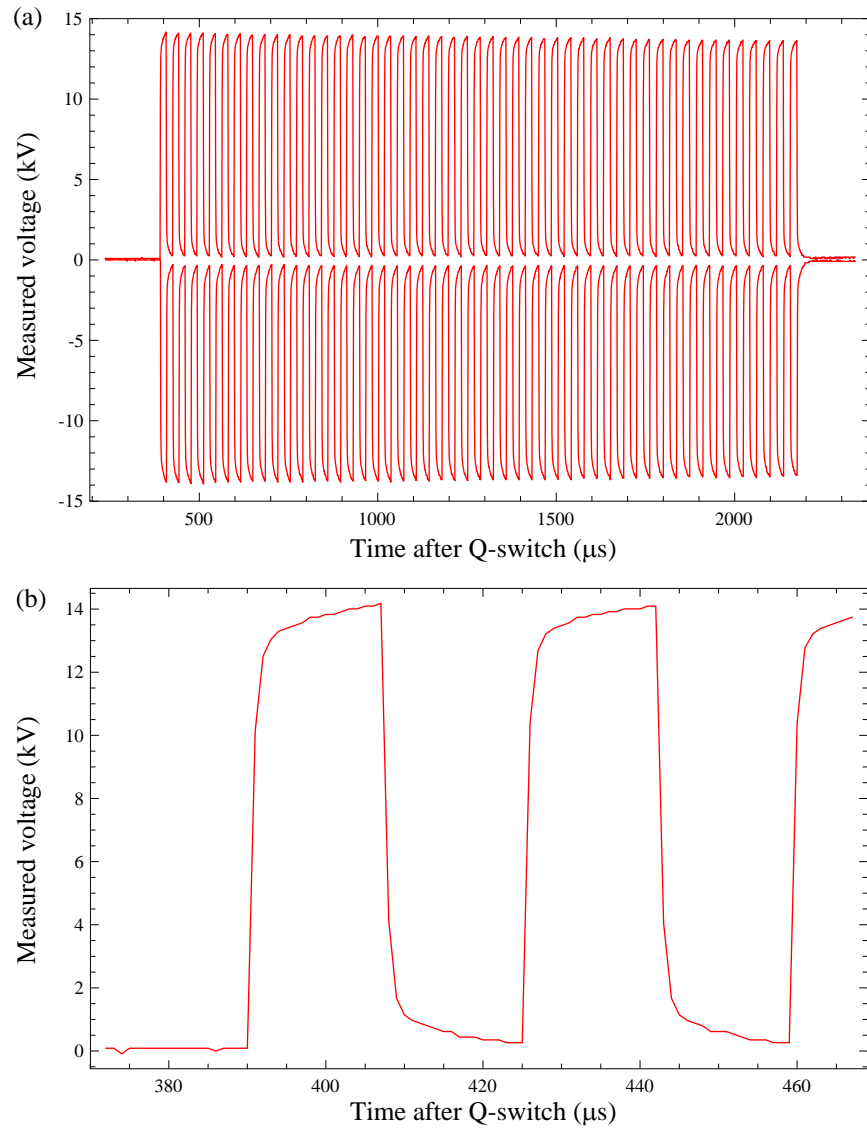


Figure 5.6: (a) The measured voltage of the two oppositely polarized electrode arrays corresponding to one set of 50 deceleration stages. (b) The first two voltage pulses measured at the positive voltage feedthrough. This ‘zoomed-in’ figure shows the lag introduced by the high voltage probe.

were charged to ± 14.0 kV, and S5 and S6 were connected directly to ground. The measured peak voltage doesn't quite reach ± 14.0 kV for two reasons. Firstly, the frequency compensation circuit of the probe is adjusted for the fastest time response, and the price paid for this high temporal resolution is some lag in the measured voltage on the longer time-scale of the pulse duration. In calibrations in which the voltages were switched more slowly the measured voltage did indeed reach the applied voltage. For the same reason the measured voltage doesn't quite reach zero when the electrodes are grounded. Secondly, it can be seen that the peak voltage drops by approximately 3% over the course of one burst. This is because the $0.5 \mu\text{F}$ capacitor, which effectively supplies the high voltage, discharges slightly each time it charges a rod. This voltage drop will affect the deceleration as the fields at the end of the decelerator will not be as great as those at the beginning, but this effect is considered to be negligible. Figure 5.6 (b) shows the first two voltage pulses measured at the positive voltage feedthrough. The rise and fall times are seen to be about 500 ns, and the time lag in reaching the correct voltage level, introduced by the probe, is clearly seen.

The second discharge route available to the positive and negative rods occurs when the switches S5 and S6 are connected to the output of the high voltage power supplies LV1 and LV2 respectively, both of which are in parallel with a resistor, labelled R_L , and capacitor, labelled C_L . The values of C_L and R_L are chosen to be identical in both discharge circuits. In this case it is desired to switch the electrodes not to ground, but to the outputs of LV1 and LV2, V_{LO} and $-V_{LO}$ respectively. The rods held high at V_{HI} are switched down to V_{LO} , and those held high at $-V_{HI}$ are switched to $-V_{LO}$. Consider discharging rod 1 with S5 connected to the output of LV1. The discharging current cannot be passed through LV1, which is unable to sink the positive current and effectively acts as a diode, and so the current travels to ground through C_L and R_L . What happens to the charge? Consider first the case when LV1 is set to 0 V. The capacitance of C_L is chosen to be much greater than that of the decelerator. Thus, when the rod discharges the charge stored at high voltage on the decelerator is transferred to C_L , which is at a much lower voltage. During one discharge the voltage across C_L increases by $\Delta V_1 = V_{HI} \frac{C_{decel}}{C_L}$. During one burst the decelerator discharges 100 times, and so the voltage across C_L increases by $\Delta V_{100} = 100V_{HI} \frac{C_{decel}}{C_L}$. During the time, τ_{rep} , between the end of one burst and the start of the next, C_L will discharge through R_L . If the voltage is V_L at the end of one burst, it will have dropped by

$$\Delta V_L = V_L \times \left(1 - \exp \left[\frac{-\tau_{rep}}{R_L C_L} \right] \right) \quad (5.1)$$

by the start of the next burst. After a few bursts a steady state will be reached in which the voltage gained during one burst will equal that lost in between bursts: $\Delta V_L = \Delta V_{100}$.

The equilibrium voltage across C_L at the beginning of each burst will then be

$$V_L^{eqm} = 100V_{HI} \times \frac{C_{decel}}{C_L} \frac{1}{\left(1 - \exp\left[\frac{-\tau_{rep}}{R_L C_L}\right]\right)}. \quad (5.2)$$

The experimental parameters used were: $\tau_{rep} = 200$ ms, $C_L = 1\mu\text{F}$ and $R_L = 660$ k Ω . These values result in an equilibrium voltage across C_L of $V_L^{eqm} = 0.038V_{HI}$. During a burst the decelerator switches between V_{HI} and $0.038V_{HI}$, with a small increase in the baseline voltage of $\Delta V_{100} = 0.01V_{HI}$ by the end of the burst. This increase is very small and is neglected in the analysis of the decelerator. The equilibrium voltage, V_L^{eqm} , is reached within only a few bursts.

Consider now the case in which LV1 is turned on and $V_{LO} > 0$. If $V_{LO} < V_L^{eqm}$ then the situation is identical to LV1 being off: LV1 neither supplies nor sinks any current. If $V_{LO} > V_L^{eqm}$ then LV1 charges C_L . It does this quickly since the output impedance of LV1 is low. The voltage across C_L still increases by ΔV_{100} during a burst, but it will discharge back to V_{LO} in less than τ_{rep} , and the equilibrium baseline voltage is V_{LO} .

The baseline voltage of the decelerator is therefore either $0.038V_{HI}$, or the value of V_{LO} set by the power supply LV1, whichever is greater. The maximum output of the supplies LV1 and LV2 is 2 kV. Thus, for a value of V_{HI} of 18 kV, V_{LO} can be varied between 680 V and 2 kV.

Figure 5.7 shows the measured voltage of the same two rods as shown in figure 5.6. In this case switches S5 and S6 were switched such that the electrodes discharged onto the capacitors C_L and resistors R_L . The power supplies LV1 and LV2 were turned off and so the baseline voltage was simply that of the charged capacitors. The measured equilibrium baseline voltages are shown by the dashed lines in figure 5.7. The positive baseline voltage starts at 900 V, and by the end of the burst this can be seen to have risen to 1.17 kV. This increase is 1.9% of V_{HI} , slightly greater than the prediction of 1%. This disparity is most likely due to an error in the measurement of the decelerator's capacitance. The results are similar for the negative pulses shown, and for the measured voltage pulses of the other two rods.

The reason for the 200 ms delay between successive deceleration bursts is that there is a third polarity state that the decelerator can be in. In this state all four high voltage switches are held in the high voltage state throughout the transit time of the molecules through the decelerator. In this case, known as the 'DC guiding state', the decelerator acts as a guide for weak-field seeking molecules. The experiment is run with a repetition rate of 10 Hz. After every deceleration shot (taken in 'burst mode'), a DC guiding shot is taken. The reasons for this are two-fold. Firstly, the molecular beam flux slowly varies, due mostly to variations in the quality of the Ca surface exposed to ablation. In order to normalize out signal drift due to this flux variation the PMT signal from each deceleration shot is compared with that of a near-simultaneous DC guiding reference shot. The DC

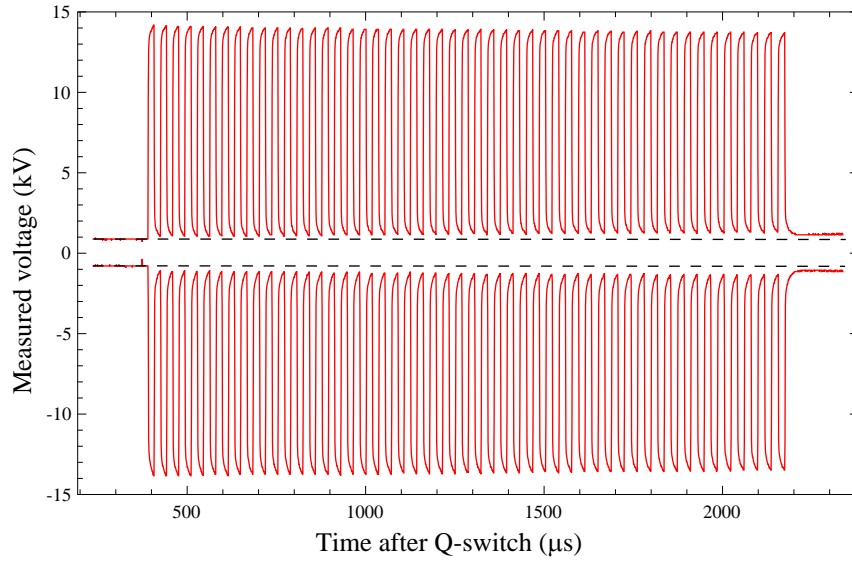


Figure 5.7: The measured voltage of the same two rods as in figure 5.6, but no longer switching to ground. In this case switches S5 and S6 cause the rods to discharge to the resistors R_L and capacitors C_L . For these measurements the power supplies LV1 and LV2 were off and so the measured baseline voltages (initially 900 V for the positive electrodes and -800 V for the negative electrodes) are caused by charging the capacitors C_L . The initial baseline voltages are highlighted by dashed lines. Over the course of one burst both baseline voltages can be seen to increase by around 1.9% of V_{HI} .

guiding shots are all taken under identical conditions (whereas the deceleration shots are taken with varying parameters, such as phase angle), and so any signal drift between two DC guiding shots must originate from flux variation. Comparing a deceleration shot time-of-flight profile with that of its succeeding (or preceding) DC guiding shot gives a scaled time-of-flight profile that is unaffected by flux variation. Secondly the LIF signals acquired with DC guiding are very large and are thus useful signals for keeping the laser parked on the chosen resonance.

The high voltage switches are controlled by a TTL pattern sent from a computer via four optical links. The exact switching timings of a given burst are determined by the computer. For a given molecule, in a given rotational state and with a given applied voltage, the switching pattern is calculated to decelerate molecules from a chosen initial speed. The pattern is designed such that a molecule with this initial speed, and that enters the decelerator when the pattern starts, is in the same position in each deceleration stage when the fields switch. This molecule is known as the synchronous molecule, and it loses the same amount of kinetic energy in each stage (this is discussed in more detail in section 5.6.1). An overall time delay, that determines when the switching pattern begins, is also a free parameter that can be tuned in the experiment.

5.4 The Stark shift and the hyperfine structure

The Hamiltonian for the $^2\Sigma$ state of CaF in an electric field is

$$\hat{H} = B\hat{N}^2 - \hat{\mu} \cdot \vec{E} + \gamma\hat{S} \cdot \hat{N} + b\hat{I} \cdot \hat{S} + c\hat{I}_{z'}\hat{S}_{z'} + C\hat{I} \cdot \hat{N}, \quad (5.3)$$

where \hat{N} is the total rotational angular momentum operator, \hat{S} is the total electronic spin operator, \hat{I} is the total nuclear spin operator, \hat{I}_z and \hat{S}_z are components along the internuclear axis, $\hat{\mu}$ is the electric dipole moment operator, and \vec{E} is the electric field. $B\hat{N}^2$ corresponds to the rotational energy of a rigid rotor (as discussed in section 2.1.5). $\hat{\mu} \cdot \vec{E}$ is the Stark interaction. $\gamma\hat{S} \cdot \hat{N}$ is the electron spin–rotation interaction. $b\hat{I} \cdot \hat{S} + c\hat{I}_{z'}\hat{S}_{z'}$ is the interaction between the magnetic dipoles associated with electron spin and nuclear spin. $C\hat{I} \cdot \hat{N}$ is the nuclear spin–rotation interaction. The last three terms are referred to as the hyperfine interactions.

In the presence of a strong electric field the first two terms dominate, and the molecule can be treated as a rigid rotor. Figure 5.8 shows the Stark shift of the $\mathcal{N} = 4$ sub-levels in the presence of electric fields typical of those created inside the decelerator. It can be seen that the $M_N = 0$ sub-level experiences the greatest Stark shift. Indeed, for a given value of \mathcal{N} , the sub-level with $M_N = 0$ always experiences the greatest Stark shift. At the greatest field strengths practically achievable inside a decelerator (around 200 kV/cm) CaF experiences the greatest positive Stark shift in the $|\mathcal{N} = 4, M_N = 0\rangle$ state. The decelerator was thus used with CaF radicals in this rotational state.

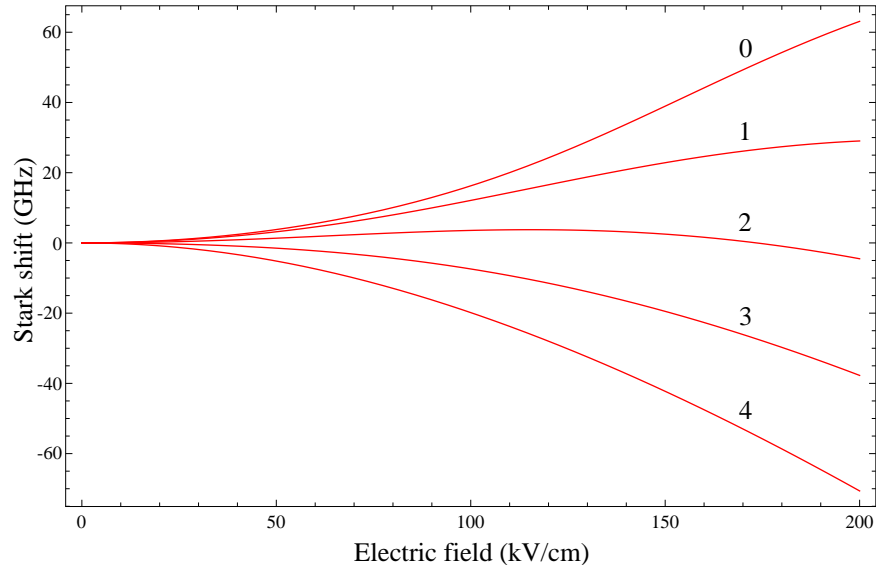


Figure 5.8: The Stark shift of the $\mathcal{N} = 4$ states of CaF. The sub-levels are numbered in terms of $|M_N|$.

In regions of low-field the molecule is described by the full Hamiltonian in equation 5.3. In this case the molecular states are described by the angular momentum quantum numbers, N , S , J , I , F and M_F . In the experiment the molecules are detected in a region of zero applied field. Careful analysis must be performed to identify the field-free states that correspond to the $|\mathcal{N} = 4, M_N = 0\rangle$ rigid rotor state.

The four field-free states belonging to the $\mathcal{N} = 4$ manifold are $|F = 5, J = \frac{9}{2}\rangle$, $|F = 4, J = \frac{9}{2}\rangle$, $|F = 3, J = \frac{7}{2}\rangle$ and $|F = 4, J = \frac{7}{2}\rangle$. These are discussed in section 3.3.3, and a spectrum of transitions from these lines to the $^2\Pi$ excited state is shown (figure 3.6). Within these four F states are contained a total of 36 M_F states. The Stark shift does not mix states of different M_F (section 2.4) and so M_F is a good quantum number in the presence of an electric field.

In a strong electric field, in which the Stark shift dominates over the spin-rotation and hyperfine interactions, the $\mathcal{N} = 4$ state has five magnetic sub-level groups, with $M_N = 0, \pm 1, \pm 2, \pm 3, \pm 4$. The sub-levels with the same value of $|M_N|$ are degenerate. Mapping which field-free M_F levels correlate to which rigid rotor M_N states can be performed simply by knowing the relative energies of the field-free $F = 5, 4, 3, 4$ states, which is shown in section 3.3.3 (figure 3.6), and by applying the rule that, in the transition from field-free to rigid rotor state, states of the same M_F cannot cross. Figure 5.9 is a schematic representation of the mapping of the 36 M_F states of the four field-free states under consideration to the 36 M_F states of the 5 rigid rotor magnetic sub-level groups. Table 5.1 shows how the field-free states correlate to rigid rotor states in the presence of an applied electric field.

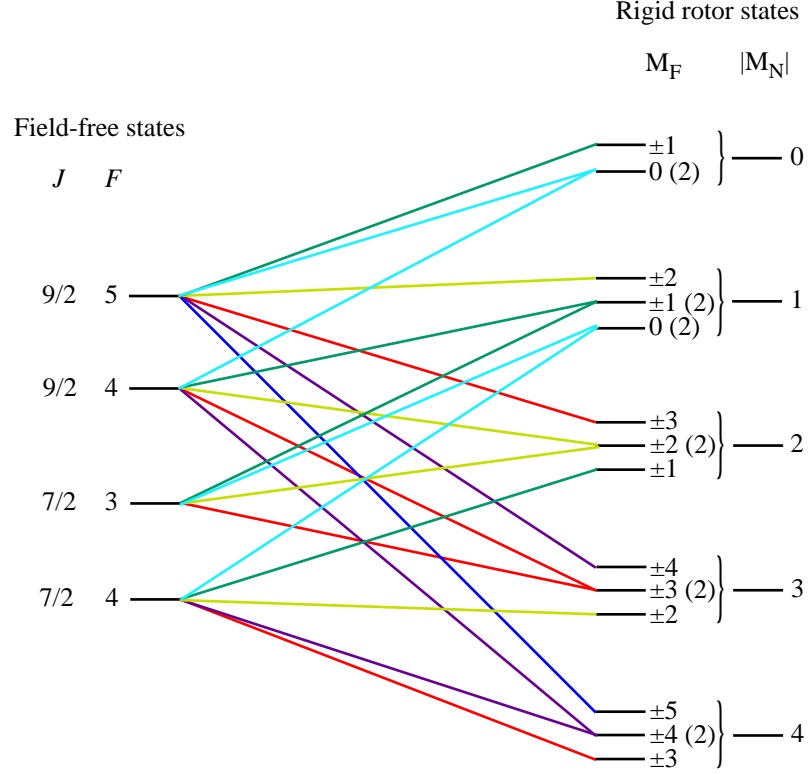


Figure 5.9: A representation of the mapping of the 36 M_F states of the four field-free states ($F = 5, 4, 3, 4$) to the five Stark-shifted rigid rotor magnetic sub-level groups ($|M_N| = 0, 1, 2, 3, 4$). The colouring scheme indicates the states of different M_F : $M_F = 0$ is shown by a turquoise line, $M_F = 1$ by a dark green line, $M_F = 2$ by a dark yellow line, $M_F = 3$ by a red line, $M_F = 4$ by a purple line, and $M_F = 5$ by a blue line.

Table 5.1: Magnetic sub-level components of the field-free states

Field-free state (peak number)	Number of states from $ N, M_N\rangle$				
	$ 4, 0\rangle$	$ 4, 1\rangle$	$ 4, 2\rangle$	$ 4, 3\rangle$	$ 4, 4\rangle$
$F = 5$ (peak 1)	3	2	2	2	2
$F = 4$ (peak 2)	1	2	2	2	2
$F = 3$ (peak 3)	0	3	2	2	0
$F = 4$ (peak 4)	0	1	2	2	4

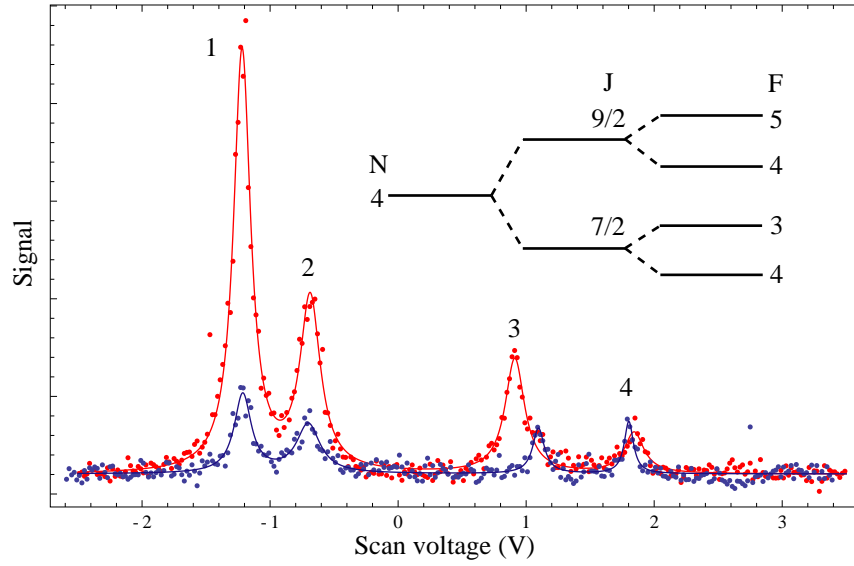


Figure 5.10: Two scans over the $Q_{11}(\frac{9}{2})$ and $R_{21}(\frac{7}{2})$ lines of CaF, taken with the decelerator off (blue points) and with ± 13 kV applied (red data). Also shown are quadruple-Lorentzian fits to the two data-sets. The peaks are labelled from 1 to 4, in accordance with the scheme used in figure 3.6. Also shown is a diagram showing the coupling of rotational, electronic spin and nuclear spin angular momenta to form the four field-free states which correspond to the four spectral peaks.

5.5 Transverse focussing of weak-field seeking molecules

Of the rigid rotor states of CaF, the $|\mathcal{N} = 4, M_N = 0\rangle$ state experiences the greatest Stark shift in the typical fields applied in the decelerator. As the detection is performed in a field-free region, it is thus necessary to deduce which field-free state has the most $|\mathcal{N} = 4, M_N = 0\rangle$ character in a strong electric field. This relationship is given in table 5.1. To investigate this experimentally the decelerator was operated in DC guiding mode. For a given applied voltage the probe laser was scanned over the four transitions from the four field-free states. Figure 5.10 shows the spectrum acquired with the decelerator turned off (blue data) and with the decelerator charged to ± 13 kV in DC guiding mode (red data). This is the same spectrum as shown in figure 3.6, where the lines were numbered from 1 to 4. The same numbering scheme is used in this analysis, where peak 1 corresponds to the transition from the $|J = \frac{9}{2}, F = 5\rangle$ state, peak 2 to the transition from the $|J = \frac{9}{2}, F = 4\rangle$ state, peak 3 to the transition from the $|J = \frac{7}{2}, F = 3\rangle$ state, and peak 4 to the transition from the $|J = \frac{7}{2}, F = 4\rangle$ state. It can be seen that the peak 1 signal strength is vastly increased by the applied field, the peak 2 and 3 signal strengths are increased but to a lesser extent, and peak 4 is largely unaffected. The slight offset between the position of peak 3 in the zero volts and ± 13 kV scans is simply a result of the nonlinearity of the laser frequency scan.

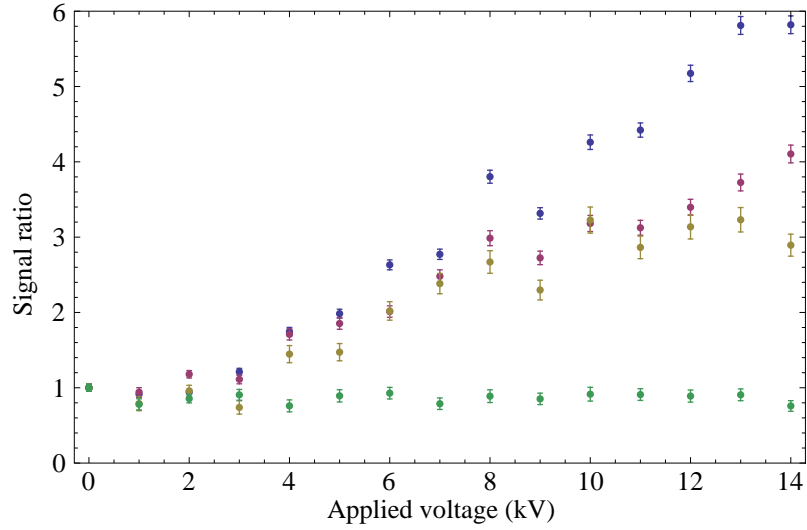


Figure 5.11: Measured signal ratios of the $Q_{11}(\frac{9}{2})$ and $R_{12}(\frac{7}{2})$ lines. The lines correspond to transitions from the $|J = \frac{9}{2}, F = 5\rangle$ state (peak 1 – blue points), the $|J = \frac{9}{2}, F = 4\rangle$ state (peak 2 – red points), the $|J = \frac{7}{2}, F = 3\rangle$ state (peak 3 – gold points) and the $|J = \frac{7}{2}, F = 4\rangle$ state (peak 4 – green points). The error bars are derived from errors in the fits.

The spectrum of the four peaks was recorded over a range of applied voltages. For each recorded scan the peaks were fitted to a quadruple-Lorentzian function. For each peak the measured amplitude at a given applied voltage was divided by the amplitude acquired with no voltage applied to the decelerator. This quotient is known as the ‘signal ratio’, and has the advantage of measuring the strength of the guiding in such a way that normalizes out flux variations in the molecular source. Figure 5.11 shows the measured signal ratios of the four peaks as a function of electric field. The transition from the $|J = \frac{9}{2}, F = 5\rangle$ state (blue points) shows the greatest signal ratios, still rising by the greatest applied voltage (14 kV). The transitions from the $|J = \frac{9}{2}, F = 4\rangle$ and $|J = \frac{7}{2}, F = 3\rangle$ states show similar behaviour, both having signal ratios that rise with voltage, but not as much as the $|J = \frac{9}{2}, F = 5\rangle$ transition. The transition from the $|J = \frac{7}{2}, F = 4\rangle$ state appears to be mostly unaffected by the electric field, maintaining a signal ratio of approximately 1 for all applied voltages. The explanation for this behaviour can be found by considering the guiding efficiency of the different M_F states in each F state. Assuming that the fields inside the guide are always great enough such that the rigid rotor approximation is good, the guiding efficiency of an M_F state depends on the Stark shift of its associated strong-field rigid rotor state. For example, consider the field free state $|J = \frac{9}{2}, F = 5\rangle$. Table 5.1 shows that this state consists of 11 M_F states which, in the presence of a strong electric field, are divided among the rigid rotor states as follows: 3 M_F states correlate to the state $|N = 4, M_N = 0\rangle$ and 1 M_F state correlates to each of the 8 states $|N = 4, M_N = \pm 1\rangle$,

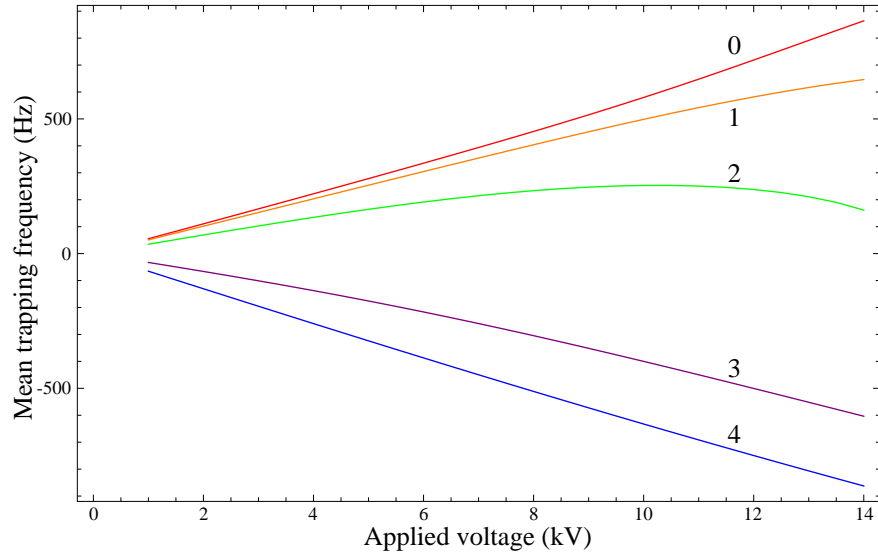


Figure 5.12: The mean trapping frequencies of the magnetic sub-levels of the $\mathcal{N} = 4$ rigid rotor state as a function of voltage applied to the 100-stage decelerator operated in DC guiding mode. The trapping frequency is a measure of the depth of the transverse Stark potential created by the DC fields inside the decelerator. The states are labelled by $|M_N|$.

$|N = 4, M_N = \pm 2\rangle$, $|N = 4, M_N = \pm 3\rangle$ and $|N = 4, M_N = \pm 4\rangle$ respectively. It is possible to calculate how strongly molecules in these states are guided by the decelerator, using the electric field geometry of the decelerator and the relevant rigid rotor Stark shifts. The electric field was calculated using a finite element model. Within a deceleration stage the electric field magnitude as a function of transverse position has a minimum along the beam-line axis. This corresponds to a potential well, the depth of which varies as a function of the longitudinal coordinate. Directly in between the electrodes there is a steep potential well with a large associated trapping frequency, whereas in between two deceleration stages the well is much shallower, with a much smaller associated trapping frequency. It is possible to calculate a mean trapping frequency over the length of the decelerator. This frequency is a function of the applied voltage and the rigid rotor state of the molecule in question. Figure 5.12 shows the mean trapping frequencies for CaF in the various $|M_N|$ states of $\mathcal{N} = 4$, calculated for the geometry of the 100-stage decelerator. A positive frequency corresponds to trapping and a negative frequency to anti-trapping. A greater trapping frequency means that the decelerator can transmit molecules with greater transverse speeds, and so it would be expected that the number of molecules transmitted should increase as the trapping frequency increases. The states with $|M_N| = \{0, 1\}$ both experience positive frequencies that increase approximately linearly with applied voltage. The $M_N = 0$ state has the greatest trapping frequency because it has the largest Stark shift. The states with $|M_N| = 2$ have a positive frequency that increases with voltage until

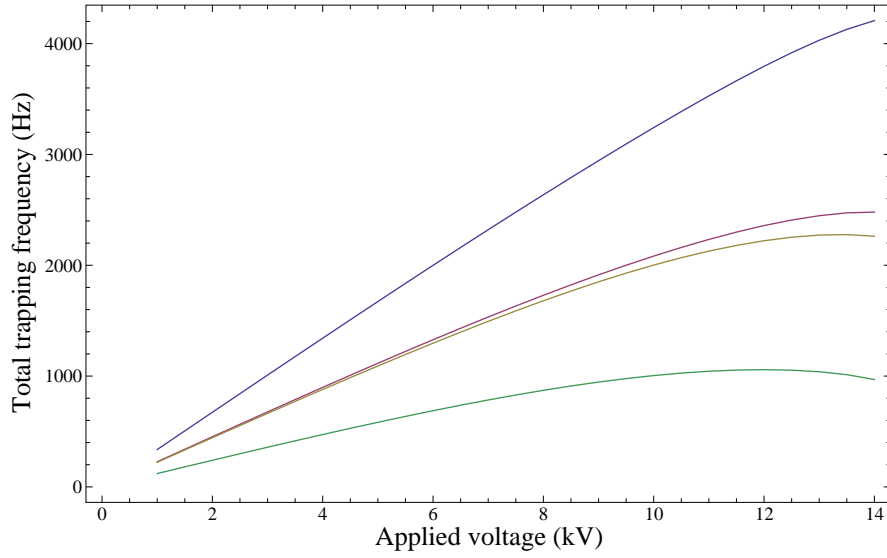


Figure 5.13: The total trapping frequency of all the guided rigid rotor states associated with the measured $Q_{11}(\frac{9}{2})$ and $R_{12}(\frac{7}{2})$ lines (figures 5.10 and 5.11). The frequencies are calculated at a given electric field by weighting and summing the mean trapping frequencies (figure 5.12) by the populations in table 5.1. The colouring scheme is the same as for figure 5.11: peak 1 (blue), peak 2 (red), peak 3 (gold), peak 4 (green).

approximately 10 kV when it starts to decrease with voltage. This turnover corresponds to the field strengths being great enough for these states to become strong-field seeking, as indicated in figure 5.8. The states with $|M_N| = \{3, 4\}$ both experience negative trapping frequencies that decrease with applied voltage because they are strong-field seekers at all fields. These states are thus not guided by the decelerator and will not contribute to the measured fluorescence signal when voltage is applied to the decelerator. Molecules in the other states will contribute to the signal as long as the electric field is not so great that they become strong-field seekers.

A qualitative understanding of the guiding data can be obtained by considering the net trapping frequency for molecules in each state. This net trapping frequency is calculated as follows: for a given electric field the trapping frequencies associated with the rigid rotor states are weighted by the populations shown in table 5.1, and then summed. Contributions from the states $|4, 3\rangle$ and $|4, 4\rangle$ have been neglected as these states do not contribute to a guided beam. The results, shown in figure 5.13, agree qualitatively with the form of the experimental data. The states associated with peak 1 in the fluorescence spectrum experience large trapping frequencies which rise with electric field, but the slope begins to decrease around 13 kV. The states associated with peaks 2 and 3 both experience roughly the same trapping frequencies, which display the same behaviour as peak 1, but always at lower trapping frequencies. The states associated with peak 4 experience the weakest net

trapping frequencies, which rise slowly with electric field, and begin to turn over around 12 kV. The data from peak 4 are the only ones that disagree with the form of the net trapping frequency, with the experimental data showing very little change over the range of applied voltages. The calculated net trapping frequencies are only a rough indicator of the guiding efficiency of the decelerator, but they nevertheless explain the physical basis for what is observed.

The rigid rotor sub-level in the $\mathcal{N} = 4$ manifold which experiences the greatest Stark shift in the fields produced in the decelerator is the $M_N = 0$ sub-level. This state is thus the easiest to guide and to decelerate. The field-free state whose magnetic sub-levels contribute the most to $|4, 0\rangle$ in the presence of an electric field is $|F = 5\rangle$. This is thus the state that was chosen to be probed by LIF, corresponding to peak 1 in figure 5.10.

5.6 Longitudinal focussing in a Stark decelerator

Chapter 2 gives an introduction to the principles of Stark deceleration. Having shown in the above section how the 100-stage decelerator can guide and focus molecules in the transverse directions, it is now necessary to understand how it can bunch and decelerate a group of molecules in the longitudinal direction. This section starts with a general description of the longitudinal dynamics of molecules in a Stark decelerator. This is then followed by a detailed analysis of the longitudinal dynamics inside the 100-stage decelerator.

5.6.1 Phase stability in a Stark decelerator

A decelerator is composed of a sequence of field stages, each one removing an amount of kinetic energy. The stages are separated centre-to-centre by L . At a given time during deceleration the field stages are alternately charged and grounded (see figures 2.3 and 5.4). In this arrangement the electric field is periodic along z with period $2L$, reaching maxima in the centre of the charged stages and minima in the centre of the grounded stages. A molecule travelling through this periodic electric field thus experiences a periodic Stark potential.

The motion of a molecule in this periodic potential can be expressed in terms of a phase angle, $\phi = \pi z/L$, where $\phi = \pi/2$ is at the centre of a charged stage and $\phi = 3\pi/2$ is at the centre of a grounded stage.

The analysis in section 2.5 considered one ball moving with kinetic energy, E_k . In practice a Stark decelerator is used with pulsed beams of molecules with a distribution of longitudinal speeds and positions. However, a given field switching sequence can be used to decelerate molecules with only one initial speed.

Consider decelerating a molecule in the beam with initial longitudinal speed, v_{sync} .

The fields are switched in such a way to remove a constant amount of energy from this molecule in each stage. To achieve this, when the fields are switched the molecule must be at the same position up the Stark potential hill in each stage. The molecule is at the same constant phase, ϕ_{sync} , in each stage when the fields are switched, where $0 < \phi_{sync} < \pi/2$ for deceleration. This molecule is known as the ‘phase-synchronous’ molecule. As the molecule slows down it will take longer to reach ϕ_{sync} in each successive stage. This delay is denoted ΔT and increases along the decelerator. To compensate for this the switching pattern slows down as the synchronous molecule travels along the decelerator. It should also be noted that ϕ_{sync} and v_{sync} are not continuous variables: they are defined only at the instant that the fields are switched.

Consider now the motion of a molecule which enters the decelerator slightly ahead of the synchronous molecule and with slightly greater longitudinal speed. It starts with phase, ϕ , slightly greater than ϕ_{sync} and speed, v , slightly greater than v_{sync} . After one field stage this molecule will have travelled up slightly more potential hill than the synchronous molecule and so will have decelerated slightly more than it. This will continue in successive field stages until $v < v_{sync}$ and $\phi < \phi_{sync}$. The molecule then experiences less potential hill in a field stage and so is decelerated less than the synchronous molecule. The synchronous molecule decelerates relative to the asynchronous molecule in question: the latter then catches up until $v > v_{sync}$ and $\phi > \phi_{sync}$. In this way molecules with phase and speed close to that of the synchronous molecule oscillate about ϕ_{sync} and v_{sync} in longitudinal phase space (v - ϕ space).

To analyse this motion more quantitatively consider the energy change experienced by molecules in one deceleration stage. A decelerator switches between two electric field states (see figure 5.4 for example). In a given state the Stark shift profile along the beam-line, expressed in terms of phase, $W_s(\phi)$, can be expanded as a Fourier series [72]. The phase has been defined such that $W_s(\phi)$ is antisymmetric about $\phi = 0$. $W_s(\phi)$ is thus an odd function and so its expansion comprises only sine terms:

$$W_s(\phi) = \frac{1}{2}W_s(0) + \sum_{n=1}^{\infty} a_n \sin n\phi. \quad (5.4)$$

The difference in Stark energy between a given instantaneous phase, ϕ , and the phase half a period away, $(\phi + \pi)$, can be evaluated using the Fourier expansion for the Stark potential along the length of the decelerator (in one field state):

$$\begin{aligned} \Delta W_s(\phi) &= \sum_{n=1}^{\infty} a_n (\sin(n\phi) - \sin(n\phi - \pi)) \\ &= 2 \sum_{n=1}^{\infty} a_n \sin(n\phi). \end{aligned} \quad (5.5)$$

Bethlem *et al.* [72] observed that when the spacing between two adjacent field stages is similar to the spacing between the electrodes of a field stage the first term in equation 5.5

dominates. Consider for now only this first term. The kinetic energy lost by the phase synchronous molecule in one deceleration stage is

$$\Delta W_s(\phi_{sync}) = W_s(\phi_{sync}) - W_s(\phi_{sync} - \pi) \approx 2a_1 \sin \phi_{sync}. \quad (5.6)$$

In a given decelerator field state the synchronous molecule travels a constant distance, L , the end-point of which is chosen by the choice of ϕ_{sync} , which is constant for a given deceleration sequence. The overall effect of the decelerator on the synchronous molecule (mass, m_{mol}) can be modelled in terms of a continuously-acting, average force:

$$\begin{aligned} \bar{F}_{sync} &= -\frac{\Delta W_s(\phi_{sync})}{L} = -\frac{2a_1}{L} \sin \phi_{sync} \\ &= m_{mol} \frac{d^2 z}{dt^2} = \frac{m_{mol} L}{\pi} \frac{d^2}{dt^2} \phi_{sync}. \end{aligned} \quad (5.7)$$

Now consider a slightly non-synchronous molecule with longitudinal speed v_{ns} and phase ϕ_{ns} . The differences between the instantaneous phase and speed of the synchronous and non-synchronous molecules are very small: $\Delta v = v_{ns} - v_{sync} \ll v_{sync}$ and $\Delta \phi = \phi_{ns} - \phi_{sync} \ll \pi$. Consequently it can be assumed that during one field state the non-synchronous molecule travels a distance almost equal to L . The effective average force exerted on this molecule over the length of the decelerator is

$$\begin{aligned} \bar{F}_{ns} &\approx -\frac{\Delta W_s(\phi_{ns})}{L} \\ &\approx -\frac{2a_1}{L} \sin \phi_{ns} \\ &= \frac{m_{mol} L}{\pi} \frac{d^2 \phi_{ns}}{dt^2}. \end{aligned} \quad (5.8)$$

Subtracting equation 5.7 from equation 5.8 yields the equation of motion of the non-synchronous molecule relative to the synchronous molecule:

$$\frac{m_{mol} L}{\pi} \frac{d^2}{dt^2} \Delta \phi = \frac{-2a_1}{L} \left(\sin(\phi_{sync} + \Delta \phi) - \sin \phi_{sync} \right). \quad (5.9)$$

For small $\Delta \phi$ equation 5.9 simplifies to

$$\frac{m_{mol} L}{\pi} \frac{d^2}{dt^2} \Delta \phi = \frac{-2a_1 \cos(\phi_{sync})}{L} \Delta \phi. \quad (5.10)$$

Equation 5.10 describes harmonic oscillation of the non-synchronous molecule's phase about ϕ_{sync} , with harmonic angular frequency $\omega = \sqrt{2\pi a_1 \cos(\phi_{sync})/m_{mol} L^2}$. For a given synchronous phase there will be an area of longitudinal $\Delta \phi$ - Δv phase-space for which any molecule falling inside this area will oscillate about the phase-synchronous molecule.

To investigate this phase-space stability more thoroughly consider the equation for energy loss per stage (equation 5.5) with all the expansion terms. Combining the equations of motion for a synchronous and non-synchronous molecule as was done for equations 5.7

and 5.8 renders the following equation of motion for the non-synchronous molecules relative to the synchronous molecule:

$$\begin{aligned} \frac{m_{mol}L}{\pi} \frac{d}{dt^2} \Delta\phi^2 &= -\frac{1}{L} \left(\Delta W_s(\phi_{ns}) - \Delta W_s(\phi_{sync}) \right) \\ &= -\frac{2}{L} \sum_{\text{odd } n} a_n \left[\sin(n\phi_{sync} + n\Delta\phi) - \sin(n\phi_{sync}) \right]. \end{aligned} \quad (5.11)$$

Analytical solutions to this equation can be found [44] by noting that the speed of the nonsynchronous molecule relative to the synchronous one is $\Delta v = \frac{L}{\pi} \left(\frac{d}{dt} \Delta\phi \right)$ and that:

$$\begin{aligned} \Delta v &= \frac{L}{\pi} \frac{d}{dt} \Delta\phi = \frac{d\Delta\phi}{d\Delta v} \frac{d\Delta v}{dt} = \frac{L^2}{\pi^2} \frac{d\Delta\phi}{d\Delta v} \frac{d^2}{dt^2} \Delta\phi \\ \Rightarrow \frac{d^2}{dt^2} \Delta\phi &= \frac{\pi^2}{L^2} \Delta v \frac{d\Delta v}{d\Delta\phi}. \end{aligned} \quad (5.12)$$

Equation 5.11 can thus be rearranged and integrated:

$$\begin{aligned} \int \pi m_{mol} \Delta v \, d\Delta v + \int 2 \sum_{\text{odd } n} a_n [\sin(n\phi_{sync} + n\Delta\phi) - \sin(n\phi_{sync})] d\Delta\phi &= 0 \\ \Rightarrow \frac{1}{2} m_{mol} \Delta v^2 - \frac{2}{\pi} \sum_{\text{odd } n} a_n \left[\frac{1}{n} \cos(n\phi_{sync} + n\Delta\phi) + \Delta\phi \sin(n\phi_{sync}) \right] &= W_{init}. \end{aligned} \quad (5.13)$$

This equation describes the relative longitudinal motion of a non-synchronous molecule that enters the decelerator with total longitudinal kinetic energy, W_{init} . Equation 5.13 shows that the total longitudinal energy of a non-synchronous molecule (relative to that of the synchronous molecule) is shared between kinetic energy and an effective potential energy:

$$W_{pot} = -\frac{2}{\pi} \sum_{\text{odd } n} a_n \left[\frac{1}{n} \cos(n\phi_{sync} + n\Delta\phi) + \Delta\phi \sin(n\phi_{sync}) \right], \quad (5.14)$$

with the energy oscillating between kinetic and potential energy as the molecule oscillates about the synchronous molecule in phase space. The stable trajectories confined by this potential well have constant energy contours in phase space which circulate about the $\{\Delta\phi, \Delta v\} = \{0, 0\}$ origin. Figure 5.14 shows W_{pot} (in GHz) for $\phi_{sync} = 0, \pi/6$ and $\pi/3$, calculated with only the first term in the Fourier expansion ($n = 1$) and with $a_1 = -23.9$ GHz, which is a realistic expansion coefficient for a weak-field decelerator (see section 5.6.2). The $n = 1$ potential energy has turning points at $\Delta\phi = 0$ and $\Delta\phi = \pi - 2\phi_{sync}$. A negative value of a_1 makes the $\Delta\phi = 0$ turning point a minimum and the $\Delta\phi = \pi - 2\phi_{sync}$ turning point a maximum.

Figure 5.14 shows that as ϕ_{sync} is increased the potential energy well depth decreases, with the maximum at $\Delta\phi = \pi - 2\phi_{sync}$ becoming less prominent. This makes sense physically. The argument for phase-space stability relies on a molecule at some phase ahead of ϕ_{sync} being decelerated down the Stark potential hill back towards the phase stable molecule. However, as the phase stable molecule is located higher up the Stark

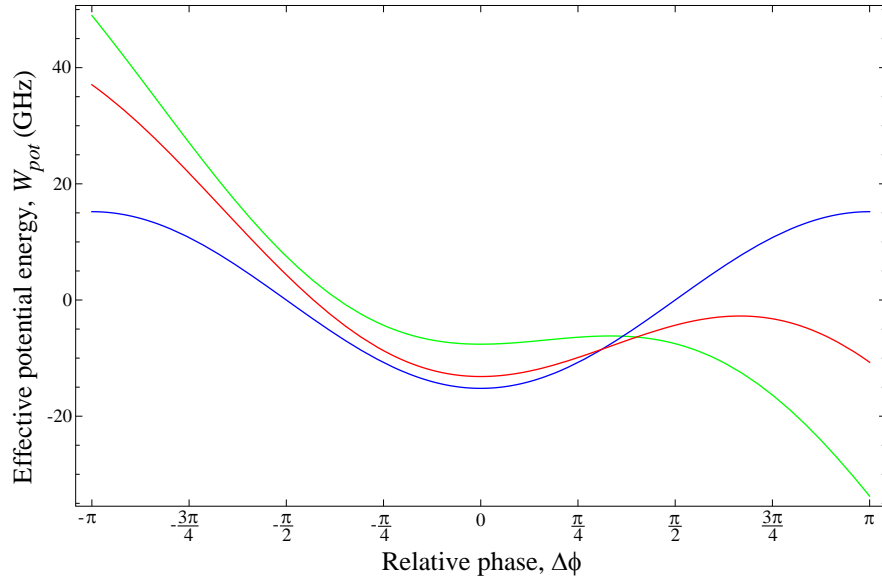


Figure 5.14: Longitudinal effective potential energy, W_{sep} , calculated with $n = 1$ and $a_1 = -23.9$ GHz for $\phi_{sync} = 0$ (blue), $\pi/6$ (red) and $\pi/3$ (green).

potential hill, there is less room between the phase synchronous molecule and the top of the potential hill. By the time the fields are switched more of the molecules ahead of the phase synchronous molecule will have gone too far and have passed this peak, after which they will be accelerated down the other side of the potential hill, away from the phase synchronous molecule. When $\phi_{sync} = \pi/2$ all non-synchronous molecules will be accelerated away from the phase synchronous molecule. In this case the turning point in W_{pot} at $\Delta\phi = 0$ is no longer a minimum, it is a point of inflection.

The phase-stable molecules circulate around the phase space origin, on contours of constant total energy. The area of phase space that contains all the possible stable longitudinal trajectories is bounded by the threshold contour, known as the ‘separatrix’. A molecule that reaches the effective potential maximum at $\Delta\phi = \pi - 2\phi_{sync}$ with zero relative speed lies on the separatrix. Substituting in $\Delta v = 0$ and $\Delta\phi = \pi - 2\phi_{sync}$ into equation 5.13 gives the total molecular energy associated with the separatrix to be:

$$W_{sep} = \frac{-2}{\pi} \sum_{\text{odd } n} a_n \left[-\frac{1}{n} \cos(n\phi_{sync}) + (\pi - 2\phi_{sync}) \sin(n\phi_{sync}) \right]. \quad (5.15)$$

Substituting W_{sep} into the right-hand side of equation 5.13 gives the equation of the separatrix:

$$\begin{aligned} \frac{1}{2}m_{mol}\Delta v^2 + \frac{2}{\pi} \sum_{\text{odd } n} a_n \left[\frac{1}{n} \left(\cos(n\phi_{sync} + n\Delta\phi) + \cos(n\phi_{sync}) \right) \right. \\ \left. + (\Delta\phi + 2\phi_{sync} - \pi) \sin(n\phi_{sync}) \right] = 0 \end{aligned} \quad (5.16)$$

The molecules are trapped in a travelling effective potential well defined by the switch-

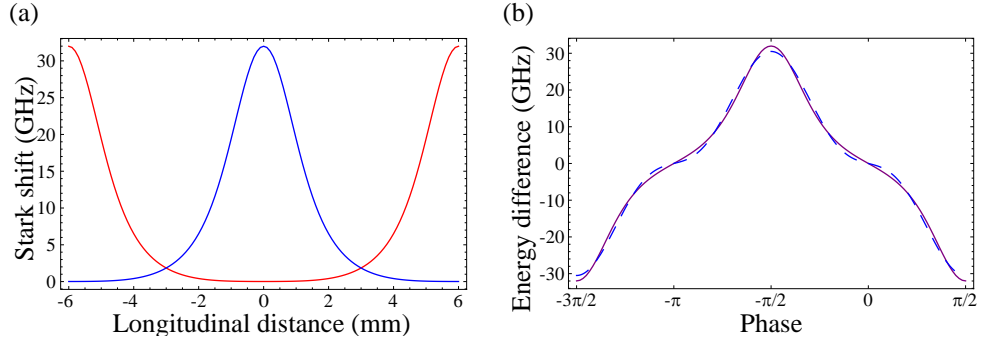


Figure 5.15: (a) The axial Stark shift profile experienced by CaF radicals in the $\mathcal{N} = 4$ state with ± 15 kV applied to the decelerator in state 1 (blue) and state 2 (red). The maximum Stark shift, 31.8 GHz, is acquired in the middle of a charged deceleration stage. (b) The difference between the Stark profiles in (a) (purple line). Also shown is a fit to this difference profile of the first two terms of the Fourier expansion given in equation 5.5 (dashed blue line).

ing electric fields. Deceleration is achieved by varying the switching period such that the potential well slows down, and adiabatically decelerates the trapped molecules.

5.6.2 Longitudinal dynamics in the 100-stage decelerator

The basis of all the equations in the above section is the shape of the axial Stark shift profile, and its expansion as a Fourier series. In particular, the shape of the difference between the Stark shift profiles in electric field states 1 and 2 is of interest.

Figure 5.4 shows the axial electric fields in states 1 and 2 of the 100-stage decelerator with an applied voltage of 15 kV. The resulting Stark shift potentials and their difference are shown in figure 5.15 (a) for CaF in the $|4, 0\rangle$ state, with 15 kV applied to the decelerator. Only the first two terms of the Fourier expansion (equation 5.5) are necessary to provide a sufficiently good description of the energy difference between the two profiles. Figure 5.5 (b) shows the energy difference, as well as a fit to the first two terms of the Fourier expansion. The expansion used in the fit was exactly the same as in equation 5.5, except that the factor of 2 was, in this case, included in the expansion coefficients. These were found to be $a_1 = -23.9$ GHz and $a_3 = 6.6$ GHz. In all the following analysis the difference between the two Stark profiles is taken to be (in GHz):

$$\Delta W_s(\phi) = a_1 \sin(\phi) + a_3 \sin(3\phi) = -23.9 \sin(\phi) + 6.6 \sin(3\phi) \quad (5.17)$$

Equation 5.13 describes the motion of non-synchronous molecules relative to the synchronous molecule. Figure 5.16 shows three solutions to this equation calculated with the decelerator charged to ± 15 kV, and using the above expansion (equation 5.17). Figure 5.16 (a) shows solutions to the relative motion equation with a synchronous phase of

$\phi_{sync} = 0$. This corresponds to no overall deceleration of the synchronous molecule. The closed trajectories around the origin correspond to the oscillation of molecules that are confined by the effective longitudinal potential well (figure 5.14). The symmetry of this effective potential about $\Delta\phi = 0$ when $\phi_{sync} = 0$ leads to trajectories that are symmetric about the line $\Delta\phi = 0$. The thick black line in figure 5.16 (a) shows the solution of the separatrix equation (equation 5.16) - this line bounds the area of phase space that contains all the confined, stable longitudinal trajectories. Trajectories that lie outside the separatrix correspond to molecules that do not oscillate about the synchronous molecule. These trajectories are modulated by the effective potential, but are not bound by it. The separatrix bounds a phase-space area between $\Delta\phi = \pm\pi$ (relative position ± 3 mm). At relative positions greater than this the figure shows new separatrices, bounding trajectories centred on $\Delta\phi = \pm 2\pi$. There are in fact many such separatrices, centred on $\Delta\phi = \pm 2n\pi$, where $n = 0, 1, 2, \dots$. These other separatrices define areas of phase space which correspond to molecules that are confined longitudinally by the switching Stark potential, but not in the same potential well as the synchronous molecules. The periodicity of the decelerator allows for molecules to be confined by the deceleration stages ahead of and behind that occupied by the synchronous molecule. In the case of $\phi_{sync} = 0$ each separatrix is joined to its nearest neighbours. Figure 5.16 (b) shows the solutions of the relative motion equation with $\phi_{sync} = \frac{\pi}{6}$. In this case the effective potential is no longer symmetric about $\Delta\phi = 0$ (figure 5.14) and is shallower, providing less of a potential barrier for $\Delta\phi > 0$. There are thus fewer stable trajectories, as can be seen by the smaller area bounded by the separatrix. The separatrix now covers a smaller range of relative positions, as those molecules far away from the synchronous molecule at the moment of switching will be accelerated towards another potential well and thus repelled from the synchronous molecule's position. The trajectories outside the separatrix show exactly this behaviour: the molecule's phase-space trajectory can make a "sling-shot" around the phase-space origin, but when the molecule is accelerated towards the synchronous molecule it overshoots towards the next potential well along. This effect is increased further at higher synchronous phase angles. Figure 5.16 (c) shows the solutions to the relative motion equations with a synchronous phase of $\phi_{sync} = \frac{\pi}{3}$. The central separatrix is now considerably smaller than in the previous two cases, leading to relatively few confined trajectories. The effective potential is now very shallow. At a synchronous phase of $\pi/2$ the synchronous molecule is at the top of the Stark potential hill when the fields are switched. All the non-synchronous molecules are accelerated away from the peak of the Stark potential and thus away from the synchronous molecule. The separatrix in this case is simply a point located at the phase-space origin.

For a given applied voltage and synchronous phase the number of molecules that can be confined about the synchronous molecule is proportional to the area bounded by the separatrix. This area, known as the longitudinal 'acceptance', is shown in figure 5.17

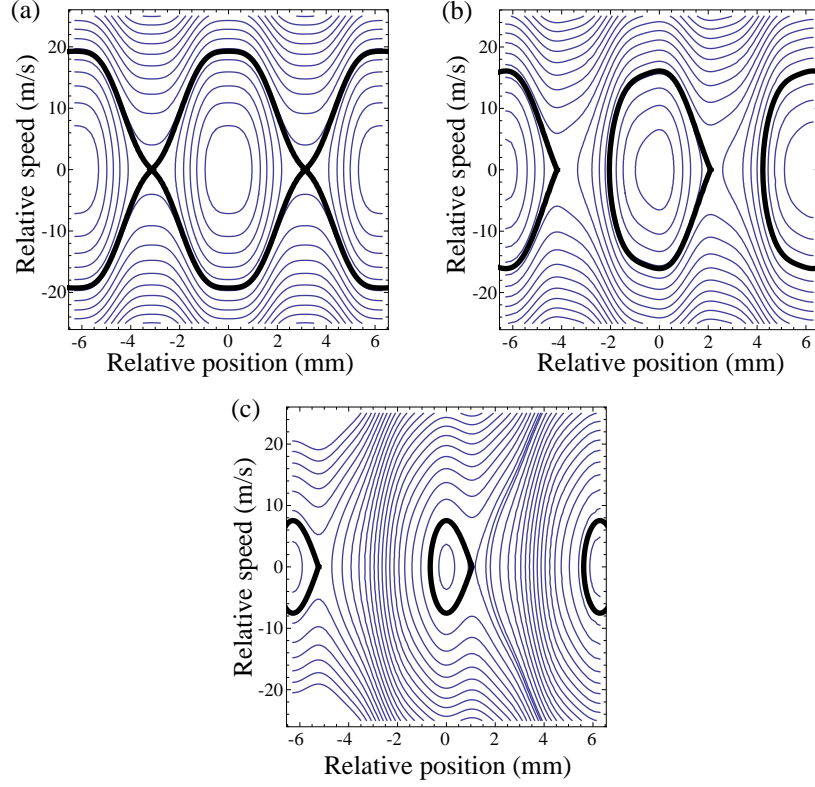


Figure 5.16: Trajectories in phase space obtained by solving the equation of motion for molecules relative to the synchronous molecule (equation 5.13). The equations were solved with the fields generated inside the decelerator with ± 15 kV applied to the electrodes. The synchronous phase is (a) $\phi_{sync} = 0$; (b) $\phi_{sync} = \frac{\pi}{6}$; (c) $\phi_{sync} = \frac{\pi}{3}$. The thick, black lines are the separatrices that bound the area of phase space containing those trajectories confined by the effective longitudinal potential well, and that correspond to molecules oscillating about the synchronous molecule in phase space.

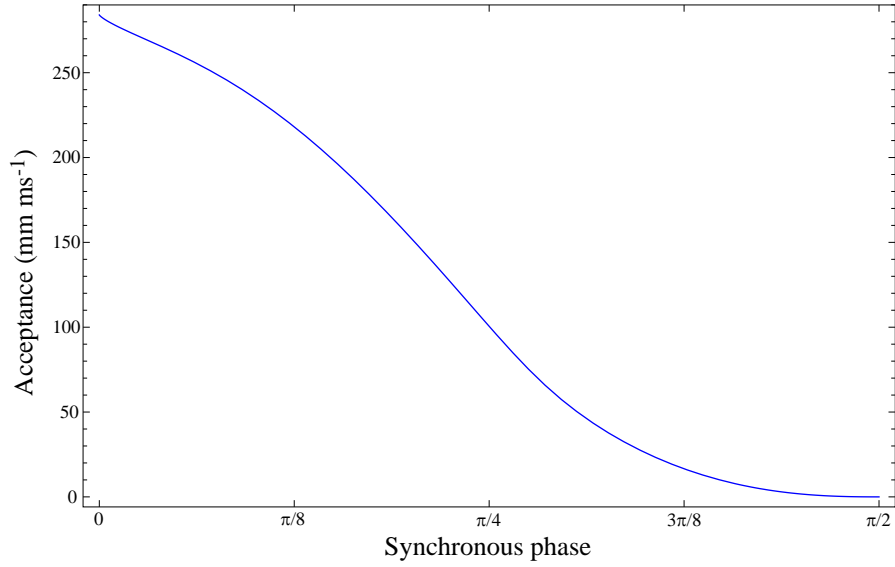


Figure 5.17: The longitudinal acceptance of the weak-field decelerator with ± 15 kV applied to the electrodes. The acceptance is the area bounded by the separatrix, calculated at a given synchronous phase by solving equation 5.16.

as a function of synchronous phase for the 100-stage decelerator charged to ± 15 kV. The acceptance was calculated by solving the equation of the separatrix for a range of synchronous phases, and then integrating to find the bounded area in each case. As expected the acceptance is maximal when $\phi_{sync} = 0$, decreases as the synchronous phase is increased, and reaches zero at $\phi_{sync} = \frac{\pi}{2}$.

5.7 Preliminary deceleration results

Figure 5.18(a) shows recorded time-of-flight (TOF) profiles for a Xe-carried beam of CaF. The data were taken with the decelerator switching between DC guiding mode and burst mode on a shot-to-shot basis, with the DC guiding signal serving as a reference signal. The decelerator was operated with $V_{HI} = 14$ kV and V_{LO} was ground. The black time-of-flight profile is the DC guiding signal. It has been scaled such that it has unity amplitude. A gaussian fit finds the central profile time to be $2194 \mu\text{s}$, corresponding to a central peak speed of 369 ms^{-1} , and the width to correspond to a longitudinal translational temperature of 5.1 K . The blue profile is the burst signal, scaled by the same factor used to normalize the DC guiding profile. For these data the high voltage switching pattern was calculated for $v_{sync} = 370 \text{ ms}^{-1}$ and $\phi_{sync} = 0$. This phase angle corresponds to no overall deceleration. The switching electric field will thus guide molecules travelling at 370 ms^{-1} , as well as all the phase-stable molecules (those travelling close enough to 370 ms^{-1} that their phase-space trajectories fall inside the separatrix). This is exactly

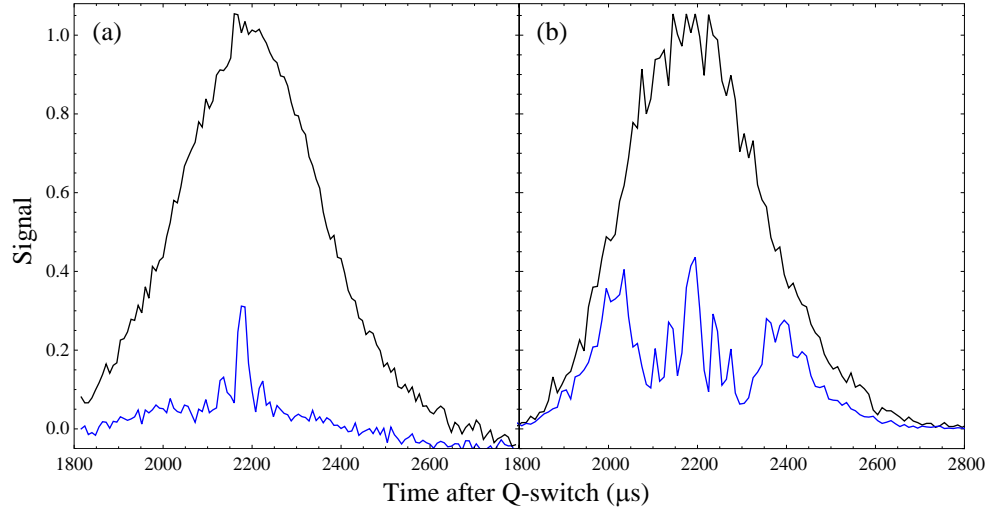


Figure 5.18: (a) Experimental time-of-flight profiles measured with the decelerator used in burst mode (blue line) and DC guiding mode (black line), with $V_{LO} = 0$, $V_{HI} = 14$ kV. In burst mode the high voltage switching pattern was calculated for synchronous molecules with an initial speed of 370 ms^{-1} and a phase angle of 0° . Both profiles have been scaled by the same factor such that the DC profile has unity amplitude. (b) Numerical simulations of the experimental data shown in (a).

what the data show. The time-of-flight profile has a peak at $2183 \mu\text{s}$, corresponding to a speed of 371 ms^{-1} , with a width determined by the phase-stable non-synchronous molecules. The profile also shows two smaller ‘satellite’ peaks around the central peak. These correspond to molecules that have been trapped in the potential wells ahead of and behind that of the synchronous molecule. The pulsed molecular beam is long enough that there will be molecules travelling at the synchronous molecule’s speed entering the decelerator before and after the entry time for which the pattern was calculated. These molecules will still be trapped by the longitudinal effective potential, but in different wells from the synchronous molecule. There are no other significant peaks in the measured time-of-flight profile. The three peaks sit on a relatively small background, indicating that the non-synchronous molecules which fall outside the separatrices are not strongly guided. This is not as expected. These non-phase-stable molecules are not trapped in the effective potential well, but should still be guided by the transverse electric field minimum along the beam-line axis. In a very naive model it might be expected that the guided signal from these molecules should be approximately one half the magnitude of the DC guided profile. The reason for this is that when the decelerator is used in DC guiding mode all the field stages are charged at the same time, whereas in burst mode, at a given time, only half the stages are charged. Therefore, in burst mode the time-averaged electric field along the transverse directions is approximately half as strong as in DC guiding mode,

which reduces the depth of the Stark potential well.

In order to investigate the disparity between expectations and experimental results, numerical simulations were performed that model the experimental procedure. The simulation starts with an ensemble of molecules at the source which are then propagated through the skimmer and towards the decelerator. The molecules are then propagated through the decelerator. The equations of motion of the molecules inside the decelerator are solved, and any molecule that crashes into an electrode or leaves the decelerator, never to return, is removed from the simulation. Those molecules that do make it out are then propagated to the detection region, where their interaction with the laser beam is simulated, with each molecule modelled as a three-level system (a simplification of the model described in chapter 4). The number of molecules detected as a function of time then makes up the simulated time-of-flight profile. Figure 5.18 (b) shows the results of simulations that match the experimental conditions under which the data shown in figure 5.18 (a) were taken. The simulated DC guiding and burst mode profiles were both scaled by the same factor that gives the simulated DC guiding profile a unity amplitude. Thus figures 5.18 (a) and (b) are directly comparable. However, the two burst profiles show a number of differences. The simulation predicts a central bunch of molecules arriving around $2187 \mu\text{s}$, as measured. However, the simulated peak is larger than the experimentally measured peak, with an area approximately 1.5 times greater. The same is true of the satellite peaks, with the simulation predicting peaks much larger than the experimental peaks. The simulation also shows two further satellite peaks, further from the central peak, neither of which was observed experimentally. However, the most striking difference between the two figures is the signal from the non-phase-stable molecules. The simulated time-of-flight profile shows two large, broad peaks away from the central phase-stable peaks.

In addition to the above $\phi_{\text{sync}} = 0$ data, deceleration data (for which $\phi_{\text{sync}} > 0$) were also taken at this voltage. Figure 5.19 (a) shows the recorded time-of-flight profiles measured under the same conditions as in figure 5.18 (a), except in this case the applied high voltage switching pattern was for $v_{\text{sync}} = 350 \text{ ms}^{-1}$ and $\phi_{\text{sync}} = 75^\circ$. When there is no deceleration, molecules travelling at 350 ms^{-1} should be detected at $2314 \mu\text{s}$. Deceleration of this velocity class will thus deplete the measured time-of-flight profile around this time and move the associated molecules to a later time. This was indeed observed. The arrow in figure 5.19 (a) is at $2314 \mu\text{s}$, where a dip in signal can be observed. A small peak of molecules is observed at $2415 \mu\text{s}$, corresponding to the decelerated molecules. The rest of the measured time-of-flight profile consists of a small, broad peak of non-phase-stable molecules guided by the decelerator. As in figure 5.18 (a) the measured non-phase-stable signal is much smaller than expected. Figure 5.19 (b) shows the results of simulations of this deceleration. The simulation shows a decelerated peak at $2426 \mu\text{s}$, which corresponds

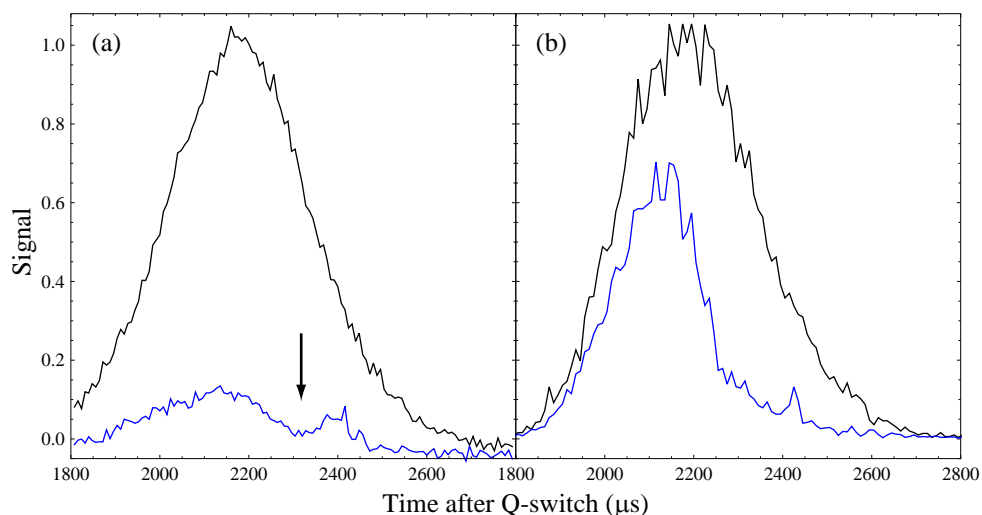


Figure 5.19: (a) Experimental time-of-flight profiles measured under the same conditions as the data in figure 5.18 (a), except now the high voltage switching pattern used to acquire the burst profile (blue line) was calculated to decelerate synchronous molecules of initial speed 350 ms^{-1} and with phase angle $\phi_{sync} = 75^\circ$. The detection time of non-decelerated molecules with speed 350 ms^{-1} is identified by an arrow. Both profiles have been scaled by the same factor such that the DC guided profile (black line) has a unity amplitude. (b) Simulated profiles produced by numerical simulations of the deceleration shown in (a).

to a deceleration from 350 ms^{-1} to 316 ms^{-1} . The simulated deceleration peak arrives at a slightly later time than the experimental peak. An explanation for this slight disparity is given in section 5.10. However, as with the $\phi_{sync} = 0$ data the greatest disparity between experiment and simulation occurs for the non-phase-stable molecules. The simulation predicts a signal from these molecules considerably greater than measured, with signals almost as great as the DC guided signal for a wide range of times. Integration of the simulated and experimental time-of-flight profiles shows that the simulation predicts a total molecular flux seven times greater than measured.

5.8 Non-adiabatic transitions

So why are the recorded time-of-flight signals so much smaller than the simulations predict? The answer lies in the changing electric field inside the decelerator. As a molecule travels along the decelerator it experiences a sequence of switching electric fields. In order to maintain its orientation the fields must change slowly enough for the molecule to follow the change adiabatically. If the fields change too rapidly they can drive non-adiabatic transitions between different rigid rotor states. Additionally, if the fields are weak at some position when they are changing, the magnetic sub-levels of a given rigid rotor state ap-

proach degeneracy, and it is thus more likely that such a transition can be driven. As has been discussed above, the electric field inside the decelerator has two alternating field states, E_1 and E_2 . During the switch from one state to the next, the field associated with one state decays exponentially, while the other rises, both changes occurring simultaneously, with the same time constant, τ . Not only does the field change in magnitude during the switch, it also rotates. On the axis of the machine (the beam-axis), E_1 and E_2 are orthogonal, and so the field must rotate through 90° when the switch is thrown. It might be possible for the rapidly switching fields to drive non-adiabatic transitions from the desired rigid rotor state to some other state, with a different Stark shift, possibly even to a strong-field seeking state. These states might not be guided as efficiently as the chosen state (the strong-field seeking states are not guided at all, they are repelled away from the beam-line). This transition mechanism was considered a likely candidate for the reduced measured signal. The simulations do not allow for the possibility of a molecule changing state and so represent the ideal time-of-flight profiles. The following analysis describes the physics of the switching fields and considers the likelihood of the field driving non-adiabatic transitions.

5.8.1 The Hamiltonian in a rotated coordinate system

The Hamiltonian of a rigid rotor in the time-varying field of the decelerator is:

$$\hat{H}(t) = B\hat{N}^2 - \mu E_1 \exp(-t/\tau) \hat{C}_0^{(1)} - \frac{\mu E_2}{\sqrt{2}} (1 - \exp(-t/\tau)) (\hat{C}_{-1}^{(1)} - \hat{C}_{+1}^{(1)}), \quad (5.18)$$

where \hat{N}^2 is the rotation operator, the eigenstates of which are the field-free rigid rotor states, and the last two terms are the Stark interaction terms (see section 2.4) associated with the two electric fields. The Hamiltonian has been written in terms of components of the rank 1 spherical harmonic operator, $\hat{C}_q^{(1)} = \sqrt{\frac{4\pi}{3}} \hat{Y}_q^{(1)}$ (as discussed in section 2.4). The origin of time is defined as the moment that the switches are thrown. It will prove instructive to write the time-dependent Hamiltonian in a rotated coordinate system such that at time t the electric field vector points along the z' -axis of the rotated frame. In this case the Hamiltonian is

$$\hat{H}'(t) = B\hat{N}^2 - \mu E(t) \hat{C}_0^{(1)}. \quad (5.19)$$

The electric field rotates about the y -axis with angular rate $\omega(t) = \frac{d\beta(t)}{dt}$, and at time t the electric field vector has rotated through an angle, $\beta(t)$. The two Hamiltonians are related by the rotation operator, $\hat{D} = \exp\left(-\hat{N}_y \beta(t)/\hbar\right)$, through the relation $\hat{H}(t) = \hat{D}^{-1} \hat{H}'(t) \hat{D}$. Before the switch begins a molecule inside a deceleration stage is in some Stark-shifted rigid rotor state $|\mathcal{N}, M_N\rangle$. During the switch the molecule is in the time-dependent state $|\alpha\rangle$ (where the time-dependence is implicit). This state can be written as a linear superposition

of the Stark-shifted rigid rotor states, with time-varying expansion coefficients, $\langle \mathcal{N}, M_N | \alpha \rangle$:

$$|\alpha\rangle = \sum_{\mathcal{N}, M_N} |\mathcal{N}, M_N\rangle \langle \mathcal{N}, M_N | \alpha \rangle. \quad (5.20)$$

The time-variation of $|\alpha\rangle$ is determined by the time-dependent Schrödinger equation. This analysis is detailed in appendix C, resulting in a differential equation governing the evolution of the above expansion coefficients (equation C.9). This equation is now rewritten here, but, for clarity, the rigid rotor quantum numbers, $\{\mathcal{N}, M_N\}$ are now represented by the index m , and the expansion coefficients are written $c_m(t) = \langle \mathcal{N}, M_N | \alpha \rangle$:

$$W_{m'} c_{m'}(t) + \sum_m \langle m' | \left(\omega(t) \hat{N}_y - \frac{i}{\omega_{sep}} \frac{\partial}{\partial t} \hat{H}'(t) \right) | m \rangle c_m = i\hbar \frac{\partial}{\partial t} c_{m'}(t), \quad (5.21)$$

where $W_{m'}$ is an eigenenergy of $\hat{H}'(t)$, evaluated at time, t , and $\omega_{sep} = (W_m - W_{m'})/\hbar$ is the angular frequency separation of any two rigid rotor states in the expansion. Equation 5.21 describes the effect of the field-switch in terms of the changing field magnitude and the field rotation.

The effects of the two operators in the matrix element of equation 5.21 can be treated using time-dependent perturbation theory. The expansion coefficients are expanded as a power series:

$$c_n(t) = c_n^{(0)}(t) + c_n^{(1)}(t) + c_n^{(2)}(t) + \dots \quad (5.22)$$

The evolution of $|\alpha\rangle$ can be treated approximately by considering only the first order term in this expansion, $c_n^{(1)}(t)$. A standard result in first order time-dependent perturbation theory (see [49] for example) is that, for a system perturbed by some interaction with Hamiltonian, $\hat{H}_{pert}(t)$, the time-evolution of the first order expansion term is given by:

$$c_n^{(1)}(t) = \frac{-i}{\hbar} \int_0^t \exp(i\omega_{ni}t') H_{ni}(t') dt', \quad (5.23)$$

where $|n\rangle$ and $|i\rangle$ are the unperturbed eigenstates with energies E_n and E_i , $\omega_{ni} = (E_n - E_i)/\hbar$, and $H_{ni}(t) = \langle n | \hat{H}_{pert}(t) | i \rangle$.

In order to investigate analytically the effect of the two perturbing terms in equation 5.21 consider now the ‘worst-case scenario’ that occurs under typical operation of the decelerator. This analysis will show, to first order, the relative scale and form of the perturbations.

5.8.2 The effect of the changing field magnitude

Consider first the term associated with the changing electric field magnitude, $\frac{i}{\omega_{sep}} \frac{\partial}{\partial t} \hat{H}'(t)$. For a given rate of change of electric field the associated matrix element, which joins states $|\mathcal{N}, M_N\rangle$ and $|\mathcal{N}', M'_N\rangle$ (separated by $\hbar\omega_{sep}$) can, with the help of equation 5.19, be written as

$$\langle \mathcal{N}', M'_N | \frac{i\mu}{\omega_{sep}} \frac{dE(t)}{dt} \hat{C}_0^{(1)} | \mathcal{N}, M_N \rangle. \quad (5.24)$$

It is known from the properties of spherical tensors (section 2.4) that the above matrix element is zero unless $M'_N = M_N$. Thus, this perturbation can only drive transitions between states of different \mathcal{N} , but the same M_N . To analyse the effect of this perturbation consider the typical time-variation of E , $\frac{dE}{dt}|_{max} \sim E_{max}/\tau$, where E_{max} is the maximum electric field inside the decelerator, and let the matrix element, $\langle \mathcal{N}', M'_N | C_0^{(1)} | \mathcal{N}, M_N \rangle$, take its maximum value, which is 1. In this approximation of constant (but large) time-variation of electric field, time-dependent perturbation theory can be used with a constant perturbation that ‘turns on’ at time $t = 0$. Integrating equation 5.23 thus gives:

$$c_n^{(1)}(t) = \frac{\mu}{\hbar\omega_{sep}} \frac{E_{max}}{\tau} \int_0^t \exp(i\omega_{sep}t') dt' = \frac{i\mu E_{max}}{\hbar\omega_{sep}^2\tau} \left[1 - \exp(i\omega_{sep}t) \right]. \quad (5.25)$$

The probability of the molecule being transferred by the changing field magnitude from some initial state, $|\mathcal{N}, M_N\rangle$ to $|\mathcal{N}', M'_N\rangle$ is thus given by the square modulus of $c_n(t)$:

$$\begin{aligned} |c_n^{(1)}|^2 &= 2 \left(\frac{\mu E_{max}}{\hbar\omega_{sep}^2\tau} \right)^2 \left(1 - \cos(\omega_{sep}t) \right) \\ &\leq 4 \left(\frac{\mu E_{max}}{\hbar\omega_{sep}^2\tau} \right)^2. \end{aligned} \quad (5.26)$$

The voltage switching pattern used with the 100-stage decelerator was calculated to decelerate molecules in the $|4, 0\rangle$ state. It was shown in section 2.4 that the maximum Stark shift of the states $|\mathcal{N}, 0\rangle$ follows roughly quadratic behaviour in \mathcal{N} : $E_{max} \approx \frac{2.46B}{\mu} \mathcal{N}^2$ (figure 2.2). The smallest value of ω_{sep} between two states, $|\mathcal{N}, 0\rangle$ and $|\mathcal{N}', 0\rangle$, occurs as $E \rightarrow 0$, and for $\mathcal{N}' = \mathcal{N} - 1$; this angular frequency being $\omega_{sep} = 4\pi B\mathcal{N}/\hbar$. Putting these expressions into equation 5.26 gives the probability of the changing electric field magnitude driving a transition from state $|\mathcal{N}, 0\rangle$ to $|\mathcal{N} - 1, 0\rangle$ to be

$$c_{(\mathcal{N}-1)}^{(1)} = \left(\frac{2.46\hbar}{8\pi^2 B\tau} \right)^2. \quad (5.27)$$

For CaF, $B = h \times 10.3$ GHz. τ has been measured to be around 500 ns. These values result in a transition probability of order 10^{-12} . Consequently transitions driven by the changing electric field magnitude can be ignored, and are not the cause of signal loss along the decelerator.

5.8.3 The effect of the electric field rotation

Consider now the rotation of the electric field. A standard result from angular momentum theory [49] is that the angular momentum ladder operators are diagonal in N , but not in M_N :

$$\langle \mathcal{N}', M'_N | \hat{N}_{\pm} | \mathcal{N}, M_N \rangle = \hbar \sqrt{(N \mp M_N)(N \pm M_N + 1)} \delta_{\mathcal{N}'N} \delta_{M'_N, M_N \pm 1}. \quad (5.28)$$

The rotation of the field is described by the operator, $\hat{N}_y = \frac{-i}{2}(\hat{N}_+ - \hat{N}_-)$. The matrix elements associated with the rotating field are thus those of the ladder operators, which are standard results.

Using the expansion in terms of field-free rigid rotor states,

$$|\mathcal{N}, M_N\rangle = \sum_N |N, M_N\rangle \langle N, M_N | \mathcal{N}, M_N\rangle, \quad (5.29)$$

the matrix elements are found to be:

$$\begin{aligned} \langle \mathcal{N}, M_N \pm 1 | \hat{N}_y | \mathcal{N}, M_N \rangle &= \mp \frac{i\hbar}{2} \sum_N \sqrt{(N \mp M_N)(N \pm M_N + 1)} \\ &\times \langle \mathcal{N}, M_N \pm 1 | N, M_N \pm 1 \rangle \langle N, M_N | \mathcal{N}, M_N \rangle. \end{aligned} \quad (5.30)$$

The effect of the rotation is described in the same manner as above: evaluate the first order perturbation term at a given rotation rate, ω . It will be shown below that transitions are more likely to occur in regions of weak field when the magnetic sub-levels are closely-spaced. In this regime the Stark interaction is weak and so the mixing of different N states is weak. Thus the sum in equation 5.30 is dominated by a single term, the one with $N = \mathcal{N}$, for which the expansion coefficient $\langle N, M_N | \mathcal{N}, M_N \rangle \approx 1$. For a given angular rotation rate, the equation for $c_{\pm 1}^{(1)}$, which links some initial state, $|\mathcal{N}, M_N\rangle$ to a final state, $|\mathcal{N}, M_N \pm 1\rangle$ (separated by $\hbar\omega_{sep}$), is thus found to be:

$$c_{\pm 1}^{(1)} = \frac{-\omega}{\hbar\omega_{sep}} \langle \mathcal{N}, M_N \pm 1 | \hat{N}_y | \mathcal{N}, M_N \rangle \left[1 - \exp(i\omega_{sep}t) \right]. \quad (5.31)$$

The transition probability between two magnetic sub-levels, $|\mathcal{N}, M_N\rangle$ and $|\mathcal{N}, M_N \pm 1\rangle$ therefore satisfies:

$$|c_{\pm 1}^{(1)}|^2 \leq 4 \frac{\omega^2}{\omega_{sep}^2} (\mathcal{N} \mp M_N)(\mathcal{N} \pm M_N + 1). \quad (5.32)$$

Equation 5.32 shows that when the rotation rate is comparable to the splitting of two adjacent magnetic sub-levels there is a sizeable probability of driving a transition between them.

Figure 5.20 shows the calculated angular rotation rate of the electric field, ω , on the beam-line axis at five positions in longitudinal phase-space. The phase angle is defined as $\phi = \pi z/L$, with an origin as shown in figure 5.4. The rates were calculated as a function of time, with the origin of time being the start of the field switch, the decelerator charged to ± 15 kV, and a switching time constant of $\tau = 500$ ns. Also shown is the calculated angular frequency separation, ω_{sep} , of the $|4, 0\rangle$ and $|4, 1\rangle$ states during the switch at these five longitudinal positions. Figure 5.20 (a) shows ω and ω_{sep} at the position $\phi = -\pi/2$. At this position, before the switch the electric field magnitude is small (see the electric field profile, E_1 , in figure 5.4). After the switch the field magnitude is large (profile E_2 in figure 5.4). Figure 5.20 (a) shows that the rotation rate is at its greatest during early

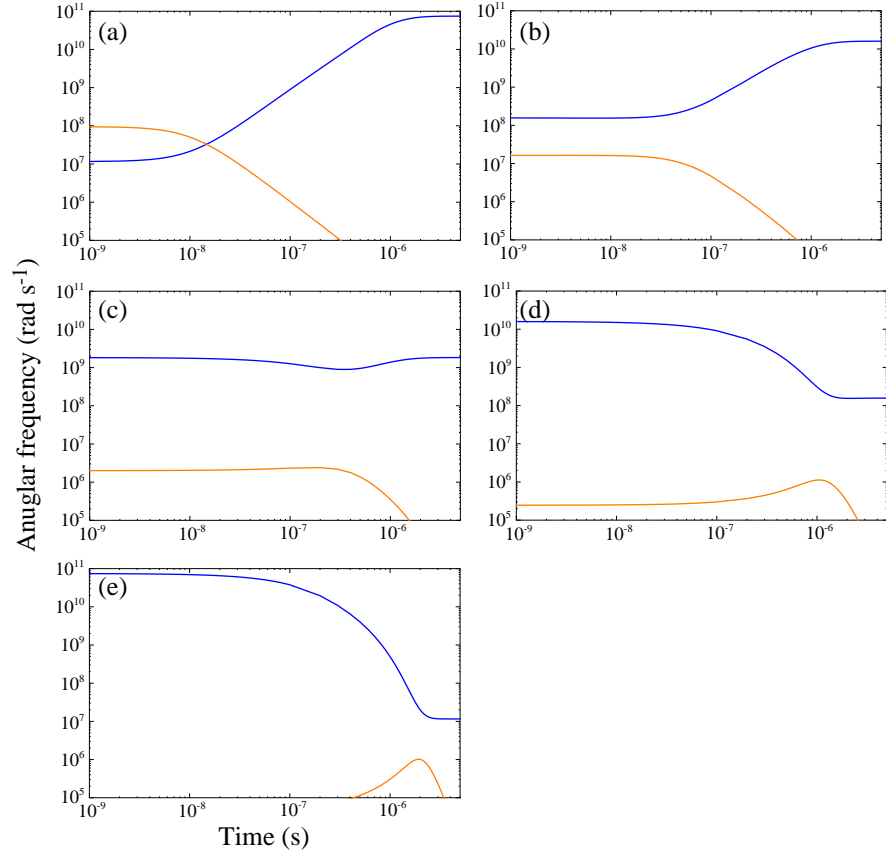


Figure 5.20: The angular rotation rate, ω , of the electric field inside the decelerator when charged to ± 15 kV (orange line). The rotation rate was calculated as a function of time, where the origin corresponds to the beginning of a field switch, and the time constant was $\tau = 500$ ns. Also shown is the angular frequency separation, ω_{sep} , of the $|4, 0\rangle$ and $|4, 1\rangle$ states as a function of time (blue line). The frequencies were calculated at the following longitudinal phase-space positions: (a) $-\pi/2$, (b) $-\pi/4$, (c) 0, (d) $\pi/4$, and (e) $\pi/2$.

stages of the switch, when the field magnitude is small. As the field is weak during this time the Stark shift is small and so the separation of the magnetic sub-levels is small. Thus, at $\phi = -\pi/2$, during the initial stage of a switch the rotation rate is great (around 10^8 rad s^{-1}) and the frequency separation of the two states under consideration is small (around 10^7 rad s^{-1}). As the frequencies evolve after the switch, ω_{sep} begins to rise as the total field magnitude increases, and ω falls as the field rotation slows down. After 15 ns the two frequencies cross-over and continue to diverge as time progresses. Thus, for at least the first 15 ns there is a high probability of the quickly-rotating field driving a transition from the $|4, 0\rangle$ state desired for deceleration (the state for which the field switching pattern has been generated) to the state $|4, 1\rangle$. This latter state experiences a different (smaller) Stark shift from the former and thus will not be decelerated and guided as efficiently as the former. Figure 5.20 (b) shows the frequencies calculated at $\phi = -\pi/4$. At this position the difference in field strength before and after the switch is smaller than in (a), and this is reflected in the reduced rotation rate, being just over 10^7 rad s^{-1} for the first 20 ns, and then falling afterwards. The greater initial field strength results in a greater initial ω_{sep} than at $\phi = -\pi/2$. For the first 20 ns the two frequencies are similar, with $\omega/\omega_{sep} \sim 0.1$. During this period the transition probability is less than at $\phi = -\pi/2$, but is still significant. Figure 5.20 (c) shows the frequencies calculated at $\phi = 0$. In this case the initial and final electric field strengths are identical, with the total magnitude changing very little during a switch. This results in a roughly constant field rotation rate throughout the switch period, as shown in the figure. Throughout, $\omega \ll \omega_{sep}$ and so there is little transition probability at this position. Figures 5.20 (d) and (e) show the effect of increasing the phase angle further. For $\phi > 0$ the situation is reversed somewhat. In these cases the electric field magnitude starts off large and ends up relatively small. Figures (d) and (e) shows that in these cases the rotation rate is initially small, only rising towards the end of a field switch period (around $1 \mu\text{s}$) when the field is small. As in figures (a) and (b) this period of fast field rotation occurs when the field strength is weak and so the state separation is small. Transitions thus seem likely; however, they are less likely than in the former cases because by this late on in a switch (roughly two time-constants from the start of the switch) the fields are changing relatively slowly in time and so ω is always much smaller than in the former cases (figures 5.20 (a) and (b)), peaking at around $0.05 \omega_{sep}$ around $1 \mu\text{s}$ at $\phi = \pi/2$.

Figure 5.21 shows the time-variation of the M_N populations after a switch. They have been calculated by solving numerically equation 5.21 using the calculated values of $\omega(t)$ and $\omega_{sep}(t)$ and a basis set restricted to the $\mathcal{N} = 4$ states. This restriction is justified by the above analysis which shows that coupling between states of different \mathcal{N} is negligible. Figure 5.21 (a) shows how the populations evolve at the $\phi = -\pi/2$ position. Figure 5.20 (a) shows that, at this position, immediately after a switch $\omega \gg \omega_{sep}$, predicting a high

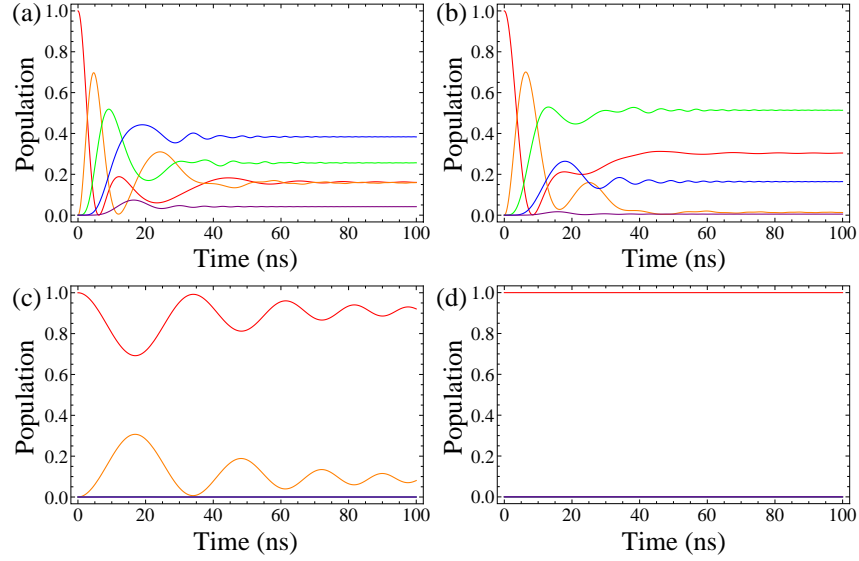


Figure 5.21: The probability of a molecule, initially in the state $|4,0\rangle$, occupying the different magnetic sub-levels of the $N=4$ state as a function of time, where the origin of time is the beginning of a switch, with time-constant 500 ns, and the decelerator is charged to ± 15 kV. The sub-levels are shown by the following colours: $|M_N|=0$ (red line), $|M_N|=1$ (orange line), $|M_N|=2$ (green line), $|M_N|=3$ (blue line), $|M_N|=4$ (purple line). The populations were calculated at the following longitudinal phase positions: (a) $-\pi/2$, (b) $-5\pi/12$, (c) $-\pi/4$, and (d) 0.

transition probability. This is exactly what is found by the numerical simulations, with figure 5.21 (a) showing considerable dynamics between the states. The molecule is initially in the state $|4,0\rangle$. As soon as the field switch begins the molecule is rapidly (over about 10 ns) driven into the $|4,1\rangle$ state, and thenceforth further transitions drive the molecule through the other states. After about 20 ns the field rotation is slow enough (see figure 5.20 (a)) that the populations begin to settle into a steady state. At this phase position the molecule is most likely to end up in the strong-field-seeking $|4,3\rangle$ state after the switch. This molecule is thus likely to be ejected from the decelerator after only one field switch. Figure 5.21 (b) shows the population dynamics at $\phi = -5\pi/12$. Here the rotation rate is not as fast and it can be seen that the transfer from $|4,0\rangle$ to $|4,1\rangle$ occurs more slowly. Transfer to the higher $|M_N|$ states is also slower, and the most probable outcome is for the molecule to end up in the $|4,2\rangle$ state. This state only ever experiences a weak Stark shift in the fields applied in the decelerator and therefore is not strongly guided. Figure 5.21 (c) shows the population dynamics at $\phi = \pi/4$. At this position ω_{sep} is always at least an order of magnitude greater than ω , and so transitions are unlikely. This is reflected in the dynamics where there is only a moderate amount of cycling between the $|4,0\rangle$ and $|4,1\rangle$ states. The other states are never significantly occupied and after the switch the

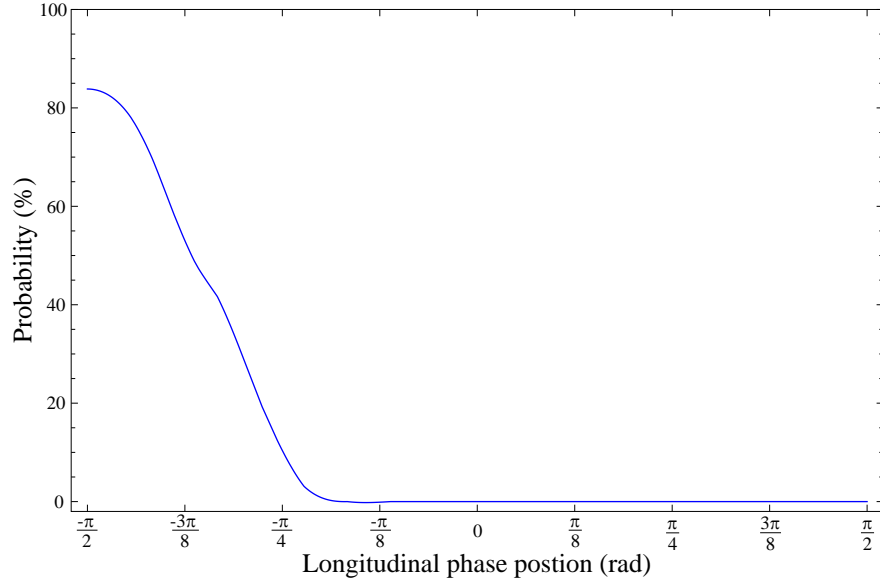


Figure 5.22: The probability of a CaF molecule, initially in the state $|4, 0\rangle$, ending up in another state after one field switch, as a function of longitudinal phase position. For these calculations the decelerator was charged to ± 15 kV, and the switching time was $\tau = 500$ ns.

molecule is most likely to be in its original $|4, 0\rangle$ state (with probability around 0.9). At the position $\phi = 0$, ω is always considerably greater than ω_{sep} and figure 5.21 (d) shows that the molecule is never driven out of its initial state.

By calculating the population probabilities after a field switch for a range of longitudinal phase-space positions it is possible to derive the total probability of a $|4, 0\rangle$ CaF molecule being driven out of this state during one field switch. The results of these calculations are shown in figure 5.22. It can be seen that the worst position for a molecule to be at when the fields are switched is $\phi = -\pi/2$, with a probability of being driven out of $|4, 0\rangle$ of 0.84. As the phase position is increased this probability drops, reaching its half-maximum around $\phi = -1$ ($= -57^\circ$), and zero around $\phi = -0.5$ ($= -28.5^\circ$). It is important to bear in mind that these probabilities correspond to one field switch. During one deceleration burst the fields switch 100 times.

Having shown which areas of longitudinal phase space are ‘safe’ and which are ‘dangerous’ for non-adiabatic field-driven transitions it is worth considering the phase-space positions of the molecules in the time-of-flight profiles in figures 5.18 and 5.19. Consider the former case: the field switching pattern (with synchronous phase, $\phi_{sync} = 0$, and synchronous speed, $v_{sync} = 370 \text{ ms}^{-1}$) bunches molecules about the centre of the pulse, with satellite peaks corresponding to synchronous molecules in adjacent potential wells. The molecules confined in the effective potential created by the switching fields occupy an area of phase space bounded by the separatrix shown in figure 5.16 (a). This separatrix

covers all longitudinal phase positions (modulo 2π). Thus the synchronous peak (and the satellite peaks) contain molecules that can occupy the dangerous areas of longitudinal phase space and so suffer from modest loss from non-adiabatic transitions to strong-field seeking states. Thus these peaks are smaller than predicted. However, the phase-stable molecules move on closed orbits in phase space, and a significant fraction never enter the dangerous regions throughout the deceleration process. For this reason the loss of phase-stable molecules is modest. The rest of the molecular pulse corresponds to molecules that are not phase-stable. These molecules do not oscillate in longitudinal phase space along the length of the decelerator. Over the length of the decelerator these molecules thus experience a large range of longitudinal positions over the 100 switches, which provides significant exposure to the ‘dangerous’ positions. Thus, over the course of the decelerator these molecules all have plenty of opportunities to be driven to strong-field seeking states and are thus poorly guided. This explains the considerable drop in signal for these molecules compared with simulations (which do not allow for a molecule to change state).

Figure 5.19 shows the effect of non-adiabatic transitions on the measured time-of-flight profile when the fields switch with synchronous phase, $\phi_{sync} = 75^\circ$, and synchronous speed, $v_{sync} = 340 \text{ ms}^{-1}$. The separatrix in this case confines the molecules in the decelerated peak to a ‘safe’ region of longitudinal space, as illustrated in the phase-space plot of figure 5.16 (c). It should thus be expected that the decelerated peak area should agree well with the simulation. The experimental peak appears to have approximately 60% the area of the simulated peak, but for the experimental peak it is difficult to choose the integration limits because the peak’s shape is not easily distinguished from other features in the time-of-flight profile. As before the non-synchronous molecules experience large loss as these molecules are likely to be at ‘dangerous’ positions in the decelerator at a significant number of the field switches.

5.9 Preventing non-adiabatic transitions

It can be seen from equation 5.32 that in order to reduce molecular loss from non-adiabatic transitions either ω_{sep} should be increased or the rotation rate, ω , be reduced. Reducing the rotation rate is possible only if the mechanical structure of the decelerator were changed or the field decay time constant, τ , reduced. The former option is of course not practical, whereas the latter is not desirable as a fast switching time is necessary for efficient deceleration (τ must be much smaller than the time taken for a molecule to leave a deceleration stage). The alternative is to increase ω_{sep} . This was achieved experimentally by increasing V_{LO} from ground. This non-zero baseline voltage can ensure that the magnetic sub-levels are always sufficiently separated by the Stark shift to reduce the probability of driving non-adiabatic transitions.

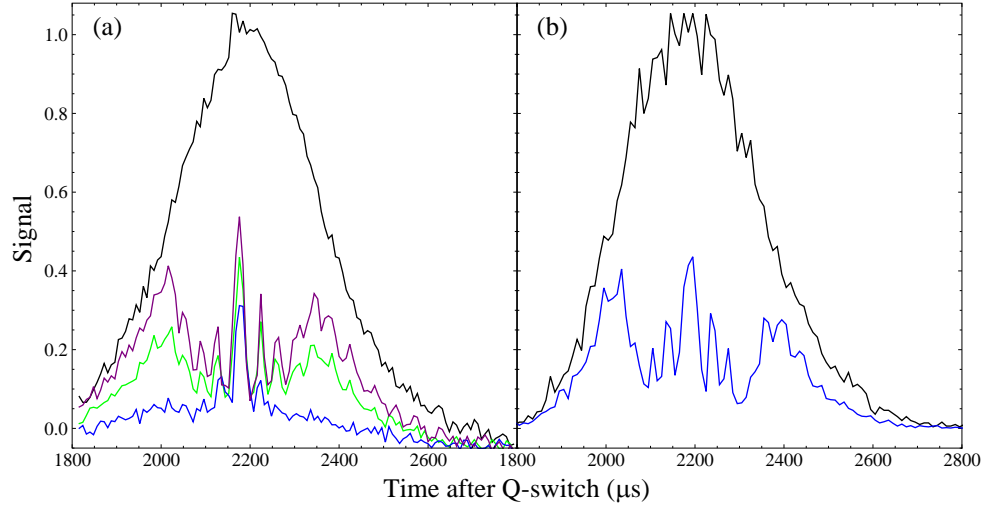


Figure 5.23: (a) Experimentally measured time-of-flight profiles with $V_{HI} = 14$ kV, $\phi_{sync} = 0$ and $v_{sync} = 370$ ms $^{-1}$. The deceleration profiles were obtained with $V_{LO} = 0$ (blue line), $V_{LO} = 0.5$ kV (green line) and $V_{LO} = 1.45$ kV (purple line). Each profile has been scaled by a factor that gives its associated DC guiding profile a unity amplitude. One of these DC guiding profiles is also shown (black line). (b) Simulated time-of-flight profiles with the above switching parameters (blue line) and in DC guiding mode (black line), also with $V_{HI} = 14$ kV. Both profiles have been scaled by a factor that results in the DC guiding profile having unity amplitude. The simulations do not include the possibility of non-adiabatic transitions along the decelerator and thus represent the best possible transmission.

Figure 5.23 (a) shows the effect of increasing V_{LO} on the measured burst-mode time-of-flight profile first shown in figure 5.18 ($\phi_{sync} = 0$, $v_{sync} = 370 \text{ ms}^{-1}$). As V_{LO} is increased from zero the time-of-flight signal increases as loss from non-adiabatic transitions is reduced. The profile shown in green was taken with $V_{LO} = 0.5 \text{ kV}$, leading to a minimum electric field of 5.3 kV cm^{-1} (increased from 2.7 kV cm^{-1} when $V_{LO} = 0$). This field increases the Stark splitting between the $|4, 0\rangle$ and $|4, 1\rangle$ states to $4.0 \times 10^7 \text{ rad s}^{-1}$. This splitting is not great enough to completely inhibit non-adiabatic transitions (see figure 5.20¹). However, the problem of non-adiabatic losses has been reduced. The purple profile was recorded with $V_{LO} = 1.45 \text{ kV}$, corresponding to a minimum electric field of 12.0 kV cm^{-1} . This profile shows much increased signal, with signal from phase-stable and non-phase-stable molecules much greater than when $V_{LO} = 0$. It was found experimentally that increasing V_{LO} further makes no further difference to the time-of-flight profile. This is to be expected as the minimum Stark splitting between the $|4, 0\rangle$ and $|4, 1\rangle$ states is $2.0 \times 10^8 \text{ rad s}^{-1}$ in this case, greater than the fastest rotation rate experienced during a switch.

Figure 5.23 (b) shows time-of-flight profiles from the simulations of the data in figure 5.23 (a) (the same simulations as shown in figure 5.18 (b)). There is excellent agreement between the simulated deceleration profile and the experimental deceleration profile acquired with $V_{LO} = 1.45 \text{ kV}$. This suggests that by applying $V_{LO} = 1.45 \text{ kV}$ the non-adiabatic loss channel has been turned off.

Figure 5.24 shows similar comparisons for the data taken with $\phi_{sync} = 75^\circ$ and $v_{sync} = 350 \text{ ms}^{-1}$. Figure 5.24 (a) shows that increasing V_{LO} from 0 to 1.95 kV significantly increases the time-of-flight profile signal. The non-synchronous molecular signal increases dramatically and the decelerated pulse area increases by a factor of 1.46, bringing it back into good agreement with the simulated peak area (figure 5.24 (b)), indicating again that the non-adiabatic loss channel has been inhibited.

5.10 Final deceleration data

Figure 5.25 shows deceleration data taken with $V_{HI} = 18 \text{ kV}$ and $V_{LO} = 1.0 \text{ kV}$. The high voltage switching pattern was generated for molecules with a synchronous speed of $v_{sync} = 340 \text{ ms}^{-1}$ and phase angles between 0° and 75° in 15° increments. Each deceleration profile has been scaled by the amplitude of its associated DC guiding profile, an example of which is shown in the figure (thick black line). Also shown are simulated time-of-flight profiles, where the simulations have matched the experimental conditions as

¹Note that the frequencies in figure 5.20 were calculated with $V_{HI} = 15 \text{ kV}$, whereas the data were taken with $V_{HI} = 14 \text{ kV}$. However, figure 5.20 still provides a good guide to acceptable Stark shift splittings to inhibit non-adiabatic transitions.

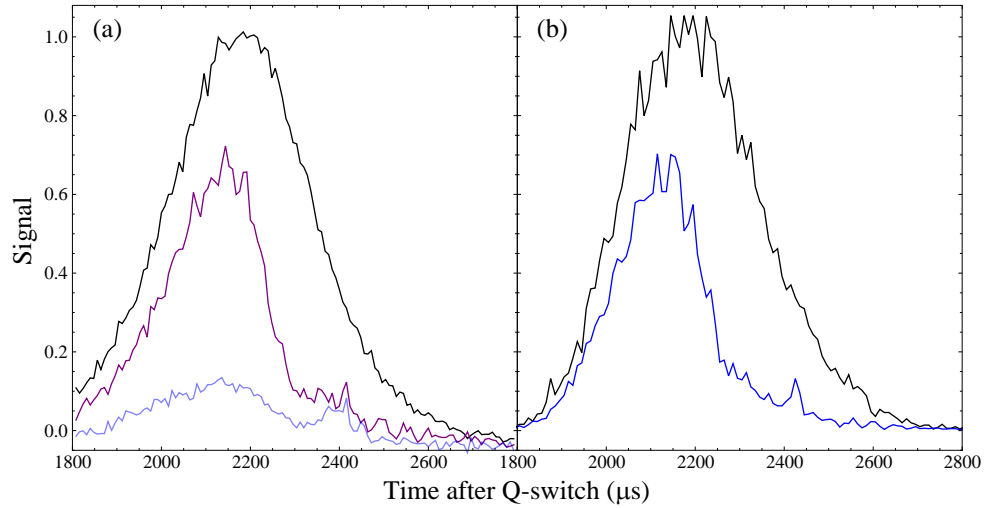


Figure 5.24: (a) Measured time-of-flight profiles with $V_{HI} = 14$ kV, $v_{sync} = 350$ ms $^{-1}$ and $\phi_{sync} = 75^\circ$. The pale blue profile was acquired with $V_{LO} = 0$, and the purple profile with $V_{LO} = 1.95$ kV. Each of the deceleration profiles has been scaled by the same factor that normalizes the amplitude of its associated DC guiding profile to unity. One of the DC guided profiles is shown (black line). (b) Simulated time-of-flight profiles taken with the same experimental parameters as the data in (a), neglecting non-adiabatic transitions.

closely as possible, except that in the simulation $V_{LO} = 0$ ². There is good agreement between the experimental and simulated profiles. The two DC guiding profiles agree very well, showing that the simulated molecular source matches well the conditions in the source chamber. The data and simulations both show a decelerated peak that starts off centred around 2360 μ s when $\phi_{sync} = 0$ and is ultimately delayed to 2730 μ s when $\phi_{sync} = 75^\circ$. The simulations show that these peaks correspond to molecules being decelerated from 343 ms $^{-1}$ to 247 ms $^{-1}$. This is a reduction in the kinetic energy of 140 cm $^{-1}$ (1.4 cm $^{-1}$ per stage). This corresponds to 48% of the initial kinetic energy being removed from the decelerated molecules. Figure 5.26 shows the 75 $^\circ$ time-of-flight profile in more detail (as well as the associated DC guiding reference profile). The decelerated peak at 2730 μ s is more clearly visible in this figure.

The simulations also show a second decelerated peak, typically detected around 50 μ s later than the peak discussed above. These correspond to molecules which were one potential well behind those already discussed. The simulated velocity profiles show that both these peaks correspond to molecules with the same final speed. Both peaks are produced by molecules with speeds very close to the synchronous molecule, but in different potential wells. In the simulations the longitudinal extent of the source is large enough that

²This should lead to the simulated molecules experiencing very slightly greater deceleration than in the experiment. However, this effect is extremely small – far too small to be observed.

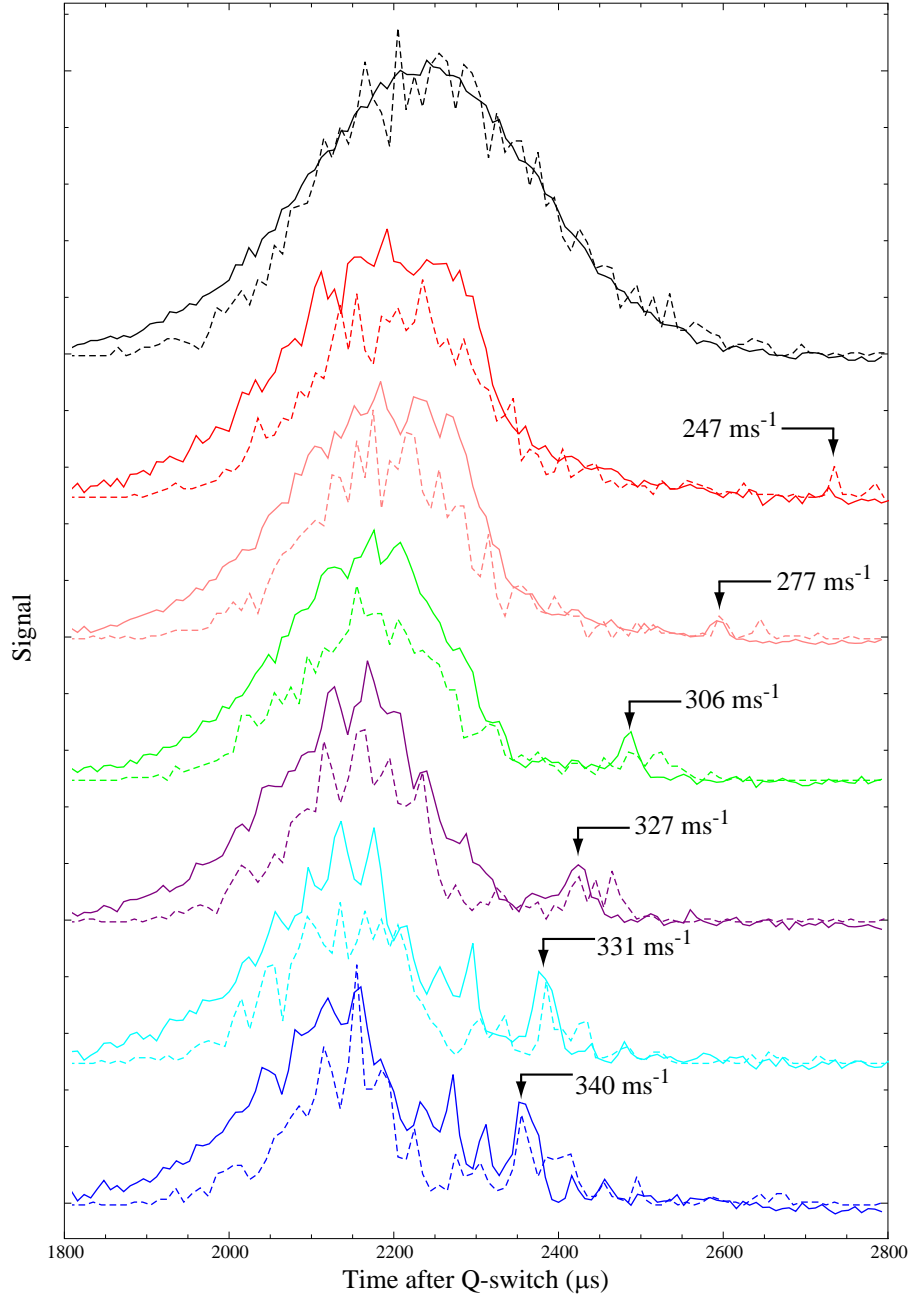


Figure 5.25: Experimental and simulated deceleration data of CaF radicals in the $|4,0\rangle$ state (thick and dashed lines respectively). The data were taken with $V_{HI} = 18$ kV, $V_{LO} = 1.0$ kV. The voltage switching pattern was generated for a synchronous speed of $v_{sync} = 340$ ms⁻¹ and a range of synchronous phase angles. Each experimental time-of-flight profile has been normalized to the amplitude of its associated DC guiding profile, an example of which is shown (black line). The deceleration profiles correspond to the following phase angles: 0° (blue line), 15° (cyan line), 30° (purple line), 45° (green line), 60° (pink line), 75° (red line).

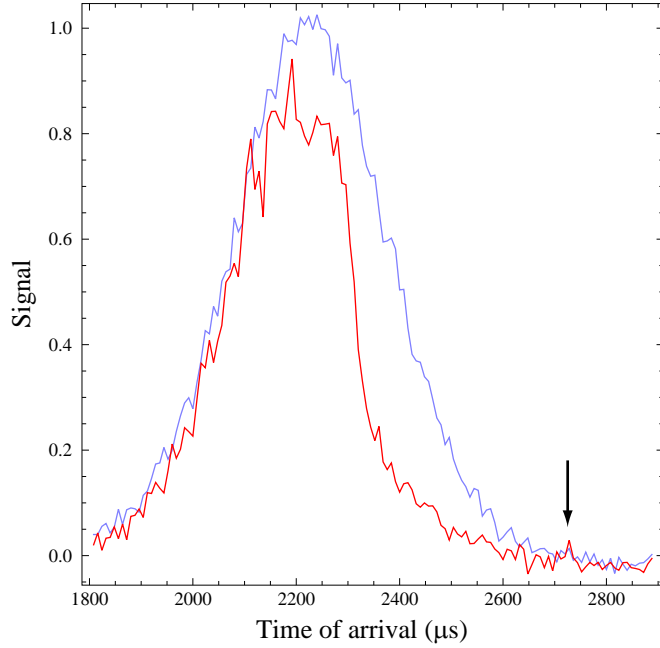


Figure 5.26: The time-of-flight profile measured with ± 18 kV applied to the 100-stage decelerator, operated with a phase angle of 75° (red line). Also shown is the associated DC guiding reference profile (pale blue line). The decelerated peak at $2730 \mu\text{s}$, indicated by the arrow, is more clearly visible in this figure than in figure 5.25.

there is a significant number of molecules of the right velocity in the rear of the pulse that are in the first deceleration stage when the fields begin to switch. These molecules then occupy the potential well behind those from the front of the pulse. They are decelerated the same amount, but leave the decelerator one period (6 mm) behind the front pulse. These second pulses were not measured experimentally, suggesting that the source is not as large as used in the simulations.

The size of each experimentally measured decelerated peak agrees well with its associated simulated peak except in the case of the $\phi_{sync} = 75^\circ$ data. Here the experimental peak is much smaller than the simulation predicts. This is very unlikely to result from non-adiabatic transitions as none of the other profiles suffers from this, and molecules at this relatively high phase angle should be fairly well shielded from such transitions. There is some uncertainty about exactly when the synchronous molecule reaches the first deceleration stage, and hence an associated uncertainty about when the switching pattern should start. Experiments at high phase angle will be more sensitive to any error in this value, because the phase-space acceptance is small at high phase angle. It is likely that varying the start time of the pattern will improve the flux in the high phase-angle deceleration peaks. The number of molecules that can be trapped in the Stark potential wells is proportional to the three-dimensional acceptance — that is, the product of the longitu-

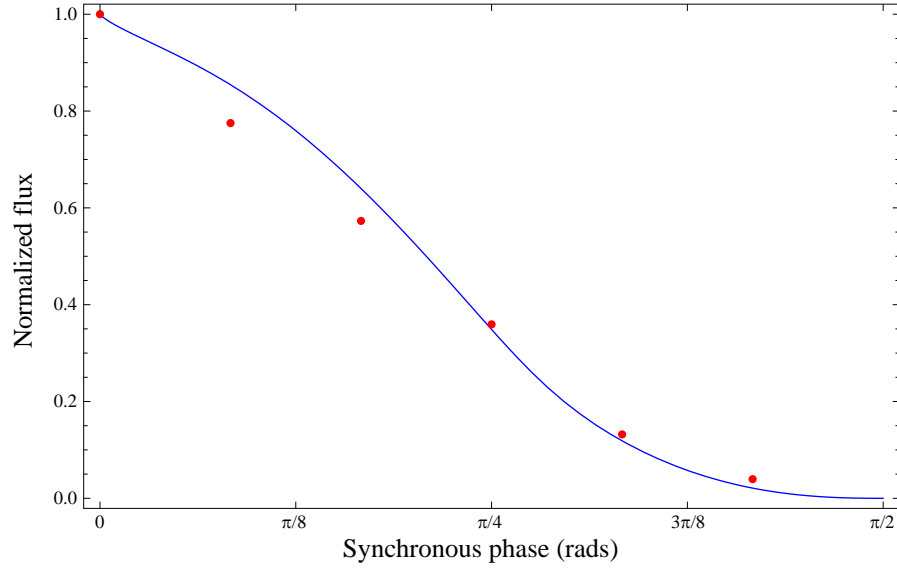


Figure 5.27: The longitudinal acceptance of the decelerator as a function of synchronous phase calculated with $V_{HI} = 18$ kV and $V_{LO} = 0$ (blue line), normalized to its value at $\phi_{sync} = 0$. Also shown is the area of the 18 kV decelerated peak at the phase angles used in the experiment (red points), also normalized to its value at $\phi_{sync} = 0$.

dinal acceptance (discussed in section 5.6.2) and the transverse acceptance (a measure of which are the transverse trapping frequencies discussed in section 5.4). Figure 5.27 shows the area of the decelerated peak as a function of phase angle (normalized to the value at $\phi_{sync} = 0$). Also shown is the longitudinal acceptance calculated with $V_{HI} = 18$ kV and $V_{LO} = 0$ (and normalized in the same way). Despite the fact that this analysis ignores the effects of the transverse acceptance, there is good agreement between the data and the longitudinal acceptance. In particular, the ratio of the $\phi = 0$ and $\phi = 75^\circ$ peak areas is in very good agreement with the associated acceptance ratio.

5.11 Conclusions

A 100-stage decelerator has been constructed and used at ± 18 kV to decelerate CaF radicals in the weak-field seeking $|4, 0\rangle$ state from 343 ms^{-1} to 247 ms^{-1} . This corresponds to a removal of 48% of their initial kinetic energy. It was found that, with the decelerator switching from high voltage to ground, the decelerator can drive transitions to different sub-levels of the $\mathcal{N} = 4$ manifold. These transitions, which can vastly reduce the molecular flux emitted by the decelerator, can be explained by the rotation of the electric field during a field switch. The rotation is particularly efficient at driving transitions when the states are nearly degenerate, which happens when the field is weak. It was found that applying a bias voltage, $V_{LO} > 0$, can inhibit these transitions, and thus increase the measured

molecular signal.

The decelerator has been used close to its maximum voltage. The high voltage switches are rated for a maximum potential difference of 20 kV. There is thus some scope for increasing the deceleration further. The reason for not running higher than 18 kV was that, when testing the decelerator at greater than this voltage the ground noise associated with the switching caused much electrical cross-talk with other experimental instruments, most damagingly the dye laser. The ground noise caused the laser to unlock and thus the laser-induced fluorescence measured no molecular signal. In addition the resistors used in the switch boxes were not able to dissipate the electrical power generated during switching. The ceramic cladding of many of the resistors cracked as they heated, allowing electrical breakdown on the resistors' surfaces. This breakdown caused significant RF radiation which also hampered detection. The next stage for this experiment is to install new resistors and to improve the experiments' shielding both from the ground noise and RF radiation generated by switching the high voltage rapidly. Simulations show that by increasing the applied voltage to ± 20 kV, and operating at a phase angle of 75° the molecules will be decelerated from 340 ms^{-1} to 220 ms^{-1} , a removal of 59% of the initial kinetic energy. Operating the decelerator at voltages greater than ± 20 kV is likely to be unfeasible, so to bring the CaF molecules to rest a longer decelerator is required. This 100-stage decelerator has been designed to allow for a second 100-stage unit to be attached to it without any interruption to the periodicity of the stages. Such a 200-stage decelerator, run at ± 20 kV, will be capable of decelerating CaF molecules from 340 ms^{-1} to 53 ms^{-1} at a synchronous phase angle of 65.7° .

Chapter 6

Guiding ground-state CaF molecules

6.1 Motivation

The ability to guide and decelerate beams of weak-field-seeking molecules is now well-researched and highly developed. In this thesis a decelerator has been used to slow CaF radicals in weak-field-seeking states from 343 ms^{-1} to 247 ms^{-1} . This equates to roughly half the longitudinal kinetic energy transferred from the molecules to the decelerator. In order to slow the molecules further two options are available: (i) increase the voltage applied to the decelerator, and (ii) make the decelerator longer. Increasing the decelerator voltage is limited both in practice and in principle. Practically, the voltage is restricted by breakdown between the decelerator field stages and breakdown across the switches. However, a more fundamental reason limits the applied voltage: in a certain electric field the Stark shift of a weak-field seeker reaches a maximum, beyond which it decreases with electric field. The weak-field seeker becomes a strong-field seeker in a strong enough electric field. A decelerator that generates fields greater than this threshold field no longer guides weak-field seekers: in fact it diverges the beam.

Molecular beams created by supersonic expansion travel at a speed determined almost entirely by the carrier gas. Thus a beam of heavy molecules will travel at the same speed as a beam of lighter molecules. A beam of heavy molecules thus has proportionally more kinetic energy for a decelerator to remove. Increasing the length of a decelerator seems, therefore, a necessary option to decelerate heavy molecules. However, this can lead to unfeasibly long decelerators, which is neither practical nor elegant. An alternative is to decelerate molecules in strong-field seeking states, particularly the ground state. The Stark shift of a ground state is always negative and, for a given strong electric field, the ground state always produces the greatest Stark shift. It makes sense, therefore to decelerate heavy molecules in their ground state.

The difficulty with this deceleration method is how to keep the beam confined about the beam-line along the length of the decelerator. The molecules will tend towards the regions of strong field: at the surface of the electrodes. The molecules will be accelerated towards the electrodes, crash into them, and nothing will make it out of the decelerator. There is no static confinement mechanism for strong-field seeking molecules. However, by creating a guide whose transverse electric field shape varies along the length of the decelerator it is possible to attain *dynamic* beam confinement.

As well as being a useful testing ground for investigating dynamic confinement, such a guide also has practical use in its own right. Sources of cold molecules, such as supersonic expansion and buffer gas cooling produce molecular beams whose populations are mostly in the low-lying rotational levels, predominantly the ground state. These methods thus produce large fluxes of strong-field seekers. A guide for strong-field seekers is thus a useful tool in transporting a high flux of molecules from a high density source to a much lower-pressure chamber, where an experiment is located, while maintaining the large phase-space density of the source.

For this reason, and for the purposes of investigating the confinement mechanisms for strong-field seekers a 1 m long alternating gradient (AG) guide was built and used to guide beams of CaF radicals.

6.2 Guiding strong-field seekers

In an applied electric field a strong-field seeking molecule experiences a force field with non-negative divergence (section 2.6), $\nabla \cdot \vec{F}(\vec{r}) \geq 0$. In the weak- and strong-field limits this means that the molecular polarizability, α_m , and effective dipole moment, μ_m , respectively are non-negative. This precludes static confinement of a beam of strong-field seekers along an axis. Confinement (and, indeed trapping) would be possible in a field with a local maximum of electric field; however, maxima of electric fields in free space are not allowed by Maxwell's equations [73].

However, it is still possible to achieve dynamic beam confinement with a varying transverse electric field. Consider a molecular beam with beam-line parallel to the z -axis. Along and around the beam-line is some configuration of charged electrodes, the fields from which are to be used to confine the beam. A field with a minimum along the beam-line would confine weak-field seekers, but it would diverge a beam of strong-field seekers, causing the molecules to crash into the electrodes or to leave the beam-line and never return. A maximum of field along the beam-line would provide the desired confinement, but this is not possible in free space¹. The next best thing is a saddle point of electric field, which

¹Of course, it is possible to create a maximum of electric field along the beam-line with an array of conductors arranged on the beam-line. Lainé and Sweeting, for example, used a sequence of crossed,

achieves the desired maximum in one transverse direction, although provides a minimum in the other. Such a field distribution can be used to provide dynamic confinement. A saddle-shaped field acts as a lens on a beam of strong-field seekers: focussing the beam in one direction (the one which experiences a maximum on the beam-line), while defocussing the beam in the orthogonal direction. Rotating the field by $\pi/2$ after the beam has travelled some distance L inside a lens now swaps the forces: the transverse direction along which the beam was previously focussed now defocusses the beam and vice versa. Selection of the optimal lens lengths will balance these transverse forces and achieve confinement along the beam-line. In fact, it will turn out that, over the length of a guide the forces do not balance, and a net focussing can be achieved. An analogy in optics is the use of an alternating sequence of positive and negative lenses to achieve net collimation of a beam of light.

6.3 A review of previous AG guiding experiments

The use of a sequence of field stages with alternating orientations to guide particles was first published by Courant, Livingston and Snyder in 1952 [81]. The authors proposed using magnetic fields to focus beams of charged particles in synchrotrons and linear accelerators. In 1958 Courant and Snyder went on to develop the method of transfer matrices with periodic elements to describe the motion of particles in an AG guide [77] (see section 6.4.2).

The theory of focussing molecular beams with alternating gradient saddle-shaped electric fields was first explored by Auerbach, Bromberg and Wharton in 1964 [51]. Amongst a number of suggested schemes was an AG guide comprising a sequence of alternately oriented two-wire field stages, held at constant voltage, and a four-electrode guide in which the field is rotated by switching the applied voltage in time. These designs were proposed as state and dipole selectors.

The first experimental AG guiding was performed by Kakati and Lainé in 1971 [82]. In this experiment a 5 cm long AG guide was constructed with 8 field stages. Each stage comprised two 1.5 mm diameter brass wires with polished hemispherical ends. The wires in a stage were positioned end-on, orthogonal to the beam-line with a 3mm separation between the ends of the two electrodes. The electrodes in a field stage were oppositely polarized. Successive field stages were alternately oriented in the transverse direction. Potential differences of up to 30 kV could be applied before breakdown occurred between the electrodes. Beams of NH_3 were launched into the guide through a gas nozzle with oppositely-charged wires to guide ammonia molecules [74]. Each pair of crossed wires has its crossing on the beam-line, thus creating a maximum of electric field at this point. Another design uses a cylindrical capacitor, with the inner electrode lying on the beam-line axis. Strong-field seeking molecules can then orbit the maximum of field created by the inner electrode [75, 76].

variable backing pressure. Detection was performed in a resonant cavity which could be tuned to a variety of microwave transitions in NH_3 . It was found that with the electrodes grounded only a small NH_3 signal was detected. However, the signal rose considerably when voltage was applied, demonstrating AG focussing of molecules for the first time.

The next development in AG guiding came in 1978 with the construction of a 1.2 m-long four-rod focuser by Lübbert, Rotzoll and Günther [83]. The focuser consisted of two field stages. The 8 mm diameter stainless steel rods were aligned parallel to the beam-axis; in the transverse cross-section they were arranged on the vertices of a square of side 8mm. The rods on one side of the square were positively charged, and the other pair negatively charged. Two of the rods (diagonally opposite each other) ran the 1.2m length of the guide, whereas the other two ran only half the length, after which they were replaced by two identical rods with their respective polarities switched. This polarity switch rotated the field through $\pi/2$. Potentials of up to 60 kV were achieved. The focuser was used on beams of ICl (created in an oven). By varying the voltage applied to the focuser different rotational states of ICl were focussed. Detection of the $|J, M_J\rangle = |0, 0\rangle, |1, \pm 1\rangle$ and $|2, \pm 2\rangle$ states at different voltages demonstrated the guide's use as a rotational state selector.

After this there was no development in the field of AG guiding until the advent of the AG decelerator. These decelerators work in an identical way to weak-field decelerators (chapter 5) in terms of longitudinal dynamics. The only difference in the deceleration is that the field is turned on when the strong-field seeking molecules are inside a field stage and left on as the molecules leave. AG deceleration will be discussed in more detail in chapter 7.

The first dedicated AG guide in recent years was used as a selector for different isomers of 3-aminophenol [84]. The guide consisted of four 1 m long electrodes of circular cross-section and with radius 2 mm. The electrodes were positioned parallel to the beam-line axis. In transverse cross-section the electrodes were arranged on the vertices of a square of side 4.9 mm. The different effective dipole of the molecules in a given strong electric field gave the peak acceptance at different lens lengths for the two isomers. At a given lens length the guide would favourably transport one isomer and not the other.

6.4 An ‘ideal’ guide

6.4.1 Equations of motion

The desired guide for strong-field seekers has an electric field which is saddle-shaped in the transverse directions. In an ideal guide the force varies linearly in the transverse coordinates, $\{x, y\}$ (corresponding to a harmonically varying Stark potential in x and y). Let the force constant magnitudes be equal in both x and y directions, $k = k_x = -k_y$.

Therefore $\nabla \cdot \vec{F}(\vec{r}) = 0$ as

$$k = \frac{\partial F_x}{\partial x} = -\frac{\partial F_y}{\partial y}, \quad k_z = \frac{\partial F_z}{\partial z} = 0. \quad (6.1)$$

Now, for a constant speed along the beam-line, v_z , $\frac{\partial^2 i}{\partial t^2} = \frac{\partial^2 i}{\partial z^2} \left(\frac{\partial z}{\partial t}\right)^2 = \frac{\partial^2 i}{\partial z^2} v_z^2$, where $i = \{x, y\}$. Defining $\kappa^2 = k/mv_z^2$ the transverse equations of motion are thus

$$\frac{\partial^2 x}{\partial z^2} \pm \kappa^2 x = 0, \quad \frac{\partial^2 y}{\partial z^2} \mp \kappa^2 y = 0, \quad (6.2)$$

depending on the orientation of the saddle.

The molecule's trajectory can be described by the time evolution of its position in $\{i, i'\}$ phase space, where $i = x, y$ and the prime denotes differentiation with respect to z . The linearity of the equations of motion allows each of the coordinates $\{i, i'\}$, evaluated at some longitudinal position, z_2 , to be written as linear functions of the coordinates at some previous position, z_1 . Consequently the coordinates at z_2 can be related to those at z_1 by some matrix, $\mathbf{M}_i(z_2|z_1)$:

$$\begin{pmatrix} i(z_2) \\ i'(z_2) \end{pmatrix} = \mathbf{M}_i(z_2|z_1) \begin{pmatrix} i(z_1) \\ i'(z_1) \end{pmatrix}, \quad i = x, y. \quad (6.3)$$

Solving the equations of motion for one of the transverse directions with the positive force constant results in a focussing trajectory that oscillates about the beam-line, whose transfer matrix is given by

$$\mathbf{M}(z_2|z_1) = \mathbf{F}(z_2 - z_1) = \begin{pmatrix} \cos(\kappa(z_2 - z_1)) & \frac{1}{\kappa} \sin(\kappa(z_2 - z_1)) \\ -\kappa \sin(\kappa(z_2 - z_1)) & \cos(\kappa(z_2 - z_1)) \end{pmatrix}. \quad (6.4)$$

Solving the equation of motion with the negative force constant renders a defocussing trajectory, with transfer matrix

$$\mathbf{M}(z_2|z_1) = \mathbf{D}(z_2 - z_1) = \begin{pmatrix} \cosh(\kappa(z_2 - z_1)) & \frac{1}{\kappa} \sinh(\kappa(z_2 - z_1)) \\ \kappa \sinh(\kappa(z_2 - z_1)) & \cosh(\kappa(z_2 - z_1)) \end{pmatrix}. \quad (6.5)$$

Consider the motion in one of the transverse directions. A region of field in which the motion in this direction is described by the transfer matrix \mathbf{F} is referred to as a focussing lens, and if it is described by the matrix \mathbf{D} it is a defocussing lens. Motion in a field free region is described by the drift matrix

$$\mathbf{M}(z_2|z_1) = \mathbf{O}(z_2 - z_1) = \begin{pmatrix} 1 & (z_2 - z_1) \\ 0 & 1 \end{pmatrix}. \quad (6.6)$$

An alternating gradient (AG) guide comprises a repeating array of focussing and defocussing lenses, each of length L , possibly with field-free drift regions of length S between

the lenses. The unit cell in such a periodic lens sequence has length $l_{cell} = 2(L + S)$ and is described by the compound transfer matrix

$$\begin{aligned} \mathbf{M}(z + l_{cell}|z) &= \mathbf{F}(z + L|z) \times \mathbf{O}(z + L + S|z + L) \\ &\times \mathbf{D}(z + 2L + S|z + L + S) \times \mathbf{O}(z + 2(L + S)|z + 2L + S). \end{aligned} \quad (6.7)$$

The transfer matrix for an AG guide comprising N unit cells is thus

$$\mathbf{M}(z + Nl_{cell}|z) = \mathbf{M}(z + l_{cell}|z)^N. \quad (6.8)$$

For a molecular trajectory along z to be stable the matrix elements of $\mathbf{M}(z + l_{cell}|z)^N$ must be finite as $N \rightarrow \infty$.

6.4.2 Courant-Snyder parameters

A guide with many field stages, N , is thus described by equations 6.7 and 6.8 in terms of a matrix whose elements are difficult to deal with analytically and from which little physical sense can be inferred. However, E.D. Courant and H.S. Snyder developed a reparameterization of these transfer matrices [77], resulting in matrices that are much easier to work with analytically and which provide a good physical description of guided trajectories. This reparameterization is discussed below.

A general unit cell transfer matrix is

$$\mathbf{M}(z + l_{cell}|z) = \begin{pmatrix} a & b \\ c & d \end{pmatrix}. \quad (6.9)$$

Courant and Snyder defined the following parameters:

$$\frac{1}{2}(a + d) = \cos \Psi, \quad (6.10)$$

$$(a - d) = 2\alpha \sin \Psi, \quad (6.11)$$

$$b = \beta \sin \Psi, \quad (6.12)$$

$$c = -\gamma \sin \Psi. \quad (6.13)$$

Here α , β and γ are functions of z , known as the ‘Courant-Snyder parameters’, and Ψ is called the phase advance per cell. The unit cell transfer matrix can now be written

$$\mathbf{M}(z + l_{cell}|z) = \begin{pmatrix} \cos \Psi + \alpha \sin \Psi & \beta \sin \Psi \\ -\gamma \sin \Psi & \cos \Psi - \alpha \sin \Psi \end{pmatrix} = \mathbf{I} \cos \Psi + \mathbf{J} \sin \Psi, \quad (6.14)$$

where \mathbf{I} is the identity matrix and

$$\mathbf{J} = \begin{pmatrix} \alpha & \beta \\ -\gamma & -\alpha \end{pmatrix}. \quad (6.15)$$

The determinants of the original transfer matrices (equations 6.4 to 6.6) are unity. The determinant of a unit cell transfer matrix (equation 6.7) is thus also unity. Applying this to the matrix in equation 6.14 renders the following relation

$$\beta\gamma - \alpha^2 = 1. \quad (6.16)$$

A molecular trajectory from some initial position, z_1 , to some final position, z_2 , is described by the matrix $\mathbf{M}(z_2|z_1) = \mathbf{M}(z_2|z_1 + \delta)\mathbf{M}(z_1 + \delta|z_1)$, where δ is some arbitrary distance. It can be seen therefore that:

$$\begin{aligned} \mathbf{M}(z_2 + l_{cell}|z_1) &= \mathbf{M}(z_2 + l_{cell}|z_2)\mathbf{M}(z_2|z_1) \\ &= \mathbf{M}(z_2 + l_{cell}|z_1 + l_{cell})\mathbf{M}(z_1 + l_{cell}|z_1) \\ &= \mathbf{M}(z_2|z_1)\mathbf{M}(z_1 + l_{cell}|z_1) \end{aligned} \quad (6.17)$$

$$\implies \mathbf{M}(z_2 + l_{cell}|z_2) = \mathbf{M}(z_2|z_1)\mathbf{M}(z_1 + l_{cell}|z_1)[\mathbf{M}(z_2|z_1)]^{-1}. \quad (6.18)$$

Thus any two matrices with different initial coordinates, but describing a trajectory over one unit cell, are similar matrices. Consequently they share many properties, such as the same trace, determinant and eigenvalues. The first of these properties, the trace, can be seen from equation 6.10 to be $2\cos\Psi$. Thus Ψ is the same for two unit cell transfer matrices with any start position z_1 and z_2 . Generally it can be seen that phase acquired over some number of unit cells, Ψ , is independent of the initial position. It can also be seen that α , β and γ are periodic, with period l_{cell} .

Noting that $\mathbf{J}^2 = -\mathbf{I}$, it can readily be seen that the product of two transfer matrices with period, l_{cell} , and unit cell phase advance, Ψ , can be written in terms of \mathbf{I} and \mathbf{J} (equation 6.14):

$$(\mathbf{I}\cos\Psi + \mathbf{J}\sin\Psi)(\mathbf{I}\cos\Psi + \mathbf{J}\sin\Psi) = \mathbf{I}\cos(2\Psi) + \mathbf{J}\sin(2\Psi). \quad (6.19)$$

This can be simply generalized to the case of N transfer matrices with period l_{cell} :

$$\mathbf{M}^N = \mathbf{I}\cos(N\Psi) + \mathbf{J}\sin(N\Psi). \quad (6.20)$$

Equations 6.10 and 6.20 thus determine the criterion for a molecular trajectory to be infinitely stable along an AG guide. For a stable trajectory, the elements of \mathbf{M}^N must oscillate as N is increased. This is met if Ψ is real. If Ψ is not real the cosine and sine terms in equation 6.20 will increase exponentially and the molecule will clearly not be bounded about the axis defined by the beam-line. Equation 6.10 thus gives the stability criterion in terms of the elements of the unit cell transfer matrix as $|a + d| < 2$, or expressed another way, $-1 < \frac{1}{2}\text{Tr}(\mathbf{M}) < 1$.

6.4.3 Molecular trajectories

Solutions to Hill's equation

To find an analytical form for molecular trajectories in an ideal, harmonic AG guide Courant and Snyder [77] describe the transverse motion by continuous equations of motion. These are generalizations of equations 6.2. In the case of motion in the x -direction this equation is

$$\frac{d^2x(z)}{dz^2} = -\mathcal{K}^2(z)x(z). \quad (6.21)$$

$\mathcal{K}(z)$ represent the force fields as a function of time as the electric field is switched during a molecule's transit of the AG guide. $\mathcal{K}(z)$ can be described as a Fourier series (for an infinitely long guide), in which case equation 6.21 is Hill's equation [78]. A trial solution for equation 6.21 is [77]:

$$x(z) = \sqrt{\beta(z)}\epsilon \cos(\phi(z) + \delta), \quad (6.22)$$

where $\phi(z)$, δ and ϵ are determined by initial conditions. $\beta(z)$ is a z -dependent amplitude term. Substitution into equation 6.21 shows that the trial solution is valid when:

$$\frac{1}{2}\beta''\beta - \frac{1}{4}(\beta')^2 + \mathcal{K}(z)^2\beta^2 = 1, \quad (6.23)$$

and

$$\phi(z) = \int_0^z \frac{1}{\beta(\tilde{z})} \tilde{z}. \quad (6.24)$$

The phase advance per cell is thus:

$$\Psi = \phi(l_{cell}) = \int_0^{l_{cell}} \frac{1}{\beta(\tilde{z})} \tilde{z}. \quad (6.25)$$

The solution in equation 6.22 is a continuous function. By considering the solutions $x(z)$ and $x'(z)$ from some arbitrary z to $z + l_{cell}$ it is possible to write $x(z + l_{cell})$ in terms of $x(z)$ and $x'(z)$. Comparing this expression with the description of $x(z + l_{cell})$ from the unit cell transfer matrix (equation 6.14) shows that the above trial solution is consistent with the transfer matrix as long as the following condition is met:

$$\beta'(z) = -2\alpha(z). \quad (6.26)$$

Molecular trajectories

Consider now the form of the trajectory in equation 6.22. The $\beta(z)$ amplitude term leads to periodic motion with a period of l_{cell} . This is modulated by a cosinusoidal oscillation with period $2\pi l_{cell}/\Psi$. It will turn out that in the optimal operation of an AG guide $\Psi < 2\pi$, and so this cosine modulation period is greater than the $\beta(z)$ oscillation. The latter is thus described as the 'micromotion', which is modulated by the larger wavelength 'macromotion'. An example of a typical molecular trajectory is shown in figure 6.1. The

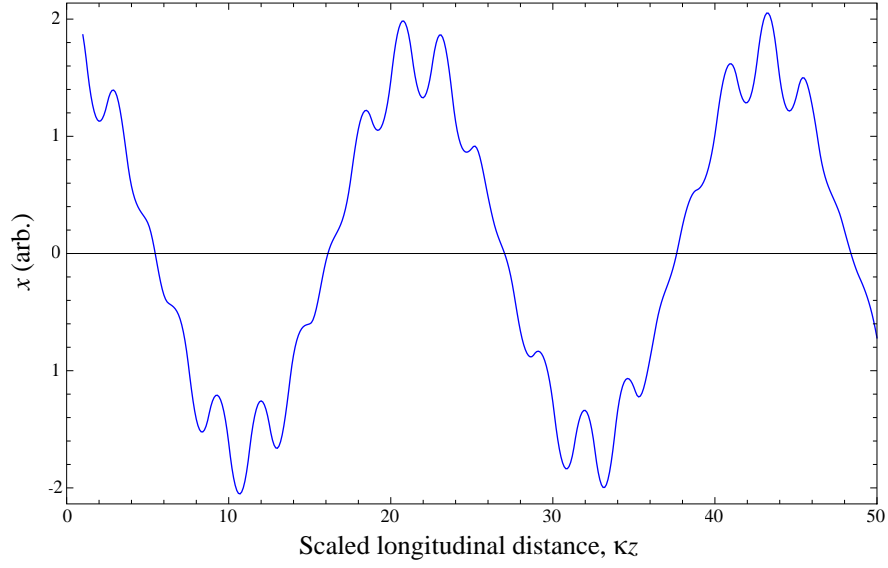


Figure 6.1: The form of a trajectory in an AG guide. The micromotion occurs on the length scale of the lenses, and is superimposed on a much larger amplitude, larger wavelength macromotion. This trajectory was calculated with $\kappa L = 1.25$ and $\kappa S = 0$.

micromotion is the result of the succession of focussing and defocussing lenses, and occurs with the same period as the unit cell. Despite the modulus of the potential gradient being the same in both focussing and defocussing lenses the force exerted by a defocussing lens will be smaller than that exerted by the previous focussing lens. This is because the action of a focussing lens is to accelerate a molecule towards the beam-line. The molecule then enters the following defocussing lens closer to the beam-line, where the force is less. This force imbalance leads to a net focussing over the length of a guide, which is manifested in the trajectory as the macromotion. Varying the length of the lenses in a guide will change the force imbalance and thus change the respective scales of the micromotion and macromotion.

By combining the Courant-Snyder expressions in equations 6.16, 6.24 and 6.26 with the expression $x^2 + (\alpha x + \beta x')^2$, it can be shown that

$$\gamma(z)x^2 + 2\alpha(z)xx' + \beta(z)(x')^2 = \epsilon. \quad (6.27)$$

This is the equation of an ellipse in x - x' phase space. Consider an ensemble of molecules entering the guide with the same longitudinal speed and the same ϵ , but with a range of δ . At a given position, z , inside the guide the phase-space positions (that is, the positions in x - v_x space) of these molecules will all lie on an ellipse defined by equation 6.27. As the molecules traverse the guide this ellipse will evolve, rotating and changing the length of the major and minor axes. However, its area, $\pi\epsilon$, will remain constant. An ensemble of molecules with a range of relative phases, δ , and a range of amplitude terms, $0 \leq \epsilon_i \leq \epsilon$,

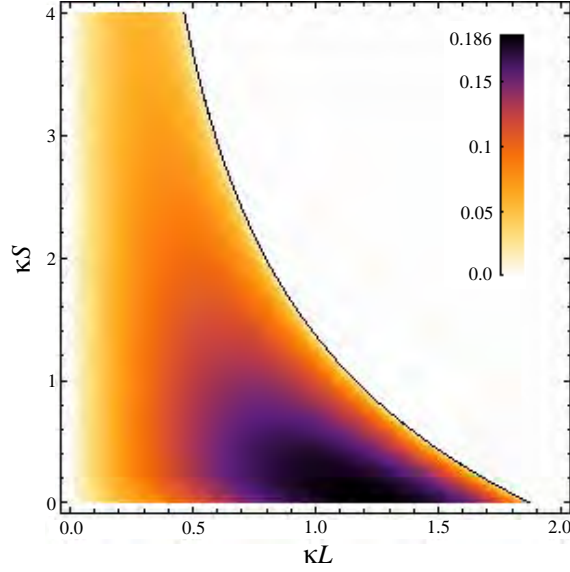


Figure 6.2: The 1D acceptance, A_{1D} , of a harmonic AG guide in units of κd^2 , where d is the physical aperture of the guide. The maximum acceptance is obtained by a gapless guide ($\kappa S = 0$) with $\kappa L = 1.25$. The black line is the line of stability obtained from the criterion that the absolute value of the trace of the unit cell transfer matrix must be less than 2.

will all lie on ellipses falling inside the ellipse define by those molecules with the maximum value, ϵ [80].

The physical aperture created by the guide's electrodes is the principle factor in limiting the range of stable trajectories supported by an AG guide. The electrode geometry determines the maximum amplitude that a molecular trajectory can have without colliding into the electrodes. It can be seen from equation 6.22 that the maximum distance from the beam-line attained by a given trajectory is determined by the value of $\sqrt{\epsilon\beta(z)}$. The maximum value of β , β_{max} , occurs in the centre of a focussing lens. β_{max} can be found by equating the elements of the Courant-Snyder unit cell transfer matrix (equation 6.14) with the explicit unit cell transfer matrix which is the product **FODO** (equations 6.4, 6.5 and 6.6). Consider a general electrode geometry that leads to a physical aperture with a square cross-section of side, d . The 'acceptance' of such a guide is defined by the area of phase space occupied by all possible stable trajectories. Such trajectories must meet the requirement that $\sqrt{\epsilon\beta_{max}} < d/2$. The acceptance is the area of the ellipse in this limiting case, the value of which is $\pi d^2/(4\beta_{max})$. Note that this acceptance is a measure of only the x - x' phase space area and so is referred to as the one-dimensional (1D) acceptance. In this case the full two-dimensional (2D) acceptance, a measure of the volume of x - x' - y - y' space, is simply the square of the 1D acceptance.

Figure 6.2 shows the one-dimensional acceptance, A_{1D} in units of κd^2 as a function

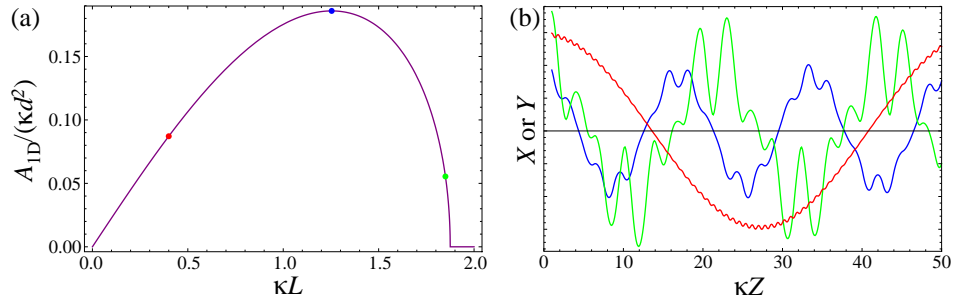


Figure 6.3: (a) The 1D phase space acceptance in units of κd^2 as a function of κL for a gapless guide. Three points on the curve are highlighted and each corresponds to one of the three trajectories shown in (b), as indicated by the colours. The red trajectory was calculated with $\kappa L = 0.4$, the blue trajectory with $\kappa L = 1.254$ and the green with $\kappa L = 1.85$.

of the scaled lens length, κL and drift space, κS . It can be seen that peak acceptance occurs when there is no drift space — no gaps between successive lenses. As κS increases from zero the range of stable κL and the peak acceptance both decrease. Clearly, adding regions of no electric field has only an adverse effect of the focussing strength. Figure 6.2 also shows the line of stability (black line) which is the boundary between stable and unstable trajectories. This line was obtained from the criterion that the trace of the unit cell transfer matrix must be less than 2 for a trajectory to be stable.

Figure 6.3 (a) shows the 1D acceptance as a function of lens length in the case of no drift space. It can be shown [79] that in the case of a gapless guide the acceptance has the analytical form

$$A_{1D} (= \sqrt{A_{2D}}) = \frac{\pi \kappa \sqrt{1 - \cos^2(\kappa L) \cosh^2(\kappa L)}}{\cosh(\kappa L) \sinh(\kappa L) + \sinh(\kappa L)}. \quad (6.28)$$

Figure 6.3 (b) shows three example trajectories corresponding to three points on the acceptance curve of a harmonic, gapless guide. The red curve was calculated with $\kappa L = 0.4$, which corresponds to a guide comprising many very short lenses. This is manifested in the relatively high frequency micromotion. Because a molecule is only in a lens for a very short length its transverse position is only slightly altered, and so each successive lens exerts approximately the same magnitude of force on it. Consequently the macromotion envelope takes many lenses to build up. In this case the macromotion is a slowly oscillating large amplitude motion in which the molecule is only weakly focussed towards the beam-line axis. The large amplitude macromotion restricts the number of trajectories that can be stably guided without leaving the central region of the guide or crashing into the electrodes. As the lens length is increased the force imbalance between a focussing lens and its successive defocussing lens grows, which leads to a more pronounced micromotion, but modulated by a more rapidly varying, smaller amplitude macromotion as the overall

focussing is increased and the molecule is more tightly confined about the beam-line axis. The blue curve in figure 6.3 (b) is a molecular trajectory calculated for $\kappa L = 1.254$, which figure 6.3 (a) shows corresponds to the peak acceptance. In this case the increased κL has resulted in a more tightly confined trajectory. This tighter focussing allows more stable trajectories to fit into the aperture of the guide, leading to a large acceptance. The trajectory shown in green was calculated with $\kappa L = 1.85$. In this regime the molecules are overfocussed by the individual lenses, resulting in a large amplitude micromotion which increases the overall trajectory amplitude, thus reducing the acceptance, as shown by the position of the green point on the acceptance curve in figure 6.3 (a). Increasing κL further causes the micromotion to destabilise the trajectories: molecules are accelerated out of the guide by individual lenses, and there is no overall stable macromotion.

6.5 A realistic guide

6.5.1 Non-linear equations of motion

Section 6.4 considered a very specific electric field, designed to produce linear transverse forces. This is a simplification. The fields produced by realistic guides are more complicated. A typical AG guide consists of a system of electrodes held around and along the beam-line. The electrodes are positioned such that, when charged to high voltage the resulting field on the beam-line has a saddle shape in the transverse cross-section. Guiding can be achieved either by switching the electric field in space or time. In the former case the AG guide comprises a number of individual field stages (such as pairs of oppositely polarized electrodes) along the beam-line, with the transverse orientation of successive stages rotating by $\pi/2$. In the latter case the guide consists of one long field stage the length of the guide, with the electrodes' polarities switching in time to achieve an alternating gradient field along the beam-line.

In general the electric potential produced by an AG guide can be described by a multipole expansion [80] of the form

$$\Phi(x, y) = \Phi_0 \left(a_1 \frac{x}{r_0} + a_3 \frac{(x^3 - 3xy^2)}{3r_0^3} + a_5 \frac{x^5 - 10x^3y^2 + 5xy^4}{5r_0^5} \right), \quad (6.29)$$

where r_0 characterizes the size of the electrode structure and Φ_0 the magnitude of the applied voltage. a_1 , a_3 and a_5 are dimensionless expansion coefficients. Changing to scaled variables, $X = x/r_0$, $Y = y/r_0$, and assuming that $a_5 \ll a_3 \ll a_1$ an expression can be found for the corresponding electric field magnitude raised to some power, n :

$$\begin{aligned} |E(X, Y)|^n = E_0^n & \left(1 + a_3 n (X^2 - Y^2) + (a_3^2 n (3 - n) - 6a_5 n) X^2 Y^2 \right. \\ & \left. + (a_3^2 n (n - 1) / 2 + a_5 n) (X^4 + Y^4) + \dots \right). \end{aligned} \quad (6.30)$$

Ignoring higher order terms this field distribution has the property that raising the field magnitude to any power, n , makes no difference to the form of the field distribution. $|E(X, Y)|^n$ has the same form of transverse coordinate dependence; n changes only the relative amplitudes of the three expansion terms.

It was seen in section 2.6 that in the limit of weak electric field, the Stark shift is quadratic in E , $W_s = -\frac{1}{2}\alpha_m|E|^2$, and in the limit of strong field the shift is linear, $W_s = -\mu_m|E|$. The force exerted by an electric field on a molecule is $\vec{F} = -\vec{\nabla}W_s$. The equations of motion in one of the electric field lenses of a guide are thus

$$X''(Z) = \eta^2 (-GX + G^2\chi Y^2X + G^2\xi X^3), \quad (6.31)$$

$$Y''(Z) = \eta^2 (GY + G^2\chi X^2Y + G^2\xi Y^3), \quad (6.32)$$

where differentiation is with respect to the scaled longitudinal coordinate, $Z = z/r_0$. $G(Z)$ is a function that alternates between $+1$ and -1 in successive lenses, and is 0 in any drift space between lenses. η is the scaled transverse force constant, defined by $\kappa = \eta/r_0$. In the limit of a quadratic Stark shift $\chi = |a_3| - 6a_5/|a_3|$, $\xi = |a_3| + 2a_5/|a_3|$ and $\eta = \alpha E_0^2|a_3|/\frac{1}{2}m_{mol}v_z^2$; for a linear Stark shift $\chi = 2|a_3| - 6a_5/|a_3|$, $\xi = 2a_5/|a_3|$ and $\eta^2 = \mu E_0|a_3|/\frac{1}{2}m_{mol}v_z^2$. The three important parameters, a_3 , χ and ξ are thus related by

$$\chi + 3\xi = 2n|a_3|, \quad (6.33)$$

where $n = 1$ in the case of a linear Stark shift and $n = 2$ for a quadratic Stark shift.

In a field in which $a_5 \ll a_3 \ll a_1$ the force is predominantly linear in $\{X, Y\}$. Ignoring the anharmonic terms — the coupling terms (X^2Y , Y^2X) and the cubic terms (X^3 , Y^3) — equations 6.31 and 6.32 become the harmonic equations of motion discussed in section 6.4. In the limit of small anharmonic terms it might be tempting to ignore the anharmonic effects on molecular trajectories. However, the situation is not as simple as this. In a given transverse direction the linear force changes sign in successive lenses, causing net focussing as discussed in section 6.4.3. However, the anharmonic terms do not change sign, they constantly apply in the same direction (the anharmonic terms are multiplied by G^2 not G in the equations of motion (equations 6.31 and 6.32)). The anharmonic terms are constantly exerting a defocussing force away from the beam-line. This divergence will cause molecules to leave the central field region or crash into the electrodes, thus reducing the guide's acceptance. The next step might be to engineer an electric field which causes the anharmonic terms in the equations of motion to disappear. However, the above relations for χ and ξ show that this is not possible. For example, consider the case of a quadratic Stark shift. The coupling term will disappear if $a_5 = \frac{1}{3}|a_3|^2$, and the cubic term will disappear if $a_5 = -\frac{1}{2}|a_3|^2$. It is not possible to eliminate both terms simultaneously. The best that can be done is to create an AG guide in which the electrode dimensions and spacings are such that the net effect of both terms is minimal.

6.5.2 Effective potential

To describe the effects of the anharmonic terms on molecular motion, Tarbutt and Hinds [79] change variables in such a way as to generate an effective potential in the equations of motion. Consider the equations of motion above (equations 6.31 and 6.32). Define now the new coordinates g and h :

$$g = \frac{X(Z)}{\sqrt{\beta(Z)}} \quad (6.34)$$

$$h = \frac{1}{\Psi} \int_0^Z \frac{1}{\beta(\tilde{Z})} d\tilde{Z} = \frac{\phi}{\Psi}. \quad (6.35)$$

The definition of g divides out the micromotion and so describes the macromotion. h is a phase that describes motion along the beam-line in terms of the phase advance per cell. The X and Y components acquire phase differently as $\beta(Z)$ is different in an F lens than a D lens. Each component of transverse motion now needs to be described in terms of its own axial phase. Thus the motion of one transverse direction is described by the coordinates g_1 and h_1 , with β_1 , while the other is described by g_2 , h_2 and β_2 .

Applying the coordinate transformations to the full equations of motion (equations 6.31 and 6.32) in both directions gives

$$\ddot{g}_1 + \Psi^2 (g_1 - G^2 \xi \eta^2 \beta_1^3 g_1^3 - G^2 \chi \eta^2 \beta_1^2 \beta_2 g_2^2 g_1) = 0 \quad (6.36)$$

$$\ddot{g}_2 + \Psi^2 (g_2 - G^2 \xi \eta^2 \beta_2^3 g_2^3 - G^2 \chi \eta^2 \beta_2^2 \beta_1 g_1^2 g_2) = 0, \quad (6.37)$$

where the dots now denote differentiation with respect to h .

Having made this transformation, Tarbutt and Hinds [79] assume that the micromotion is much smaller in amplitude and period than the macromotion. This is indeed the case in an AG guide with lens lengths chosen to optimize the acceptance. In this regime $\beta(Z)$ can be assumed to be constant: $\beta_1 = \beta_2 = \beta_0$. Equation 6.24 then gives $\beta_0 = L_{cell}/\Psi$ and equation 6.35 gives $h_1 = h_2 = Z/\beta_0\Psi = Z/L_{cell}$. Because the micromotion period is much smaller than the macromotion G^2 oscillates very rapidly. In this approximation G^2 is replaced by its mean value², $\langle G^2 \rangle$. Thus, in the limit of small micromotion it can be seen that the effects of the individual lenses are ‘washed’ out. In this limit the equations of motion (6.36 and 6.37) become

$$\ddot{X} + \Psi^2 X - b_1 X^3 - b_2 Y^2 X = 0 \quad (6.38)$$

$$\ddot{Y} + \Psi^2 Y - b_1 Y^3 - b_2 X^2 Y = 0, \quad (6.39)$$

where $b_1 = \langle G^2 \rangle \xi \eta^2 L_{cell}^2$ and $b_2 = \langle G^2 \rangle \chi \eta^2 L_{cell}^2$. Note that the transverse variables have been transformed back to X and Y , but these are still functions of h and differentiation

²For a gapless guide this mean is simply unity. However, for a guide with regions of drift space, G^2 is sometimes zero, which will be reflected in the mean value of G^2 .

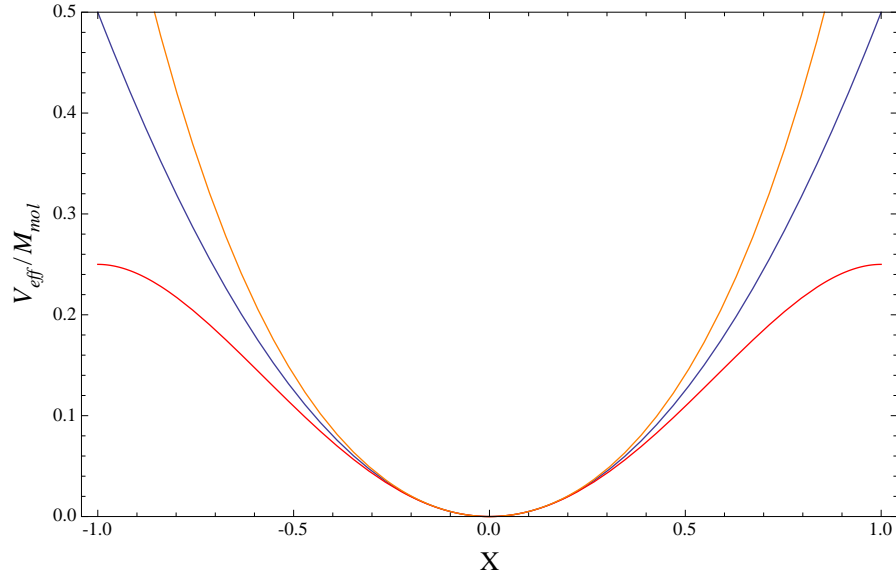


Figure 6.4: The effect of the cubic term on the effective potential along the transverse direction, X . The blue line shows the harmonic potential when $b_1 = 0$ (no cubic term). The red line shows the potential with $b_1 = 1$ and the orange line shows the potential with $b_1 = -1$. In all cases $\Psi = 1$ and the coupling term can be anything as this term is zero along the X and Y axes.

is with respect to h . It can be seen from these equations that the motion of a molecule in this limiting, but experimentally relevant case can be modelled in terms of motion in an effective potential, V_{eff} defined by

$$V_{eff}/M_{mol} = \frac{1}{2}\Psi^2 (X^2 + Y^2) - \frac{1}{4}b_1 (X^4 + Y^4) - \frac{1}{2}b_2 X^2 Y^2. \quad (6.40)$$

Equation 6.40 makes it clear how the anharmonic terms can degrade the height of the confining potential.

Cubic term

Consider firstly the effect of the cubic terms ($b_1 X^3$ and $b_1 Y^3$) in the equations of motion (6.38 and 6.39). Figure 6.4 shows how the effective potential along X changes as a result of the cubic term with both negative and positive values of b_1 . It can be seen that a cubic term with a positive coefficient (b_1) causes a smaller potential gradient away from $X = 0$ and eventually causes the potential to turn over at some distance, $X_C = \Psi/\sqrt{b_1}$ from the beam-line. Molecules whose trajectories take them outside X_C will not be guided; they will in fact be repelled from the beam-line along the major axes (X and Y). This decreased potential will reduce the number of confined trajectories and thus decrease the guide's acceptance. Furthermore, if the turnover at X_C occurs within the physical aperture of the guide (that is, if $X_C < d/2$) then the acceptance will be dramatically reduced. However,

the orange curve in figure 6.4 (generated with $b_1 = -1$) shows that a negative cubic term increases the steepness of the potential well and so can increase the acceptance.

Coupling term

The coupling terms (b_2X^2Y and b_2Y^2X) are a more complicated matter, whose effects are less easily explained in terms of analytical models. There are two main effects that a coupling term has on molecular trajectories, described in great detail numerically in [79]. However, Tarbutt and Hinds [79] have found qualitative explanations which describe the physical effects of this term.

The first effect is, as the name suggests, that the motions in the X and Y directions become coupled, resulting in a periodic transfer of energy from motion in one direction to the other. Consider a trajectory which fits into the guide when there is no coupling. When the coupling term is introduced energy can be transferred from motion in one transverse direction to the other such that the trajectory in this latter direction takes the molecule too far from the beam-line, crashing into an electrode or leaving the guide. In this way the coupling term can decrease the acceptance, and is found to decrease it regardless of the sign of b_2 [79]. The other effect can be described by the effective potential. Figure 6.5 (a) shows the effective potential in a guide in which there is a cubic term ($b_1 = 1$) but no coupling term ($b_2 = 0$). Figure 6.5 (b) shows the effect on the effective potential of a positive coupling term ($b_2 = 1.5$). The effect of the positive coupling term is to reduce the potential along the diagonals, in this example so much so that the potential at the corners turns over and ceases to be confining. This will reduce the acceptance in the same manner as the cubic term. However, figure 6.5 (c) shows that a negative coupling term ($b_2 = -1.5$ in this case) increases the slope of the potential well, thereby increasing the number of potentially confined trajectories, and thus the acceptance.

A detailed numerical investigation of the net effects of the coupling term [79] found that, for a weak coupling interaction, as the modulus of b_2 was increased from zero the acceptance dropped, both for negative and positive b_2 . This drop was caused by energy being transferred between the two transverse motions, an effect which can only decrease acceptance. In the case of a larger, positive coupling term the acceptance was found to drop quite rapidly, because of the increasingly unfavourable effective potential. However, for a negative coupling term it was found that, after a sudden, small drop in acceptance caused by transverse energy transfer, as b_2 was decreased further the effective potential became sufficiently more confining to balance the energy exchange losses. Consequently, for a negative coupling term the acceptance was found to be very insensitive to b_2 .

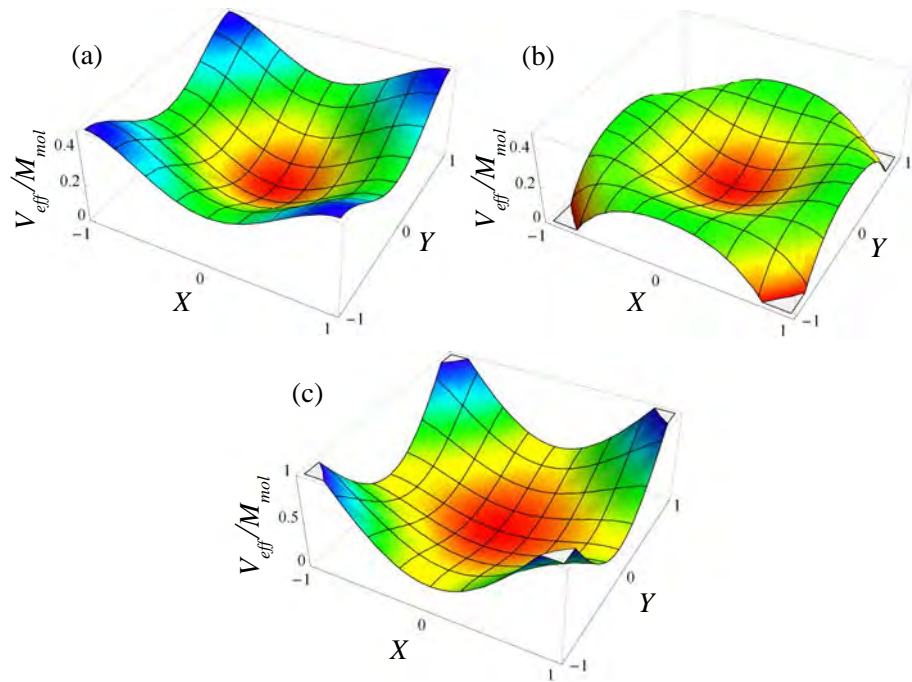


Figure 6.5: The shape of the effective potential in a guide with a cubic term ($b_1 = 1$) and (a) no coupling term ($b_2 = 0$); (b) a positive coupling term ($b_2 = 1.5$); and (c) a negative coupling term ($b_2 = -1.5$). Note the larger scale on the V_{eff}/M_{mol} axis in (c).

Optimal acceptance

The question of the values of the parameters, a_3 , χ , ξ in the equations of motion (6.31 and 6.32) that maximize a guide's acceptance is not a trivial one, and has been treated in detail in [79]. Equation 6.28 states that, for a harmonic guide $A_{2D} \propto \kappa^2$. In the limit of strong electric field $\kappa^2 \propto |a_3|$ (as discussed in section 6.5.1). Therefore, the two-dimensional acceptance of a purely harmonic guide is proportional to $|a_3|$, and so it might seem that to maximize a_3 is to optimize the acceptance. However, when anharmonic terms are considered the matter becomes complicated. It was shown above that the three parameters are linked by $\chi + 3\xi = 2n|a_3|$ (equation 6.33), where n is the power of the E-field in the Stark shift dependence. It can be seen that a large a_3 necessarily leads to a large sum of the anharmonic terms. Consider the case in which this sum contains a large value of χ . This leads to a large drop in acceptance through the transfer of transverse motion energies as well as a shallow effective potential well. Decreasing the value of χ by increasing ξ gains little as this increases the cubic term, which again leads to a shallow effective potential.

In [79] the best parameters were investigated by numerical simulations. The conclusion found is that a good guide should have the parameters $a_3 \simeq 0.11$, $\xi \simeq 0.075$, and $\chi \simeq -0.005$. Note that the optimal acceptance is found to occur when the coupling term is close to zero.

6.6 Experimental details

In this experiment ground state CaF radicals were transported from the source region to the detection region by a 1m long AG guide [85]. Figure 6.6 shows photographs of the guide while being cleaned, prior to its installation in the vacuum chamber. The guide comprises four 1m long electrodes — stainless steels rods with circular cross-section, radius 3mm, and spherically rounded ends (radius 3mm). The electrodes are arranged parallel to the beam-line axis. In transverse cross-section the electrodes are arranged on the vertices of a square of side 7.87 mm (the guide was aligned such that the centre of the square corresponded to the beam-line axis, and so the molecular beam was centred on the guide's aperture). A 1 m-long, 3 mm-radius stainless steel rod is quite flexible, and will bow noticeably when held horizontally at both ends. In order to achieve the best parallel alignment each electrode was held in place by a much more rigid 1 m-long, 16 mm-diameter steel support rod. The rods were attached at both ends to thick steel support rings by insulating ceramic stand-offs. The support rods were located at the vertices of a square with side 33.9 mm and centred on the same square which locates the electrodes. Each electrode is attached to its support rods by five steel dowels at positions equally spaced along the electrode (if one end of an electrode is located at $z = 0$ cm and

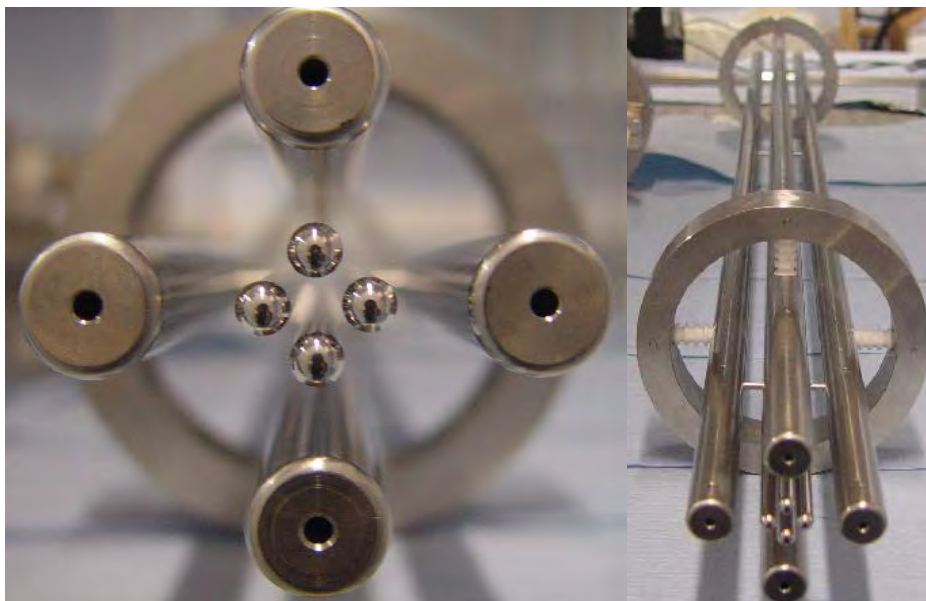


Figure 6.6: Two photographs of the AG guide.

the other at $z = 100$ cm, the dowels were located at positions $z = 10$ cm, $z = 30$ cm, $z = 50$ cm, $z = 70$ cm and $z = 90$ cm). Despite this arrangement, the electrodes were observed to suffer from a certain amount of ‘bendiness’. The dowels held the electrodes at fixed positions at the five positions listed above, but in between these positions the electrodes were observed to bow in and out, each electrode assuming a wave-like shape, with the wave vertices located at the dowel positions. The nearest separation between two electrodes was on average $7.87 - 3 - 3 = 1.87$ mm as discussed above. However, all four nearest neighbour spacings were measured with calibrated slip-gauges at 11 positions along the length of the guide (the five dowel positions, the four positions symmetrically between two dowel positions and both ends of the guide). It was found that the smallest gap between electrodes occurred at the centre of the guide, where distances approximately 5% smaller than the mean were measured. The electrodes were observed to splay outwards at the ends, where the electrode spacings were measured to be around 15% greater than the mean spacing.

The guide was located in the main chamber, with its front end 55 mm downstream of the skimmer and its far end 90 mm upstream of the centre of the detection region (that is, the centre of the probe laser beam). The source-to-detector distance was 1215 mm. Figure 6.7 shows the experimental set-up in the guiding experiment. The orientation of the guide determined the coordinate axes: z points along the direction of the molecular beam; x and y both make an angle of $\pi/4$ with the horizontal.

The molecules were detected by laser-induced fluorescence (LIF), with the probe laser scanning over the $Q_{11}(\frac{1}{2})$ transitions from the two ground state hyperfine levels ($F = 1$

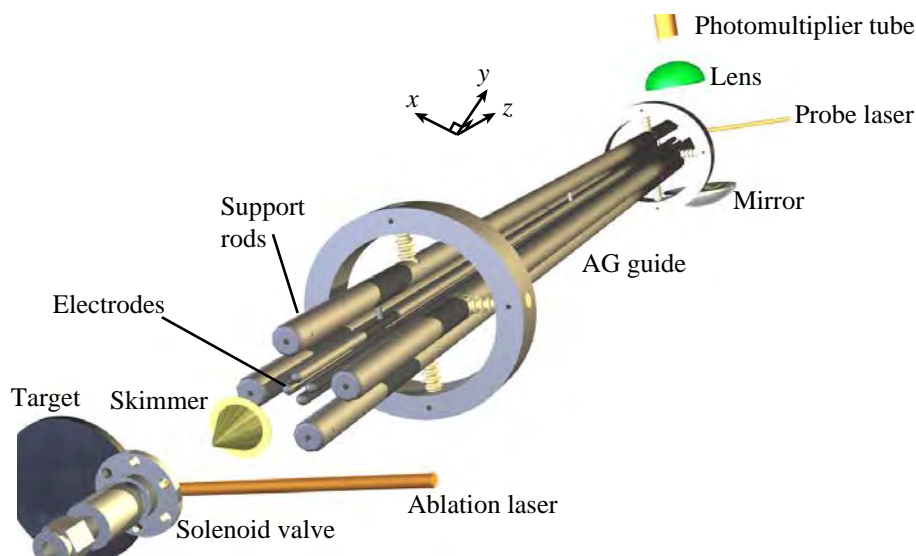


Figure 6.7: Set-up of the AG guiding experiment. The source-to-detector distance was 1.215 m.

and $F = 0$). The probe laser beam was shaped to have a roughly top-hat intensity profile with circular cross section, diameter 2.8 mm. The beam power was measured to be around $220 \mu\text{W}$. The laser beam travels along the horizontal. It is linearly polarized in the vertical direction (making a $\pi/4$ radian angle with the x -axis). Located 45 mm upstream of the detection region was a 5.8 mm-diameter aperture, the purpose of which was to limit the divergence of the detected beam. The aperture also proved useful in an investigation of DC-focussing of molecules into the detection region (section 6.9).

Each electrode was connected via high voltage (HV) feedthroughs to the output of a positive or negative HV power supply. Two diagonally-opposite electrodes were connected directly to a positive and a negative HV power supply respectively. The other two were each connected to the output of a HV switch (the same switches as used with the weak-field decelerator). One side of each switch was connected to a positive HV supply and the other to a negative supply. The switches were operated such that when one electrode was held at positive HV the other was held at negative HV. Switching both switches simultaneously flips the polarity of the two diagonal electrodes. The switches were rated for a maximum potential difference of 20 kV, limiting the polarity of the electrodes to ± 10 kV. The guide was operated in two switch states, shown in figure 6.8. In state 1 the two electrodes on the left of the figure are polarized to some positive HV (10 kV in this example) and the right-hand two electrodes are polarized to the same magnitude voltage, but negative. This results in a saddle-shaped electric field distribution which has a minimum in the x -direction and a maximum in the y -direction. In state 2 the polarity of two diagonal electrodes has been flipped, thus rotating the electric field by $\pi/2$. These two states are the focussing and defocussing lenses. The field was never switched off and so this was a

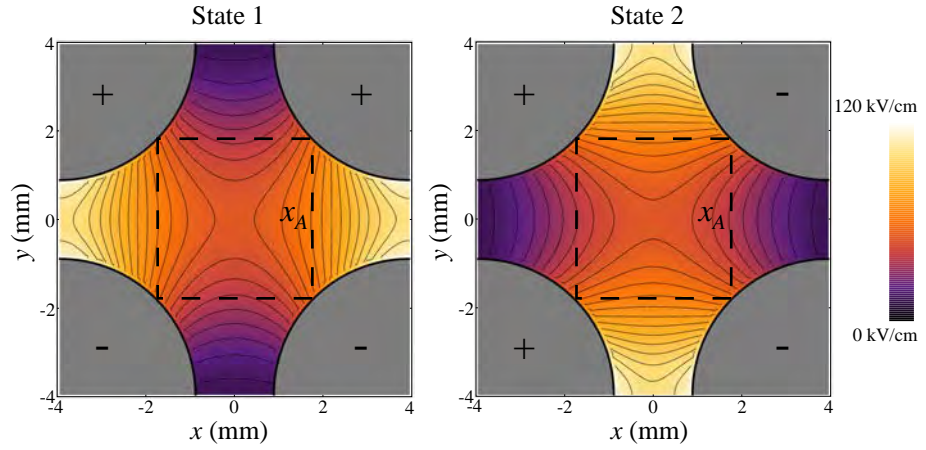


Figure 6.8: The electric field inside the the guide, calculated by a finite element analysis for the guide charged to ± 10 kV. The square (dashed line) of side x_A defines the acceptance area for the analytical models described in figure 6.9.

gapless guide (no drift space). The guide was used on Ar-buffered beams of CaF, with a central speed of 605 m/s. Holding the electrodes in one state for a given time, T , exposed the molecules to a given lens for that time, corresponding to a lens length of $L = T \times v_z$. The fractional width of the speed distribution, v_z in the measured time-of-flight profiles was sufficiently small that most of the molecules experienced the same lens durations. However, it was observed that the molecular speed distribution had a small effect on the experimental data, as discussed in section 6.8.

The probe beam was sufficiently intense that the amplitudes of the $F = 1$ and $F = 0$ peaks (see figure 4.5 for an example) are well saturated. The LIF signal was thus proportional to the number of molecules exiting the guide. The $F = 1$ peak amplitude is considerably larger than that of the $F = 0$ peak (by a factor of 4.5 – see section 4.5) and so the $F = 1$ peak amplitude was chosen as the measure of the number of transmitted molecules. In order to account for signal variation from changes in molecular flux (see section 4.4.5) the shots in a spectral scan alternated between those in which the AG guide was operated, and those in which the guide was turned off, and the electrodes grounded. Over the course of a scan the $F = 1$ peak amplitude measured with the guide turned off served as a reference amplitude. Dividing the ‘AG guided’ amplitude by the reference amplitude gave a measure of the number of guided molecules, unaffected by source variation. This number is referred to as the ‘signal ratio’.

In order to characterize the guide the amplitude was measured over a range of lens durations for a given applied voltage. Three voltages were applied: 5.5 kV, 8 kV and 9.5 kV.

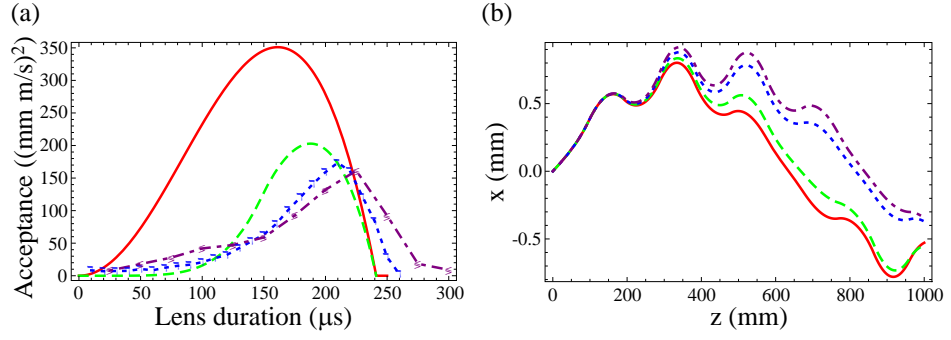


Figure 6.9: (a) The acceptance and (b) an example trajectory for the constructed AG guide calculated by four different models. The red curves show the results of the analytical Courant-Snyder model for a harmonic guide. The green dashed data show the result of an analytical model including the harmonic and cubic terms. The blue dashed data were calculated with a numerical model including the harmonic, cubic and coupling terms. Finally, the purple dot-dashed data show the results of a full numerical model, including the full electric field distribution and shape and a complete numerical Stark shift.

6.7 Modelling the AG guide

The shape of the electric field generated by the guide was calculated by a finite element model. Fitting this shape to an electric field function of the form shown in equation 6.30 with $n = 1$ (neglecting higher order terms not shown in equation 6.30) yields the best fit values $E_0 = 4.395V$ kV/cm, $a_3 = 0.120$ and $a_5 = 0.0022$, where V is the modulus of the voltage applied to the electrodes, measured in kV. These numbers lead to values of the cubic and coupling terms parameters of $\chi = 0.131$ and $\xi = 0.0363$ respectively. These values do not lie far from the ‘optimal’ values calculated for a guide operated with $\kappa L = 1$ (section 6.5.2).

To investigate the effect of the AG guide on molecular trajectories simulations were performed, including a varying number of the terms in the electric field expansion (equation 6.30). These simulations were performed with an applied voltage of ± 8 kV to the electrodes. In the limit of a harmonic field (ignoring the cubic and coupling terms) this voltage can be characterized in terms of the scaled harmonic force constant $\kappa = 12.9 \text{ m}^{-1}$. Figure 6.9 shows the simulated effects of the non-linear terms on the guide’s acceptance and on an example trajectory. The case of the purely harmonic guide has been treated analytically and the results shown as the red curves in figures 6.9 (a) and (b). Figure 6.9 (a) shows the acceptance calculated for the guide. It has the exactly the form described in section 6.4. The aperture used to define the acceptance was the box of side x_A bounded by the electrodes shown in figure 6.8.

It has been shown [79] that when only the harmonic and cubic terms are included an

analytical expression for the acceptance can be found. This was calculated for the guide with $\xi = 0.0363$, $\chi = 0$, and with the same aperture as in the harmonic case. It is shown as the green dashed curve in figure 6.9 (a). The acceptance has clearly been reduced for almost all lens durations. This is a result of the shallower effective potential well from the positive cubic term. The acceptance was most reduced for small lens durations; in this regime the macromotion focussing is already weak and so the cubic term has a large effect, knocking out a large proportion of the trajectories. As a result the lens duration that gives maximum acceptance is increased from that in the purely harmonic case. The green dashed curve in figure 6.9 (b) shows the effect of the cubic term on the trajectory. The macromotion amplitude has clearly increased, a result of the weaker effective potential well.

When the coupling term is included the acceptance must be treated numerically. For the purposes of comparison with the two previous acceptance curves the acceptance including the coupling term was calculated with the same square aperture. The resulting acceptance and example trajectory are shown by the blue dotted line. The coupling term reduces the acceptance further, but not by the same amount as the cubic term. The example trajectory's macromotion amplitude is seen to have increased, a result of the further weakened effective potential well and the coupling of transverse energies. Note that in the numerical 'cubic-and-coupling' model (blue dotted line) the acceptance was found to have increased in the short and long lens duration limits compared with the analytical cubic model. This is because the two analytical models were calculated for an infinitely long guide, whereas the numerical model realistically assumes a 1m long guide. In this latter case there are trajectories that are not 'infinitely' stable, but are able to survive for 1 m. These effects are most obvious in the limits of short and long lenses because in these regimes there are proportionally many more 'disallowed' trajectories than for intermediate lens durations.

Finally the purple dot-dashed curves in figure 6.9 show the results of full numerical simulations. The full area of the field was considered (not just that area within the square of side x_A) and the Stark shift was calculated numerically, not assumed to be purely linear as in the above simulations. The electric field was considered exactly, thus including the higher order terms neglected so far (equation 6.30). Again, the guide was taken to be 1 m long. The resulting acceptance and example trajectory are very similar to those derived from the numerical cubic-and-coupling model, thus showing the relative insignificance of the higher order terms. Nevertheless these terms do decrease the effective potential well depth slightly, and so are seen to reduce the acceptance slightly and increase the macromotion amplitude of the example trajectory.

6.8 AG results

Figure 6.10 shows the measured signal ratio as a function of lens duration, τ , for the three voltages applied to the guide. Each point corresponds to the weighted mean of many $F = 1$ amplitude signal ratios. The error bars originate in the error on the individual peak fits which are then combined in the weighted mean to give a standard error. Qualitatively the shape of the signal flux data match well the shape of the simulated acceptance plots shown in figure 6.9. It was shown in section 6.4.3 that in the harmonic approximation the peak acceptance occurs for a given value of κL . Since the speed along the guide, v_z , is constant, it is possible to use the equivalent parameter, $\Omega\tau (= \kappa L)$, where $\Omega = \kappa v_z$ is the harmonic trapping frequency. τ is the time that the molecules spend inside each lens, known as the lens duration. Ω is proportional to $\sqrt{E_0}$ and so increasing the applied voltage will increase Ω and thus decrease the optimal lens duration. The data confirm this, showing that as the voltage was increased the optimal lens duration decreased, maintaining the maximum acceptance at around $\Omega\tau \simeq 1.5$. This is greater than the value predicted for a harmonic guide ($\Omega\tau = 1.254$) as a result of the anharmonic terms, as discussed in section 6.7. It can also be seen that the maximum signal ratio increases with increasing voltage. There is no analytical expression for how the peak acceptance depends on voltage for a realistic (anharmonic) guide, however, it was stated in equation 6.28 that the two-dimensional acceptance of a gapless harmonic guide is proportional to κ^2 and thus is proportional to Ω^2 . The harmonic frequency for the three voltages was calculated to be 6120 rad s⁻¹ at 5.5 kV, 7776 rad s⁻¹ at 8.0 kV, and 8640 rad s⁻¹ at 9.5 kV. Thus, when increasing the voltage from 5.5 kV to 8.0 kV there would be an expected increase in peak acceptance of $(7776/6120)^2 \simeq 1.6$. The increase in peak signal ratio from the 5.5 kV dataset to the 8.0 kV dataset is observed to be 1.6, in good agreement with the harmonic model. Further increasing the voltage from 8.0 kV to 9.5 kV it would be expected that the acceptance should increase by a factor of $(8640/7776)^2 \simeq 1.2$. However, the data show no observed increase in peak signal ratio between these two datasets.

The signal ratio data were simulated as follows. The molecular source at the valve nozzle was modelled by a large ensemble of ground-state molecules with gaussian position and speed distributions along the transverse directions. The transverse position and speed distributions had their respective centres on the beam-line and had full-width half-maxima (FWHM) of 4.7 mm and 38 ms⁻¹. These widths are a source of uncertainty in the simulations as relatively little is known about the molecular source, especially in the transverse directions. However, these numbers can be estimated from what is known of the supersonic expansion and the Doppler width of the spectral peaks in the LIF signal. It was found that changing these parameters within the range of reasonable values made little difference to the simulation results. The molecules were assumed to start at the same

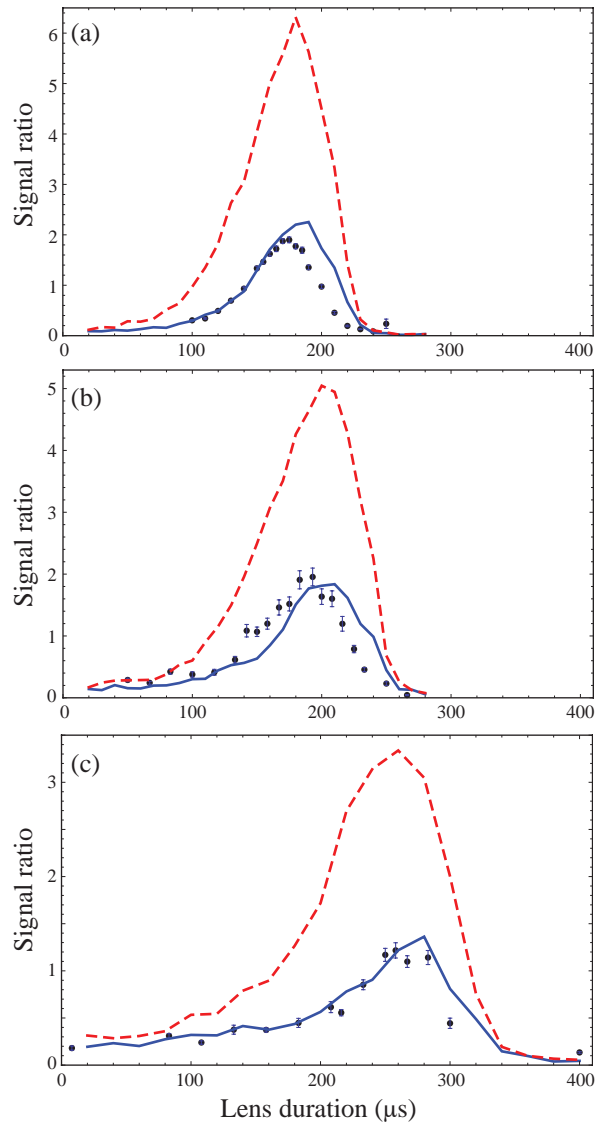


Figure 6.10: Experimental data (blue points) showing measured signal ratio versus lens duration. (a), (b) and (c) show the data for 5.5 kV, 8.0 kV and 9.5 kV respectively. The results of full numerical simulations are also shown (red dashed curve) as well as simulations including a 2 mm misalignment of the laser probe beam (blue curve).

longitudinal position, $z = 0$ and speed, $v_z = 605\text{ms}^{-1}$. The molecules were then propagated forwards to the skimmer. The beam of molecules that made it through the skimmer were then propagated up to and through the guide. Those molecules whose trajectories took them out of the guide, never to return, or that crashed into the electrodes were then discounted. The successful molecules that traversed the guide were then propagated to the aperture, and those that made it through were propagated to the detection region where their interaction with the probe beam was modelled in the same way as in the saturation of LIF experiment (chapter 4), and using the molecular parameters found in that experiment. The molecular state population rate equations were simplified by considering the molecules to be only three-level systems.

The effect of the bendiness of the guide was crudely accounted for in the simulations. It would be extremely time-consuming to account for the changing electric field shape as the electrode spacing varied. Consequently a much faster method was employed in which the entire geometry of the electrodes and the subsequent field was scaled along the length of the guide by the same scaling factor that was measured for the guide. The simulations shown in figure 6.10 include this variable scaling factor to account for the type of bendiness measured in the guide.

The electric fields produced at the ends of the electrodes are clearly of different shape to that inside the guide. Indeed, the electric field varies along z at the ends, and so in these regions the molecules will experience a slight acceleration when they enter the guide and an identical deceleration on leaving the guide. These effects were considered to be negligible. Simulations were performed which both accounted for and ignored the end-fields respectively and negligible difference was found in the results. For completeness the simulations shown here do include the end-fields.

The simulations were designed to match as closely as possible the experimental procedure. For a given voltage and lens duration the number of photons scattered by the molecules that successfully made it to the detection region was calculated over a range of frequencies, thus building up a spectral scan over the same frequency range as in the experimental data. This scan was then fitted to a double Lorentzian lineshape. The procedure was then performed for a simulation with a grounded AG guide. The quotient of the $F = 1$ peak amplitudes for these two simulations was the signal ratio, calculated in the same way as in the experimental data. The resulting simulated signal ratio data are shown in figure 6.10 along with the experimental data. It can be seen that, for each voltage, the shape of the simulated data is similar to that of the experimental data. In particular, the experiments and simulations agree well on the optimal lens durations. However, the simulations predict much greater signal ratios than were measured. Reasons for these discrepancies include uncertainties in the simulated beam source, electrode misalignment, the bendiness of the guide, and misalignment of the probe laser. It was found that reduc-

ing the divergence of the simulated molecular beam reduced the measured signal ratios. This makes sense as the ratio is the quotient of guided molecules to non-guided molecules. With the guide turned off, reducing the divergence of the beam will clearly increase the flux of molecules able to traverse the guide. This reduces the signal ratio. However, it was found that reducing the beam divergence changed the shape of the simulated signal ratio data. It was found that, for a given voltage, to make the peak simulated signal ratio match that in the experimental data required a source with far too small a divergence to be reasonable, and caused the signal ratio data shape to differ substantially from that measured. It was concluded that the source distribution parameters described above gave the best agreement with the shape of the measured data and the position of the peak signal ratio.

The possibility of a misalignment between the probe laser beam and the guide orientation was investigated and found to be a likely cause of the disparity in the size of simulated and measured signal ratios. The laser beam enters the vacuum chamber through a Brewster window on the end of a 250 mm-long tube. Having traversed the detection region the laser beam then leaves the vacuum chamber through an identical Brewster window on the other side of the vacuum chamber. Inside the tubes are baffles designed to reduce the background scatter from room lights. The vertical distance through which the probe laser beam can be moved is thus severely limited before scattering off the baffles causes a huge rise in the LIF background signal. The AG guide was aligned when it was placed in the chamber. This process was performed at room pressure with the source chamber removed. Cross-hairs were used to mark the transverse centre of the beginning and end of the main chamber³. A theodolite was aligned with both sets of cross-hairs. By viewing the image formed by the telescope while varying its focus it was possible to view the alignment of the electrodes down the entire length of the guide. Both ends of the guide could be moved vertically and horizontally by fine-adjustment screws on which the cradle holding the guide was resting. This procedure should align both ends of the guide to within 1mm. However, introducing a vertical misalignment between the guide and the probe beam of 2 mm was found to bring the simulated signal ratios into much better agreement with the measured data. The simulated results including a 2 mm probe misalignment are shown by the blue lines in figure 6.10. The signal ratio shape and peak value agree much better with the measured values when this misalignment is included.

However, the threshold lens duration in the limit of long τ was still found to be greater in the simulations. The trajectories in this limit are very sensitive to electrode misalignments as they are dominated by the micromotion caused by the individual lenses. Any change in field strength between successive lenses will lead to an imbalance in the

³A window in the far end of the main chamber was marked with cross-hairs and light shone through to illuminate these cross-hairs, as well as those at the upstream end of the main chamber.

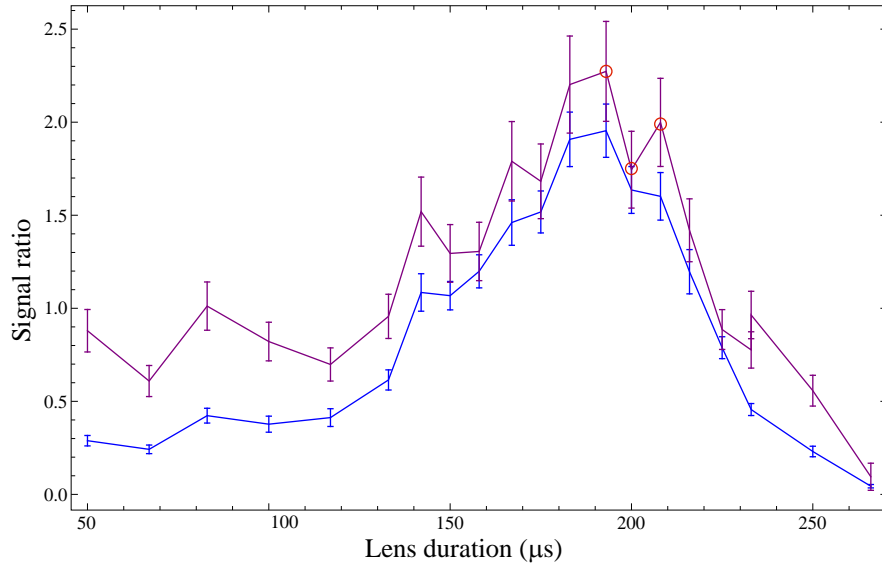


Figure 6.11: The $F = 1$ peak amplitude (blue data) and area (purple data) signal ratios measured with the guide operated at 8.0 kV. The data-points are joined to guide the eye. Three points in the area data are highlighted by red circles. These data-points will be discussed in greater detail.

lens forces and can easily destabilise a trajectory. Simulating the signal ratio data without including the guide's bendiness causes the predicted threshold lens duration to increase further, implying that the discrepancy shown in figure 6.10 results from the bendiness of the guide's electrodes.

Phase effects

Close inspection of the experimental data in figure 6.10 shows a slight modulation of peak amplitude signal ratios on top of the expected variation in lens duration. Figure 6.11 shows the $F = 1$ peak amplitude signal ratio data taken at 8.0 kV. Also shown are the $F = 1$ area ratios (the ratio of the area under the $F = 1$ peak with the guide on to the area with the guide off). The area data are more strongly modulated than the amplitude data. The error bars on the area data are larger than those on the amplitude data because of the non-linearity of the laser scan. This leads to a large error in the width that increases the error on the area measurement. Modulation in the amplitude data would result from a modulation in the number of molecules being transported into the detection region. The more pronounced modulation evident in the area signal ratio data suggests that the Doppler broadening of the spectral line is modulated, reflecting a modulation in the beam divergence at the detector. This happens because the AG guide focusses molecules into the detection region. The square wave high voltage pattern used to switch the guide always started at the same time, and continued until after the molecular packet had left

the guide. The observed signal modulation is due to the phase of the square wave at the time when the molecules enter and leave the guide. This phase depends on the switching frequency. The ellipses that describe the acceptance of the guide in $\{x, v_x\}$ and $\{y, v_y\}$ phase space depend on this phase. The overlap between the phase space volume occupied by the incoming molecules and the acceptance of the guide determines the number of molecules that can be guided. Of the molecules that survive to the end of the guide, only those that are focussed through the aperture and into the probe beam can be detected. The degree of focussing depends on the phase of the square wave at the moment when the molecules leave the guide. The effect of this last lens will be more important in a guide with long lens durations, where the molecules are strongly focussed and defocussed by the individual lenses.

To investigate the cause of the signal ratio modulation consider the phase of the HV switching pattern at the time that the molecules enter and exit the guide. The molecular beam is not mono-energetic along z : the Ar-buffered beam in the guide experiments typically has a mean speed of 605 ms^{-1} and a FWHM of 40 ms^{-1} . Figure 6.12 shows the HV guiding pattern for three lens durations from the 8.0 kV dataset. The lens durations are $193 \text{ }\mu\text{s}$, $200 \text{ }\mu\text{s}$ and $208 \text{ }\mu\text{s}$, which correspond to a peak, a trough and a peak in the signal modulation respectively. These three points are identified in the area data on figure 6.11 by red circles. The blue line in figure 6.12 (a) shows the switching HV pattern sent to the guide with the lens duration set to $193 \text{ }\mu\text{s}$. The pattern alternates between states 1 and 2. The red line represents the time that molecules with a speed of 605 ms^{-1} spend in the guide: the line goes high when they are in the guide. The green and orange lines show the same, but for the 625 ms^{-1} and 585 ms^{-1} velocity groups respectively. Note that the start of the guide is close enough to the source that these three characteristic velocity groups enter the guide at approximately the same time (between $203 \text{ }\mu\text{s}$ and $217 \text{ }\mu\text{s}$), but by the time they leave they are spread out, with the 625 ms^{-1} group leaving the guide at $1803 \text{ }\mu\text{s}$ and the 585 ms^{-1} leaving at $1926 \text{ }\mu\text{s}$. Figure 6.12 (a) and (c) both correspond to HV patterns that give maxima in the signal modulation. In both of these cases the molecules entered the guide at the start of a lens. Figure 6.12 (b) corresponds to a HV pattern that leads to a minimum in the signal modulation. It shows that the molecules entered in the middle of a lens. Similar analysis of the timing sequences for the rest of the 8.0 kV data indicate that this is the dominant effect in the modulation pattern: if the molecules entered the guide at the start of a lens it is likely that there will be a maximum in the modulation. This indicates that the overlap of the guide's acceptance and the phase space distribution of the incoming molecules is important in transporting high fluxes of molecules using an AG guide. The phase of the molecules in the HV pattern when leaving the guide is found to have a weaker effect on the modulation. This is due, at least partly, to the spread of the molecules when leaving the guide: some velocity groups

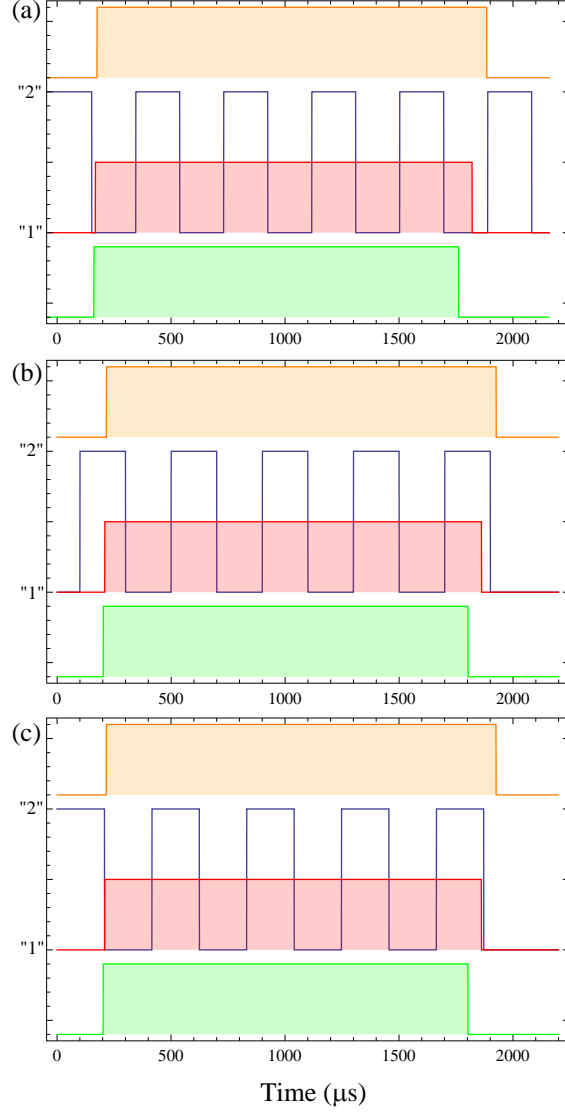


Figure 6.12: The HV switching pattern (blue line) for three different lens durations: (a) $193 \mu\text{s}$; (b) $200 \mu\text{s}$; (c) $208 \mu\text{s}$. The pattern shows how the AG guide switches between states “1” and “2” for these lens durations. The green, red and orange lines show the position of the velocity groups 585 ms^{-1} , 605 ms^{-1} and 625 ms^{-1} respectively. When the lines are high the molecules are inside the guide. Note that the three velocity groups enter the guide at roughly the same time, but their exit times are spread over $123 \mu\text{s}$.

will be in a beneficial position in a lens to be focussed into the detection region, whereas other velocity groups will not be. The effect of the end of the guide is thus ‘washed out’ by the spread of the molecules.

6.9 DC results

Despite the large effects that the non-linear terms have on the acceptance curve (figure 6.9) the shape of the curve is always the same: for very short lenses the acceptance is small; as the lenses get longer the acceptance increases, eventually reaching a maximum after which it rapidly falls to zero. For values of $\Omega\tau$ greater than the cut-off there are no stable trajectories. The full numerical simulation shown in figure 6.9 gives a cut-off of $\Omega\tau = 2.33$. If the guide is kept in one state for the whole duration that the molecules are inside it the guide acts as a single lens, focussing in one direction and defocussing in the other. In order for any molecules to make it out of the guide the voltage must be very low, as the molecules are going to be constantly defocussed out of the guide in one direction over its entire length. In other words, for a lens duration long enough such that all the molecules see one lens, the value of Ω (and thus the applied voltage) must be small for there to be stable trajectories. The linear acceptance curve for a very long guide comprising 1 m-long lenses gives this critical voltage to be 0.74 kV, beyond which no molecules are guided successfully. To investigate this the AG guide was operated in ‘DC’ mode: the guide was held in one state at high voltage for the entire duration from the Q-switch until after the detection had occurred. This was performed at variable voltage. The data were taken and analysed in the same way as above: the laser was scanned over the $F = 1$ and $F = 0$ peaks; the resulting spectrum was fitted to a double-Lorentzian from which the $F = 1$ peak amplitude was found and used as a measure of the number of guided molecules. The ratio of the amplitude with the guide turned on at some constant voltage and with it grounded defines the signal ratio. Figure 6.13 shows the measured signal ratio as a function of applied voltage. As the voltage is increased from zero the signal ratio drops, as might be expected. However, it drops very much more slowly than the linear model predicts. The signal ratio drops to a minimum of 0.23 at 2.5 kV and then starts to rise again, reaching a maximum of 0.64 at 5.5 kV, before finally dropping again. This is a surprising results.

To understand it, the experiment was modelled numerically in exactly the same way as the AG guiding experiment in section 6.8, except the model here ignored the end-fields and the bendiness of the guide. The results are shown by the red dashed curve in figure 6.13. The simulation agrees well with the experimental data between 0 V and 2.5 kV. After this point, as the applied voltage is increased, the simulated signal ratio rises more rapidly, peaking around 1 at 4.25 kV, before dropping again to zero. For applied voltages

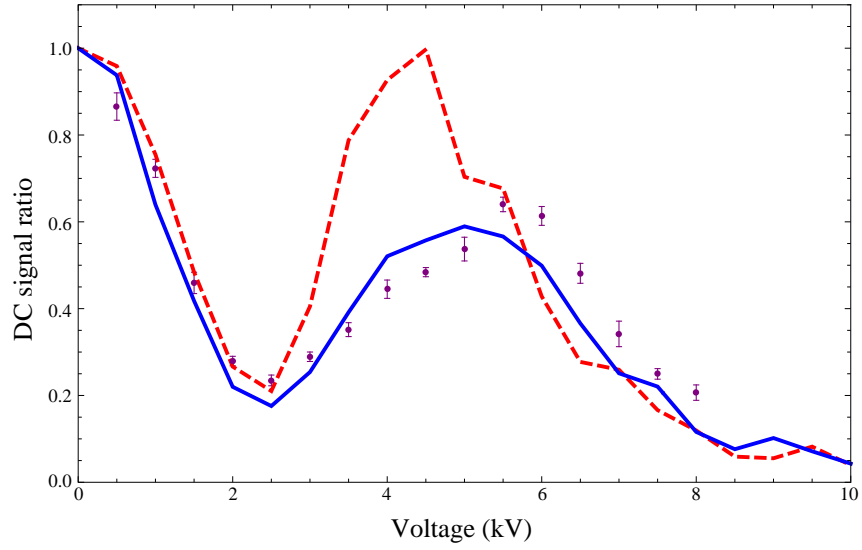


Figure 6.13: The signal ratio with the AG guide used in ‘DC’ mode, in which it acts as a single 1 m-long lens. The purple points show the experimental data. The red dashed line shows the results of full numerical simulations, exactly the same in form as those for the above guiding data (figure 6.10), except now the ends of the electrodes and the guide’s ‘bendiness’ are not accounted for. The blue solid line shows the results of simulations with the probe laser beam misaligned vertically by 2 mm, again exactly as above.

greater than 5.5 kV the simulations agree better with the experimental data, although they predict slightly smaller signal ratios in this region. As well as predicting a greater peak signal ratio the shape of the simulated signal ratio data is different from the experimental data. Repeating the simulations, but with the probe beam misaligned by 2 mm vertically (exactly as before) brings the simulation results into much better agreement with the data (blue solid line in figure 6.13).

The explanation for this behaviour comes from literally thinking outside the box. The acceptance calculated by the linear, cubic, and ‘cubic-and-coupling’ models (figure 6.9) is defined by the square of side x_a bounded by the electrodes, and covering most of the inside of the guide (figure 6.8). Any molecule that leaves this square is considered to have left the guide, never to return. The full numerical simulations of both the switching AG guide and the DC guide include the full electric field inside and around the guide. This field map is shown in figure 6.14 (a), calculated with the electrodes charged to ± 10 kV. It can be seen that along the x -axis there is a maximum of electric field in the centre of the guide exactly as expected. Along the y -axis there is a minimum of electric field in the centre of the guide, with the field strength reaching a maximum in the region between the oppositely-polarized electrodes. However, travelling further from the centre of the guide the field strength decreases again.

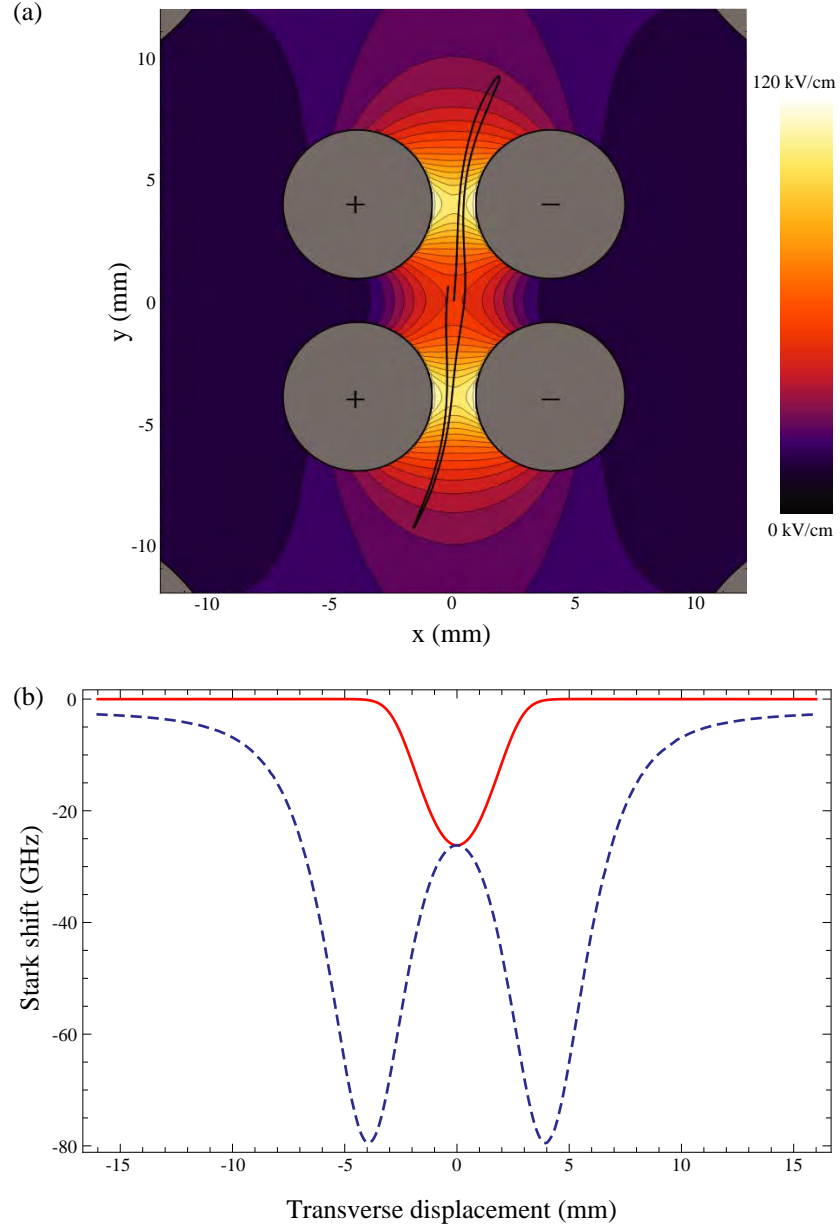


Figure 6.14: (a) The electric field produced by the guide charged to ± 10 kV. The field was calculated by a finite element model that included the full structure of the guide (electrodes shown in grey), including its grounded support rods (shown in grey and just visible in the corners of the field-map). Also shown is an example trajectory (black line) made by a molecule with initial transverse speeds $v_x = 1 \text{ ms}^{-1}$ and $v_y = 13 \text{ ms}^{-1}$, and when a static voltage of ± 6 kV is applied to the electrodes. (b) The Stark shift experienced by ground-state CaF along the lines $y = 0$ (red line) and $x = 0$ (blue dashed line) with ± 8 kV applied to the electrodes.

The resulting Stark shifts experienced by ground-state CaF along the x - and y -axes are shown in figure 6.14 (b) for applied voltages of ± 8 kV. Along the x -axis CaF molecules experience a minimum of Stark shift in the centre of the guide and are thus focussed towards the beam-axis in this direction. Along the y -axis there is a maximum of Stark shift on the beam line, surrounded by minima between the two oppositely polarized electrodes. There are some quasi-stable trajectories, such as the one shown in figure 6.14 (a), where the molecules can oscillate in the vertical direction without crashing into the electrodes. The molecule shown in figure 6.14 (a) survives for 3.7 ms which is much longer than a 600 ms^{-1} molecule takes to travel the length of the guide. This duration was chosen to illustrate the form of the motion exhibited by the DC-guided molecules. Simulations show that many similar trajectories can survive for hundreds of milliseconds. The molecule shown has a very small transverse speed along x (1 ms^{-1}) — if it didn't it would quickly be accelerated onto the surface of an electrode, or permanently out of the guide. The speed along y (13 ms^{-1}) is about half the maximum transverse speed in the simulated source distribution. The molecule's motion along the y -direction can be explained with reference to the double-well potential shown in figure 6.14 (b). The molecule enters the guide on the beam-line axis. It is then accelerated towards the minimum of one of the Stark potential wells. It overshoots this minimum, decelerates, and is then accelerated back towards the centre of the same potential well. Overshooting again the molecule is then accelerated towards the centre of the other potential well. The same behaviour of overshooting and decelerating is then repeated, bringing the molecule back to the beam-line axis.

Only a limited volume of initial phase space can supply molecules for these DC-guided trajectories. v_x must be small to allow for motion predominantly along the y -direction. v_y cannot be too small, because in this case the molecule will spend too long in between the two oppositely polarized electrodes, increasing the chance of crashing into one them. If v_y is too large the molecule simply escapes from the guide. Figure 6.14 (b) shows that, with the guide charged to ± 8.0 kV, the maximum value of the on-axis Stark shift along y is -26 GHz. Thus a molecule entering the guide on the axis must have a kinetic energy along y of at least 26 GHz to be able to escape. For CaF this corresponds to $v_y = 19 \text{ ms}^{-1}$.

Figure 6.15 shows the effect of increasing the applied voltage on an example trajectory. The molecule enters the guide on-axis with $v_x = 0$, $v_y = 12.5 \text{ ms}^{-1}$ and $v_z = 600 \text{ ms}^{-1}$. For low voltage the potential wells in y are shallow and the molecule is accelerated out and does not return. As the voltage is increased the molecule is increasingly accelerated back towards the beam-line axis. An applied voltage of 6 kV is seen to return the molecule to the beam-axis by the end of the guide. Increasing the voltage further causes more rapid focussing towards the beam-line axis, until, by 12 kV, one complete period fits into the guide. The peak in the signal ratio data around 5.5 kV corresponds to molecules being focussed through the aperture and into the detection region. It was found from simulations

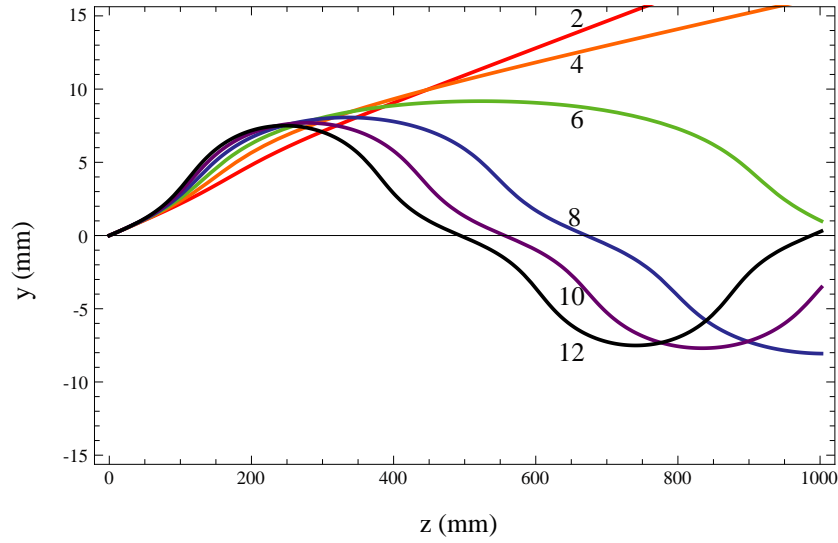


Figure 6.15: Simulated trajectories along the guide for a molecule travelling at 600 ms^{-1} with initial coordinates $\{x, v_x\} = \{0, 0\}$, $\{y, v_y\} = \{0, 12.5 \text{ ms}^{-1}\}$. Trajectories are shown in the y -direction for voltages in the range 2 kV – 12 kV, as indicated. Note that the trajectory at 6 kV (green line) shows the molecule being focussed back towards the beam-line axis just after the end of the guide.

that the focussing period was not strongly affected by the oscillation amplitude and so at this voltage a large portion of the initial molecular phase-space area, $\{y, v_y\}$ can be focussed into the probe beam. The simulations show the peak signal ratio lies closer to 4 kV - in this case the molecules were found to be tightly focussed into the detection region and so the signal at this voltage is very sensitive to the probe beam position. For this reason a vertical misalignment of the probe beam of 2mm was found to decrease the signal ratio dramatically around 4 kV and bring the simulations into much better agreement with the experimental data.

It might be expected that as the voltage is increased further the signal ratio should increase again, peaking in the region of 11 kV, corresponding to molecules making almost one complete period of oscillation in y along the guide and then being focussed into the detection region. However, increasing the voltage beyond that value does not increase the peak amplitude, rather it broadens the spectral line considerably. The DC guiding described here requires fairly large transverse speeds along y . This leads to a Doppler broadening in the spectral lines. As the voltage is increased the double-well potential becomes very deep and favours molecules with large values of $|v_y|$, thus increasing the Doppler broadening. For voltages greater than 8 kV the $F = 1$ line was observed to have split into two components, corresponding to molecules with the positive and negative optimal transverse speeds, $\pm v_y$. The amplitudes were not observed to increase as the signal was spread over a large Doppler-broadened frequency range.

6.10 Conclusions

A 1 m-long AG guide was built and was used to transport ground-state CaF molecules travelling at 605 ms^{-1} from the supersonic source to the detection region, 1.215 m downstream of the source. The properties of the guide were tested over a range of lens lengths for three applied voltages, ± 5.5 , ± 8.0 kV and ± 9.5 kV. It was found that the optimal acceptance was achieved with a scaled lens duration of $\Omega\tau = 1.5$. This is slightly greater than the optimal duration predicted for a purely harmonic AG guide ($\Omega\tau = 1.254$), a consequence of the non-linear terms in the transverse equations of motion. The experimental data were modelled by numerical simulations. Good agreement was found in terms of the shape of the data, with the simulations agreeing well with the experimental data on the position of the optimal lens duration for the three voltages. However, the simulations predict that greater molecular fluxes should be detected out of the guide. The disagreement was found to be well-explained by a 2 mm vertical misalignment of the laser probe beam with respect to the AG guide. Accounting for this misalignment in the simulations brings the simulated results into very good agreement with the experimental data. The simulations still predict a larger value for the maximum stable lens duration, which is considered to be most likely the result of the ‘bendiness’ of the electrodes.

The AG guide was also operated with a static electric field, so that it acts as a single 1 m-long lens, focussing in one direction and defocussing in the other. It was not expected that this set-up should guide any molecules at all for voltages greater than about 740 V. However, it was found that the 1 m-long lens was able to transport molecules with applied voltages much greater than this. Simulations of this experiment show that the DC-guided molecules are those that make large amplitude oscillations in one transverse direction, taking the molecule out of the guide and back, and very small amplitude oscillations in the other transverse direction. This is because, when considering the total field created by the AG guide, and not just the field inside the guide, the Stark shift maximum that occurs in one transverse direction is actually surrounded by a minimum on either side of it. Molecules within a range of speeds in this transverse direction can oscillate between these two minima. The maximum signal out of the DC-operated guide was found to occur with an applied voltage of 5.5 kV, which corresponds to molecules that, along the length of the guide, make one half-oscillation in this transverse direction, and are focussed into the detection region. Initial simulations found quite good agreement with the DC-guiding data, but predicted greater detected molecular fluxes. Including the same 2 mm misalignment as in the previous data brought the simulations into much better agreement with the experimental data, adding weight to the theory that the AG guide was slightly misaligned relative to the probe beam.

With the AG guide operated in ‘switching mode’ signal ratios of up to around 2 were

measured, meaning that the guide was transporting around twice the number of molecules into the detection region than would be there if the guide were turned off. The simulations indicate that, if properly aligned with the probe laser beam, signal ratios of up to around 6 would be measured. This is an encouraging result, but it must be noted that the definition of the signal ratio is slightly arbitrary. The signal ratio is defined as the signal strength with the guide on, compared with the signal from the divergent beam were the guide turned off. The molecular flux density of the unguided beam drops with $1/L^2$, where L is the distance between the source and the detection region. If a 2 m-long guide had been built the signal ratios would have been 4 times as great as measured above. The same effect would happen if the source-to-detector distance were kept constant, but the molecular beam speed were halved. Put simply, the AG guide becomes more useful when transporting a slow, divergent beam over a long distance. An obvious application of the AG guide is transporting slow molecules from a buffer-gas cell. An example of this is discussed in [85], where a buffer-gas cell of CaF radicals is considered. An aperture in one side of the cell allows the molecules to effuse out with a mean beam speed of 80 ms^{-1} . Simulations were performed with an AG guide operating at $\pm 8 \text{ kV}$ and with a lens duration of $200 \text{ }\mu\text{s}$, and positioned such that the upstream-end of the guide is located 8 mm from the buffer-gas cell aperture. With an ablation source of CaF in the buffer-gas cell it is reasonable to expect around 10^{12} molecules in the effusive beam per pulse [85]. Simulations of this source show that around 0.5% of these molecules will be guided, resulting in around 10^{10} molecules transported away from the source per pulse. This is an extremely encouraging prediction. The combination of a buffer-gas cell and an AG guide offers the prospect of transporting a large numbers of molecules from a high pressure region to a much lower pressure region an arbitrary distance away, while maintaining the high phase-space density of the source. For comparison, a source using supersonic expansion and laser ablation produces beams with around 10^9 ground-state molecules per steradian per pulse [38]. In the beam machine described in this thesis there is a 1 mm-radius skimmer located 70 mm downstream of the valve nozzle, which results in a beam of around 10^6 molecules per pulse passing through the skimmer. Even if all of these were to be transported by the guide, an experiment with a buffer-gas source would be capable of transporting around 10^4 more molecules per pulse.

Finally, it is worth discussing the potential use of the observed DC guiding. The simulations show that, if properly aligned, the guide is capable of achieving a signal ratio of around 1. Could this be increased by increasing the length of the guide (as it is in conventional AG guiding discussed above)? The answer relies on the stability of the trajectories. In AG guiding, in which the field lenses of optimal length are used, the trajectories are stable along an infinitely long guide. However, simulations of DC guiding found that these trajectories are not stable. The molecules oscillate between the electrodes in one direction, and have some small velocity in the other transverse direction. Eventually motion in

this other transverse direction will destabilise the trajectory, causing the molecule to hit an electrode. In the current experiment the molecules take 1.7 ms to traverse the length of the guide. Simulations found that with the source used in this experiment, molecules could survive in a DC guide for up to 500 ms, but that after 9 ms the molecular flux has dropped by a factor of 10, and that by 50 ms it has dropped by a factor of 50. Despite offering a much simpler method of guiding strong-field seeking molecules (as there are no switching fields), DC guiding is not stable over long distances and, even over 1 m, doesn't offer the signal ratios achieved by switching the fields in an optimal AG timing sequence.

Chapter 7

Decelerating ground-state CaF molecules

7.1 Motivation and general physical principles

As discussed in chapter 6, ground-state molecules always experience the greatest Stark shift in a given electric field, and are thus the best candidates for efficient Stark deceleration. However, the Stark shift of a ground-state molecule is always negative, and so the molecule is always a strong-field seeker. Thus, any electrode geometry to slow the molecules must also be designed to achieve alternating gradient (AG) guiding. The structure of such an AG decelerator is thus a combination of the weak-field decelerator discussed in chapter 5, and the AG guide discussed in chapter 6.

An AG decelerator consists of a sequence of deceleration stages which produce a Stark potential well in the longitudinal direction (along the beam-line), and a saddle-shaped field in the transverse direction. Typical AG decelerators use two-electrode stages. Figure 7.1 shows a typical AG deceleration stage: a pair of parallel, rod-like, oppositely-polarized electrodes. The electrodes are parallel to the z -axis (the direction of the molecular beam). The electric field inside the stage has a minimum on the z -axis along the x -direction, and a maximum along the y -axis. This transverse field will focus strong-field seeking molecules towards the z -axis in the y -direction (shown by the green cross in figure 7.1) and defocus them away from the z -axis in the x -direction (blue arrows). A sequence of these deceleration stages, in which each successive stage is rotated by $\pi/2$ about the z -axis can be used to achieve AG guiding. For a given applied electric field, the length of the field stages, and of the drift space between successive stages will determine the stability of guided trajectories, and thus the acceptance of the decelerator. At the end of a stage the field decreases along z , and as a strong-field seeking molecule leaves the field stage it will experience a retarding force (red arrow in figure 7.1) which decelerates it.

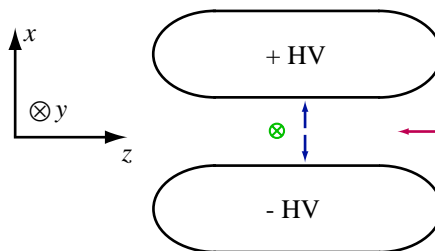


Figure 7.1: A typical deceleration stage in an AG decelerator. The stage comprises a pair of oppositely-polarized electrodes, parallel to the beam-line axis (z). The electrodes create a saddle-shaped electric field in the x - y plane, which focusses strong-field seekers in one transverse direction (y in this figure), and defocusses them along the other (x). The fringe fields around the end of the electrodes decrease in strength along z , and can be used to decelerate the molecules.

7.2 A brief review of previous research

The first proposal of using electric fields in an alternating gradient device was made in 1966 by Auerbach, Bromberg and Wharton [51]. In fact the proposed device was to be used as a linear accelerator for neutral molecules. Further descriptions of this device are given in [87] and [88].

The first Stark deceleration of a strong-field seeker was in fact on an atom, not a molecule. In 1999 Maddi *et al.* [89] used a single 2.2 cm-long field stage to bunch and decelerate a beam of Cs atoms. The atoms were launched vertically from a magneto-optical trap, with an initial speed of 2 ms^{-1} . The 1.7 cm-wide electrodes were separated between 6 mm and 8 mm apart, and were used to create electric fields of up to 50 kV/cm. The pulsed Cs beam was measured before and after the field stage using laser absorption. The field stage was used to reduce the temporal width of the Cs pulse at the downstream laser probe from 16 ms (with the field off) to 3 ms, and to reduce the pulse's central speed from 2 ms^{-1} to 1.2 ms^{-1} .

The first deceleration of strong-field seeking molecules was reported by Bethlem *et al.* [90] in 2002. In this experiment a pulsed beam of metastable CO molecules was decelerated from 275 ms^{-1} to 260 ms^{-1} (and also accelerated from 275 ms^{-1} to 289 ms^{-1}) using a 12-stage AG decelerator. The deceleration stages were arranged in a sequence of alternating focussing and defocussing “lenses”, with each subsequent lens being rotated through $\pi/2$ with respect to the previous stage. As discussed in chapter 6 the effect of a focussing lens can be described by a matrix, \mathbf{F} , that of a defocussing lens by a matrix, \mathbf{D} , and free space by a drift matrix, \mathbf{O} . The alternating sequence of lenses in the AG decelerator is thus described as a *FODO* sequence. Each stage consisted of two 2 mm-thick electrodes, facing each other end-on. The sides of the electrodes facing each other were rounded off

with a 1 mm radius of curvature. A separation of 2 mm between the electrodes allowed for fields of up to 90 kV/cm to be applied on the beam-line axis. The decelerator worked much as predicted, however, simulations of the resulting time-of-flight profiles predicted molecular signals 20 times greater than found experimentally. It was found that applying a random misalignment of ± 0.2 mm to the simulated electrodes caused this discrepancy to disappear, indicating that mechanical misalignments in the decelerator were the cause of the reduced measured signals.

The next AG deceleration was reported by Tarbutt *et al.* in 2004 [91]. In this experiment a pulsed beam of ground-state YbF was decelerated by a 12-stage AG decelerator. Each stage comprised a pair of parallel rod-like electrodes, 20 mm long, 6 mm in diameter, and with hemispherical ends. With a separation of 2 mm between the two electrodes, a stage charged to ± 10 kV was able to produce an axial field of almost 100 kV/cm. The stages were arranged with a $(FO)^3(DO)^3$ unit cell. This sequence of three focussing stages followed by three defocussing stages effectively increases the lens lengths by a factor of three, while achieving three times as much deceleration per lens than in a more usual *FODO* sequence. It was also reported that this sequence is less sensitive to electrode misalignments [90]. The decelerator was used to decelerate YbF molecules from an initial speed of 298 ms^{-1} to 287 ms^{-1} , removing 7% of the molecules' initial longitudinal kinetic energy.

The most recent published AG deceleration of strong-field seeking molecules was reported in 2008 by Wohlfart *et al.* [92]. In this experiment a 553 mm-long AG decelerator was constructed, with 27 field stages arranged in a $(FO)^3(DO)^3$ pattern. The field stages consisted of a pair of 13 mm-long rod-like electrodes, with 6 mm diameter and hemispherically-rounded ends. The spacing between the two electrodes was 2 mm. When charged to ± 15 kV the electrodes produced a field on the beam-line axis of 143 kV/cm. The decelerator was used on a pulsed beam of benzonitrile ($\text{C}_7\text{H}_5\text{N}$), and decelerated ground-state molecules from 320 ms^{-1} to 289 ms^{-1} , removing 18% of the molecules' initial kinetic energy.

7.3 Experimental set-up

A 21-stage alternating gradient (AG) decelerator was constructed. Each stage consists of a pair of rod-like stainless steel electrodes parallel to the beam-line. The electrodes are 14 mm long and 6 mm in diameter, with hemispherically-rounded ends of radius 3 mm. The two electrodes are separated by 2 mm from surface to surface. When the electrodes in a stage are oppositely polarized to some high voltage there is a saddle-shaped field between the electrodes, with the electric field reaching a maximum in one direction and a minimum in the other. This field will focus a molecule in one transverse direction and defocus it

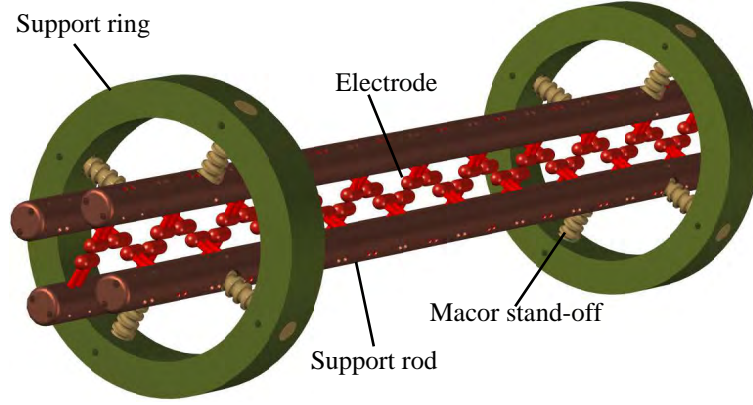


Figure 7.2: A diagram of the AG decelerator.

in the other. Successive deceleration stages are rotated through $\pi/2$, which rotates the field and allows for AG guiding in exactly the same way as is achieved by the AG guide described in chapter 6, except in the decelerator the transverse field switches in space, not time. There is a drift space of 10 mm between successive deceleration stages. It was shown in chapter 6 that, in the harmonic approximation, the acceptance of a guide is maximal when there is no drift space. However, this device was designed to decelerate strong-field seekers, and so it is necessary for there to be a zero-field drift space after a stage so that the molecules climb up a steep potential hill.

Each electrode was attached by two dowels to one of four 16 mm-diameter support rods. Each support rod was attached by insulating macor stand-offs to two stainless steel support rings (one at either end of the decelerator). These support rings were then mounted in a cradle inside the vacuum chamber. Figures 7.2 and 7.3 illustrate the decelerator: the former is a diagram of the AG decelerator, and the latter is a photograph of three deceleration stages.

The decelerator's total length is 504 mm. The decelerator was placed in the vacuum chamber such that its front end was 122 mm downstream of the source, and the detection region was 184 mm downstream of the end of the decelerator. The total distance from the source to the detector was thus 810 mm. The AG decelerator was used with beams of CaF carried by either Kr or Xe.

High voltage was applied to the decelerator's electrodes in the same way as for the 100-stage weak-field seeker decelerator (section 5.3.2), except with the AG decelerator $V_{LO} = 0$ throughout.

7.4 The axial electric field

Figure 7.4 shows the electric field produced along the axis of the decelerator when ± 15 kV is applied. Beneath the electric field profile are shown the associated deceleration

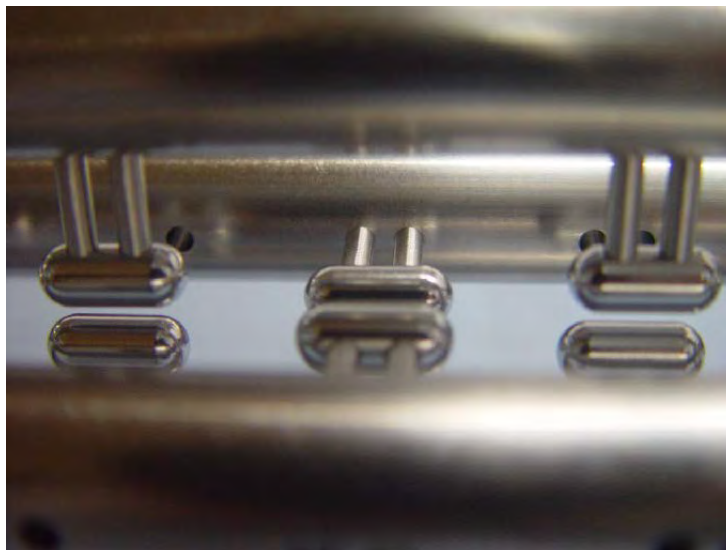


Figure 7.3: A photograph of three deceleration stages in the AG decelerator. The electrodes can be seen to be attached to the support rods by dowels.

stages. The stages can be seen to alternate between being horizontal (the left-most stage shown) and vertical. As with the 100-stage decelerator there are two high-voltage states that the AG decelerator can occupy: in state 1 (blue line) all the vertical stages are charged to $\pm V_{HI}$, while all the horizontal stages are grounded. In state 2 the situation is reversed (red line). It can be seen that the shape of the axial field profile is much more ‘rectangular’ than in the 100-stage decelerator: in a given state the electric field alternates between long regions of zero field and flat peaks of strong field, with a relatively steep slope between these regions. The lower part of figure 7.4 shows the axial Stark shifts experienced by a CaF radical in the $|\mathcal{N} = 0, M_N = 0\rangle$ state in the fields shown in the upper part of the figure. It can be seen that, for a given applied voltage, the axial electric fields created inside the AG decelerator are of roughly the same strength as in the 100-stage decelerator. However, the $|0, 0\rangle$ state experiences considerably greater Stark shifts, by a factor of around 5 in the case of $V_{HI} = 15$ kV. The axial Stark shift profiles associated with states 1 and 2 have very similar shapes to the field profiles, narrow and almost ‘top-hat’ in shape. As a consequence of this ‘top-hat’ shape, unlike the 100-stage decelerator, the AG decelerator was not switched simultaneously from field state 1 to state 2; each time the decelerator switched from one state to the next there was a period between the two states in which the entire decelerator was grounded. Simultaneous switching between the two field states worked in the 100-stage decelerator because in this case when a molecule was near the top of a Stark potential hill inside one stage it was possible to switch to the other electric field state and for the molecule to be near the bottom of the next potential well. The molecule might travel ‘down’ a small bit of potential hill, but would always end up travelling up much more, and thus gaining a net deceleration. However, the relatively steep

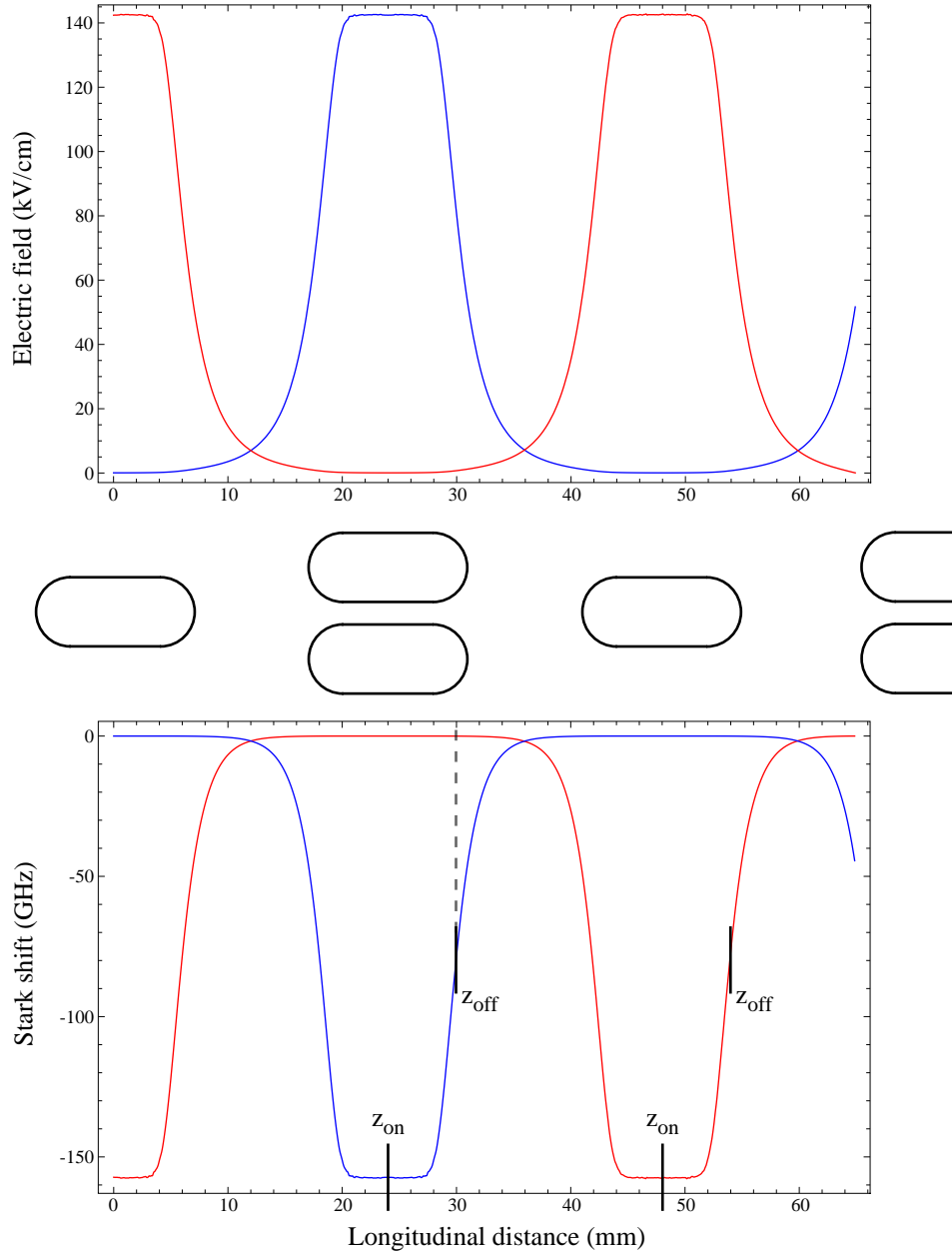


Figure 7.4: *Upper part*: The axial electric field profile of the two states of the AG decelerator when $V_{HI} = \pm 15$ kV. State 1 (blue line) corresponds to the vertical stages polarized and the horizontal stages grounded. State 2 (red line) corresponds to the opposite arrangement. *Lower part*: the Stark shifts associated with the above profiles experienced by a CaF radical in the $|\mathcal{N} = 0, M_N = 0\rangle$ state in the two electric field states (same colour scheme as above). Also shown are the positions of the synchronous molecule when the field is turned on (z_{on}) and off (z_{off}) for two successive deceleration stages. *Middle part*: A diagram of the deceleration stages associated with the profiles in the *upper* and *lower* parts.

and narrow potential wells of the AG decelerator prevent this from happening. Consider the example shown in the lower part of figure 7.4. A molecule travels up the potential hill inside the vertical field stage, with the decelerator in state 1. It is decelerated. The fields are switched off at position z_{off} when the molecule is some way up the potential hill. Were the decelerator to switch immediately to state 2, the dashed line shows that the molecule would find itself in a region of approximately zero Stark shift outside the next field stage. Upon entering the next field stage it would then ‘roll down’ the potential well, accelerating towards the centre of this stage. Having ‘rolled down’ all the way to the bottom of the potential well there is now no way of achieving a net deceleration. Instead, after the decelerator is switched out of state 1 (that is, the vertical stages are grounded), the entire decelerator remains grounded until the synchronous molecule is inside the next stage. Only then is the decelerator switched into state 2.

7.5 Dynamics inside the AG decelerator

7.5.1 Longitudinal dynamics

The field switching pattern employed in the AG decelerator is constructed such that a chosen synchronous molecule is at the same position in each field stage each time the field switches on or off. The synchronous molecule is at z_{on} when the fields are turned on, and is at z_{off} when they are turned off. As described in section 5.6.1, the effect of the decelerator can be described in terms of a continuously-acting force, $\bar{F}(z)$, averaged over the stage-to-stage distance, D . The longitudinal dynamics of the non-synchronous molecules relative to the synchronous molecule are described by the same equations of motion as in section 5.6.1, except now both the ‘on’ and ‘off’ positions are included. The synchronous positions are defined only at the moments of switching the fields on or off; however, in this continuous analysis the synchronous molecule’s position is described by the continuous variable, z_{sync} . The axial position of a non-synchronous molecule relative to the synchronous molecule is $\Delta z = z - z_{sync}$. By definition, the synchronous molecule travels a distance D between one switch-on and the next. It is approximated that non-synchronous molecules that are close in phase space to the synchronous molecule also travel this same distance, D , during this time interval. It is also assumed that the longitudinal offset of a non-synchronous molecule, Δz , changes only negligibly between z_{on} and z_{off} . With these approximations the equation of motion of a non-synchronous molecule relative to a synchronous molecule is

$$\bar{F}(\Delta z) = M \frac{d^2 \Delta z}{dt^2} = \frac{1}{D} \left[W_s(z_{on} + \Delta z) - W_s(z_{on}) - W_s(z_{off} + \Delta z) + W_s(z_{off}) \right]. \quad (7.1)$$

By the same analysis shown in equation 5.12, it can be shown that $\frac{d^2 \Delta z}{dt^2} = \Delta v \frac{d\Delta v}{d\Delta z}$, where Δv is the non-synchronous molecule’s speed relative to the synchronous molecule.

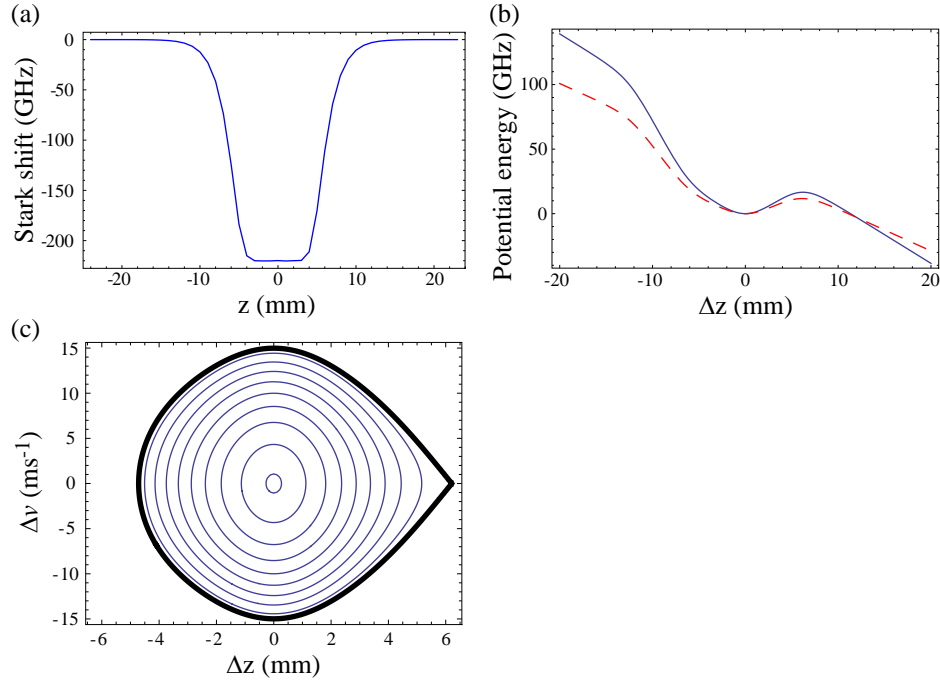


Figure 7.5: (a) The Stark shift along the axis of the AG decelerator for CaF radicals in the $|\mathcal{N} = 0, M_N = 0\rangle$ state, when the electrodes are charged to ± 20 kV. (b) The effective longitudinal potential experienced inside the AG decelerator (charged to ± 20 kV) by CaF radicals in the $|0, 0\rangle$ state, calculated by equation 7.3, with $z_{on} = 0$ and $z_{off} = 6$ mm (blue line). Also shown is the potential well calculated with the same parameters, except $V_{HI} = 15$ kV, allowing for a comparison with the effective potential calculated at this voltage for the 100-stage decelerator described in chapter 5 (dashed red line). (c) Phase-space trajectories calculated with the AG decelerator operating at ± 20 kV and with $z_{on} = 0$ mm and $z_{off} = 6$ mm. The black line is the separatrix.

Equation 7.1 can thus be integrated to give:

$$\frac{1}{2}M\Delta v^2 + U_{eff}(\Delta z) = W_0, \quad (7.2)$$

where W_0 is the total longitudinal translational energy of the non-synchronous molecule relative to the synchronous molecule, and $U_{eff}(\Delta z)$ is an effective longitudinal potential energy associated with the effective force:

$$U_{eff}(\Delta z) = - \int_0^{\Delta z} \bar{F}(\Delta z') d\Delta z'. \quad (7.3)$$

Equation 7.2 shows how a non-synchronous molecule can be bound by a longitudinal potential well, centred on the synchronous molecule. Figure 7.5 shows two effective potential wells calculated from equation 7.3 for $V_{HI} = 15$ kV and 20 kV respectively. The potentials have the same form as those calculated for the 100-stage decelerator. The potential depths of the 15 kV and 20 kV longitudinal wells are found to be 11.7 GHz and 16.6

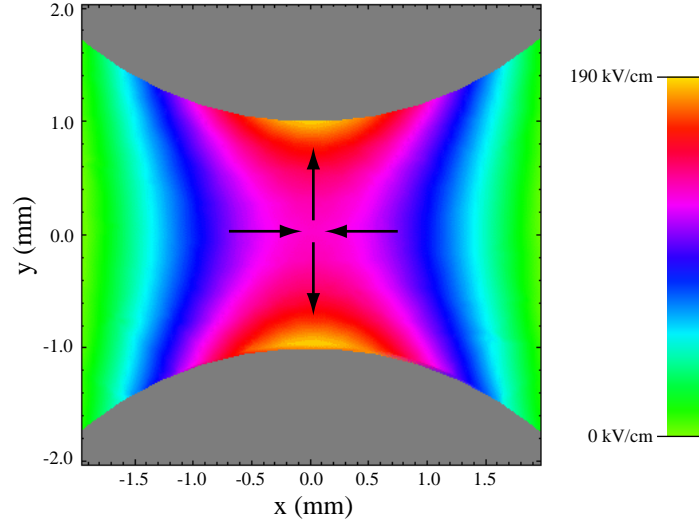


Figure 7.6: Electric field magnitude on the $z = 0$ plane (a plane that cuts the electrodes in half) with ± 20 kV applied to the AG decelerator. The electrodes are shown in grey. The arrows show the direction of the force exerted on a strong-field seeking molecule travelling near the beam-line.

GHz respectively. These are of the same scale as the potential depths created inside the 100-stage decelerator with similar deceleration patterns.

Figure 7.5 (c) shows examples of phase-space trajectories of phase-stable molecules about the phase-synchronous molecule. The trajectories were calculated by integrating equation 7.1, with the AG decelerator operated at ± 20 kV, and with $z_{on} = 0$ mm and $z_{off} = 6$ mm. Each trajectory corresponds to a molecule oscillating about the synchronous molecule with a constant total energy relative to the synchronous molecule. As a molecule travels along a trajectory its total relative energy is divided between kinetic energy and effective potential energy as it moves in the effective potential well (figure 7.5 (b)). The black line is the separatrix, which is the trajectory of a molecule whose total relative energy is equal to the depth of the effective potential well. It bounds the area of phase space that contains all the phase-stable trajectories.

7.5.2 Transverse dynamics

Figure 7.6 shows the shape of the transverse electric field in the centre of a deceleration stage charged to ± 20 kV. Around the origin the electric field is saddle-shaped. At the origin the field is a maximum along x , and a minimum along y . A strong-field seeking molecule will thus be focussed towards the centre of the stage along x , and defocussed away from the centre along y . The alternating orientation of successive deceleration stages can thus achieve dynamic confinement and focussing of the molecular beam by rotating these transverse axes. As was discussed in chapter 6, the ideal shape of the transverse Stark

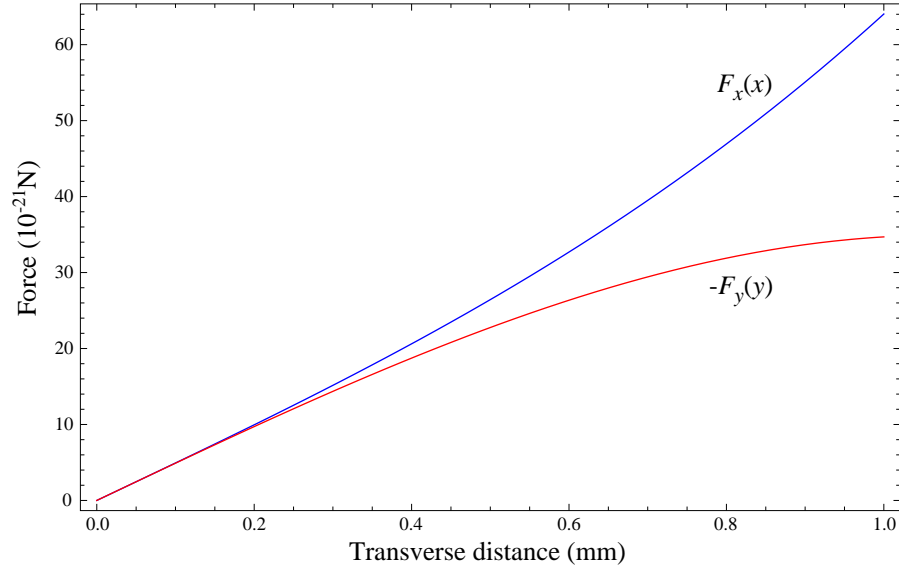


Figure 7.7: The transverse forces, $F_x(x)$ (blue line) and $-F_y(y)$ (red line), exerted on a CaF radical in the $|4, 0\rangle$ state as a function of transverse coordinate inside the centre of a stage charged to ± 20 kV. It can be seen that near the beam-line the forces vary linearly with the transverse coordinates, because the Stark potential is harmonic in this region. Further from the beam-line (> 0.2 mm) the forces diverge, a result of the anharmonic terms in the electric field.

potential for maximal acceptance is harmonic. The AG decelerator was operated with strong electric fields (around 190 kV/cm in the centre of a deceleration stage charged to ± 20 kV). In this limit the Stark shifts induced in the ground-state molecules are well into the linear limit, $W_s = -\mu|E|$. The transverse forces are thus proportional to the first derivative of the electric field distribution:

$$\vec{F} = -\nabla W_s = \mu \nabla |E|. \quad (7.4)$$

Figure 7.7 shows the transverse forces, $F_x(x)$ and $-F_y(y)$ as a function of transverse coordinate inside a stage charged to ± 20 kV. It can be seen that near the centre of the stage (< 0.2 mm from the beam-line) the forces are linear and equal-and-opposite. Further from the axis the forces diverge from linear and are no longer equal-and-opposite. This results from the anharmonic terms in the transverse electric field.

To analyse these forces in more detail the transverse electric field map (figure 7.6) was fitted to the function $E(x, y)$ given in equation 6.30:

$$|E(X, Y)|^n = E_0^n \left(1 + a_3 n (X^2 - Y^2) + (a_3^2 n (3 - n) - 6a_5 n) X^2 Y^2 + (a_3^2 n (n - 1) / 2 + a_5 n) (X^4 + Y^4) + \dots \right). \quad (6.30)$$

The fit matches the shape of the field very well, with parameters $a_3 = 0.146$ and $a_5 = 0.021$. This is exactly what is expected for the decelerator's geometry. For an electric field created

by a pair of rod-like electrodes the parameters a_3 and a_5 are found analytically [79] to be $a_3 = (r_0/R)/(2 + r_0/R)$ and $a_5 = (a_3)^2$, where R is the radius of the rod, and $2r_0$ is the gap between the rods. The values for the AG decelerator ($R = 3$ mm and $r_0 = 1$ mm) give $a_3 = 0.143$ and $a_5 = 0.020$. These parameters agree well with the fit parameters, showing that the finite element analysis and fit are both good.

The transverse dynamics inside an AG guide were discussed in chapter 6. In the approximation that the field inside a stage varies quadratically in the transverse coordinates, the motion of a molecule along a transverse direction, for example x , is described by the following equation:

$$\frac{\partial^2 x}{\partial z^2} \pm \kappa^2 x = 0, \quad (6.2)$$

depending on whether the molecule is in a focussing or defocussing lens. κ is a force constant (in units of m^{-1}). In the limit of a linear Stark shift this force constant is given by $\kappa = \frac{1}{r_0} \sqrt{\mu E_0 |a_3| / \frac{1}{2} m_{mol} v_z^2}$, where m_{mol} is the mass of the molecule. For a typical beam speed of 430 ms^{-1} (typical of a Kr-carried beam which was used in all experiments reported in this chapter) and an applied voltage of ± 20 kV κ is 0.056 mm^{-1} . The 1D acceptance of a harmonic AG guide is shown in figure 6.2. This plots the acceptance in units of κd^2 , where d is the aperture of the guide. In the discussion of this decelerator, $d = 2r_0$. The maximum acceptance is found to occur in a gapless guide, and has the value $0.74 \kappa r_0^2$ ($0.186 \kappa d^2$ in figure 6.2). This maximum occurs at the scaled lens length, $\kappa L = 1.25$. The AG decelerator, however, necessarily has gaps. These are of length $S = 10$ mm, giving $\kappa S = 0.56$ with the decelerator operating at ± 20 kV. For this value of κS the 1D acceptance now reaches a maximum of $0.66 \kappa r_0^2$, occurring at a lens length of $\kappa L = 0.89$. The actual length of the decelerator's lenses is 14 mm, giving $\kappa L = 0.78$. This is slightly smaller than the optimal length for the given drift space, with a 1D acceptance of $0.65 \kappa r_0^2$. In more useful units this is 15.8 mm ms^{-1} for a ground state CaF molecule travelling at 430 ms^{-1} . The corresponding 2D transverse acceptance is simply the square of the 1D acceptance: $249.5 \text{ mm}^2 (\text{ms}^{-1})^2$

The electric field does not, however, vary purely quadratically in the transverse coordinates. This results in non-linear terms in the equations of motion, as discussed in chapter 6. These non-linearities require a numerical analysis. Extensive numerical simulations were performed in [79] for a ‘typical’ AG decelerator with a two-rod decelerator stage of scaled length, $\kappa L = 0.7$, and scaled drift space length, $\kappa S = 0.7$. These are similar to the parameters of the AG decelerator when operated at ± 20 kV with ground state CaF. The acceptance of the ‘typical’ decelerator was calculated as a function of the parameter, a_3 . It was found that the maximal 2D transverse acceptance, $55 \text{ mm}^2 (\text{ms}^{-1})^2$, is achieved with $a_3 \approx 0.08$. This corresponds to a rod separation-to-radius ratio of 5.7, larger than the ratio of 3 found in the AG decelerator used in this experiment. The value of a_3 in the

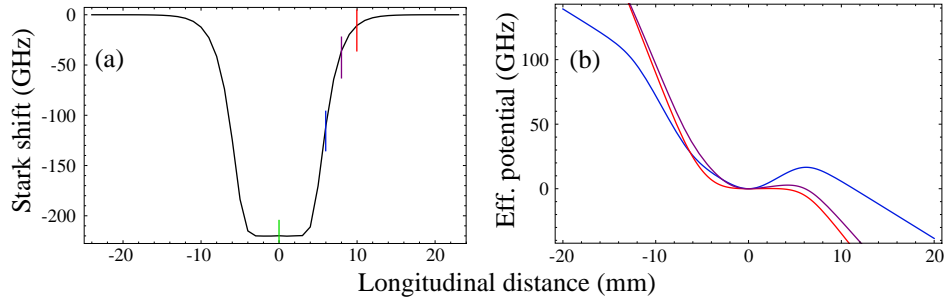


Figure 7.8: (a) The Stark potential inside a deceleration stage of the AG decelerator, charged to ± 20 kV. Also shown are the on-position (green line) of $z_{on} = 0$ mm (corresponding to the centre of a deceleration stage) and three off-positions: $z_{off} = 6$ mm (blue line), $z_{off} = 8$ mm (purple line), and $z_{off} = 10$ mm (red line). (b) The effective potential wells created inside the AG decelerator with the on- and off-positions shown in (a) (and with the same colour scheme).

AG decelerator leads to an acceptance of approximately $40 \text{ mm}^2(\text{ms}^{-1})^2$, around 70% of the maximal value.

7.6 Experimental procedure

For much of the data presented in this chapter the AG decelerator was operated at ± 20 kV, and with $z_{on} = 0$ mm and $z_{off} = 6$ mm ($z = 0$ is defined to be the centre of a deceleration stage). These on- and off-positions ensure that the synchronous molecule travels up approximately half the Stark potential, while maintaining phase-stability. This on-position ensures that the synchronous molecule is at the bottom of the Stark potential when the fields are applied. It might be considered that the off-position should be chosen to maximize the amount of deceleration experienced per stage. However, large values of the off-position reduce the longitudinal phase-space acceptance because there is little room ahead of the synchronous molecule for non-synchronous molecules to be decelerated back towards the synchronous molecule. Figure 7.8 (a) shows three on-/off-positions on the Stark potential well created inside a stage charged to ± 20 kV. In all cases $z_{on} = 0$, the centre of the stage. The three off-positions are $z_{off} = 6, 8, 10$ mm respectively. Figure 7.8 (b) shows the effective potential well (calculated from equation 7.3) for each of these three cases. It can be seen that with $z_{off} = 6$ mm, there is plenty of room for non-synchronous molecules to be ahead of the synchronous molecule, and to experience a relative force back towards the latter. The resulting effective potential well (blue line) has a depth of 16.6 GHz. As z_{off} is increased to 8 mm, there is now very little potential well ahead of the synchronous molecule at the turn-off position, and this is reflected in the effective potential well (purple line), whose depth is reduced to 2.8 GHz. Finally, an off-position of $z_{off} = 10$

mm occurs at almost the top of the Stark potential well, and switching the fields with this pattern creates an extremely shallow effective potential well (red line), with a depth of only 0.16 GHz.

All the data presented in this chapter were taken with ground-state CaF radicals in Kr-carried beams, with mean longitudinal speeds around 430 ms^{-1} .

7.7 Results

7.7.1 Deceleration with $z_{on} = 0 \text{ mm}$ and $z_{off} = 6 \text{ mm}$

Figure 7.9 (a) shows experimental time-of-flight profiles acquired with the AG decelerator operating at $\pm 20 \text{ kV}$, and with $z_{on} = 0 \text{ mm}$ and $z_{off} = 6 \text{ mm}$. These parameters correspond to an on-axis kinetic energy reduction for the synchronous molecule of 3.65 cm^{-1} per stage. These data shall be referred to as the “0/6” data. The profiles were taken with a varying number of deceleration stages used, starting with the far end of the decelerator: the high-voltage switching pattern was calculated such that it started when the molecules were n stages from the end of the decelerator, and then continued until the molecules reached the end of the decelerator. Data were taken with n taking all odd values between 1 and 21. The reason for using the last n stages was that, if only the first few stages were used, the molecules would hit the remaining electrodes and would not be transmitted. By using the last stages, the molecules could always be focussed into the detection region. For the sake of clarity only a selection of the profiles are shown in figure 7.9: those with $n = 3, 5, 9, 13, 17, 19$ and 21 . Each profile is the average of several hundred shots with the probe laser on-resonance with the $Q_{11}(\frac{1}{2})$ transition. In order to normalize out fluctuations in the source flux and laser intensity, reference profiles were recorded with the decelerator turned off. The bottom profile (black points) shows the average of all the reference profiles taken with the “0/6” data. It has been fitted to a Gaussian function (black line), which fits well and finds the central time-of-arrival to be $1870.5 \mu\text{s}$ and the width to correspond to a longitudinal translational temperature of 2.6 K . Each deceleration profile was normalized by dividing by the amplitude of the Gaussian fit of its associated reference profile. The experiment was alternated between ‘deceleration mode’ and ‘reference mode’ on a shot-to-shot basis, and so the deceleration profiles were normalized to near-simultaneous reference profiles.

The deceleration time-of-flight profiles have been fitted to a triple-Gaussian function, $G(t)$, which is the sum of three Gaussians with independent parameters, except for a shared offset:

$$G(t) = G_1(t) - G_2(t) + G_3(t). \quad (7.5)$$

The rationale for this choice of fitting function is as follows. $G_1(t)$ is a broad function representing the shape that the profile would have if the decelerator were off. It represents

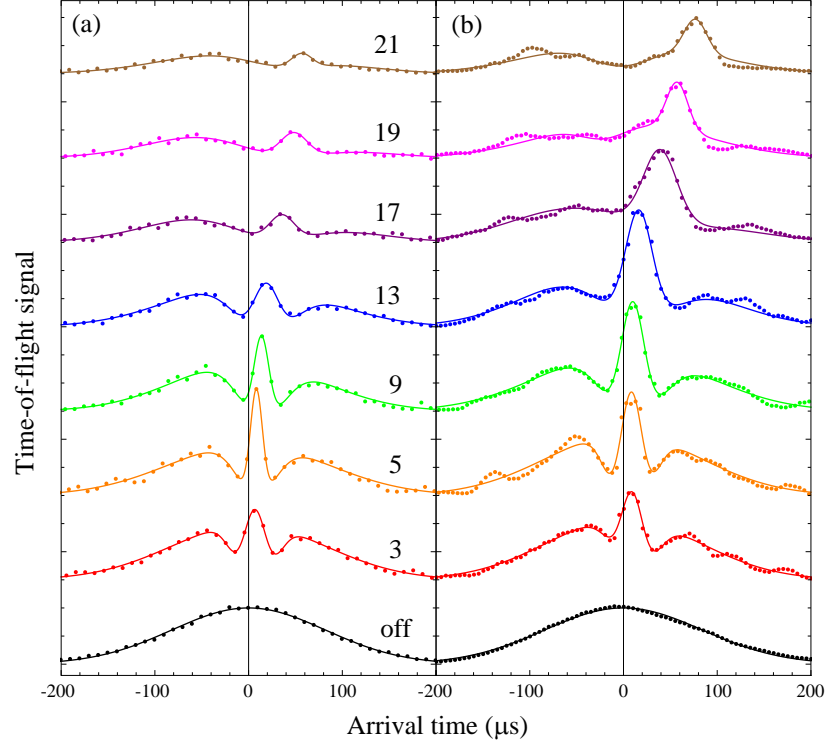


Figure 7.9: (a) Deceleration data (points) taken with the AG decelerator operating at ± 20 kV, and with $z_{on} = 0$ mm and $z_{off} = 6$ mm. The plot shows time-of-flight profiles taken with a variable number of stages, with the bottom profile (black points) corresponding to the profile measured when the decelerator is off. The profiles are labelled by the number of stages used. For the sake of clarity the profiles have been offset vertically from one another. Also shown are fits to the data of the triple-Gaussian function given in equation 7.5 (lines). The origin of time of each deceleration profile has been shifted to the centre of its associated reference profile. (b) The results of simulations of all the data in (a). The simulation profiles (points) have been also been fitted to the triple-Gaussian function (lines).

the molecules whose longitudinal speeds are unaffected by the decelerator. $G_2(t)$ is a narrower and shorter peak which subtracts from $G_1(t)$, and represents the distribution of phase-stable molecules that are removed from the ‘field-free’ profile and bunched into the travelling effective potential well. These bunched molecules are decelerated and so appear at a new, later position in the time-of-flight profile, and are then described by $G_3(t)$.

Numerical simulations were performed for all the deceleration data taken. The simulations were of the same form as described for the AG guide and the 100-stage decelerator, except that these simulations neglect the effect of the laser probe beam. The simulated profiles shown in figure 7.9 (b) were formed from all the simulated molecules that successfully made it out of the decelerator and into the detection region. The simulated profiles were analysed in exactly the same way as the experimental data, each profile’s signal being normalized to the amplitude of a reference profile (generated by a simulation in which the decelerator field is zero), and then fitted to the same triple-Gaussian function.

Delay data

The time-of-flight profiles shown in figure 7.9 show the effect of the decelerator on a beam of molecules. The deceleration stages bunch molecules about the chosen synchronous molecule, creating a narrow peak in the profile. As more stages are used these molecules are decelerated more, and the peak moves to later times. The simulated time-of-flight profiles generally match the experimentally measured profiles well, especially in terms of the behaviour of the decelerated peak. However, the simulations predict greater profile signals for the decelerated peak, indicating that the AG decelerator is more “lossy” than expected. The time-of-flight profiles fit well to the triple-Gaussian function, indicating that the physical model of the triple-Gaussian (described above) is a good description. However, the simulated profiles show some small oscillations in the undecelerated distribution, which is not accounted for by this model.

The deceleration data were taken with all experimental parameters kept constant except the number of stages and the initial speed of the synchronous molecules (v_{sync}). It was a mistake to vary this latter parameter. The purpose of varying it was that, over the course of the data-run, the mean speed of the non-decelerated beam changed by a few metres per second (due to slow source drifts). In order to maximize the number of decelerated molecules, the initial speed was varied very slightly for data-runs corresponding to different numbers of stages, such that v_{sync} always corresponded to molecules at the centre of the non-decelerated time-of-flight profile. This corresponded to only a slight variation in v_{sync} , from 430 ms^{-1} to 437 ms^{-1} (although most data were taken within the much narrower range of 431 ms^{-1} to 433 ms^{-1}). However, this slightly complicates the interpretation of the data.

The profiles in figure 7.9 show that when very few stages are used the amount of

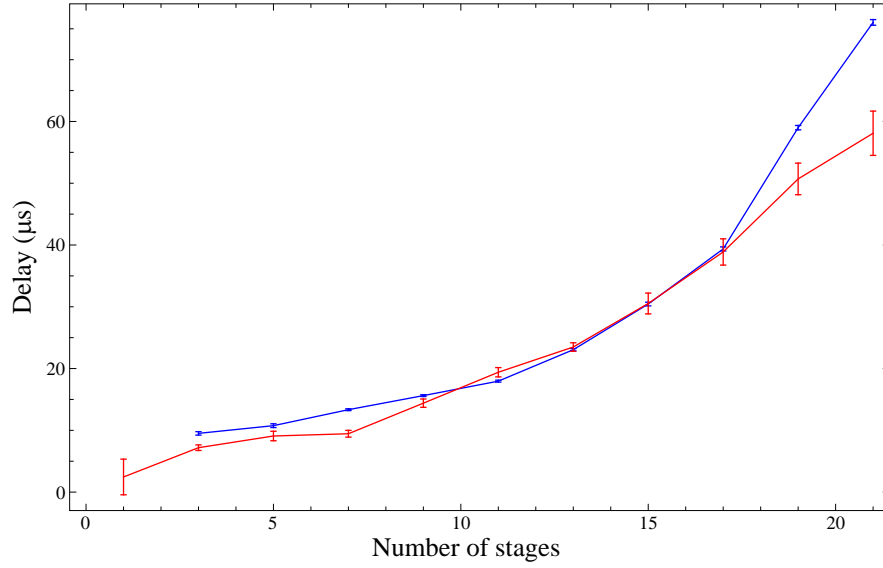


Figure 7.10: The delay between the arrival time of the decelerated molecules with a given initial speed and the arrival time of molecules with that initial speed if the decelerator were off. The delay is plotted as a function of the number of stages used. The data were taken with the decelerator operated at ± 20 kV, and with $z_{on} = 0$ mm and $z_{off} = 6$ mm. The delays were calculated from the fits to the function, $G(t)$, for both the experimental data (red points) and simulations (blue points). The error bars originate from the errors in the profile fits. The points have been joined to guide the eye.

deceleration is small, and the effect of the decelerator is principally to bunch the phase-stable molecules about the synchronous molecule. As the number of stages is increased these molecules are decelerated more and more, and are thus detected at later and later times. A measure of this deceleration is the ‘delay’, which is the arrival time of the decelerated bunch relative to the centre of the corresponding reference peak, taken with the decelerator turned off. The arrival time of the decelerated peak is given by the centre of $G_3(t)$. Figure 7.10 shows the delay of the decelerated molecules as a function of the number of stages used for the “0/6” experimental data (red points) and simulations (blue points). The error bars for both data-sets were calculated from the errors on the triple-Gaussian fits. The errors were smaller for the simulated data because the decelerated peaks are larger in this set and so can be fitted with greater certainty. There is good agreement between experiment and simulations for most of the data, with the molecules moving to later times as they are increasingly decelerated. However, the two sets of delays diverge for a large number of stages (19 and 21). By 21 stages the simulations predict that the decelerated molecules should be detected with a delay of $76 \pm 0.5 \mu\text{s}$, whereas the experimental data show a delay of $58.1 \pm 3.6 \mu\text{s}$. The reason for this disparity is not understood. If there were an error in the simulation then it ought to be consistently

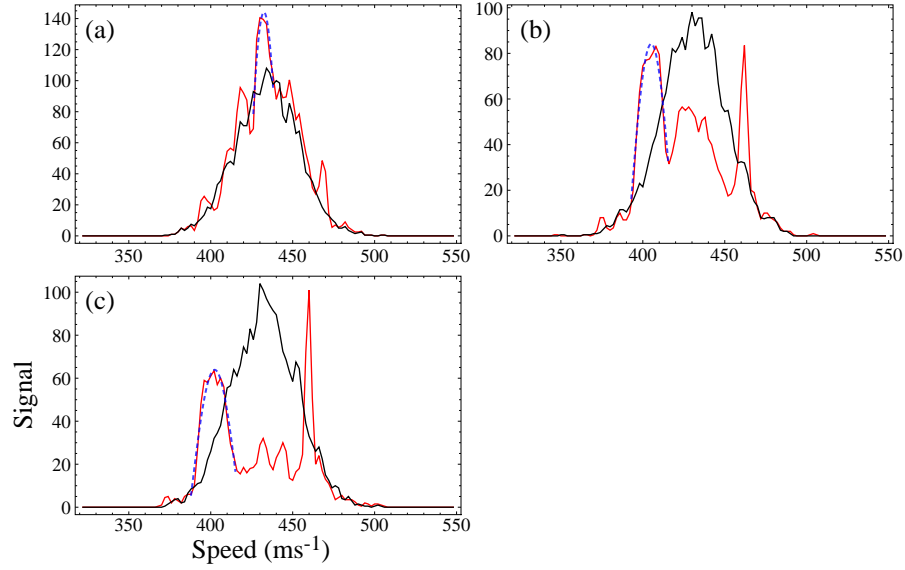


Figure 7.11: Simulated longitudinal speed profiles calculated with the AG decelerator operating at ± 20 kV, with $z_{on} = 0$ and $z_{off} = 6$ mm (red data), and with the decelerator turned off (black data). The simulations were calculated with (a) the last 3 stages used; (b) the last 19 stages used; (c) and all 21 stages used. The profile of the decelerated molecules has been fitted to a Gaussian function (blue, dashed lines) which has been used to determine the central speed of these molecules to be (a) 432.5 ms^{-1} , (b) 405 ms^{-1} , and (c) 402.4 ms^{-1} .

obvious in all the simulated profiles, and yet for most of the delay data excellent agreement is found with the experimental data. However, a small error in the simulation, or in the prediction of the applied electric fields would lead to an error in the Stark shift induced in a deceleration stage. This would lead to an error in the energy lost per stage. This energy error would have a smaller effect on faster molecules and so might not become obvious until the molecules were significantly decelerated. This would explain the disparity becoming evident for large amounts of deceleration, however, the relatively small speed differences achieved (see below) would render this effect quite small. It is possible that there is a mechanical problem with one of the deceleration stages, possibly a misalignment, which would affect the applied electric fields and thus the Stark shift. However, close inspection of the decelerator revealed no such misalignments.

In order to assess the implications of this delay disparity on the final molecular speed, consider the speed profiles associated with the simulated time-of-flight profiles. Figure 7.11 shows the simulated speed profiles of molecules in the detection region when (a) three stages, (b) 19 stages, and (c) 21 stages are used. Figure 7.11 (a) shows that the effect of three stages of the decelerator is to bunch molecules around the synchronous molecule and decelerate this bunch a small amount. This simulation matches the parameters under

which the associated experimental data were taken, with an initial synchronous speed of 435 ms^{-1} . The peak in the speed profile corresponding to the decelerated molecules has been fitted to a Gaussian function, which finds the central speed to be 432.5 ms^{-1} , a deceleration of 2.5 ms^{-1} for the synchronous molecule. The Gaussian fit is not good enough to give a reliable width to this peak, but a manual analysis finds the full-width of the decelerated peak to be 11 ms^{-1} . Figure 7.11 (b) shows the effect of using 19 deceleration stages. A Gaussian fit of the decelerated peak shows that the molecules have been slowed to 405 ms^{-1} (from an initial synchronous speed of 432 ms^{-1} in this case). Figure 7.11 (c) shows that using all 21 stages slows the molecules to a final speed of 402.4 ms^{-1} (down from 433 ms^{-1}). The delay achieved experimentally with 21 stages is very similar to that predicted by the simulations for 19 stages ($59.0 \pm 0.4 \mu\text{s}$). It is therefore reasonable to expect that the molecules decelerated with all 21 stages have a final speed given by the simulation for 19 stages, 405 ms^{-1} . It is possible to estimate the final speed from the experimentally measured time-of-flight profile by assuming that the decelerator applies a constant average deceleration along its length. Solving the equations of motion for a molecule in the centre of the decelerated packet and with 21 stages used (with initial speed 433 ms^{-1} , traversing the 504 mm-long decelerator and detected 810 mm downstream of the source at $1947 \mu\text{s}$) gives the molecule's final speed to be 402 ms^{-1} . It is difficult to determine exactly what the final speed of these molecules was, but it seems likely to be in the range 402 to 405 ms^{-1} , and so the final velocity will be taken to be $403.5 \pm 1.5 \text{ ms}^{-1}$. This final speed corresponds to a deceleration of 29.5 ms^{-1} , with a decrease in kinetic energy of 60.8 cm^{-1} (2.9 cm^{-1} per stage). The decelerator has removed 13% of the molecules' initial kinetic energy.

Signal strength

In addition to the amount of deceleration, the other result of interest in the time-of-flight profiles shown in figure 7.9 is the molecular flux emerging from the decelerator. In order to quantify the flux the 'signal ratio' is defined, very similarly to how it was defined in previous chapters. Each of the time-of-flight profiles shown in figure 7.9 has been normalized to the amplitude of its associated reference profile, taken with the decelerator turned off. To investigate the behaviour of the decelerated molecular flux as a function of the number of stages used the 'decelerated signal ratio' was calculated by dividing the area under the decelerated packet of molecules (that is, the area of $G_3(t)$) by the total area underneath the associated reference profile. The experimental and simulated decelerated signal ratio data are shown in figure 7.12 (a). When few stages are used the decelerated peak is small and the fits to $G_3(t)$ have large errors. For the simulations with 1 and 5 stages, and the experimental data with 1 and 3 stages the decelerated signal ratios are not shown because the large fitting errors rendered the results meaningless. Between 5

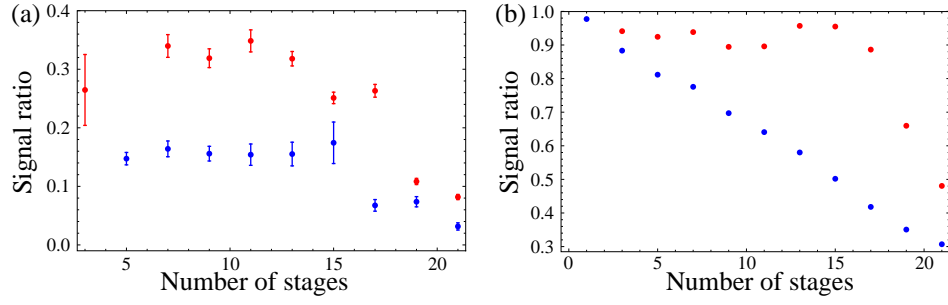


Figure 7.12: (a) The signal ratio of the decelerated peak as a function of the number of stages used, as calculated for the experimental (blue points) and simulated (red points) time-of-flight profiles. The area of the decelerated peak is that of $G_3(t)$. The error bars originate in the errors in the fitting parameters. (b) The signal ratio of the entire time-of-flight profile as a function of the number of stages used. Here the areas are calculated simply by integrating the profile data.

and 15 stages the experimental signal ratio holds steady around 15%. There is a drop after 15 stages, and when all 21 stages are used the signal ratio has dropped to 3%. It might be expected that the signal ratio should increase with the number of stages used. Increasing the number of stages moves the start of the electric field pattern closer to the source, where there is greater overlap between the molecular phase-space distribution and the decelerator's acceptance. However, neither the experimental or simulated results find such an increase. The simulated and experimental signal ratios agree well in terms of the dependence of signal ratio on the number of stages used: the signal holds steady until around 15 stages and then drops off. The experimental data measure consistently smaller signal ratios than the simulations, by a factor of roughly 2. The shape of the signal ratio data can be explained in terms of two competing effects. Firstly, as the number of stages is increased the effective entrance of the decelerator moves closer to the source, meaning that more molecules can be captured by the decelerator. However, there is also some loss associated with each stage (see below). The combination of these two effects balances well for most of the data, until a large number of stages is used. In this case the effect of moving the effective decelerator entrance closer to the source becomes less significant and the effect of the loss dominates.

So what is this source of loss? An AG guide comprises electric field ‘lenses’ which exert equal and opposite forces along two transverse directions, x and y . Inside the stages of the AG decelerator, this AG focussing and defocussing is indeed achieved. This can be seen by considering the divergence of the force, \vec{F} , exerted on a molecule on the beam-line axis¹. It can be shown [80] that, for the potentials created by a two-rod field stage, this

¹The divergence of the force away from the axis is much more complicated to analyse and is not described here.

divergence is given by:

$$\nabla \cdot \vec{F} = \frac{\mu}{E} \left(\frac{\partial E}{\partial z} \right)^2, \quad (7.6)$$

where E is the magnitude of the electric field. Inside a deceleration stage $\frac{\partial E}{\partial z} = 0$ and $\frac{\partial F_z}{\partial z} = 0$, and so the transverse force constants are equal and opposite:

$$k_x = -\frac{\partial F_x}{\partial x} = -k_y = \frac{\partial F_y}{\partial y}. \quad (7.7)$$

Thus, on the axis, the strength of focussing and defocussing forces are equal and AG guiding can be achieved. However, near the end of a field stage the electric field changes along z . This is, of course, required for deceleration and is the region of the field that will be used in every stage. However, the changing axial component of electric field disturbs the balance of the transverse forces. Consider the region of the axis where $\frac{\partial E}{\partial z} \neq 0$ and $\frac{\partial F_z}{\partial z} \neq 0$. In the case of a linear Stark shift ($W_s = -\mu|E|$) the first derivative of the force along z is $\frac{\partial F_z}{\partial z} = -\mu \frac{\partial^2 E}{\partial z^2}$. The sum of the two transverse force constants is thus found from equation 7.6 to be:

$$k_x + k_y = -\mu \left(\frac{1}{E} \left(\frac{\partial E}{\partial z} \right)^2 - \frac{\partial^2 E}{\partial z^2} \right). \quad (7.8)$$

In this region the force constants are no longer equal and opposite, and the molecules are either defocussed or overfocussed. This causes molecules to crash into the electrodes or to leave the decelerator, never to return. The very part of the electric field responsible for deceleration is also a source of loss.

Figure 7.13 shows $k_x + k_y$ (in units of $\text{cm}^{-1}/\text{mm}^2$) along the axis inside a deceleration stage charged to ± 20 kV (red line). A positive value for this quantity means that transverse defocussing is stronger than transverse focussing. Also shown (in arbitrary units) are the axial electric field profile (black line), the Stark shift of a ground state CaF molecule (orange line) and a diagram of one of the electrodes. It can be seen that $k_x + k_y$ rises rapidly when moving from the cylindrical section to the hemispherical end, peaking shortly after this transition. Highlighted on the figure are the field on- and off-positions for the data discussed above (green line and blue line respectively). It can be seen that the region of the stage used in the above data is exactly that region that is badly affected by the focussing/defocussing imbalance. Thus in each stage the molecules receive a transverse ‘kick’. This ‘kick’ is the loss mechanism experienced by molecules in every deceleration stage.

The simulations show the effects of this defocussing loss mechanism extremely clearly. Figure 7.14 shows results of a simulation of the AG decelerator, with 17 stages used, and operated at ± 20 kV, with $z_{on} = 0$ mm, $z_{off} = 6$ mm, and a synchronous speed of $v_{sync} = 436 \text{ ms}^{-1}$. The simulations start with an initial source of molecules, which are then propagated through the decelerator and to the detection region. The simulation identifies

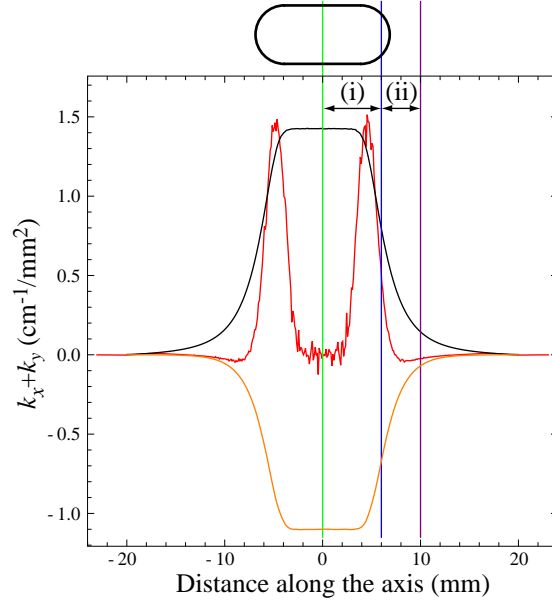


Figure 7.13: The sum of the transverse force constants, $k_x + k_y$, along the beam-line axis inside a deceleration stage charged to ± 20 kV (red line). Also shown (in arbitrary units) are the axial electric field (black line) and Stark shift experienced by a CaF molecule in the $|0, 0\rangle$ state (orange line), and the outline of an electrode. When the electrode changes from being cylindrical to hemispherical there is a rapid change in electric field along z . This results in a large peak in $k_x + k_y$, where the two force constant are clearly far from equal and opposite. Also shown are the lines representing on-/off-positions (i) $z_{on} = 0/z_{off} = 6$ mm (green and blue lines), and (ii) $z_{on} = 6/z_{off} = 10$ mm (blue and purple lines).

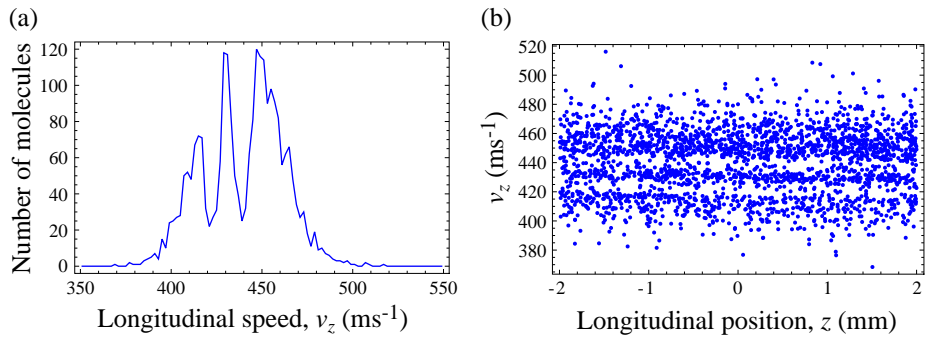


Figure 7.14: The distribution of molecules at the source that successfully make it through the decelerator and into the detection region, found by a simulation of the AG decelerator with 17 stages used, operated at ± 20 kV, with $z_{on} = 0$ mm, $z_{off} = 6$ mm, and $v_{sync} = 436$ ms^{-1} . (a) The longitudinal velocity distribution of these molecules. (b) The z - v_z phase-space distribution of the successful molecules.

those molecules which successfully make it through the decelerator and into the detection region. Having identified these molecules it is possible to extract information about where in the initial phase-space distribution they originated. Figure 7.14 (a) shows the initial longitudinal velocity profile *in the source* of these successful molecules. The effect of the decelerator on the initial source is clear: some velocity groups are well transmitted, whereas others are only poorly transmitted. In particular, two velocity groups, centred on 421 ms^{-1} and 440 ms^{-1} , are poorly transmitted. Figure 7.14 (b) shows the longitudinal phase-space distribution (z - v_z) of the successful molecules. The molecules occupy a uniform area of phase-space, but with two lines of constant v_z showing strongly depleted populations. These are the 421 ms^{-1} and 440 ms^{-1} velocity groups. Figure 7.14 (b) shows that these velocity groups are transmitted poorly, regardless of the position of the molecules in the source.

The explanation for this behaviour is found by considering the positions that these molecules occupy in a deceleration stage when the fields are switched. Figure 7.15 (a) shows the same simulated source velocity distribution as figure 7.14 (a), but with coloured lines marking out five velocity groups of interest: a cyan line at 421 ms^{-1} , a green line at 430 ms^{-1} , a yellow line at 436 ms^{-1} , an orange line at 440 ms^{-1} , and a purple line at 447 ms^{-1} . The 421 ms^{-1} and 440 ms^{-1} lines mark the centres of the poorly transmitted velocity groups. The 430 ms^{-1} and 447 ms^{-1} lines mark the well transmitted velocity groups. The line at 436 ms^{-1} marks the initial speed of the synchronous molecule in this simulation. It can be seen that the synchronous molecule lies near the centre of a poorly transmitted group. Consider now where molecules with these speeds are when the fields switch. Figures 7.15 (b)–(f) show the positions of these molecules inside the first stage when the fields are turned on and off²: these positions are marked by a coloured rectangle superimposed on top of the Stark shift profile in the first stage (red line). The colour scheme of the rectangles is the same as in figure 7.15 (a). Also shown is the sum $k_x + k_y$ (blue line). It can be seen from figure 7.15 (b) that the synchronous molecule has $z_{on} = 0 \text{ mm}$ and $z_{off} = 6 \text{ mm}$ (by definition) and experiences almost all of the defocussing peak in $k_x + k_y$. Figure 7.15 (c) shows that the 440 ms^{-1} group is 2 mm ahead of the synchronous molecule when the fields switch. This group experiences all of the $k_x + k_y$ peak and suffers the worst from defocussing loss. Figure 7.15 (d) shows that molecules with 430 ms^{-1} are 3 mm behind the synchronous molecule when the fields switch. These molecules experience the centre of the field stage, and almost completely avoid the two peaks in $k_x + k_y$. Figure 7.15 (e) shows that this velocity group is well transmitted, representing a peak in transmission. Figure 7.15 (f) shows that molecules with 421 ms^{-1} are 8 mm behind the synchronous molecule when the fields switch. These molecules experience all

²In this particular simulation only the last 17 stages were used. The ‘first’ stage referred to here is the first stage to be charged, which is not the same as the first stage in the AG decelerator.

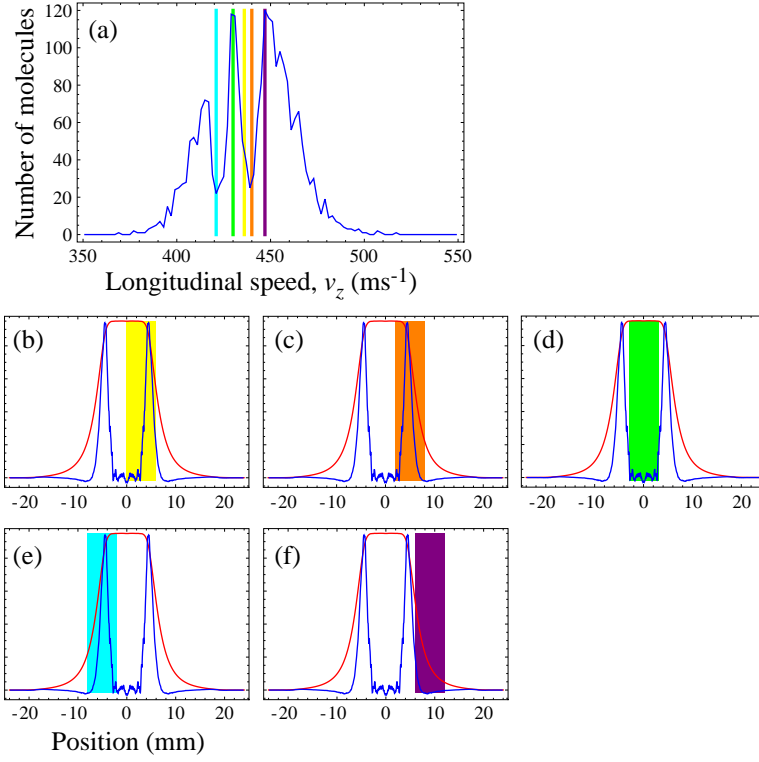


Figure 7.15: (a) The simulated source velocity profile of those molecule that make it through the decelerator. This is the same profile as shown in figure 7.14 (a), except with coloured lines superimposed, marking out five velocity groups of interest: 421 ms^{-1} (cyan line), 430 ms^{-1} (green line), 436 ms^{-1} (yellow line), 440 ms^{-1} (orange line), and 447 ms^{-1} (purple line). (b)–(f) The part of the decelerator experienced by each of these velocity groups inside the first stage of the decelerator to be charged, shown by a rectangle with the same colouring scheme as (a). Also shown in each case are the Stark shift profile and $k_x + k_y$ inside the deceleration stage.

of the peak in $k_x + k_y$ near the beginning of the stage and are indeed poorly transmitted. Finally, figure 7.15 (f) shows that those molecules with 447 ms^{-1} are 6 mm ahead of the synchronous molecules when the fields switch. These molecules experience very little of the peak in $k_x + k_y$ at the end of the field stage and are very well transmitted.

This analysis considers only the first deceleration stage, but it is clear that it describes the mechanism by which molecules are lost from the AG decelerator: those molecules that experience either peak in $k_x + k_y$ inside a charged deceleration stage will experience an overall defocussing kick and are unlikely to be guided to the end of the decelerator.

Figure 7.12 (b) shows the total signal ratio as a function of the number of stages. This was calculated by integrating under the entire deceleration profile (and normalizing in the same way as above). Here the difference between experiment and simulation is striking. The experimental data show an almost linear drop in signal ratio with the number of stages used, whereas the simulated signal ratio remains roughly constant at around 0.95 until 15 stages, after which it drops off rapidly. Given the relatively good agreement between simulations and experimental data for the decelerated molecules, this striking difference must originate in the behaviour of the non-synchronous molecules. This can be seen in the time-of-flight profiles (figure 7.9): in the experimental data the broad Gaussian, upon which the decelerated peak sits can be seen to decrease in amplitude steadily with the number of stages used, whereas in the simulations it remains roughly constant for most of the profiles. The reason for this discrepancy is not understood. Given the good agreement with so many other data, it seems very likely that the simulations are working well, but are missing some information about the experiment, possibly a misalignment of the decelerator.

7.7.2 Deceleration with $z_{on} = 6 \text{ mm}$ and $z_{off} = 10 \text{ mm}$

Delay data

It can be seen from figure 7.13 that there is a region in a deceleration stage towards the end of the electrodes where $k_x + k_y$ is close to zero, and where there is sufficient Stark potential depth to achieve deceleration. The figure shows an on-position at $z = 6 \text{ mm}$ (blue line) and off-position at $z = 10 \text{ mm}$ (purple line). The Stark potential difference between these on- and off-positions is 100 GHz, almost as great as the 109 GHz with the previous on- and off-positions. Thus these new positions offer almost the same amount of deceleration, but with the advantage of avoiding the defocussing ‘kick’ from the transverse force imbalance. Deceleration data were thus taken at $\pm 20 \text{ kV}$ with $z_{on} = 6 \text{ mm}$ and $z_{off} = 10 \text{ mm}$. As in the previous data-set, these data were taken with the number of stages, n , varying from $n = 3$ to $n = 21$. This data-set shall henceforth be referred to as the “6/10” data.

Figure 7.16 (a) shows experimental time-of-flight profiles measured with $n = 3, 5,$

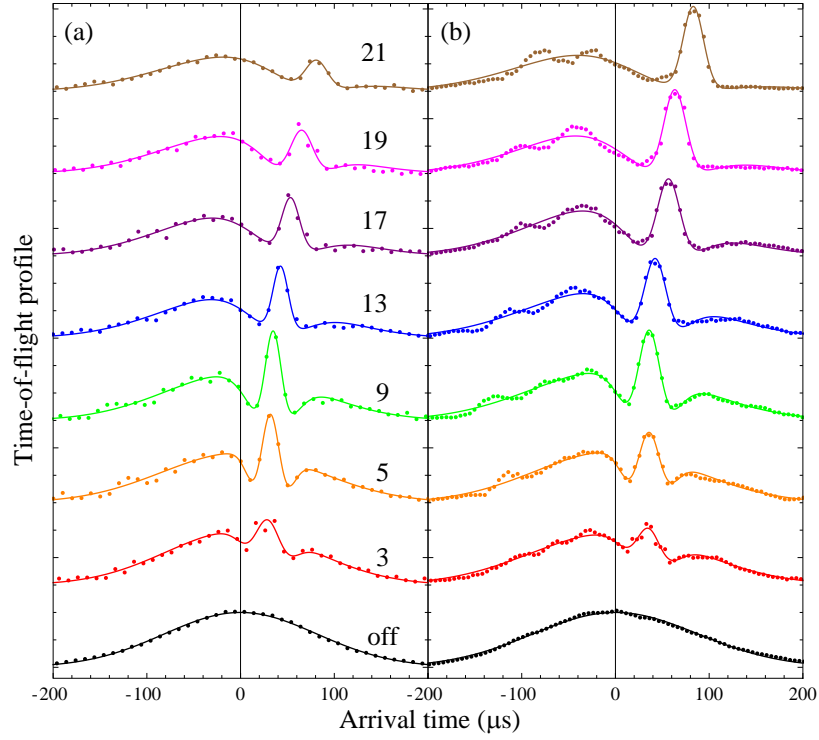


Figure 7.16: (a) Experimental time-of-flight profiles measured with the decelerator charged to ± 20 kV, and used with $z_{on}/z_{off} = 6/10$ mm. Each profile has been normalized by the same factor that gives its associated reference profile a unity amplitude. The time origin of each profile is the central time of the associated reference profile. The profiles are labelled by the number of stages used. For clarity, not all of the profiles are shown here. The profiles have been fitted to the triple-Gaussian function, $G_3(t)$. The bottom profile (black) is the average of all the reference profiles. (b) Simulated profiles corresponding to the experimental profiles shown in (a), and with the same colour scheme. The simulated data (points) have also been fitted to the triple-Gaussian function (lines).

9, 13, 17, 19 and 21. Other profiles have not been shown for the sake of clarity. The profiles have been fitted to the same triple-Gaussian function as above. Figure 7.16 (b) shows the results of simulations. It can be seen immediately that there is good agreement between the two data-sets in terms of the delay of the decelerated packet, and much better agreement in terms of the signal ratios than in the previous data-set, particularly with respect to the undecelerated molecules. The experimental and simulated decelerated peaks look very similar to each other, both in terms of their delay and amplitude. This good agreement lasts for all the data except those data taken with 19 and 21 stages; in these cases the amplitude of the experimental decelerated peak is smaller than that predicted by simulations. The position of the experimental and simulated decelerated peak appears to match well for all the data. As well as the decelerated peak, the behaviour

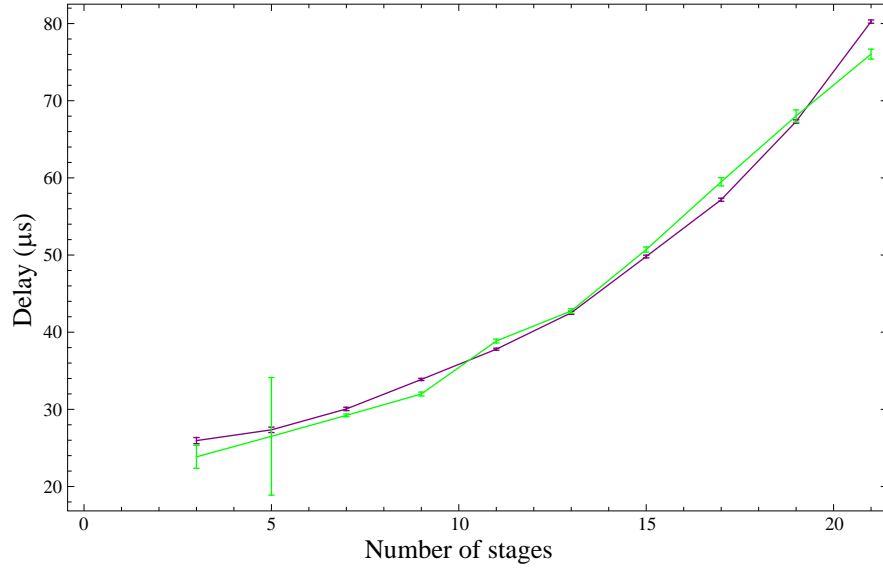


Figure 7.17: The delay between the time-of-arrival of the decelerated peak, with a given initial speed, and the time at which molecules with that initial speed would be detected were the decelerator off. The data were recorded with the decelerator operating at ± 20 kV, and with $z_{on}/z_{off} = 6/10$ mm. The delay is shown versus the number of stages used for experimental (green points) and simulated (purple) time-of-flight profiles. The delay is calculated from the triple-Gaussian fit, and the error bars are calculated from the errors in the fit parameters. The points have been joined to guide the eye.

of the undecelerated molecules agrees well in both experimental and simulated data-sets. Unlike the “0/6” data, the amplitude of the undecelerated signal is well matched in both simulations and experimental data, with $G_1(t)$ maintaining a noticeably greater amplitude as the number of stages is increased (unlike the “0/6” data where the undecelerated amplitude decreases rapidly as the number of stages is increased.)

Figure 7.17 shows the delay between the time-of-arrival of the decelerated packet, with a given initial speed, and the time when molecules with that initial speed would have arrived were the decelerator off. There is good agreement between the experimental data (shown in green) and the simulation results (shown in purple). The error bars are calculated from the errors in the triple-Gaussian fit parameters. There is a slight discrepancy between experimental data and simulations when all 21 stages are used (with the simulations predicting a delay of $80.3 \mu\text{s}$, and the experimental data measuring a delay of $76 \mu\text{s}$), but this is not very large, and is smaller than the discrepancy in the “6/10” data. The delays measured in this data-set are very similar to those measured with $z_{on}/z_{off} = 0/6$ mm, despite the slightly smaller potential hill presented by each deceleration stage. This might indicate that the amount of deceleration is comparable. However, it is clear from figure 7.17 that as the number of stages tends to zero, there is

still some non-zero delay. This cannot result from deceleration as there is no deceleration when no stages are used. The experimental and simulated delays taken with 3 stages are found to be $23.8 \mu\text{s}$ and $26.0 \mu\text{s}$ respectively. This is too large a delay to result from only three stages. The speed profiles generated by the simulations for few stages indicate that the decelerated velocity class has a slightly lower initial speed than the initial speeds for which the deceleration patterns were generated. These patterns were calculated with initial speeds in the range of 429.7 ms^{-1} to 432.5 ms^{-1} (with a mean value of 431.4 ms^{-1}). Simulations of the data find that for 3 and 21 stages used the final speed of the decelerated molecules is 425.0 ms^{-1} and 408.9 ms^{-1} respectively. It is simple to calculate the initial speed of molecules before entering the decelerator that results in these two final speeds, assuming nothing other than a constant energy loss per stage. This initial speed is 427.6 ms^{-1} , slower than the initial synchronous speeds used to calculate the deceleration patterns in the simulations (and experiments).

To explain this discrepancy it is instructive to consider the longitudinal effective potential created on the axis by the switching fields. This is shown for $z_{on}/z_{off} = 6/10 \text{ mm}$ in figure 7.18 (a). The origin of the position axis in this figure represents the position of the synchronous molecule. It can be seen that the synchronous molecule in the calculated effective potential for the $z_{on}/z_{off} = 6/10 \text{ mm}$ pattern is situated on a maximum of potential, rather than a minimum. There are thus no phase-stable molecules oscillating about the synchronous molecule. There is a minimum 3.8 mm behind the maximum. This minimum traps phase-stable molecules. A molecule whose speed is v_{sync} , and whose position relative to the synchronous molecule is $z = -3.8 \text{ mm}$ will be stationary at the bottom of this well.

The purpose of using the on- and off-positions $z_{on} = 6 \text{ mm}$ and $z_{off} = 10 \text{ mm}$ was for the synchronous molecule to avoid the ‘dangerous’ region of each deceleration stage. However, the effective potential created by this switching pattern causes the phase-stable molecules to lie behind the synchronous molecule, and they in fact still experience this defocussing end-effect. This explains why the decelerated peak signal ratios are not significantly better than in the “0/6” data.

The offset in the delay data can in part be explained by molecules being trapped in the potential minimum behind the synchronous molecule. The high voltage switching pattern was generated such that the synchronous molecule was to be taken from the centre of the molecular packet. The molecular packet entering the decelerator is long enough that there are enough molecules 3.8 mm behind this centre for there to be a significant number of molecules that can be trapped and decelerated in the effective potential well. The 3.8 mm retardation will add an offset to the measured delays of around $10 \mu\text{s}$. This is significant, but clearly does not account for the total delay offset on its own.

The remainder of the offset arises because the slower molecules are the ones that

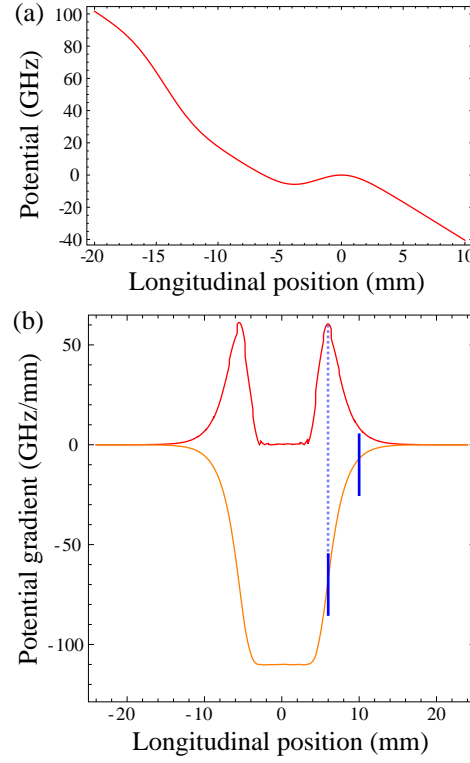


Figure 7.18: (a) The effective potential well experienced by ground-state CaF molecules, calculated for $z_{on}/z_{off} = 6/10$ mm, with the AG decelerator charged to ± 20 kV. (b) The first derivative of the Stark potential well as a function of z inside a deceleration stage, charged to ± 20 kV. Also shown are the on- and off-positions, $z_{on} = 6$ mm and $z_{off} = 10$ mm (blue lines). It can be seen that in the region of z bounded by these limits the slope of the potential well is always decreasing, and there are no phase-stable molecules oscillating about the synchronous molecule. The dashed blue line shows that $z_{on} = 6$ mm occurs at exactly the position that the potential gradient starts to decrease.

tend to arrive later than the synchronous molecule, and thus the average speed of the molecules trapped in the effective potential well will be slightly less than v_{sync} . The exact offset created by this effect depends on the overlap of the phase-space acceptance of the decelerator and the phase-space area occupied by the incoming molecules. If the acceptance is filled by the molecules then the average speed of the trapped molecules is v_{sync} and there is no offset. If it is not completely filled then the average trapped speed will be less than v_{sync} and there will be an offset. An average trapped speed of around 428 ms^{-1} (compared with a typical synchronous speed of $v_{sync} = 431.4 \text{ ms}^{-1}$) adds enough delay to fully explain the remainder of the observed offset.

Having explained the form of the delay data, it is now possible to analyse the amount of deceleration. The good agreement between the simulations and experiments indicates that the simulated speed profiles describe well the experimental speed profiles. These show that, with all 21 stages used, and the decelerator charged to $\pm 20 \text{ kV}$, ground-state CaF molecules were decelerated with the pattern discussed above from 427.6 ms^{-1} to 408.9 ms^{-1} . This corresponds to a total energy loss of 38.5 cm^{-1} . In this case the decelerator has removed 8.6% of the molecules' initial kinetic energy.

Signal ratios

The purpose of decelerating with $z_{on} = 6 \text{ mm}$ and $z_{off} = 10 \text{ mm}$ was to escape the region inside each deceleration stage where $k_x + k_y$ peaks, and thereby to increase the molecular flux out of the decelerator. However, these on- and off-positions do not provide an effective potential well centred on the synchronous molecule. Instead all of the phase-stable molecules lie behind the synchronous molecule, meaning that they are decelerated in almost exactly the same 'dangerous' region as for the "0/6" data. It might thus be expected that the signal ratios should be very similar to those measured with $z_{on} = 0 \text{ mm}$ and $z_{off} = 6 \text{ mm}$.

The signal ratios were analysed for the "6/10" data in the same way as for the "0/6" data. Figure 7.19 (a) shows the signal ratio of the decelerated peak versus the number of stages used, calculated from the experimental data (blue points) and simulations (red points). These signal ratios were calculated from the triple-Gaussian fits to the profiles and the error bars result from the fit parameter errors. The signal ratio data for small numbers of stages are not shown as the fits have very large errors in these cases: the position of the decelerated peak is found well, but its amplitude is much more difficult to determine as the peak is not well distinguished from the undecelerated molecules. There is good agreement between the experiments and simulations, with both data-sets having similar shapes, although the simulated signal ratios are on average 1.7 times greater than the experimentally measured ratios.

The total profile signal ratio data (figure 7.19 (b)) also show good agreement between

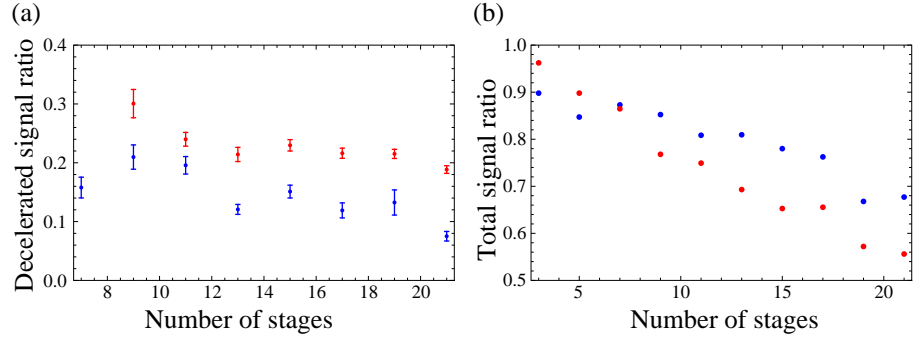


Figure 7.19: Signal ratio data taken with the AG decelerator operating at ± 20 kV, and with $z_{on}/z_{off} = 6/10$ mm. (a) The signal ratio of the decelerated peak as a function of the number of deceleration stages used. (b) The signal ratio of the entire recorded time-of-flight profile as a function of the number of stages used. In both cases the experimental data are shown in blue, and simulations in red.

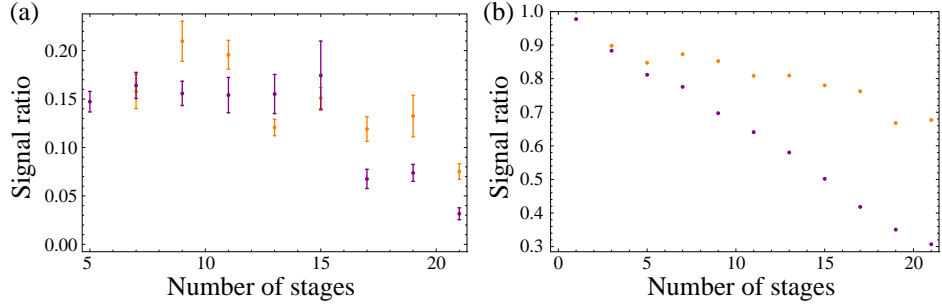


Figure 7.20: The experimental signal ratios taken with the AG decelerator operating at ± 20 kV, and with $z_{on}/z_{off} = 0/6$ mm (purple points) and $z_{on}/z_{off} = 6/10$ mm (orange points). (a) Signal ratio of the decelerated peaks. (b) Total profile signal ratios.

simulations and experiment. In both cases the signal ratio falls steadily from around 0.95, with three stages used, to between 0.5 and 0.7 with all 21 stages used. The simulations tend to give greater signal ratios than the experimental data, but the agreement is much better than in the same analysis for the “0/6” data.

Figure 7.20 (a) compares the measured decelerated peak signal ratios in the “0/6” and “6/10” experimental data-sets. It can be seen that both data-sets agree very well. This makes sense as in both cases the decelerated molecules experience almost the same region of each deceleration stage, and so experience the same amount of loss per stage from the peak in $k_x + k_y$.

Figure 7.20 (b) compares the total time-of-flight profile signal ratios for both data-sets. Both data-sets show the same form of behaviour: a steady, almost linear drop as the number of stages is increased. However, the 6/10 data have a much smaller slope, experiencing less loss per stage than the 0/6 data. When all 21 stages are used the

0/6 data-set has a total signal ratio of 0.3, whereas the 6/10 data-set has a much larger signal ratio, 0.76. The total signal ratios are generally dominated by the behaviour of the undecelerated molecules. These molecules are not subject to ideal AG guiding as they do not experience the same lens lengths along the decelerator: each undecelerated molecule is at a different position in each stage when the fields are switched on and off. The focussing and defocussing kicks experienced by the undecelerated molecules mostly average to nothing, but not quite as the defocussing kicks are slightly stronger than the focussing kicks (as shown in figure 7.13). As more of the decelerator is used there is a greater chance of an undecelerated molecule experiencing a net defocussing, and so fewer undecelerated molecules make it through the decelerator. In the “0/6” data the decelerator was on for 50% longer than in the “6/10” data, and so it is expected that there will be fewer undecelerated molecules in the “0/6” time-of-flight profiles.

7.8 Conclusions

A 21-stage AG decelerator has been used to decelerate ground-state CaF molecules from 433 ms^{-1} to $403.5 \pm 1.5 \text{ ms}^{-1}$. This corresponds to a total loss in kinetic energy of 60.8 cm^{-1} (2.9 cm^{-1} per deceleration stage) and the removal of 13% of the initial kinetic energy.

The deceleration pattern used to achieve this was defined by the on- and off-positions, $z_{on}/z_{off} = 0/6 \text{ mm}$ for the synchronous molecule. However, it was found that this timing sequence placed the molecules in a region of the deceleration stages where the transverse forces were not well-matched, and the decelerator was thus lossy, with the detected molecular fluorescence signal dropping with the number of stages used. In order to avoid this region data were taken with the later on-/off-positions of $z_{on}/z_{off} = 6/10 \text{ mm}$. Unfortunately, it was found that this pattern does not produce an effective longitudinal potential well around the synchronous molecule and so does not bunch and decelerate molecules around it. However, this switching pattern does generate an effective potential well whose minimum is located 3.8 mm behind the synchronous molecule, and molecules were trapped in this well and decelerated. The deceleration was not quite as much with this pattern: slowing from 427.6 ms^{-1} to 408.9 ms^{-1} . This corresponds to a reduction in the kinetic energy of 38.5 cm^{-1} , which is 8.6 % of the initial kinetic energy.

Extensive numerical simulations were performed, and generally agreed well with the experimental data. The amount of deceleration was measured by the delay of the decelerated peak, and the simulations agreed well with the measured delays, particularly for the “6/10” data-set. For this latter data-set, the shape of the simulated and experimental signal ratio data were similar for both the decelerated peak area and the total time-of-flight profile. The simulations consistently predict slightly greater decelerated signal ratios than the experimental data by an average factor of 1.7. For the “0/6” data,

the agreement between experiment and simulation was not as good, with the simulations predicting decelerated peak signal ratios approximately twice as great on average, and the simulations predicting a somewhat larger delay with all 21 stages used than observed in the experiments. A major disagreement between experimental and simulated data was found in the total profile signal ratios for the “0/6” data, where the simulations find this area to remain steady around unity when the number of stages is varied between 3 and 15, whereas the experimental data shows a steady decline in this ratio. This discrepancy has not been understood.

In both the “0/6” and “6/10” data-sets, a scaling factor of around 2 is required to bring the measured decelerated peak signal strengths into good agreement with the simulated profiles. This is considerably smaller than the disagreement found in previous AG deceleration experiments. Analysis of the AG deceleration of CO by a 12-stage decelerator [90] found that a scaling factor of around 20 was required to bring the experimental signals into agreement with the simulations. Further simulations indicated that this discrepancy could be explained by a typical electrode misalignment of ± 0.2 mm. Deceleration of benzonitrile by a 27-stage AG decelerator [92] found a slightly smaller disagreement factor of 17, which could be explained by a misalignment of ± 0.1 mm in the electrodes’ positions. It was known from measurements of the AG decelerator that the electrodes’ positions were accurate to at least ± 0.1 mm. Given the large disagreements with simulations found by the above two experiments, it is very likely that the smaller discrepancies in signal strengths found in the experiment reported here can be explained by misalignments smaller than ± 0.1 mm.

Chapter 8

Conclusions and Outlook

8.1 Measuring molecular parameters

Several important molecular parameters of CaF have been measured by the saturation of laser-induced fluorescence. The interaction of ground-state molecules with a laser probe beam has been modelled by rate equations, and this model has been used to reproduce experimental data relating to the width and amplitude of two spectral lines as a function of laser intensity. The parameters measured were the natural lifetime and hyperfine interval of the $A^2\Pi_{\frac{1}{2}}(v=0)$ state, which were found to be 19.2 ± 0.7 ns and 4.8 ± 1.1 MHz, and the Franck-Condon factor of the $A-X$ (0–0) transition, which was found to be $0.987^{+0.013}_{-0.019}$.

The experimental method used for these methods is considerably simpler than is typically used to make the above measurements in molecules. The $A^2\Pi_{\frac{1}{2}}(v=0)$ state lifetime measurement is consistent with a theoretically calculated value of 19.48 ns [59], and more accurate than the previous experimental measurement of 21.9 ± 4 ns [60]. The excited state hyperfine interval of the $A^2\Pi_{\frac{1}{2}}(v=0)$ state had not been measured previously, and the measurement is useful as the hyperfine interval can now be incorporated into future spectroscopic models of CaF. The value of the measured Franck-Condon factor agrees well with a theoretical calculation of 0.964 [59].

The Franck-Condon factor is very close to unity, meaning that a CaF molecule excited to the $A^2\Pi_{\frac{1}{2}}(v=0)$ state is unlikely to decay to vibrationally excited levels in the ground electronic state. This is a very useful result indeed as decay channels to excited vibrational states are an experimental barrier to laser cooling molecules. In a laser cooling scheme, if there were no vibrational leak from the excited state then there would need to be only rotational (and hyperfine) repumping. This vastly reduces the number of laser frequencies required. The Franck-Condon factor for decay to vibrational states with $v > 0$ is not zero, of course. Detailed theoretical analysis of the Franck-Condon factors in BeF, MgF and CaF has been performed [59]. It can be shown from this analysis that the following approximation holds well for these molecules: if the Franck-Condon factor of a transition

from a state with $v'' = 0$ to a state with $v' = i$ is labelled Z_{0i} , then $Z_{01} = (1 - Z_{00})$, and $Z_{02} = (1 - Z_{00})^2$. Therefore a molecule with $Z_{00} \approx 1$ will need only limited vibrational repumping to make laser cooling a practical possibility. For example, as discussed in chapter 4, DeMille has reported that with repumping from the ground electronic rotational levels and the first excited vibrational state, SrF molecules have been measured to scatter around 105 molecules before entering a dark state [58]. DeMille calculates that adding just one more vibrational repump frequency will increase this scattering to 10^5 photons per molecule, which would allow effective laser cooling. These measurements and calculations are based on SrF, with $Z_{00} = 0.98$ and $Z_{01} = 0.02$. The value of the Franck-Condon factor of CaF reported in this thesis suggests that CaF is a very strong candidate for laser cooling.

8.2 Guiding ground-state CaF

A 1m-long four-rod alternating gradient (AG) guide has been built and used to transport ground-state CaF molecules from the supersonic source and focus them into the detector. The guide is charged to high voltage, which creates a saddle-shaped electric field on the beam-line axis. This field acts as a ‘lens’, focussing the molecules in one transverse direction, and defocussing them in the other. By switching the applied voltage in time between two states it is possible to periodically rotate this saddle-shaped field, and balance the effects of the focussing and defocussing forces. In fact the guide can be used to achieve an overall net focussing. By changing the timing of the switching pattern it is possible to vary the length of the field lenses. The guide was operated at three different voltages, ± 5.5 kV, ± 8.0 kV and ± 9.5 kV. The applied voltage was limited by the potential difference for which the high voltage switches were rated. At each voltage the molecular flux was measured over a range of lens durations. For each voltage an optimal lens duration was observed, the value of which was found to decrease with increasing applied voltage.

The dynamics of molecules in an AG guide were discussed, in particular the effects of the shape of the transverse electric field. A harmonically-varying field gives the greatest acceptance, meaning that the guide can stably transport a large number of molecular trajectories. However, the presence of anharmonic terms in the transverse field reduces this acceptance, particularly for short lens lengths, where the overall focussing is weak.

The experimental results were compared with numerical simulations. Good agreement was found between the experimental and simulated data in terms of the shape of the molecular flux as a function of lens duration. In particular the simulations agreed well with the measured lens durations for optimal flux. However, the simulations predicted larger fluxes than were observed. It was found that introducing a 2 mm misalignment of the probe laser beam relative to the AG guide brought the simulated data into very

good agreement with the experimental data. This result was not discovered until after a considerable number of simulations had been performed. The obvious next step would be to fix this misalignment and repeat the experiments. Unfortunately, by the time the misalignment was discovered the AG guide had been removed from the vacuum chamber in order to make way for the 100-stage decelerator. It would be possible to reinstall the guide inside the vacuum chamber and then transport molecules after very careful alignment. However, the properties of the AG guide have been thoroughly investigated and the purpose of this experiment would be merely to confirm the previous misalignment. Simulations have shown that the AG guide is capable of transporting a very large flux of molecules from a buffer-gas source [85]. It seems that a much more profitable future project would be to transport YbF molecules from the buffer-gas cell that has been constructed at Imperial College [45].

As well AG guiding with switching fields, it was found that the guide is still capable of transporting molecules when held at constant high voltage. In this ‘DC’ operation the guide acts as one long lens, focussing in one direction, but defocussing in the other. It seems unlikely that any molecules should be able to survive for one metre in such a lens. However, when the full transverse electric field was considered, including the field outside the guide, it was found that there are stable trajectories that take a molecule on large-amplitude oscillations in one transverse direction, but that require the molecule to have only a very little motion in the other transverse direction. This limits the acceptance of the DC guide. The technical simplicity of such a device suggests that this might be a good way of transporting strong-field seeking molecules. Simulations were performed of the long-term stability of these trajectories. Although some molecules were found to survive for a long time in such a guide (up to 500 ms), the acceptance is small for long DC guides, and the trajectories are not completely stable. This reduces the guide’s usefulness when operated in DC guiding mode, and it is considered that, although a surprising and unexpected result, DC guiding is not a practical method of transporting large fluxes of molecules over the distances typically required in the laboratory.

8.3 Decelerating CaF

Two types of Stark decelerator have been built and used to slow beams of CaF. A 100-stage decelerator has been used to slow CaF molecules in the $|\mathcal{N} = 4, M_N = 0\rangle$ state from 343 ms^{-1} to 247 ms^{-1} . This is a removal of 48% of the molecules’ initial kinetic energy. It was found that the switching electric fields inside the decelerator are able to drive transitions between different states. In particular the rotation of the electric field is able to drive transitions between different M_N sub-levels of a given \mathcal{N} manifold. These transitions drive the molecules into states that are not properly decelerated or guided,

reducing the detected flux of both decelerated and undecelerated molecules. It was found that the undecelerated molecules suffered much more from these non-adiabatic transitions, which resulted in a vastly reduced flux of undecelerated molecules. These transitions are more likely when the electric fields are weak (and the sub-levels are closely spaced) and rapidly rotating. Applying a bias voltage to the decelerator induces a baseline Stark shift, keeping the interval between the sub-levels large enough to suppress these transitions. It was found that applying a bias voltage can inhibit these transitions, and that when this is done the number of molecules detected is greatly increased. Simulations were performed, in which there were no non-adiabatic transitions. Applying bias voltages of around 1 kV brings the experimental time-of-flight profiles into good agreement with the simulations, indicating the the non-adibatic loss-channel had indeed been inhibited.

The decelerator was operated at a maximum voltage of ± 18 kV. The high voltage switches are rated for a maximum potential difference of 20 kV. This limits the applied voltages to 20 kV (or slightly more with a bias voltage applied). However, it was very difficult to operate the decelerator above 18 kV because this led to significant radio-frequency radiation emitted by the switches, cables and feedthroughs, as well as considerable ground-noise, and these interfered with other crucial components of the experiment, most notably the frequency of the dye laser.

The decelerator was designed such that another, identical 100-stage decelerator can be attached to it without breaking the periodicity of the field stages. The resulting 200-stage decelerator will be capable of decelerating CaF molecules to rest. Simulations have been performed which show that the 200-stage decelerator can decelerate CaF molecules in the $|\mathcal{N}, M_N\rangle$ state from 340 ms^{-1} to 53 ms^{-1} with a phase angle of 65.7° . The result of these simulations are shown in figure 8.1. Of all the molecules exiting the guide the fraction decelerated to low velocity is 0.3%. The ratio of the signal due to the slow molecules to the signal obtained with the decelerator turned off is estimated to be approximately 25%. It should be noted that these simulations were designed to match the experimental data presented in this thesis, except with twice as many deceleration stages. The synchronous molecule in these simulations was chosen from the low-velocity wing of the molecular speed distribution. This reduces the number of phase-stable molecules. This could have been easily increased by selecting the synchronous molecule to come from the centre of the speed distribution. However, this would have increased the initial speed, and thus the final speed too. A better approach is to cool the initial molecular source, which will slow the initial beam, as well as reduce the width of the distribution. This can be used to increase the number of phase-stable molecules. This can be achieved by cooling the valve, which is a promising subject for future work. Note also that the final speed of 53 ms^{-1} was chosen to make sure that the molecules do exit the guide. A very small increase in phase angle would bring them to rest.

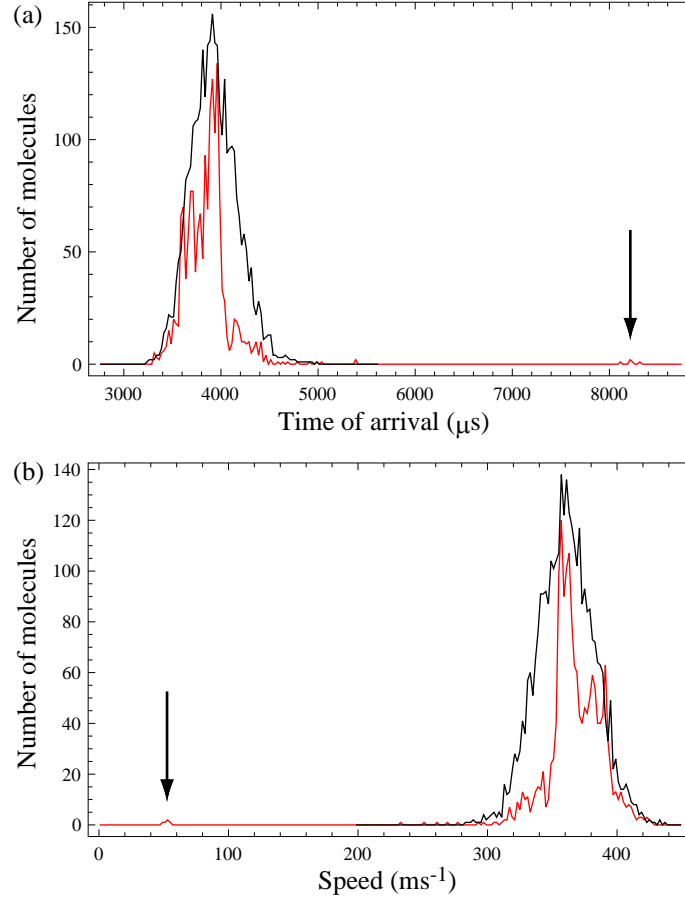


Figure 8.1: (a) Simulated time-of-flight profile for molecules detected 88 mm downstream of the 200-stage decelerator, operated at ± 20 kV. The red line shows the profile with the decelerator switching with a synchronous phase angle of 65.7° . A small decelerated peak can be seen (indicated by an arrow) at $8225 \mu\text{s}$. The black line shows the reference profile generated with the decelerator operated in DC guiding mode, centred on $3916 \mu\text{s}$. (b) The corresponding simulated velocity profile, with the same colour scheme as in figure (a). The red line shows that the decelerated molecules (indicated by an arrow) have been decelerated to 53 ms^{-1} .

A 21-stage alternating gradient (AG) decelerator was constructed and used to decelerate ground state ($|\mathcal{N} = 0, M_N = 0\rangle$) CaF molecules from 433 ms^{-1} to 403.5 ms^{-1} . This is a removal of 13% of the molecules' initial kinetic energy. The decelerated molecules were found to suffer from loss in each deceleration stage. This has been mostly explained by a net defocussing force experienced by the molecules near the end of each stage, where the electric field starts to change along the beam-line. This is exactly the part of the field required for deceleration, but unfortunately is responsible for reducing the molecular flux. A region of the electric field further away from the end of a stage was identified as giving the required amount of Stark deceleration, while also avoiding the defocussing force. Data were taken with the decelerator operated in this region. However, it was found that, with the decelerator operated with this high voltage switching sequence, the phase-stable molecules do not oscillate about the synchronous molecule. Rather they are trapped in an effective potential well several millimetres behind the synchronous molecule, in exactly the same lossy region that was supposed to be avoided! Nevertheless, the timing sequence in this case involved the decelerator being charged for less time than in the previous data, and the measured data suffered from less loss than before. However, the amount of deceleration was not as great as before, decelerating the molecules from 427.6 ms^{-1} to 408.9 ms^{-1} .

Although the simulations account for this defocussing, the data still show decelerated signals smaller than predicted, by a factor of around 2. This discrepancy is almost certainly due to electrode misalignments on a scale smaller than $\pm 0.1 \text{ mm}$.

Figure 8.2 shows the one-dimensional acceptance of an AG guide in units of κd^2 , where d is a measure of the physical aperture of the guide. The acceptance is shown as a function of κL and κS , where L is the lens length, S is the length of drift space between lenses, and κ is a scaled transverse force constant. For a range of κL and κS the guide can support stable trajectories. Outside this range there are no stable trajectories. The line of stability dividing these two spaces is shown as a black line in figure 8.2. A green point locates the position in κL - κS space of the AG decelerator operated at $\pm 20 \text{ kV}$ for molecules travelling at 430 ms^{-1} , $\{0.78, 0.56\}$. This is well within the stable region. It can be seen from the definition of κ (section 6.4) that $\kappa \propto 1/v_z$. Thus, as the molecules are slowed in the AG decelerator, κ increases. Given that L and S are constant, the position in κL - κS moves along a line (green line in figure 8.2) towards the stability boundary. The speed at which the position in κL - κS space lies on the stability boundary dictates the lowest speed that can possibly be reached by this decelerator. Molecules travelling slower than this cannot be guided by the decelerator and will not be transmitted. It has been found that, for this AG decelerator operated at $\pm 20 \text{ kV}$ this minimum speed is 276 ms^{-1} (shown by the right-hand green point in figure 8.2). For reference the position in κL - κS space of the decelerator with molecules travelling at 340 ms^{-1} is shown by the red point. It would be

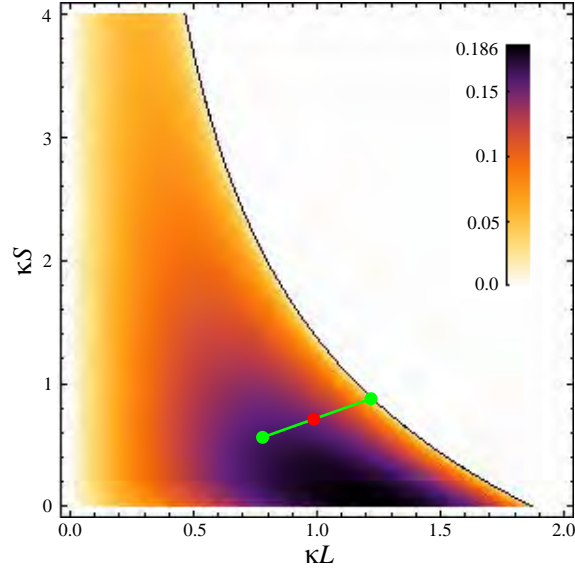


Figure 8.2: The 1D acceptance of an AG guide in units of κd^2 . The green points show the change in acceptance of the AG decelerator operated at ± 20 kV as the beam speed is reduced from 430 ms^{-1} (left-hand green point) to 276 ms^{-1} (right-hand green point). The red point shows the 1D acceptance of the AG decelerator operated at ± 20 kV with a beam speed of 340 ms^{-1} .

interesting to use the AG decelerator with a Xe-carried beam, and to decelerate molecules from 340 ms^{-1} , as in the experiment with the 100-stage decelerator. If the amount of deceleration applied to the molecules at 430 ms^{-1} had been applied to molecules at 340 ms^{-1} , then these latter molecules would have been decelerated to 302 ms^{-1} , which is still within the stability boundary. Experiments using the AG decelerator with Xe-carried beams were attempted, but the signals were too small to draw any firm conclusions.

A natural question to address in this conclusion is this: which decelerator is better? The 100-stage decelerator has removed more energy from the molecules than the AG decelerator. It has produced much slower molecules, without the complications of transverse stability. The 100-stage decelerator can be made longer and used to bring CaF molecules to rest. The AG decelerator is limited by the necessity for it to ensure stable AG guiding of the strong-field seeking molecules at the same time as decelerating them. In a comparison between the two decelerators described in this thesis the 100-stage decelerator is the more useful device for producing slow-moving molecules. However, deceleration of heavier molecules in weak-field seeking states, such as the biomolecules considered in [92, 93], would require far longer decelerators, and would need molecules to be prepared in even higher-lying rotationally-excited states. For such heavy molecules, AG deceleration may be the only feasible option.

It is useful to consider possible improvements to the design of the AG decelerator. The

design of future AG decelerators has been discussed by Tarbutt *et al.* in [44]. Firstly, the problem of the defocussing kick was addressed by proposing electrodes with a different shape. Instead of a hemispherical end, the suggested design has a semi-ellipsoidal end, with the electrode tapering off more gently and over a greater length. It is shown that this design can reduce the peak in $k_x + k_y$ at the end of a decelerator and thus reduce the scale of the defocussing force. As well as suggesting how the transmission of an AG decelerator can be improved, Tarbutt *et al.* investigate a method of increasing the amount of deceleration that can be achieved. The limiting parameter is the length of the deceleration stages, L . As the molecules slow down κ increases and moves the decelerator closer to the line of stability. In the proposed design the decelerator is made of lenses of varying length [44]. Each deceleration stage is the same length, but arranged in a sequence of $(FO)^n(DO)^n$, with each lens made of n stages. By reducing n along the decelerator it is possible to account for the increase in κ , and to keep the molecules stable for longer, thus increasing the amount of deceleration possible. Simulations performed for a 139-stage AG decelerator showed that this decelerator can slow YbF molecules from 340 ms^{-1} to 66 ms^{-1} [44]. However, the technical complexities of decelerating and guiding very slow-moving strong-field seeking molecules might require the final stages of deceleration to be accomplished with the molecules in a weak-field seeking state.

CaF is a useful molecule as a control for the measurement of the electron EDM, but it is not the molecule used for the actual measurement. This is YbF, which is much heavier. Calculations have shown that optimal deceleration of YbF in a weak-field seeking state requires a 444-stage decelerator acting on molecules in the $|\mathcal{N} = 5, M_N = 0\rangle$ state [44]. This is capable of decelerating YbF molecules from 340 ms^{-1} to rest. Measuring 5.328 m in length, this is a long decelerator, and it might seem tempting to use the AG decelerator described above. However, this decelerator is still very long, measuring 4.818 m in length. The relatively small decrease in length is unlikely to overcome the technical difficulties associated with using an AG decelerator at low speeds, particularly if a weak-field decelerator has to be used at the low-velocity end to achieve the final stages of deceleration. Detailed numerical simulations of the deceleration of YbF in these two proposed decelerators finds the six-dimensional acceptance of the weak-field decelerator to be $352 \text{ mm}^3 (\text{ms}^{-1})^3$, and of the AG decelerator to be $254 \text{ mm}^3 (\text{ms}^{-1})^3$ [44].

To conclude, an AG decelerator can be designed to give better transmission and deceleration than the AG decelerator reported in this thesis, but this decelerator would become very complicated for decelerating the molecules to rest. Simulations of this improved AG decelerator, and of a 444-stage weak-field decelerator have found that there is little if any length advantage to an AG decelerator, and a disadvantage in terms of phase space acceptance. It seems therefore that decelerating molecules in weak-field seeking states is a much easier and more practical method of producing these slow-moving molecules.

8.4 Outlook

An important motivation for the experiments reported in this thesis was the production of a slow-moving beam of molecules for the measurement of the electron electric dipole moment (EDM). The sensitivity of this measurement is discussed in section 1.3, and is proportional to $\frac{1}{\tau\sqrt{N}}$, where N is the number of participating molecules, and τ is the time that they spend in the experiment. Therefore it is desirable to produce a high density beam of many slow-moving molecules that spend a long time in the experiment.

CaF molecules in the $|\mathcal{N} = 4, M_N = 0\rangle$ state have been decelerated from 342 ms^{-1} to 247 ms^{-1} , and further deceleration is possible by doubling the length of the decelerator. These slow molecules ought to spend longer interacting with the fields in the electron EDM experiment, and thus increase the sensitivity of the measurement. However, it can be seen from the measured time-of-flight profiles, and the simulated profiles above, that the number of molecules decelerated is a small fraction of the initial molecular beam. So τ has been increased, but N has been vastly reduced.

It has been proposed to measure the electron EDM with trapped molecules [44]. An AC trap for strong-field seeking ground state molecules and a ‘chain-link’ DC trap [94] are considered. The switching electric fields associated with the AC trap make it undesirable for high precision measurements. The acceptance of such a trap for YbF molecules is calculated to be about $50 \text{ mm}^3 (\text{ms}^{-1})^3$. The chain-link trap has no such problems with switching fields, and is calculated to have a much greater acceptance of $10^4 \text{ mm}^3 (\text{ms}^{-1})^3$. This trap is thus investigated as the basis for a new experimental set-up to measure the electron EDM. However, it is found in [44] that the motion of the molecules in the spatially-inhomogeneous electric field in the trap causes rapid spin-decoherence, which limits the value of τ to a few milliseconds. This time is of the order of the time the supersonic beam of molecules spends inside the current experiment, and so does not improve the sensitivity of the experiment. Tarbutt *et al.* conclude that an alternative experimental set-up which allows for a large coherence time would be a molecular fountain. Such an experiment would make use of Stark decelerated molecules, as suggested by Bethlem *et al.* in their design of a molecular fountain for precision measurements [95]. The molecules exiting a Stark decelerator leave as a divergent beam, which limits their use in a long experiment. To solve this problem Bethlem *et al.* propose using a sequence of quadrupole fields to collimate the beam. By using quadrupole fields to increase the spread of transverse positions in the molecular distribution, the velocity spread is reduced in order to maintain a constant phase-space density. This method creates a wide, but collimated molecular beam. In the experiment proposed in [95] a Stark decelerator slows NH_3 molecules from 300 ms^{-1} to 4 ms^{-1} . This beam is then collimated, with a final width of about 10 mm. After the quadrupole lenses the molecular fountain travels up approximately 40 cm before

the molecules turn over and fall.

A slow-moving molecular fountain can be used to provide a long coherence time for a precision measurement. There is now an experiment beginning at Imperial College to laser cool CaF molecules formed either by a supersonic or a buffer-gas source. One goal of this project will be to provide slow molecules for a molecular fountain. This will be performed either by direct laser cooling, or by a combination of Stark deceleration and laser cooling. In this latter experimental set-up, transverse laser cooling will be used as a ‘beam-brightener’ to increase the phase-space density in the initial beam. Longitudinal cooling can then be used to bunch the molecules around a particular velocity class, v_L . This high phase-space density beam can then be loaded into a Stark decelerator with the synchronous speed $v_{sync} = v_L$. In this way the Stark decelerator is used to decelerate a large number of molecules which can then be collimated and form the fountain.

The experiments described in this thesis have investigated methods of controlling cold, heavy, polar molecules. In addition, a spectroscopic study of CaF has confirmed that it is a good candidate for laser cooling. It is fitting that these methods can now be combined to provide a new, more sensitive measurement of the electron electric dipole moment.

Appendix A

Branching ratios

Matrix A.1 shows the branching ratios between the $N = 0$ and $N = 2$ levels of ground-state CaF and the $A^2\Pi_{(\frac{1}{2})}$ excited state, corresponding to the transitions shown in figure 4.1. Each row corresponds to a ground electronic state, labelled by (N, F, M_F) , and each column corresponds to an excited state, labelled by (F', M'_F) . The two ground state $N = 2$ levels with $F = 2$ are distinguished by a '+' sign after the F value, for the higher energy level, and a '-' sign for the lower energy level. The numerical values were calculated in [62].

	(0, 0)	(1, -1)	(1, 0)	(1, 1)
(0, 0, 0)	0	2/9	2/9	2/9
(0, 1, -1)	2/9	2/9	2/9	0
(0, 1, 0)	2/9	2/9	0	2/9
(0, 1, 1)	2/9	0	2/9	2/9
(2, 2-, -2)	0	1/8	0	0
(2, 2-, -1)	0	1/16	1/16	0
(2, 2-, 0)	0	1/48	1/12	1/48
(2, 2-, 1)	0	0	1/16	1/16
(2, 2-, 2)	0	0	0	1/8
(2, 1, -1)	1/9	1/36	1/36	0
(2, 1, 0)	1/9	1/36	1/36	0
(2, 1, 1)	1/9	0	1/36	1/36
(2, 2+, -2)	0	1/24	0	0
(2, 2+, -1)	0	1/48	1/48	0
(2, 2+, 0)	0	1/144	1/36	1/144
(2, 2+, 1)	0	0	1/48	1/48
(2, 2+, 2)	0	0	0	1/24

(A.1)

Appendix B

The Optical Bloch Equations and Rate Equations

The analysis in this section is based, in part, on the derivation of the optical Bloch equations given in [63].

Consider a two-level system, with states $|1\rangle$ and $|2\rangle$, separated by energy $\hbar\omega_0$. Applying near-resonant laser light of angular frequency ω_L to this system mixes the two states, such that the new state of the system is $|\alpha\rangle = C_1(t)|1\rangle + C_2(t)|2\rangle$. Let the radiation be plane-polarized along the z -direction, with electric field at a given position, $\vec{E}(t) = \vec{E}_0 \cos(\omega_L t)$. The Hamiltonian associated with the electric dipole interaction is $\hat{H}_{dip} = \vec{d} \cdot \vec{z} E_0 \cos(\omega_L t)$, where \vec{d} is the electric dipole operator. The matrix element $\langle 1|\hat{H}_{dip}|2\rangle = E_0 z_{12} \cos(\omega_L t)$, where $z_{12} = \langle 1|d_z|2\rangle$. The Rabi frequency is defined by $\Omega = E_0 z_{12}/\hbar$. The states $|1\rangle$ and $|2\rangle$ are eigenstates of the field-free Hamiltonian, \hat{H}_0 . The time-dependent Schrödinger equation (TDSE) in the presence of the applied light has total Hamiltonian $\hat{H}_{tot} = \hat{H}_0 + \hat{H}_{dip}$. Taking the field-free parts from both sides of the TDSE leave the equation for the time-variation of the amplitudes $C_1(t)$ and $C_2(t)$:

$$\hat{H}_{dip} [C_1(t)|1\rangle + C_2(t)|2\rangle] = i\hbar \left[|1\rangle \frac{dC_1(t)}{dt} + |2\rangle \frac{dC_2(t)}{dt} \right]. \quad (\text{B.1})$$

Dividing by \hbar and premultiplying both sides of equation B.1 by $\langle 1|$ and $\langle 2|$ respectively gives:

$$\langle 1|\hat{H}_{dip}|1\rangle \frac{C_1(t)}{\hbar} + \langle 1|\hat{H}_{dip}|2\rangle \frac{C_2(t)}{\hbar} e^{-i\omega_0 t} = \Omega \cos(\omega_L t) e^{-i\omega_0 t} C_2(t) = i \frac{dC_1(t)}{dt}, \quad (\text{B.2})$$

$$\langle 2|\hat{H}_{dip}|1\rangle \frac{C_1(t)}{\hbar} e^{i\omega_0 t} + \langle 2|\hat{H}_{dip}|2\rangle \frac{C_2(t)}{\hbar} = \Omega \cos(\omega_L t) e^{i\omega_0 t} C_1(t) = i \frac{dC_2(t)}{dt}. \quad (\text{B.3})$$

The 2×2 density matrix associated with a two-level system is defined by the elements ρ_{ij} , where $\rho_{11}(t) = |C_1(t)|^2$, $\rho_{22}(t) = |C_2(t)|^2$, $\rho_{12} = \rho_{21}^* = C_1(t)C_2^*(t)$. ρ_{11} and ρ_{22} are known as the ‘populations’ as they are a normalized measure of the populations of the states, N_1/N and N_2/N respectively, where N is the number of systems interacting with

the light field, N_1 is the number of systems in state $|1\rangle$ at a given time, and N_2 is the number of systems in state $|2\rangle$ at that time. Equations B.2 and B.3 can be written in terms of the density matrix elements as

$$\frac{d\rho_{22}(t)}{dt} = -\frac{d\rho_{11}(t)}{dt} = -i\Omega \cos(\omega_L t) (e^{i\omega_0 t} \rho_{12}(t) - e^{-i\omega_0 t} \rho_{21}(t)), \quad (\text{B.4})$$

$$\frac{\rho_{12}(t)}{dt} = \frac{\rho_{21}^*(t)}{dt} = i\Omega \cos(\omega_L t) e^{-i\omega_0 t} (\rho_{11}(t) - \rho_{22}(t)). \quad (\text{B.5})$$

Writing the cosine terms in equations B.4 and B.5 in terms of exponential terms renders terms in these equations with either $(\omega_0 + \omega_L)$ or $(\omega_0 - \omega_L)$ in the exponent. The exponential terms with $(\omega_0 + \omega_L)$ in the exponent are assumed to be very rapidly varying whose effects ‘wash out’ compared with the effects of the exponential terms with $(\omega_0 - \omega_L)$ in the exponent. Henceforth these former terms are neglected, an approximation known as the ‘rotating wave’ approximation. For the sake of conciseness the remaining exponential terms will be hidden by defining $\tilde{\rho}_{12}(t) = e^{i(\omega_0 - \omega_L)t} \rho_{12}(t)$ and $\tilde{\rho}_{21}(t) = e^{i(\omega_0 - \omega_L)t} \rho_{21}(t)$. So far the lifetime of state $|2\rangle$ has been ignored. The effects of this lifetime can be included in the equations for the populations and coherences by including its inverse, the excited state decay rate, Γ , in equations B.4 and B.5 [63]. Equations B.4 and B.5 thus become

$$\frac{d\rho_{22}(t)}{dt} = -\frac{d\rho_{11}(t)}{dt} = -\frac{1}{2}i\Omega (\tilde{\rho}_{12}(t) - \tilde{\rho}_{21}(t)) - \Gamma \rho_{22}(t), \quad (\text{B.6})$$

$$\frac{d\tilde{\rho}_{12}(t)}{dt} = \frac{d\tilde{\rho}_{21}^*(t)}{dt} = \frac{1}{2}i\Omega (\rho_{11}(t) - \rho_{22}(t)) + (i(\omega_0 - \omega_L) - \Gamma/2). \quad (\text{B.7})$$

These are the optical Bloch equations. The state $|2\rangle$ decay rate can be generalized to decay to many levels, not just state $|1\rangle$. The coherences reach steady state on the time-scale of the state $|2\rangle$ lifetime. The molecules’ transit time through the laser probe beam in the detection of CaF is much greater than this time-scale and so in the analysis of laser-induced fluorescence it can be assumed that $\frac{d\tilde{\rho}_{12}}{dt} = \frac{d\tilde{\rho}_{21}}{dt} = 0$. Equations B.6 and B.7 thus give:

$$\tilde{\rho}_{12} = \frac{\frac{1}{2}i\Omega (\rho_{11} - \rho_{22})}{-i\delta - \Gamma/2}, \quad (\text{B.8})$$

$$\tilde{\rho}_{21} = \frac{-\frac{1}{2}i\Omega (\rho_{11} - \rho_{22})}{i\delta - \Gamma/2}, \quad (\text{B.9})$$

where $\delta = \omega_L - \omega_0$ is the laser detuning. Combining equations B.8 and B.9 into equation B.6 gives the rate equation of the $|1\rangle$ and $|2\rangle$ state populations:

$$\frac{d\rho_{22}}{dt} = \frac{\Gamma\Omega^2}{\Gamma^2 + 4\delta^2} (\rho_{11} - \rho_{22}) - \Gamma\rho_{22} \quad (\text{B.10})$$

$$\Rightarrow \frac{dN_2}{dt} = R(\delta) (N_1 - N_2) - \Gamma N_2, \quad (\text{B.11})$$

where $R(\delta) = \frac{\Gamma\Omega^2}{\Gamma^2 + 4\delta^2}$ is the laser excitation rate.

Appendix C

Stark interaction in a rotating frame

The analysis in this appendix is based on material from [55].

Consider a molecule initially in state $|\mathcal{N}, M_N\rangle$ in field state 1 of the 100-stage decelerator (see figure 5.4). During the switch from state 1 to state 2 the electric field changes magnitude and rotates about the y -axis (the beam-line axis) with a time-varying angular rotation rate $\omega(t)$. During this switch the molecule is in the time-varying state $|\alpha\rangle$, the evolution of which is given by the time-dependent Schrödinger equation:

$$\hat{H}(t)|\alpha\rangle = i\hbar \frac{\partial}{\partial t} |\alpha\rangle. \quad (\text{C.1})$$

Transformation of the Schrödinger equation and molecular states from the laboratory-fixed frame to the rotating frame that follows the electric field is performed by applying the rotation operator, $\hat{D} = \exp\left(-\hat{N}_y \beta(t)/\hbar\right)$, where \hat{N}_y is the angular momentum operator associated with the rotation about y , and the angular rotation rate is given by $\omega(t) = \frac{d\beta(t)}{dt}$. In this rotating frame the state is given by $|\alpha'\rangle = \hat{D}|\alpha\rangle$, governed by the Schrödinger equation:

$$\hat{H}'(t)|\alpha'\rangle = i\hbar \hat{D} \frac{\partial}{\partial t} \left(\hat{D}^{-1} |\alpha'\rangle \right), \quad (\text{C.2})$$

where $\hat{H}'(t) = \hat{D} \hat{H}(t) \hat{D}^{-1}$. Noting that the first derivative of \hat{D}^{-1} is $\frac{\partial \hat{D}^{-1}}{\partial t} = \frac{i\hat{N}_y}{\hbar} \frac{\partial \beta(t)}{\partial t} \hat{D}^{-1}$ gives:

$$\begin{aligned} \hat{H}'(t)|\alpha'\rangle &= i\hbar \hat{D} \left[\hat{D}^{-1} \frac{\partial}{\partial t} |\alpha'\rangle + \frac{i}{\hbar} \hat{N}_y \frac{\partial \beta(t)}{\partial t} \hat{D}^{-1} |\alpha'\rangle \right] \\ &= i\hbar \frac{\partial}{\partial t} |\alpha'\rangle - \hat{N}_y \frac{\partial \beta(t)}{\partial t} |\alpha'\rangle \\ \Rightarrow \quad &\left(\hat{H}'(t) + \hat{N}_y \frac{\partial \beta(t)}{\partial t} \right) |\alpha'\rangle = i\hbar \frac{\partial}{\partial t} |\alpha'\rangle. \end{aligned} \quad (\text{C.3})$$

In the following analysis the terms in the Hamiltonian on the left-hand side of equation C.3 are written $\hat{H}_{tot}(t) = \hat{H}'(t) + \omega(t)\hat{N}_y$. $\hat{H}'(t)$ satisfies the eigenvalue equation, evaluated at time t , $\hat{H}'(t)|\mathcal{N}, M_N\rangle = W_{\mathcal{N}, M_N}(t)|\mathcal{N}, M_N\rangle$. Applying the identity operator, $\sum_{\mathcal{N}, M_N} |\mathcal{N}, M_N\rangle\langle\mathcal{N}, M_N|$ to both sides of equation C.3 and premultiplying by $\langle\mathcal{N}', M'_N|$ gives:

$$\begin{aligned} \sum_{\mathcal{N}, M_N} \langle\mathcal{N}', M'_N| \hat{H}_{tot}(t) |\mathcal{N}, M_N\rangle \langle\mathcal{N}, M_N| \alpha'\rangle \\ = i\hbar \sum_{\mathcal{N}, M_N} \langle\mathcal{N}', M'_N| \frac{\partial}{\partial t} \left(|\mathcal{N}, M_N\rangle \langle\mathcal{N}, M_N| \alpha'\rangle \right) \\ = i\hbar \sum_{\mathcal{N}, M_N} \left[\left(\langle\mathcal{N}', M'_N| \frac{\partial}{\partial t} |\mathcal{N}, M_N\rangle \right) \langle\mathcal{N}, M_N| \alpha'\rangle \right. \\ \left. + \langle\mathcal{N}', M'_N| \mathcal{N}, M_N\rangle \left(\frac{\partial}{\partial t} \langle\mathcal{N}, M_N| \alpha'\rangle \right) \right] \\ \Rightarrow \sum_{\mathcal{N}, M_N} \langle\mathcal{N}', M'_N| \left(\hat{H}_{tot}(t) - i\hbar \frac{\partial}{\partial t} \right) |\mathcal{N}, M_N\rangle \langle\mathcal{N}, M_N| \alpha'\rangle = i\hbar \frac{\partial}{\partial t} \langle\mathcal{N}', M'_N| \alpha'\rangle \quad (C.4) \end{aligned}$$

Now $\hat{H}'(t) = \sum_{\mathcal{N}, M_N} \hat{H}'(t) |\mathcal{N}, M_N\rangle \langle\mathcal{N}, M_N| = \sum_{\mathcal{N}, M_N} W_{\mathcal{N}, M_N} |\mathcal{N}, M_N\rangle \langle\mathcal{N}, M_N|$, and so:

$$\begin{aligned} \frac{\partial}{\partial t} \hat{H}'(t) &= \sum_{\mathcal{N}, M_N} \left[\left(\frac{\partial}{\partial t} W_{\mathcal{N}, M_N}(t) \right) |\mathcal{N}, M_N\rangle \langle\mathcal{N}, M_N| \right. \\ &\quad + W_{\mathcal{N}, M_N}(t) \left(\frac{\partial}{\partial t} |\mathcal{N}, M_N\rangle \right) \langle\mathcal{N}, M_N| \\ &\quad \left. + W_{\mathcal{N}, M_N}(t) |\mathcal{N}, M_N\rangle \left(\frac{\partial}{\partial t} \langle\mathcal{N}, M_N| \right) \right]. \\ \Rightarrow \langle\mathcal{N}', M'_N| \frac{\partial}{\partial t} \hat{H}'(t) |\mathcal{N}, M_N\rangle &= W_{\mathcal{N}, M_N}(t) \langle\mathcal{N}', M'_N| \frac{\partial}{\partial t} |\mathcal{N}, M_N\rangle \\ &\quad + W_{\mathcal{N}', M'_N}(t) \left(\frac{\partial}{\partial t} \langle\mathcal{N}', M'_N| \right) |\mathcal{N}, M_N\rangle. \quad (C.5) \end{aligned}$$

The last term in equation C.5 can be rewritten using the following equation¹:

$$\left(\frac{\partial}{\partial t} \langle\mathcal{N}', M'_N| \right) |\mathcal{N}, M_N\rangle = -\langle\mathcal{N}', M'_N| \frac{\partial}{\partial t} |\mathcal{N}, M_N\rangle. \quad (C.6)$$

Equation C.5 thus simplifies to:

$$\langle\mathcal{N}', M'_N| \frac{\partial}{\partial t} \hat{H}'(t) |\mathcal{N}, M_N\rangle = \left(W_{\mathcal{N}, M_N}(t) - W_{\mathcal{N}', M'_N}(t) \right) \langle\mathcal{N}', M'_N| \frac{\partial}{\partial t} |\mathcal{N}, M_N\rangle. \quad (C.7)$$

Equation C.7 gives an expression for the second term on the left-hand side of equation C.4, which now becomes:

$$\begin{aligned} \sum_{\mathcal{N}, M_N} \langle\mathcal{N}', M'_N| \left(\hat{H}_{tot}(t) \right. \\ \left. - \frac{i\hbar}{W_{\mathcal{N}, M_N} - W_{\mathcal{N}', M'_N}} \frac{\partial}{\partial t} \hat{H}'(t) \right) |\mathcal{N}, M_N\rangle \langle\mathcal{N}, M_N| \alpha'\rangle = i\hbar \frac{\partial}{\partial t} \langle\mathcal{N}', M'_N| \alpha'\rangle. \quad (C.8) \end{aligned}$$

¹ $\frac{\partial}{\partial t} \langle\mathcal{N}', M'_N| \mathcal{N}, M_N\rangle = \left(\frac{\partial}{\partial t} \langle\mathcal{N}', M'_N| \right) |\mathcal{N}, M_N\rangle + \langle\mathcal{N}', M'_N| \frac{\partial}{\partial t} |\mathcal{N}, M_N\rangle = 0$

Finally, $\hat{H}_{tot}(t)$ can be written in terms of its constituent parts, and the $\hat{H}'(t)$ term can be taken out of the matrix element as it has eigenvalues $|\mathcal{N}, M_N\rangle$. Defining $W_{\mathcal{N}, M_N} - W_{\mathcal{N}', M'_N} = \hbar\omega_{sep}$:

$$\begin{aligned} & W_{\mathcal{N}', M'_N} \langle \mathcal{N}', M'_N | \alpha' \rangle \\ & + \sum_{\mathcal{N}, M_N} \langle \mathcal{N}', M'_N | \left(\omega(t) \hat{N}_y - \frac{i}{\omega_{sep}} \frac{\partial}{\partial t} \hat{H}'(t) \right) | \mathcal{N}, M_N \rangle \langle \mathcal{N}, M_N | \alpha' \rangle = i\hbar \frac{\partial}{\partial t} \langle \mathcal{N}', M'_N | \alpha' \rangle. \end{aligned} \quad (\text{C.9})$$

Equation C.9 describes the evolution of the state $|\alpha'\rangle$ as a result of the electric field rotating (first term in the matrix element) and changing in magnitude (second term in the matrix element).

Bibliography

- [1] C.S. Wu, E. Ambler, R.W. Hayward, D.D. Hoppes and R.P. Hudson, Phys. Rev. **105**, 1413-1415 (1957)
- [2] V.L. Fitch, Rev. Mod. Phys. **53**, 3 (1981)
- [3] E.A. Hinds, Physica Scripta., **T70**, 34-41 (1997)
- [4] C.A. Baker, D.D. Doyle, P. Geltenbort, K. Green, M.G.D. van der Grinten, P.G. Harris, P. Iaydjiev, S.N. Ivanov, D.J.R. May, J.M. Pendlebury, J.D. Richardson, D. Shiers and K.F. Smith, Phys. Rev. Lett. **97**, 131801 (2006)
- [5] L.I. Schiff, Phys. Rev. **132**, 2194-2200 (1963)
- [6] E.D. Commins, J.D. Jackson and D. DeMille, Am. J. Phys. **75**, 6 (2007)
- [7] E.D. Commins, S.B. Ross, D. DeMille and B. Regan, Phys. Rev. A **50**, 2960 (1994)
- [8] Z.W. Liu and H.P. Kelly, Phys. Rev. A **45**, 7 (1992)
- [9] B.E. Sauer, H.T. Ashworth, J.J. Hudson, M.R. Tarbutt and E.A. Hinds, in Atomic Physics 20, edited by C. Roos, H. Häffner and R. Blatt, AIP Conf. Proc. No. 869, (AIP, Melville, NY, 2006), p. 44
- [10] J.J. Hudson, *Measuring the electric dipole moment of the electron with YbF molecules*, DPhil thesis, Univeristy of Sussex (2001)
- [11] J.J. Hudson, B.E. Sauer, M.R. Tarbutt and E.A. Hinds, Phys. Rev. Lett. **89**, 023003 (2002)
- [12] H.T. Ashworth, *Towards an improved measurement of the electron electric dipole moment*, PhD thesis, Univeristy of London (2008)
- [13] M.G. Kozlov and D. DeMille, Phys. Rev. Lett. **89**, 133001 (2002)
- [14] N.E. Shafer-Ray, Phys. Rev. A **73**, 034102 (2006)

- [15] P. Sivakumar, C.P. McRaven, D. Combs, N.E. Shafer-Ray and V. Ezhov, *Phys. Rev. A* **77**, 062508 (2008)
- [16] A.C. Vutha, W.C. Campbell, Y.V. Gurevich, N.R. Hutzler, M. Parsons, D. Patterson, E. Petrik, B. Spaun, J.M. Doyle, G. Gabrielse and D. DeMille, *J. Phys. B* **43**, 074007 (2010)
- [17] J.-P. Uzan, *Rev. Mod. Phys.* **75**, 2 (2003)
- [18] J.K. Webb, M.T. Murphy, V.V. Flambaum, V.A. Dzuba, J.D. Barrow, C.W. Churchill, J.X. Prochaska and A.M. Wolfe, *Phys. Rev. Lett.* **87**, 091301 (2001)
- [19] M.T. Murphy, J.K. Webb and V.V. Flambaum, *Mon. Not. R. Astron. Soc.* **345**, 609-638 (2003)
- [20] N. Kanekar, C.L. Carilli, G.I. Langston, G. Rocha, F. Combes, R. Subrahmanyam, J.D. Stocke, K.M. Menten, F.H. Briggs and T. Wiklind, *Phys. Rev. Lett.* **95**, 261301 (2005)
- [21] S. Schiller and V. Korobov, *Phys. Rev. A* **71**, 032505 (2005)
- [22] A. Shelkovernikov, R.J. Butcher, C. Chardonnet and A. Amy-Klein, *Phys. Rev. Lett* **100**, 150801 (2008)
- [23] H.L. Bethlem and W. Ubachs, *Faraday Discuss.* **142**, 25-36 (2009)
- [24] M. Quack, *Angew. Chem. Int. Ed.* **41**, 4618-4630 (2002)
- [25] Ch. Daussy, T. Marrel, A. Amy-Klein, C.T. Nguyen, Ch. J. Bordé and Ch. Chardonnet, *Phys. Rev. Lett* **83**, 8 (1999)
- [26] J.K. Laerdahl, P. Schwerdtfeger and H.M. Quiney, *Phys. Rev. Lett.* **84**, 17 (2000)
- [27] P. Bargueño, I. Gonzalo and R.P. de Tudela, *Phys. Rev. A* **80**, 012110 (2009)
- [28] D.H. Levy, *Science* **214**, 4518 (1981)
- [29] L.D. Carr, D. DeMille, R.V. Krems and J. Ye, *New J. Phys.* **11**, 055049 (2009)
- [30] B. Friedrich and J.M. Doyle, *Chem. Phys. Chem.* **10**, 604-623 (2009)
- [31] K.M. Jones, E. Tiesinga, P.D. Lett and P.S. Julienne, *Rev. Mod. Phys.* **78**, 2 (2006)
- [32] J. Deiglmayr, A. Grochola, M. Repp, K. Mörtlbauer, C. Glück, J. Lange, O. Dulieu, R. Wester and M. Weidemüller, *Phys. Rev. Lett.* **101**, 133004 (2008)
- [33] E.A. Donley, N.R. Claussen, S.T. Thompson and C.E. Wieman, *Nature* **417**, 529-533 (2002)

- [34] K.E. Strecker, G.B. Partridge and R.G. Hulet, Phys. Rev. Lett. **91**, 8 (2003)
- [35] K. Xu, T. Mukaiyama, J.R. Abo-Shaeer, J.K. Chin, D.E. Miller and W. Ketterle, Phys. Rev. Lett. **91**, 21 (2003)
- [36] J.G. Danzl, E. Haller, M. Gustavsson, M.J. Mark, R. Hart, N. Bouloufa, O. Dulieu, H. Ritsch and H.-C. Nägerl, Science **231**, 1062 (2008)
- [37] H.L. Bethlem, G. Berden and G. Meijer, Phys. Rev. Lett. **83**, 8 (1999)
- [38] M.R. Tarbutt, B.E. Sauer, J.J. Hudson, E.A. Hinds, V.A. Ryzhov, V.L. Ryabov and V.F. Ezhov, J. Phys. B **35**, 5013 (2002)
- [39] J.M. Doyle, B. Friedrich, J. Kim and D. Patterson, Phys. Rev. A **52**, 4 (1995)
- [40] J.D. Weinstein, R. deCarvalho, T. Guillet, B. Friedrich and J.M. Doyle, Nature **395**, 148-150 (1998)
- [41] L.D. van Buuren, C. Sommer, M. Motsch, S. Pohle, M. Schenk, J. Bayerl, P.W.H. Pinkse and G. Rempe, Phys. Rev. Lett. **102**, 033001 (2009)
- [42] M-F Tu, J-J Ho, C-C Hsieh and Y-C Chen, Rev. Sci. Instrum. **80**, 113111 (2009)
- [43] S.E. Maxwell, N. Brahms, R. deCarvalho, D.R. Glenn, J.S. Helton, S.V. Nguyen, D. Patterson, J. Petricka, D. DeMille and J.M. Doyle, Phys. Rev. Lett. **95**, 173201 (2005)
- [44] M.R. Tarbutt, J.J. Hudson, B.E. Sauer and E.A. Hinds, Faraday Discuss. **142**, 37-56 (2009)
- [45] S.M. Skoff, R.J. Hendricks, C.D.J. Sinclair, M.R. Tarbutt, J.J. Hudson, D.M. Segal, B.E. Sauer and E.A. Hinds, New J. Phys. **11**, 123026 (2009).
- [46] G. Herzberg, *Molecular spectra and molecular structure. Vol. I: Spectra of diatomic molecules* (van Nostrand Reinhold, 1950)
- [47] B.H. Bransden and C.J. Joachain, *Physics of atoms and molecules* (Longman, 1983)
- [48] J. Wang, *Laser and radiofrequency spectroscopy of ytterbium fluoride ground state*, PhD thesis, Yale University (1996)
- [49] J.J. Sakurai, *Modern Quantum Mechanics*, (Addison-Wesley, 1994)
- [50] J.M. Brown and A. Carrington, *Rotational spectroscopy of diatomic molecules* (Cambridge University Press, Cambridge, 2003)
- [51] D. Auerbach, E.E.A. Bromberg and L. Wharton, J. Chem. Phys. **45**, 6 (1966)

- [52] G. Scoles (ed.), *Atomic and molecular beam methods* (Oxford University Press, Oxford, 1988)
- [53] R.V.B. Darnley, PhD thesis, University of London (2007)
- [54] L.A. Kaledin, J.C. Bloch, M.C. McCarthy, R.W. Field, *Journal of Molecular Spectroscopy* **197**, 289-296 (1999)
- [55] T.E. Wall, S.K. Tokunaga, E.A. Hinds, M.R. Tarbutt, *Phys. Rev. A* **81**, 033414 (2010)
- [56] W.J. Childs and L.S. Goodman, *Phys. Rev. A* **21**, 1216 (1980)
- [57] M.D. DiRosa, *Eur. Phys. J. D* **31**, 395 (2004)
- [58] E.S. Shuman, J.F. Barry, D.R. Glenn and D. DeMille, *Phys. Rev. Lett.* **103**, 223001 (2009)
- [59] M. Pelegrini, C.S. Vivacqua, O. Roberto-Neto, F.R. Omellasa and F.B.C. Machado, *Braz. J. Phys* **35**, 950 (2005)
- [60] P.J. Dagdigian, H.W. Cruse and R.N. Zare, *J. Chem. Phys.* **60**, 2330 (1974)
- [61] W.R. Anderson, S.W. Bunte and A.J. Kotlar, *Chem. Phys. Lett.* **110**, 2 (1984)
- [62] T.E. Wall, J.F. Kanem, B.E. Sauer, J.J. Hudson, D. Cho, M.G. Boshier, E.A. Hinds and M.R. Tarbutt, *Phys. Rev. A* **78**, 062509 (2008)
- [63] R. Loudon, *The Quantum Theory of Light* (Oxford University Press, Oxford, 2006)
- [64] A. Corney, *Atomic and laser spectroscopy* (Oxford University Press, Oxford, 1979)
- [65] H.L. Bethlem, G. Berden, F.M.H. Crompvoets, R.T. Jongma, A.J.A. van Roij and G. Meijer, *Nature* **406**, 491-494 (2000)
- [66] E.R. Hudson, J.R. Bochinski, H.J. Lewandowski, B.C. Sawyer and J. Ye, *Eur. Phys. J. D* **31**, 351-358 (2004)
- [67] S.Y.T. van de Meerakker, P.H.M. Smeets, N. Vanhaecke, R.T. Jongma and G. Meijer, *Phys. Rev. Lett.* **94**, 023004 (2005)
- [68] S.Y.T. van de Meerakker, I. Labazan, S. Hoekstra, J. Küpper and G. Meijer, *J. Phys. B* **39**, S1077-1084 (2006)
- [69] E.R. Hudson, C. Ticknor, B.C Sawyer, C.A. Taatjes, H.J. Lewandowski, J.R. Bochinski, J.L. Bohn and J. Ye, *Phys. Rev. A* **73**, 063404 (2006)

- [70] S. Jung, E. Tiemann, C. Lisdat, Phys. Rev. A **74**, 040701 (2006)
- [71] S.K. Tokunaga, J.M. Dyne, E.A. Hinds and M.R. Tarbutt, New J. Phys. **11** 055038 (2009)
- [72] H.L. Bethlem, G. Berden, A.J.A. van Roij, F.M.H. Crompvoets and G. Meijer, Phys. Rev. Lett. **84**, 25 (2000)
- [73] W.H. Wing, Prog. Quantum Electron. **8**, 181 (1984)
- [74] D.C. Lainé and R.C. Sweeting, Phys. Lett. **34A**, 3 (1971)
- [75] H.J. Loesch, Chem. Phys. **207**, 427-436 (1996)
- [76] H.J. Loesch and B. Scheel, Phys. Rev. Lett. **85**, 13 (2000)
- [77] E.D. Courant and H.S. Snyder, Ann. Phys **3**, 1-48 (1958)
- [78] G.W. Hill, Acta Mathematica **8**, 1-36 (1886)
- [79] M.R. Tarbutt and E.A. Hinds, New Journal of Physics **10**, 073011 (2008)
- [80] H.L. Bethlem, M.R. Tarbutt, J. Küpper, D. Carty, K. Wohlfart, E.A. Hinds and G. Meijer, J. Phys. B: At. Mol. Opt. Phys **39**, R263 (2006)
- [81] E.D. Courant, M.S. Livingston and H.S. Snyder, Phys. Rev. **88**, 5 (1952)
- [82] D. Kakati and D.C. Lainé, J. Phys. E **4**, 269 (1971)
- [83] A. Lübbert, G. Rotzoll and F. Günther, J. Chem. Phys. **69**, 11 (1978)
- [84] F. Filsinger, U. Erlekam, G. von Helden, J. Küpper and G. Meijer, Phys. Rev. Lett. **100**, 133003 (2008)
- [85] T.E. Wall, S. Armitage, J.J. Hudson, B.E. Sauer, J.M. Dyne, E.A. Hinds and M.R. Tarbutt, Phys. Rev. A **80**, 043407 (2009)
- [86] M.R. Tarbutt, J.J. Hudson, B.E. Sauer and E.A. Hinds, Chapter 15 of *Cold molecules: theory, experiment, applications*, edited by R.V. Krems, B. Friedrich and W.C. Stwalley (CRC Press, 2009)
- [87] R. Wolfgang, Scientific American **219**, 44 (1968)
- [88] E.E.A. Bromberg, PhD thesis, University of Chicago (1972)
- [89] J.A. Maddi, T.P. Dinneen and H. Gould, Phys. Rev. A **60**, 5 (1999)
- [90] H.L. Bethlem, A.J.A. van Roij, R.T. Jongma and G. Meijer, Phys. Rev. Lett. **88**, 13 (2002)

- [91] M.R. Tarbutt, H.L. Bethlem, J.J. Hudson, V.L. Ryanov, V.A. Ryzhov, B.E. Sauer, G. Meijer and E.A. Hinds, Phys. Rev. Lett. **92**, 17 (2004)
- [92] K. Wohlfart, F. Grätz, F. Filsinger, H. Haak, G. Meijer and J. Küpper, Phys. Rev. A **77**, 031404(R) (2008)
- [93] J. Küpper, F. Filsinger and G. Meijer, Faraday Discuss. **142**, 155-173 (2009)
- [94] N.E. Shafer-Ray, K.A. Milton, B.R. Furneaux, E.R.I. Abraham and G.R. Kalbfleisch, Phys. Rev. A **67**, 045401 (2003)
- [95] H.L. Bethlem, M. Kajita, B. Sartakov, G. Meijer and W. Ubachs, Eur. Phys. J. Special Topics **163**, 55-69 (2008)